Charge Waves on photoexcited type I $Al_xGa_{1-x}As/GaAs$ superlattices, under constant voltage and current bias.

José Ignacio Arana Tabernero

DOCTOR'S DEGREE ON MATHEMATICAL ENGINEERING
Departamento de Ciencia e Ingeniería de Materiales e Ingeniería Química
Universidad Carlos III de Madrid

ADVISOR:

L. L. Bonilla

Leganes July 2011

Nemo mortalium omnibus horis sapit (Plinio)

To my wife
To my daughter

ACKNOWLEDGEMENTS

Working through and finishing this PhD Thesis has been a complicated enterprise, which finally has come to its end. Now with joy, I can see it as a thing of the past seeking ways to combine work, family, politics and studies.

First of all, I want to express my special gratitude to Professor Luis L. Bonilla, for his confidence, his support, his patience and his dedication during all these years. Also, I also extend my gratitude to Gloria Platero for introducing me too, to the wonderful world of research.

Among all the people that I have known this years, I want to express my eternal gratitude to my friend Jose María Gambi because without him this work would have not been possible. Also I want to emphasize my gratitude towards Mario Salas, Maria del Carmen Rodriguez, Maria Luisa Garcia del Pino and Juan Jose Teixido; I think that we have been really good colleagues.

I would like to thank all the Gregorio Millán Institute lecturers, visitors and researchers who helped me, especially Holger T. Grahn, Stephen W. Teitsworth, Antonio Marquina, Ana Carpio, Ramon Escobedo, Manuel Kindelan, Miguel Angel Moscoso and Maria Angeles Hernandez Vozmediano whose classes in the PhD program I have enjoyed.

I am also in debt with Ana Maria Glavan, Rossmary Villegas, Natalia Irishina, Paul Medina, Guido dell'Acqua, Francisco Bernal, Ignacio Plans, Javier Hernandez Benitez, Alberto Portal, Alvaro Perales, Alfredo Deaño and Julio de Vicente for their friendship and for the all those good moments that we lived studying at the university.

I would like to honor my work ex-companions of the data processing center of the B.B.V.A., who know the meaning of being an externalized worker with 24×7 shifts. Specially to Alberto Trujillo, Armando Rolo, Juncal C. Romero and many others.

And Finally, I am grateful for my friends Adolfo Lazaro, Enrique Lainez, Jose Maicas and Jordi Ranz for his friendship in these last months.

I am sure that I forget to mention the name of many persons, who should be in this section. Sorry to all of them, I will thank them personally.

Contents

Chapter 1

Introduction

The intention of this PhD Thesis centres on the description, the study and the mathematical development of the charge waves on photoexcited type I $Al_xGa_{1-x}As/GaAs$ superlattices, under constant voltage and current bias. For that reason, in the second chapter, we introduce the basic and necessary concepts in order to understand the superlattices physics. By the semicondutor band structure we are able to study and define, the superlattice types and its main charge transport regime. The scattering processes are crucial to understand the charge drift velocity and the negative differential conductivity (NDC). The electron scattering process can be regulated by temperature and by the industrial growth of the superlattice.

An initial mathematical interlude is necessary. In the third chapter, the pulse solution of the spatially discrete excitable FitzHugh-Nagumo (FHN) system is approximately constructed using matched asymptotic expansions in the limit of large time scale separation (as measured by a small dimensionless parameter ϵ). The pulse profile typically consists of slowly varying regions of the excitatory variable separated by sharp wave fronts. In the FHN system, the velocity of a pulse is decided by the interaction between its leading and trailing fronts, but the leading order approximation gives only a fair result when compared with direct numerical solutions. A higher order approximation to the wave fronts comprising the FHN pulse is found. Our approximation provides a pulse velocity that depends on ϵ and compares much better with the velocity obtained from numerical solutions. As a result, the reconstruction of the FHN pulse using the improved wave fronts also agrees much better with the numerically obtained pulse.

In the fourth chapter, a model for charge transport in undoped, photo-excited semiconductor superlattices, which includes the dependence of the electron-hole recombination on the electric field and on the photo-excitation intensity through the field-dependent recombination coefficient, is proposed and analyzed. The photoexcitation is expressed by two dimensionaless parameters which

define the superlattice dynamics. Undoped and strongly photoexcited semiconductor superlattices with field-dependent recombination behave like excitable or oscillatory media with spatially discrete nonlinear convection and diffusion. In the following chapters, we use this model to explain and to find, the dc current and voltage biased superlattices behavior, including chaos.

Infinitely long dc current biased superlattices behaving as excitable media exhibit wave fronts with increasing or decreasing profiles whose velocities can be calculated by means of asymptotic methods. These superlattices can also support pulses of the electric field. Pulses moving downstream with the flux of electrons can be constructed from their component wave fronts whereas pulses advancing upstream do so slowly and experience saltatory motion. Large photoexcited superlattices can also behave as oscillatory media and exhibit wave trains. With small photoexcitation the dipole movement is described and compared with the large photoexcitation solutions.

Under dc voltage bias and high photo-excitation intensities, there appear self-sustained oscillations of the current due to a repeated homogeneous nucleation of a number of charge dipole waves inside the superlattice. In contrast to the case of a constant recombination coefficient, nucleated dipole waves can split for a field-dependent recombination coefficient in two oppositely moving dipoles. The key for understanding these unusual properties is that these superlattices have a unique static electric-field domain. At the same time, their dynamical behavior is akin to the one of an extended excitable system: an appropriate finite disturbance of the unique stable fixed point may cause a large excursion in phase space before returning to the stable state and trigger pulses and wave trains. The voltage bias constraint causes new waves to be nucleated when old ones reach the contact.

For a several superlattices, we use an algorithm that allow the estimation of the non-negative Lyapunov exponents from an experimental time series. In order to find chaos is advisable to use first other methods as Poincare's maps. The observed chaos is tiny and is found in superlattices with large photoexcitation and with small NDC region.

In the appendices we detail those important aspects that stem from the chapters; like the photoluminescence process, the stationary solutions of the model in dc current bias, the front pinning theory, other numerical solutions of the model as the unstable pulses at the first peak of the current, and so on. In addition, there is attached a relation of the constants and physical parameters. Finally there is annexed the relation of figures and movies used in previous sections, that we have attached in a CD with this PhD Thesis

Chapter 2

General Concepts on semiconductor superlattices

2.1 Introduction

The consecutive alternation of thin layers, of two or more materials, or compounds, (Metallics, insulatings, semiconductors, superconductors, magnetics, ferroelectrics, etc.), makes possible the creation of a new artificial superstructure which it is named a superlattice.

In case of the superlattices with different types of semiconductors compounds. Due to the diferent band gaps of alternating layers, the superstructure creates a periodic potential, of the valence and the conduction band, along the growth direction of the crystal lattice. This periodic potential consists in a succession of quantum wells and barriers for electrons and holes particles.

There are many types of semiconductor superlattices, depending on its own composition, as well as on the doping applied to the materials, on the layers thickness, etc. Semiconductor superlattices are used in the science and industry as high frequency oscillators, quantum lasers, photodetectors, pollution detectors, medical diagnosis, and control of the catalysis combustion in the industry of the automotion, etc..

This chapter introduces the basic physical concepts which have an importance in the context of this PhD Thesis. In the first part of this section, a few basic properties of $Al_xGa_{1-x}As/GaAs$ heterostructures are discused. Later we will focuses on electronic states in superlattices without and with applied electric fields. Finally we will see the main mechanism of vertical transport and the principal scattering processes.

2.2 Heterostructures and important aspects of the structure of bands

If a material have an applied electrical current, we can infer the existence of free charge carriers, untied from the atoms, moving inside it. Basically, depending on the resistance of the material at the movement of this free charge carriers, we can classify this material as insulator, conductor, semiconductor or superconductor. In this PhD Thesis, we will focus on $Al_xGa_{1-x}As$ semiconductors.

There are two basic types of "particles" that contribute on the total current, the electrons and the holes. The electrons, are the fundamental particles with negative charge, that if they find a electric difference potential they move towards the smallest potential. Nevertheless, the holes that have positive charge and represent the absence of an electron in a individual atom configuration, move towards the highest potential if they find a electric difference potential. The total current depends on the contribution of both movements in the material, but in some cases, like $GaAs$ semiconductor, the electrons mobility is much more greater than the holes mobility, so we can approach that electron current is the total current.

In crystalline solids such as semiconductors, the individual atoms are located on a periodic array of sites called the crystal lattice. The 3-dimensional crystal lattices can be classified in only 14 types Bravais lattices. The compounds GaAs and AlAs belong to the group III-V and they crystallize in the zinc-blende structure, or also known as fcc (*face centered cubic*) in the Bravais's classification. A difference between GaAs and AlAs crystals are the lattice constant a which differ by 0.14%. So the volume of the unit cell are similar in both cases. This offers in the crystal growth process an opporttunity to align materials with different properties with a great structural interface quality.

The lattice constant in $Al_xGa_{1-x}As/GaAs$ superlattices depends only weakly on x. Therefore $Al_xGa_{1-x}As/GaAs$ alloys with diferent x-content may be grown on the top of each other with a very little lattice strain.

The electronic and optical properties of these compounds, are determined by the energy band structure which also depends on the Bravais's lattice and on molecular orbitals from the atoms of the lattice. There are several mathematical and physical methods to obtain the band structure of a material, like the $k \cdot p$ *model, Tight binding...* Anyway, in semiconductor materials the allowed energy states are two, the valence band and the conduction band. In the valence band, there are the electrons tied to the atoms and the different types of holes. In the conduction band there are the free electrons. Between both bands there is a energy gap that no free charge carrier can be found or located

The first Brillouin zone contains a number of points of higher symetry, which are particulary useful in describing the band structure and the optical properties of the superlattices. In the next table some of this points are listed. Γ denotes the center of the Brillouin zone, while other points with lower symmetry are also indicated in *figure 2-1 (c)*.

Coordinates	Γ	Δ	Λ	Σ	L	W	X
fcc	000	$0k_y0$	$k_xk_yk_z$	k_xk_y0	$\frac{1}{4}\frac{1}{4}\frac{1}{4}$	$\frac{1}{4}\frac{1}{2}0$	$0\frac{1}{2}0$

In the figure 2-1(a)(b), we describe the band structure of the $GaAs$ and $AlAs$ semiconductors. Where the energies of the free charge carriers are represented. Two valence bands with diferent effective masses, called *heavy holes* and *light holes* band, coincide energetically at the Γ point for the $GaAs$ and $AlAs$ semiconductors. The conduction band of the $GaAs$ has three important minima at different position in k-space at Γ, X, and L points.

For the GaAs the Γ minimum is the lowest state in the conduction band. This allows a direct recombination of electrons and holes without the emision or obsortion of a phonon particle. $GaAs$ is therefore called a direct-gap semiconductor. In $AlAs$, in contrast, the lowest conducction band is the X minimum which makes $AlAs$ an indirect semiconductor material. This means that the recombination of electrons and holes can be facilitated by other particles like the phonons. So, the absorbed energy of the electron-hole creation is not necessary greater to the energy gap.

When two semiconductors with different energy gap are joined to each other, the balance condition is reached equalizing the Fermi's levels. This fact explains the existence of discontinuities in the spatial value of the conduction and valence band in the superlattices. If two or more discontinuities are sufficiently close, a sequence of quantum wells and barriers, have been created.

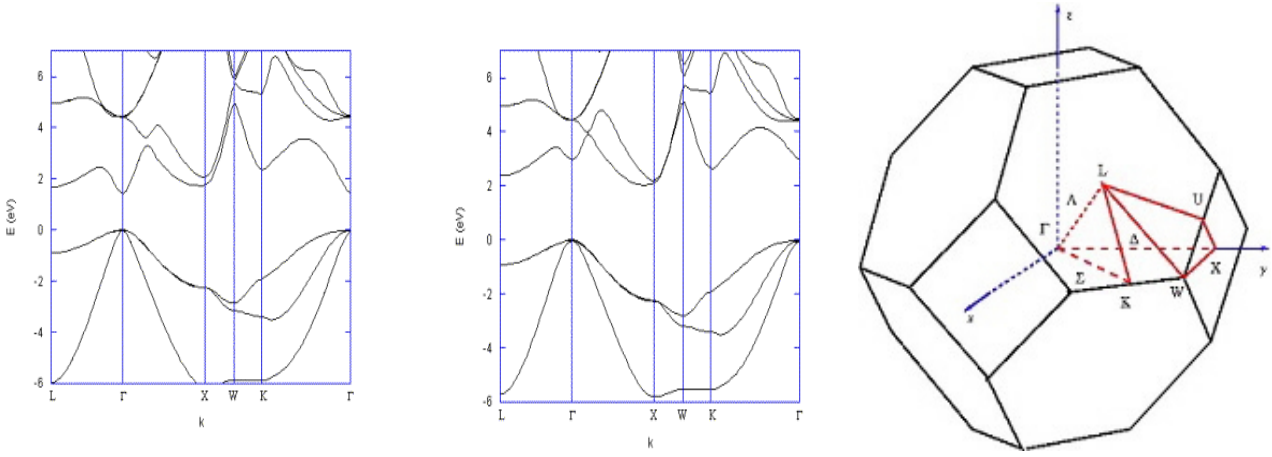

Figure 2-1:(a) Band structure of GaAs (direct gap) and **(b)** AlAs (indirect gap) **(c)** The simmetry points of the first Brillouin zone for the fcc lattice.

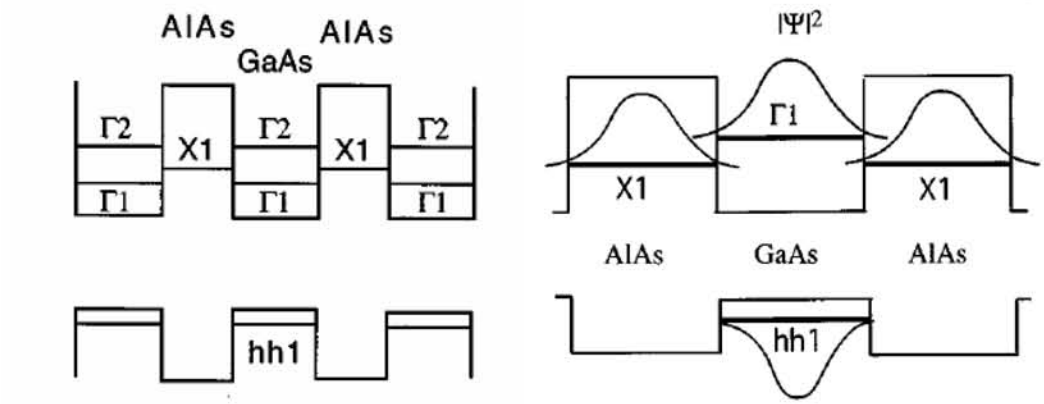

Figure 2-2 Diagrams of the periodic modulation of the Γ minimum of the conduction band and valence band in a GaAs/AlAs superlattices without any applied electric field. The position of the lower energy level of the Γ, X quantum wells define the **(a)** type I and **(b)** type II superlattices, [56].

In $AlAs/GaAs$ superlattices, the modulation of the conduction band in all positions in k-space creates different types of barriers and quantum wells. The Γ and L quantum wells are placed in the $GaAs$ material, and the X quantum wells are situated in the $AlAs$ compound. Finally, light hole and heavy hole quantum well are always placed in the $GaAs$ layers.

The different electronic quantum wells (Γ, X and L) have different energy levels of distinct magnitude, and these, are occupied according to the temperature of the semiconductor and according to the value of these energy levels. At low temperatures, the most occupied energy level is situated in the quantum well with lower energy level. The position, in the GaAs or AlAs materials, of the most populated electron quantum well, as well as the holes quantum well position, defines the type of the superlattice. If the electron quantum well is placed over the holes quantum well, the superlattice is defined as the type I, [57].

If these conditions are not fulfilled, the $Al_xGa_{1-x}As/GaAs$ superlattice is defined as type II (*figure 2-2 (b)*). The recombination electron-holes couples is bigger in the type I superlattices (*figure 2-2 (a)*). In addition unlike those of type II, the electron-holes recombination decreases with the applied electrical field.

The position of the energy levels of all types of quantum wells in the $Al_xGa_{1-x}As/GaAs$ superlattices depends on the x-content. The position of the energy levels is also affected by the quantum-confined Stark effect. But basically, the periodicity of the superlattice, as well as the difference of effective masses of the free charge carriers, are the key to define the type superlattice that we are working on it.

2.3 Transport regimes

When an electrical field, $-\tilde{F}$, is applied to a semiconductor, in the $\tilde{z}$ direction, the conduction band inclines with a potential $e\tilde{F}\tilde{z}$. Being defined the electron charge as $-e < 0$. The free charge carriers move in the $\tilde{z}$ direction, electrons to the right and holes to the left. The energy distribution of the carriers is also affected, the scattering time itself depends on energy. In order to determine, how the distribution function $f(\tilde{z}, k, \tilde{t})$ is influenced by an electric field, we have to solve the Boltzmann´s equation:

$$\frac{df(\tilde{z},k,\tilde{t})}{d\tilde{t}} = \frac{\partial f(\tilde{z},k,\tilde{t})}{\partial r}\frac{d\tilde{z}}{d\tilde{t}} + \frac{\partial f(\tilde{z},k,\tilde{t})}{\partial k}\frac{dk}{d\tilde{t}} + \frac{\partial f(\tilde{z},k,\tilde{t})}{\partial \tilde{t}} = \left(\frac{\partial f(\tilde{z},k,\tilde{t})}{\partial \tilde{t}}\right)_{scatt}$$

$$v(\tilde{z},k,\tilde{F},\tilde{t})\cdot\nabla_{\tilde{z}} f(\tilde{z},k,\tilde{t}) - \frac{e}{\hbar}\tilde{F}\cdot\nabla_k f(\tilde{z},k,\tilde{t}) + \frac{\partial f(\tilde{z},k,\tilde{t})}{\partial \tilde{t}} = \left(\frac{\partial f(\tilde{z},k,\tilde{t})}{\partial \tilde{t}}\right)_{scatt} \tag{2.1}$$

The first term describes the diffusion procesess, since it requires a change of f in real space. The second term shows the variation of f under the application of an external electric field. The third term gives the variation due to the explicit time dependence. Finally the last term is the collision term which is the most dificult term. To express it, can be used the relaxation-time approximation:

$$\left(\frac{\partial f(\tilde{z},k,\tilde{t})}{\partial \tilde{t}}\right)_{scatt} = \frac{f(\tilde{z},k,\tilde{t})_{eq} - f(\tilde{z},k,\tilde{t})}{\tau(k)}$$

Where $f(\tilde{z},k,t)_{eq}$ represents the balance distribution function of the charge carriers and τ is the average scattering time.

If we assume that the distribution function does not have temporal and $\tilde{z}$ spatial dependence, we can obtain the following expression for the current density in a semiconductor:

$$J_z(T,\tilde{F}) = e^2 n\tilde{F}\frac{\int d^3k\ \tau(k)v_z^2\frac{\partial f(k)}{\partial E}}{\int d^3k\ f(k)}$$

Nevertheless in the superlattices, the distribution function and the relaxation time scattering depend on the spatial direction. Depending on the type of free charge carriers distribution function type, the superlattice will have a different transport regime. We distinguish three different transport regimes types:

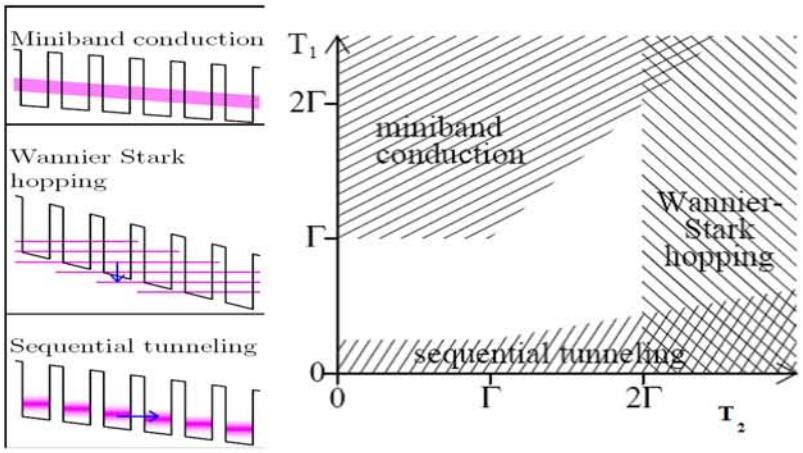

Figure 2-3 (a) Diagram transport regimes in a $Al_xGa_{1-x}As/GaAs$ superlattice **(b)** Ranges of validity of transport regimes, at the limit $\tilde{T} \to 0$. [60]

- Conduction by minibands, where the charge carriers are distributed in energy bands that occupies the whole superlattice,

- Conduction by Wannier-Stark hopping, when the free charge carriers are distributed in a long energy band that occupy several quantum wells; and finally,

- Conduction by Sequential Tunneling, when the charge carriers are located only in a quantum well.

Where the range of validity of these transport regimes are described in the *figure 2-3.* This range depends on temperature, the interwell coupling (T_1) and the potential drop per period ($T_2 = eF\tilde{l}$). Being $\tilde{l}$, τ and $\Gamma = \hbar/\tau$, the period of the superlattice, the lifetime of the carriers in the energy levels and the width of the energetic broadening.

2.3.1 Conduction by minibands

The solution of the schrödinger equation for a periodic one-dimensional potential was first obtain by Kronig and Penney in 1931. Two different values for the potential and the effective mass are used in the length period.

$$E_n^c \Psi_k(\tilde{z}) = \left(-\frac{\hbar^2}{2}\frac{d}{d\tilde{z}}\left(\frac{1}{m^*(\tilde{z})}\frac{d}{d\tilde{z}}\right) + \tilde{V}(\tilde{z})\right)\Psi_k(\tilde{z}), \tag{2.2}$$

$$m^*(\tilde{z}) = \begin{cases} m_w^* & 0 < \tilde{z} - n\tilde{l} < \tilde{L}_w \\ m_b^* & \tilde{L}_w < \tilde{z} - n\tilde{l} < \tilde{L}_w + \tilde{L}_b \end{cases} \quad \tilde{V}(\tilde{z}) = \begin{cases} 0 & 0 < \tilde{z} - n\tilde{l} < \tilde{L}_w \\ \Delta E_c & \tilde{L}_w < \tilde{z} - n\tilde{l} < \tilde{L}_w + \tilde{L}_b \end{cases}$$

Where $\tilde{L}_w$ is the length of the quantum wells and $\tilde{L}_b$ is the length of the barriers. ΔE_c is the band offset which depends on the Al content on the barrier.

As the superlattices have a periodic profile of the valence and conduction band in the $\tilde{z}$ direction, it is possible to apply the Bloch's theorem to find the allowed estates of the free charge carriers:

$$\begin{aligned} \Psi_k(\tilde{z}-\tilde{l}) &= \Psi_k(\tilde{z})e^{-ik\tilde{l}} \\ \left.\frac{d\Psi_k(\tilde{z})}{d\tilde{z}}\right|_{\tilde{z}-\tilde{l}} &= \left.\frac{d\Psi_k(\tilde{z})}{d\tilde{z}}\right|_{\tilde{z}} \end{aligned}$$

The possible solution of this problem will exist and can be calculated if the following expression is satisfied, [46]:

$$\begin{aligned} \cos(k_z\tilde{l}) &= G(k_w,\kappa_b) = \cos(k_w\cdot\tilde{L}_w)\cdot cosh(\kappa_b\cdot\tilde{L}_b) - \frac{1}{2}(\xi-1/\xi)\cdot sin(k_w\cdot\tilde{L}_w)\cdot sinh(\kappa_b\cdot\tilde{L}_b); \\ \xi &= \frac{m_b^* k_w}{m_w^*\kappa_b} \quad k_w = \sqrt{2m_w^* E}/\hbar \quad \kappa_b = \sqrt{2m_w^*(\Delta E_c - E)}/\hbar \end{aligned} \tag{2.3}$$

The solution of this equation, can be obtained numerically and consists in a succession of allowed energies and band gaps. The center of these energy bands, E_n^c, can be numericaly approximated. A valid typical approximation, when the gap between minibands is much larger than their widths, yields tight binding dispersion relation, [16]:

$$E_n(k_w) = E_n^c + (-1)^n\frac{\Delta_n}{2}\cos(k_w\tilde{l}) \tag{2.4}$$

Where $k_w\tilde{l}$ runs from $-\pi$ to π. The energy at the center of the band is obtained, when $k_w\tilde{l} = \pi/2$. Δ_n is the energy broadening of the miniband that is defined by the following expression:

$$\Delta_n = \frac{8(\Delta E_c - E_n^c)}{\kappa_b(E_n^c)\frac{dG}{d\kappa_b}(E_n^c)}\exp(-\kappa_b(E_n^c)\cdot\tilde{L}_b) \tag{2.5}$$

The widths of the energy bands increases with increasing energy, while the widths of the gaps remains almost constant.

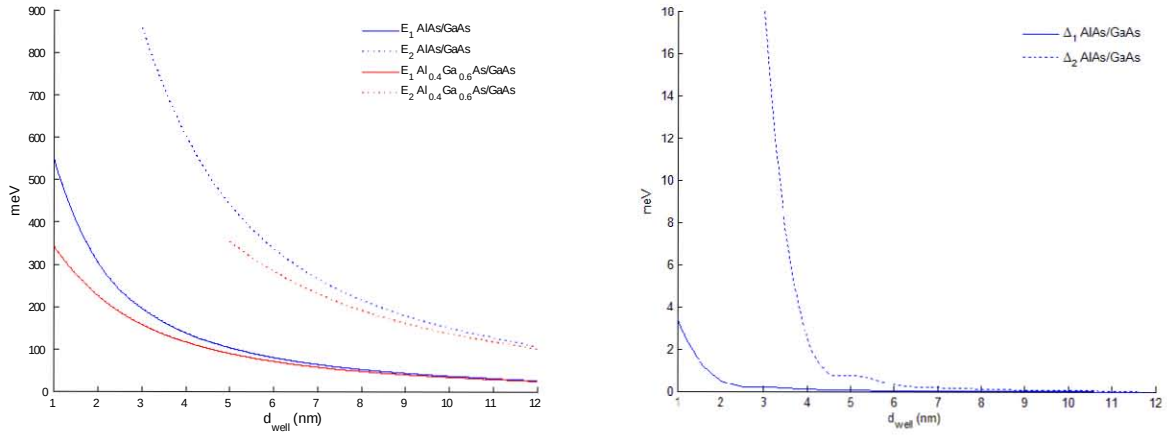

Figure 2-4 (a) Miniband energy levels and **(b)** broadening of the miniband energy level, for superlattices with $\mathrm{d}_{barrier} = 4\ nm$ of barrier width.

For a superlattice whose the only populated miniband is the lowest energy level, we can apply the Boltzmann-Poisson-Bhatnagar-Gross-Krook (BPBGK) system for 1D electron transport of a strongly coupled dopped SL is, [71]:

$$
\begin{aligned}
-\vartheta_{imp}\mathfrak{A}f - \vartheta_{en}(f - f^{FD}) &= \frac{1}{\hbar}\frac{\partial \mathcal{E}_1}{\partial k}\frac{\partial f}{\partial \tilde{z}} + \frac{e}{\hbar}W(\tilde{z})\frac{\partial f}{\partial k} + \frac{\partial f}{\partial t} \qquad (2.6)\\
\varepsilon\frac{\partial^2 W}{\partial \tilde{z}^2} &= \frac{e}{\tilde{l}}(\tilde{n} - N_D)\\
\tilde{F} &= \frac{\partial \tilde{W}}{\partial \tilde{z}}\ ,\\
0 &= \frac{e}{\tilde{l}}\frac{\partial \tilde{n}}{\partial t} + \frac{\partial \tilde{J}_n}{\partial \tilde{z}}\\
\tilde{J}_n(\tilde{z},t) &= \frac{e}{2\pi}\int_{-\pi/\tilde{l}}^{\pi/\tilde{l}} v(k) f(\tilde{z},k,t)dk\\
f^{FD}(k;\tilde{n}) &= \frac{m^* k_B \tilde{T}}{\pi\hbar^2}\int_{-\infty}^{\infty} \ln[1+\exp\left(\frac{\mu - E}{k_B\tilde{T}}\right)]\frac{\sqrt{2}\Gamma^3/\pi}{[E-\mathcal{E}_1(k)]^4 + \Gamma^4}dE\\
\tilde{n}(\tilde{z},t) &= \frac{\tilde{l}}{(2\pi)}\int_{-\pi/\tilde{l}}^{\pi/\tilde{l}} f(\tilde{z},k,t)dk = \frac{\tilde{l}}{(2\pi)}\int_{-\pi/\tilde{l}}^{\pi/\tilde{l}} f^{FD}(n(\tilde{z},t),k)dk
\end{aligned}
$$

Here $v(k)$, $\tilde{\mu}$, $\tilde{J}_n$, $\mathfrak{A}f = \frac{1}{2}[f\ (z,k,t) - f(z,-k,t)]$, $f^{FD}(k;n)$, $\tilde{n}$, N_D, $\mathcal{E}_1$, W, ε, k_B, ϑ_{en} , ϑ_{imp} and Γ are the electron group velocity, the chemical potential, the electron current density, the odd part of the one-particle distribution function, the 1D local equilibrium distribution function, the

2D electron density, 2D doping density, the miniband dispersion relation, the electric potential, the SL permittivity, the Boltzmann´s constant, the constant frequency of the inelastic collisions responsible for energy relaxation, the constant frequency of the elastic impurity collisions and the energy broadening of the equilibrium distribution due to collisions, respectively.

The main idea behind these equations is to substitute the linear Boltzmann collision terms, which are nonlocal in k by a nonlinear collision term. This system preserves charge, but not momentum or energy. After some math, can be obtained the following generalized drift-diffusion equation which is a form of the Ampère's law:

$$\varepsilon\frac{\partial\tilde{F}}{\partial\tilde{z}}+\frac{ev_m}{\tilde{l}}\mathcal{N}\left(\tilde{F},\frac{\partial\tilde{F}}{\partial\tilde{z}}\right)=\varepsilon\mathcal{D}\left(\tilde{F},\frac{\partial\tilde{F}}{\partial\tilde{z}}\right)\frac{\partial^2\tilde{F}}{\partial\tilde{z}^2}+\mathcal{A}\left(\tilde{F},\frac{\partial\tilde{F}}{\partial\tilde{z}}\right)J(\tilde{t}) \tag{2.7}$$

where

$$\begin{aligned}
v_m &= \frac{\Delta_1\tilde{l}I_1(M)}{4\hbar\tau_eI_0(M)}, \qquad \tau_e=\sqrt{1+\frac{\vartheta_{imp}}{\vartheta_{en}}}\ , \qquad F_M=\frac{\hbar\tau_e\vartheta_{en}}{e\tilde{l}},\\
\mu &= \frac{\tilde{\mu}}{k_B\tilde{T}}, \quad \mathcal{F}=\tilde{F}/F_M, \quad I_m(\mu)=\frac{\tilde{l}}{(2\pi)}\int_{-\pi}^{\pi}\gamma(\frac{\mathcal{E}_1(k)}{k_B\tilde{T}}-\mu)\cos(mk\tilde{l})dk\\
\gamma(E) &= \frac{m^*k_B\tilde{T}}{\pi\hbar^2}\int_{-\infty}^{\infty}\ln[1+e^{-s}]\frac{\frac{\sqrt{2}}{\pi}\left(\frac{\Gamma}{k_B\tilde{T}}\right)^3}{[s-E]^4+\left(\frac{\Gamma}{k_B\tilde{T}}\right)^4}ds\\
\mathcal{N} &= \tilde{n}\mathcal{V}\mathcal{M}_1\mathcal{A}-\frac{e\Delta_1\tilde{l}^2}{\hbar^2\tau_e^2\vartheta_{en}^2}\frac{\mathcal{B}}{1+\mathcal{F}^2}\frac{\partial\tilde{F}}{\partial\tilde{z}}, \quad \mathcal{M}_m(\tilde{n}/N_D)=\frac{I_m(\mu)I_0(M)}{I_1(M)I_0(\mu)}\\
\mathcal{V} &= \frac{2\mathcal{F}}{1+\mathcal{F}^2}, \quad \mathcal{A}=1+\frac{2e^2v_m[1-(1+2\tau_e^2)\mathcal{F}^2]}{\varepsilon\hbar\vartheta_{en}^2\tau_e^2(1+\mathcal{F}^2)^3}\tilde{n}\mathcal{M}_1\\
\mathcal{B} &= \frac{\tilde{n}\mathcal{M}_2\mathcal{F}(5-4\mathcal{F}^2)}{(1+4\mathcal{F}^2)^2}-\frac{4\hbar v_m(1+\tau_e^2)}{\Delta_1\tilde{l}\tau_e}\tilde{n}\mathcal{M}_1(\tilde{n}\mathcal{M}_1)'\mathcal{F}\frac{1-\mathcal{F}^2}{(1+\mathcal{F}^2)^3},\\
\mathcal{D} &= \frac{\Delta_1^2\tilde{l}^2}{8\hbar^2\vartheta_{en}\tau_e^2(1+\mathcal{F}^2)}(1-\frac{4\hbar v_m\tau_e\mathcal{C}}{\Delta_1\tilde{l}})\\
\mathcal{C} &= (\tilde{n}\mathcal{M}_2)'\frac{1-2\mathcal{F}^2}{1+4\mathcal{F}^2}+\frac{8(1+\tau_e^2)\hbar v_m}{\Delta_1\tilde{l}\tau_e}\left(\frac{\mathcal{F}(\tilde{n}\mathcal{M}_1)'}{1+\mathcal{F}^2}\right)^2
\end{aligned}$$

In the limit of high temperatures, $k_B\tilde{T} >> \max(\Delta_1, \pi\hbar^2N_D/m^*)$, equation (2.7) has the usual Esaki-Tsu drift velocity form represented in *figure 2-5*. Here, the electron mobility and the diffusion coeficient are:

$$\mu_e(\tilde{F})=\frac{e\tilde{l}^2\Delta_1^2}{8k_B\tilde{T}\hbar^2\vartheta_{en}}\frac{1}{1+\left(\frac{e\tilde{F}\tilde{l}}{\hbar\vartheta_{en}}\right)} \qquad D(\tilde{F})=\frac{k_B\tilde{T}}{e}\mu_e(\tilde{F}) \tag{2.8}$$

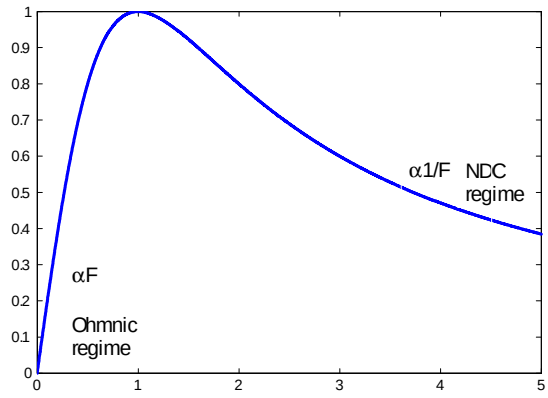

Figure 2-5 Nondimensional miniband drift velocity.

Numerical solutions of the previous system of equations display self-sustained current oscillations due to repeated nucleation and motion of charge dipole waves.

As we can see in the *figure 2-4*, the thickness and the number of minibands depends on the well and the barrier size. As the width of quantum well grows, the energy broadening of the miniband have a minor value. As a consequence, the free charge carriers will have less allowed states inside the miniband. If the thickness of the minibands is excessively small, this transport regime will already not be possible in the superlattice.

Therefore, as in reference [72], if the collision broadening is greater than the miniband width or the mean free path $\lambda = v(\tilde{F}_c)\tau$ fulfills the relation $\lambda < N\tilde{l}$, where N is the number of quantum wells in the superlattice, the conduction will not be by minibands and the superlattice will start to conduct by *Wannier-hopping regime*

2.3.2 Conduction by *Wannier-Stark hopping.*

The periodic potential of the equation (2.2) depends on the electrical field by the form $\tilde{V}(\tilde{z}) - e\tilde{F}\tilde{z}$ and energy spectrum of (2.2) he can be obtained by symmetry considerations: if $\chi^{\nu}(\tilde{z})$ is an eigenfunction of (2.2) with energy ε , then $\chi^{\nu}(\tilde{z} - n\tilde{l})$ is also an eigenfunction with energy $\varepsilon - en\tilde{F}\tilde{l}$.

It is possible to look for the solution of the equation (2.2) by a *Wannier* function basis, [45]:

$$\chi^{\nu}(\tilde{z} - n\tilde{l}) = \sum_{m} c^{\nu}(n-m) w^{\nu}(z - m\tilde{l})$$

Where:

$$
\begin{aligned}
c^{\nu}(n-m) &= \frac{\tilde{l}}{2\pi}\int_{-\pi/\tilde{l}}^{\pi/\tilde{l}} e^{-i[k\tilde{l}(n-m)-\frac{1}{e\tilde{F}}\int_{-\pi/\tilde{l}}^{k}\varepsilon(k')dk']}dk \\
w^{\nu}(z-m\tilde{l}) &= \sqrt{\frac{d}{2\pi}}\int_{-\pi/\tilde{l}}^{\pi/\tilde{l}} e^{-im\tilde{l}k}\Psi_k(\tilde{z})dk
\end{aligned}
$$

The *Wannier* function is centered in $z = m\tilde{l}$ and is ortonormal to other *Wannier's* functions:

$$
\int_{-\infty}^{\infty}\bar{\chi}^{\mu}(z-m\tilde{l})\chi^{\nu}(z-n\tilde{l}) = \delta_{\mu\nu}\delta_{mn}
$$

The coefficient $c^{\nu}(n-m)$ decreases when the difference $|n-m|$ is increased and can be approached to zero when $\tilde{l}|n-m|$ is comparable to $\Delta_n/e\tilde{F}$.

If $\lambda = \Delta_n/e\tilde{F}$ fulfills the relation $\lambda < \tilde{l}$, *Wannier* functions are localized in a different well. As consequence, the superlattice will not conduct by *Wannier-Stark hopping*, and only is able to conduct by subbands conduction.

The electrons movement in the direction of electrical field can be approached by the following expression, [62]:

$$
v(\tilde{F}) = \sum_{\nu=1}^{\infty}\nu\tilde{l}t_{0\to\nu}(\tilde{F})(1-e^{-\nu e\tilde{F}\tilde{l}/k_b\tilde{T}}), \tag{2.9}
$$

being $t_{0\to\nu}$ the ratio of $0 \to \nu$ transition and his value can be obtained by:

$$
t_{0\to\nu} = \frac{2}{\tilde{n}^{(2D)}}\sum_{k}\sum_{k'} f(k)[1-f(k')]S(0k,\nu k')
$$

where $f(k)$ is the initial distribution function of the electrons and $f(k')$ the final distribution function. The solution of the Bolzmann´s equation allows the calculation of the electron distribution in k-space. The scattering ratio $S(0k,\nu k')$ and therefore the total drift velocity, depends on the scattering processes in the superlattice, and can be calculated by the Fermi's golden rule.

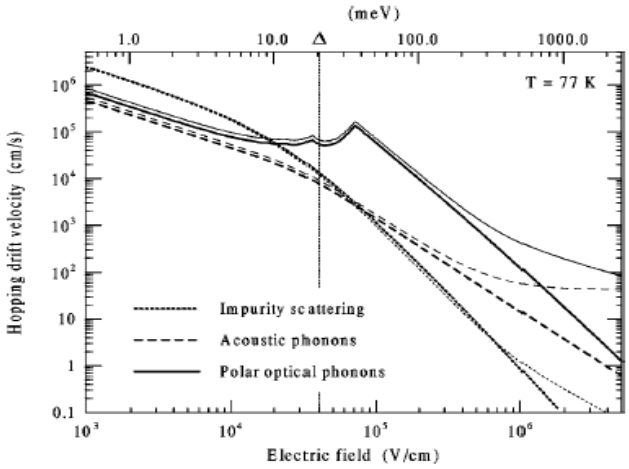

Figure 2-6 (a) Comparison of the Wannier-Stark hopping drift velocity for different scattering processes of in a doped AlAs/GaAs(1.7/3.4) superlattice, [64].

In *figure 2-6* there is a peak in the hopping drift velocity at the polar optical phonon energy. This means that LO phonon scattering between adjacent Wannier-stark states is the dominant scattering process at low temperature. Here, scattering times are much larger than tunnelling times.

2.3.3 Conduction by subbands.

In this regime, the electrons are located in an energetic level situated in a single quantum well. This is due to the fact that the coupling between the different quantum wells is very weak. In spite of the fact that the coupling is weak, the electrons can jump between the contiguous quantum wells by the tunnel effect. The probability of this process depends on the broadening and on the alignment of the energy levels of the neighboring quantum wells.

In a superlattice where no electrical field is applied to it, all the energy levels are aligned. As consequence, the electron jumping probability is the same in relation to the neighboring wells, no current could be possible or, in other words, the electron average drift velocity is equal to zero.

If we apply a small voltage to the superlattice, the energetic levels of the quantum wells are not perfectly aligned. But in this case, the electrons use the energy broadening to be able to jump to the contiguous well by the tunnel effect. As an electrical field exists over the superlattice, the probability of jumping to the neighboring wells will not be the same. And therefore there is an average electronic speed with a non zero value.

If a greater voltage is applied, the energy levels stop being aligned and the process of electron transport by tunnel effect is reduced. In this range of values of the applied electrical field, we say that the quantum wells are in the region of *Negative Differential Conductance* (**NDC**).

For bigger values of the electrical field, the first energetic level of the quantum well will line up with the second or the third energetic level of the neighbor quantum well; in these values of the electrical field, peaks in the current will appear (*figure 2-7*). This process is known as Resonant sequential tunneling (**RST**).

As depicted in *figure 2-7 (a),* when the first level and the second level is line up, an additional intersubband relaxation must take place before the next tunneling event can occur. The relaxation time is smaller than the tunneling time, so can be ignored.

The energetic position of the subbands respect to the applied electrical field and the width of quantum well determines all the regime properties of the superlattice. If the thickness of the GaAs is the sufficiently small, the subband with less energy will not be situated in the Γ quantum well, *figure 2-8 (a)*, and as consequence the superlattice will conduct by the X quantum wells, placed in the $Al_xGa_{1-x}As$ compound, being a type II superlattice .

The transmission of electrons through the $Al_xGa_{1-x}As$ barriers may not only occur due the tunneling procesess between Γ subbands of adjacent wells, but also due to transport via $X-$states within barriers. While for small fields the $\Gamma-\Gamma$ tunneling process dominates, for electric fields above the first $\Gamma - X$ resonance, transport through the lowest X-levels becomes the dominant transport process.

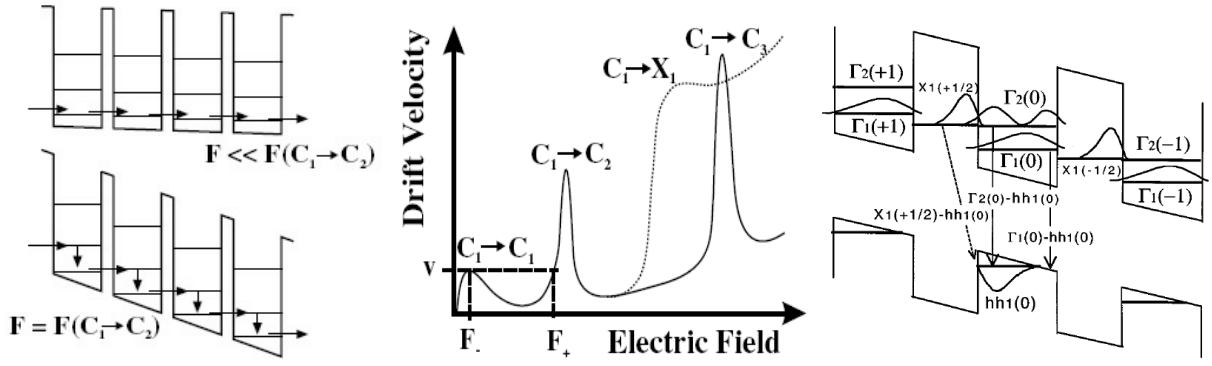

Figure 2-7 (a) Diagram and **(b)** drift velocity function of the electrons transport by resonant sequential tunnel effect. **(c)** $\Gamma - X$ resonance diagram in a $AlGa/GaAs$ superlattice, [43], [56].

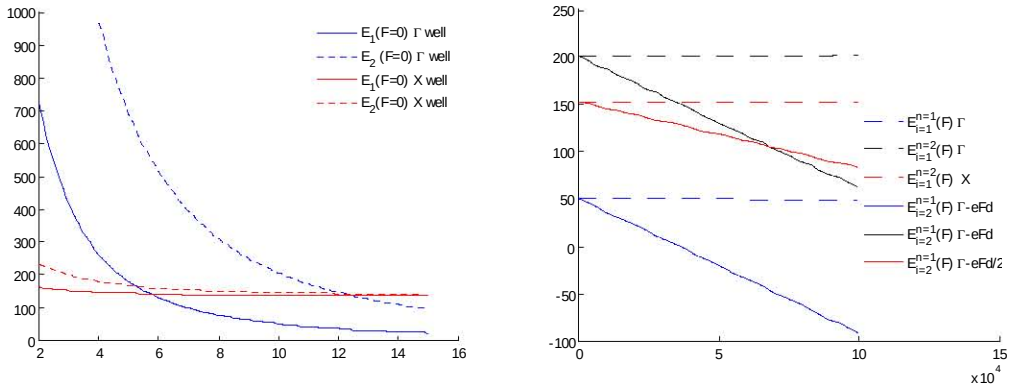

Figure 2-8 (a) First Γ and X subbands versus the width of the well, without applied electric field. **(b)** The two lower Γ and X energy levels (meV) versus electric field (V/cm), of an adjacent wells, in a AlAs/GaAs(4/10) SL.

The electrical field applied to a well modifies the energetic value of all the subbands which it contains, by the *quantum-confined stark effect*. As we can see in *figure 2-8,* depending on the periodicity of the superlattice and as well as the composition of aluminium in the barriers, the resonance of the subbands $\Gamma - X$, occurs in a certain value of the electrical field.

2.4 Scattering processes

The mobility is a key magnitude in the semiconductors physics, and is closely related with the speed of the devices and electronic components. It also has relation with the energy broadening by the Heisenberg uncertainty principle. It is proportional to the average time of the *scattering* processes, or relaxation time τ_i, and inverse dependent to the free carrier effective mass.

There are multiple *scattering* processes that slow down the movement of the free charge carriers. The total mobility on the semiconductor layers can be determined by the worst mobility of all the s*cattering* processes, or in other words, for the lower relaxation time:

$$\frac{1}{\mu_f} = \frac{m^*}{e} \sum_i \frac{1}{\tau_i}$$

The predominant scattering processes in a semiconductor, for which an electron stops in his movement and returns to be accelerated by the electrical field, are the collisions processes with phonons and the impurities of the crystalline lattice.

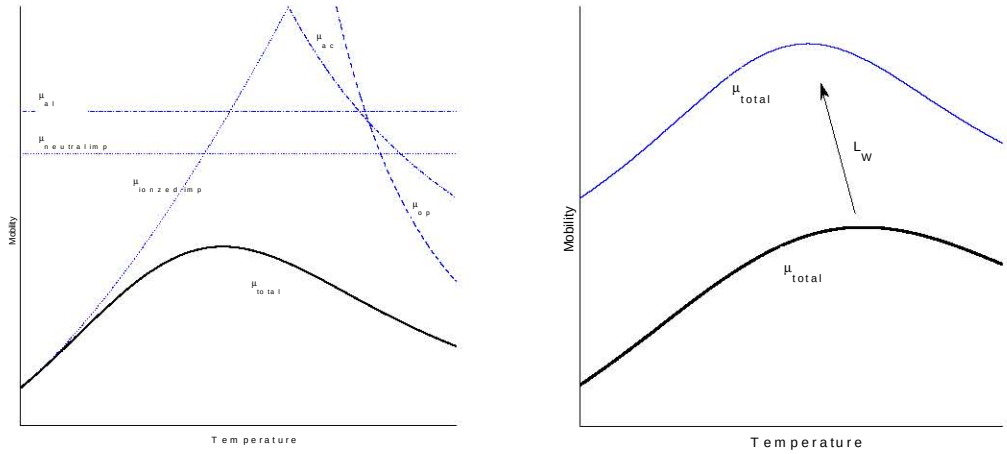

Figure 2-9 (a) Sketch of the total SL mobility versus temperature, the contribution of the principal scattering processes are also represented. **(b)** quantum well length dependence on the mobility value versus temperature, [73].

The phonons oscillations modulate the valence and conduction band by the variation of the lattice constant. The stress of any material semiconductor to be deformed by pressure also changes the lattice constant, and in addition, can induce to a macrocospic effect of interaction called piezo-electrical effect. These processes, at high temperature, influence notably the collisions statistics of the electrons in the superlattice.

Both charge carriers, the electrons and the holes can be scattered with impurities, which can be ionized or neutral. In case of neutral impurities the charge carriers interact with the atom, and not with the long range coulombic interaction that has the ionized impurity. In any case, at extremely low temperatures, all the impurities become neutral.

The dependence of the relaxation time, of the different *scattering* processes, with the temperature, is defined in the following expression, which is only valid in the limit of Maxwell-Bolzmann statistics:

$$\tau(T) = \frac{\int_0^\infty \tau(E) E^{3/2} f(E) dE}{\int_0^\infty E^{3/2} f(E) dE}$$

Some important bulk *scattering* processes appear in the following table, as well as their temperature dependence, [16]:

μ	Prefactor	Temperature dependence
acustic phonon	$\frac{2\sqrt{2\pi}e\hbar^4 c_l}{3m^{*5/2}\varepsilon_{ac}^2}$	$(K_bT)^{-3/2}$
optical phonon	$\frac{4\sqrt{2\pi}e\hbar^2 c\rho\sqrt{K_b\theta_d}}{3m^{*5/2}D^2}$	$(\theta_d/T)^{5/2}(\mathrm{e}^{\theta_d/T}-1)$
neutral impurity	$\frac{e^3 m^*}{80\pi\hbar^3\varepsilon\varepsilon_0 N_I}$	1
ionized impurity	$\frac{128\sqrt{2\pi}(\varepsilon\varepsilon_0)^2}{Z^2\sqrt{m^*}e^3 N_I}$	$(K_bT)^{3/2}$

Where ε_{ac} is the acoustic deformation potential and it depends on the semiconductor material, c_l is the elastic longitudinal constant, θ_d is the Debye´s temperature, ρ is the cristal density, D is the optical deformation potential, N_I is the density of impurities, Ze denotes the ion charge.

When an electrical field is applied in the SL, the electrons can acquire enough energy so that they can be transfered to another conduction band minimum. In a $Al_xGa_{1-x}As/GaAs$ SL, the mobilty of the $X-$ and $L-$valley is smaller than that of the $\Gamma-$valley, since the effective mass in those valleys is larger. See appendix A.10.

Many types of sccatering processes exist and have been studied intensively this decades. Some of them can be industrially regulated or reduced, the following processes have this property.

2.4.1 Interface roughness *scattering*

The well - barrier interface is never perfect. In the SL growth process structural defects are made, sometimes it happens that some atoms of the well spread into the barrier and vice versa, or simply that the atoms do not occupy his own position in the crystalline lattice (*figure 2-10*). In addition, due to these defects, the imbalance of the crystal lattice generates stress in the interface well-barrier and as consequence, generate a new valuable density of defects and lattice dislocations, [74].

If we suppose that a defect is characterized by his depth h along the axis of growth, and the ideal barrier begins in $z = 0$ with a lateral extension, l_x, l_y, we have:

$$V_{def}(r,\rho) = V_b\Theta(z(h-z))\Theta(\frac{l_x^2}{4}-(x-x_i)^2)\Theta(\frac{l_y^2}{4}-(y-y_i)^2)$$

For a defect centred in $\rho_i = (x_i - y_i)$, the scattering time can be obtained by the following expression, [44]:

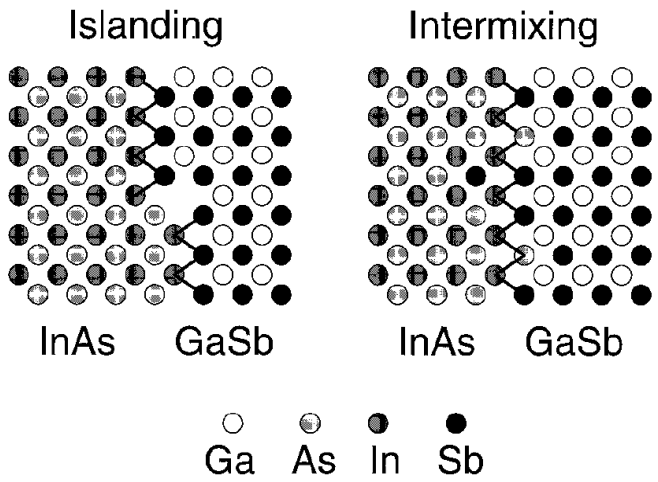

Figure 2-10 (a) Defects types diagram in a InAs/GaSb SL, [67].

$$\frac{\hbar}{\tau_{roug}(\varepsilon_F)} = 16V_b^2h^2N_{def}\chi_1^4(0)\frac{m_1}{\pi\hbar^2}\times \int_0^{\pi}\frac{d\theta}{\varepsilon^2(2k_F sen\frac{\theta}{2})}\times\frac{sen^2(\frac{1}{2}k_F l_x(\cos\theta-1))}{k_F^4 sen^2\theta(1-\cos\theta)}\times sen^2(\frac{1}{2}k_F l_y sen\theta)$$

Where $k_F=(2\pi n_e)^{1/2}$ is the Fermi´s autovector, N_{def} is the defects concentration and $\chi_1(\tilde{z})$ is the eigenfunction Fang Howard who can be found in [44].

2.4.2 Alloy *Scattering*

This scattering process takes place in semiconductors that are a ternary materials of the III-V compounds. In the $Al_xGa_{1-x}As$ layers, one of the constituting atoms (As) occupies the site of one of the face-centred cubic lattices of the zinc blende crystal.

The other atoms types (Al and Ga) are randomly distributed on the sites of the second face-centred cubic lattice. Thus, although the underlying lattice is periodic, the crystal potential is actually non-periodic.

Respect $Al_xGa_{1-x}As/GaAs$ SLs. If the electron gas is essentially located in the binary material then are faintly experiences of the alloy scattering in the ternary barrier. For $X-$tunneling, the electron gas is essentially localized in the ternary alloy and weakly penetrates in the GaAs barrier, so this *scattering* process has to be considered.

To be able to treat this problem, there are two used methods, the coherent potential approximation and virtual crystal approximation. In the last mentioned method, the not periodic potential, due to the atoms that are randomly distributed in a fcc lattice, is replaced by a periodic potential produced by an " average atom" that occupies this lattice.

The difference between the real potential and this virtual crystal potential, is what produces the alloy scattering. This alloy scattering, can be considered as a sum of scatterings produced by short range potentials, $\delta V(r)$ (or a sum of uncorrelated delta-like potential).

The averaged scattering matrix element is proportional to the integral of $\chi_n^4(z)$ (Part of the wave function that contains the dependence in z of the eigenstates) over the part of the heterostructure where we have the ternary alloy. The mobility and the scattering time can be obtained by the following equations:

$$\mu_{al} = \frac{e\tau_{al}(\varepsilon_F)}{m_1} \qquad \frac{1}{\tau_{al}(\varepsilon_F)} = m_1 \frac{\Omega_0}{\hbar^3}[\delta V(r)]^2 x(1-x) \int \chi_n^4(z) dz,$$

where Ω_0 is the volume of the unit cell and x is the percentage of the alloy$A_x B_{1-x} C$. The mobility is obtained evaluating the integral of the previous equation, so, it is necessary to to obtain $\chi_n(z)$ for the specific SL. The definition of the transport regime in the SL is also cruzial to evaluate it.

Chapter 3

Mathematical interlude: Velocity of pulses in discrete excitable systems

3.1 Introduction

Many physical and biological systems made up of smaller interacting components such as atoms, quantum wells, cells, etc. can often described by spatially discrete nonlinear equations. They are differential-difference equations (DDEs) whose continuum limits are partial differential equations (PDEs). Examples include the motion of dislocations and their pinning due to the crystalline lattice [19, 20], crystal growth and interface motion in crystalline materials [21], the pinning and motion of domain walls in semiconductor superlattices [22, 23, 24], sliding of charge density waves [25], and pulse propagation through myelinated nerves [26, 27, 28].

In spatially extended continuum media described by PDEs, travelling waves are functions of a moving coordinate and therefore they can be found by solving the associated dynamical system in the moving coordinate. Nonlinear DDEs can also have traveling waves among their solutions: these waves are easy to find numerically by comparing the time evolution of neighboring cells but proofs of their existence do not abound [29, 30, 31].

The most significant difference between nonlinear DDEs and their limiting PDEs is that the discrete systems usually have coupling thresholds for propagation of wave fronts. For instance, a

bistable parabolic PDE with a cubic source term typically has wave front solutions moving with a diffusion dependent velocity: For

$$\partial_t u = D\,\partial_x^2 u + g(u), \quad -\infty < x < \infty, \tag{3.1}$$

$$g(u) = u(u-a)(2-u), \tag{3.2}$$

with $0 < a < 2$ such that $\int_0^2 g(u)\,du < 0$, there is a wave front solution $u(x,t) = U(x-ct)$ moving with positive velocity $c > 0$ and boundary conditions $U(\pm\infty) = 1 \pm 1$ [32]. The DDE obtained by substituting centered finite differences instead of derivatives in the PDE (3.1),

$$\dot{u}_n = d\,(u_{n+1} + u_{n-1} - 2u_n) + g(u_n), \tag{3.3}$$

where $\dot{u} = du/dt$, has traveling wave front solutions only if the diffusion d (which measures coupling between neighboring cells) is larger than a certain positive threshold value. For smaller diffusions, the corresponding stable solution is a stationary wave front and we say that the wave front is pinned. If we vary the parameter a, (3.1) has wave front solutions with zero velocity for the single value $a = 1$, such that $\int_0^2 g(u)\,du = 0$, and the wave fronts move with positive (resp. negative) speed if $a > 1$ (resp. $a < 1$) [32].

In contrast with this simple behavior, (3.3) has wave front solutions that move with non-zero speed for $a < a_{cl}(d)$ and $a > a_{cr}(d)$ (see Fig. 1.2(a) of [38] and chapter 4 of [24]). In the continuum limit, $\epsilon \to 0$, $d = D/\epsilon^2$, the width of the pinning interval given by $a_{cr} - a_{cl}$ tends exponentially fast to zero. Mathematical understanding of the propagation failure of wave fronts in DDE was much advanced by Keener's use of comparison principles to characterize the pinning and motion of wave fronts for spatially discrete reaction-diffusion equations such as (3.1) [33].

To describe asymptotically pinning and the depinning transition, we can resort to different perturbation techniques. In the continuum limit, King and Chapman used exponential asymptotics to obtain an approximation to F_c [34]. For a piecewise linear source $g(u)$, Fáth found an exact description of wave fronts using special functions from which the depinning transition can be obtained [35]. However, the details of the transition are different for the generic case of smooth $g(u)$. In this case, the depinning transition is a global saddle-node bifurcation describing how a smooth wave front becomes step-like and loses regularity as a decreases toward a_{cr} or it increases toward a_{cl} [36, 37].

The key idea of the asymptotic study is that, except near the continuum limit, there are finitely many u_n between the limiting values 0 and 2 of the wave front profile. Using these limiting values as

boundary conditions, (3.3) becomes a system of finitely many ordinary differential equations (ODEs): one ODE in the weak coupling case in which $d \ll 1$ [36]. The behavior of a single point, say $u_0(t)$, can be used to reconstruct the wave front profile, as $U(-ct) = u_0(t)$. For $a_{cl} < a < a_{cr}$, this system has one stable and one unstable stationary solutions which coalesce in a saddle-node bifurcation at $a = a_{cr}$ and at $a = a_{cl}$. For $a > a_{cr}$ close to a_{cr} (and similarly for $a < a_{cl}$), the stationary solutions disappear and the points $u_n(t)$ remain close to their location at $a = a_{cr}$ for a long time, proportional to $(a - a_{cr})^{-1/2}$. The difference is given by an eigenvector times the amplitude of the bifurcating solution. The latter blows up at one large positive and one large negative time. At these times, all the points $u_n(t)$ move simultaneously to the next location of the stable stationary solution for $a = a_{cr}$. The reciprocal of the interval between the blow up times gives the wave front velocity and the wave front profile can be reconstructed by matched asymptotic expansions [37].

The step-like wave front profile comprises long segments where $U(n - ct)$ is almost constant and sharp transitions between them. The motion of a single $u_n(t)$ is *saltatory*: $u_n(t)$ remains quiescent for a long interval of time and it jumps quickly to a different value at precise instants [27]. Despite appearances, this saltatory motion of the points $u_n(t)$ is due to the passage of a *step-like* wave front with a precise constant velocity $c \propto (a - a_{cr})^{1/2}$. The same construction can be used for wave fronts in discrete models of weakly coupled doped semiconductor superlattices [22, 23].

As it could have been expected, systems of DDEs exhibit a greater variety of waves and dynamical behavior than scalar DDEs. As in the case of continuous extended excitable systems [28], excitable systems described by systems of DDEs display pulses and wave trains among their solutions. For the discrete FitzHugh-Nagumo (FHN) system, pulses and wave trains are asymptotically constructed in [38] and in [14], respectively. The asymptotic construction of pulse and wave train solutions for a discrete excitable medium with Hodgkin-Huxley dynamics is given by Carpio [39]. The strategy in all these constructions is to assume that, as in the scalar case, the solutions are waves traveling with constant velocity and then to exploit the large separation in time scales characteristic of these excitable media.

Assuming that the waves travel with constant velocity allows us to reconstruct the wave profiles from the motion of a single point. The existence of different time scales allows us to separate the regions of pulses and wave trains where there are sharp variations of u_n from those regions where u_n varies smoothly. Typically the regions of sharp variations are approximated by traveling waves of a scalar DDE [38]. All these constructions of traveling waves use leading order asymptotics and yield wave velocities that are independent of the small perturbation parameter ϵ. Comparison with numerical solutions shows that there are significant differences between the predicted and numerically calculated wave speeds [38]. Thus it seems natural to correct the results of leading order asymptotics to attain better agreement.

When dealing with PDEs, rescaling the space variable is an usual ingredient of a perturbation scheme, but we cannot do this with a DDE. In this chapter we propose a general way to correct leading order constructions of traveling waves for systems of DDEs and, for the sake of simplicity, we shall present our results for the FHN system. In section 3.2, we recall the leading order construction of the pulses for the FHN system [38]. The correction to the leading order result for the leading and trailing wave fronts comprising a pulse is given in section 3.3. This section also includes graphs of the wave front velocity versus ϵ. The corrected descriptions of the leading and trailing fronts are used to obtain a corrected description of the FHN pulse in section 3.4. Section 3.5 contains a comparison with the numerical solution of the FHN system and the last section states our conclusions.

3.2 Leading order construction of the FHN pulse

In this section, we recall the asymptotic construction of pulses for the discrete FHN system given in [38]. The following nondimensional equations govern the discrete FHN system:

$$\epsilon\,\dot{u}_n = d\,(u_{n+1} - 2u_n + u_{n-1}) + g(u_n) - v_n, \tag{3.4}$$

$$\dot{v}_n = u_n - Bv_n, \tag{3.5}$$

$n = 0, \pm 1, \ldots$, $g(u) = u(u-a)(2-u)$ and $\epsilon \ll 1$. u_n and v_n are called the excitatory (or potential) and recovery variables, respectively. For $0 < B < B_1 \equiv 4/(2-a)^2$, the only uniform stationary solution is $u_n = 0 = v_n$ (critical point), whereas for $B > B_1$, there are two other critical points, one over each of the other two branches of the cubic source $g(u)$. We fix the parameters $0 < B < B_1$, $d > 0$, $a < a_{cl}(d)$ (the case $a > a_{cr}(d)$ follows by symmetry) and ϵ smaller than a certain critical value, $\epsilon_c(a, d)$, which we shall calculate approximately below.

The leading order description of a pulse is as follows. A pulse consists of regions of smooth variation of u on the time scale t, separated by sharp interfaces in which u varies rapidly on the time scale t/ϵ. In the regions where u varies smoothly, we can set $\epsilon = d = 0$, thereby obtaining the reduced problem,

$$0 = g(u_n) - v_n, \tag{3.6}$$

$$\frac{dv_n}{dt} = u_n - B\,v_n. \tag{3.7}$$

These regions are separated by sharp interfaces (moving fronts) at which u_n varies rapidly as $u_n(t) = \mathcal{U}(z)$, $v_n(t) = \mathcal{V}(z)$, with $z = n - ct/\epsilon$. There, to leading order,

$$-c\,\frac{d\mathcal{U}}{dz} = d\,[\mathcal{U}(z+1) - 2\mathcal{U}(z) + \mathcal{U}(z-1)] + g(\mathcal{U}(z)) - \mathcal{V}(z), \tag{3.8}$$

$$-c\,\frac{d\mathcal{V}}{dz} = 0. \tag{3.9}$$

Thus $\mathcal{V}$ is a constant equal to the value $v_n(t)$ at the last point in the region of smooth variation before the front. Equation (3.8) is a scalar DDE having two different wave front solutions $u = \mathcal{U}(z)$. *Increasing front* (IF) solutions satisfy $d\mathcal{U}/dz > 0$ and $\mathcal{U}(-\infty) = u^{(1)}(\mathcal{V})$ and $\mathcal{U}(\infty) = u^{(3)}(\mathcal{V})$, whereas *decreasing front* (DF) solutions have $d\mathcal{U}/dz < 0$ and $\mathcal{U}(-\infty) = u^{(3)}(\mathcal{V})$, $\mathcal{U}(\infty) = u^{(1)}(\mathcal{V})$. Here $u^{(1)}(v) < u^{(2)}(v) < u^{(3)}(v)$ are the three zeros of $g(u) - v$ for appropriate values of v. We can now discuss different regions in the asymptotic description of a pulse:

a. The region of smooth variation of u in front of the pulse, described by (3.6) and (3.7). In this region, $u_n = u^{(1)}(v_n)$, so that

$$\frac{dv_n}{dt} = u^{(1)}(v_n) - B\,v_n,$$

and initial data evolve exponentially fast towards equilibrium, $u_n = v_n = 0$.

b. The pulse leading edge. Let $v(t)$ be the value of v_n at the last point of the region in front of the pulse. Eventually, $v \to 0$. At the leading edge, $u_n(t) = \mathcal{U}(n - ct/\epsilon)$ is a DF satisfying $\mathcal{U}(-\infty) = u^{(3)}(v)$, $U(\infty) = u^{(1)}(v)$, and moving towards the right with speed $C = c(a, d, v)/\epsilon$ measured in points per unit time t. It is convenient to call $c_-(v) = c(a, d, v)$. Eventually, $C \sim c_-(0)/\epsilon$, and u_n decreases from $u_n = 2$ to $u_n = 0$ across the leading edge of the pulse.

c. Region between fronts: $u_n = u^{(3)}(v_n)$ and

$$\frac{dv_n}{dt} = u^{(3)}(v_n) - B\,v_n.$$

There are finitely many points in this region. On its far right, $v_n = v \to 0$. As we move towards the left, v_n increases until it reaches a certain value $V(t)$ corresponding to that in the trailing wave front.

d. Trailing wave front: $v_n(t) = \mathcal{V}(z) = V$, and $u_n(t) = \mathcal{U}(z)$ is an IF satisfying (3.8) with boundary conditions $\mathcal{U}(-\infty) = u^{(1)}(V)$ and $\mathcal{U}(\infty) = u^{(3)}(V)$. This front increases monotonically with z and it moves with speed $C = c(a, d, w)/\epsilon$ measured in points per unit time t. It is convenient to denote $c_+(V) = c(a, d, V)$. We shall indicate how to determine V below. Clearly, if the pulse is to move rigidly, we should have $c_+(V) = c_-(0)$ after a sufficiently long transient period.

e. Pulse tail. Again $u_n = u^{(1)}(v_n)$ and $dv_n/dt = u^{(1)}(v_n) - Bv_n$. Sufficiently far to the left, $v_n = u_n = 0$.

The number of points between wave fronts of the pulse is not arbitrary. Let τ be the delay between fronts, i.e. the time elapsed from the instant at which the leading front traverses the point $n = N$ to the instant when the trailing front is at $n = N$. Clearly,

$$\tau = \int_{v(t-\tau)}^{V(t)} \frac{dv}{u^{(3)}(v) - Bv}\,. \tag{3.10}$$

The number of points between fronts, $l(t)$, can be calculated as

$$l = \frac{1}{\epsilon} \int_{t-\tau}^{t} c_-(v(t))\, dt\,. \tag{3.11}$$

On the other hand, the separation between fronts satisfies the equation

$$\frac{dl}{dt} = \frac{c_-(v(t)) - c_+(V(t))}{\epsilon}\,. \tag{3.12}$$

The three equations (3.10), (3.11) and (3.12) can be solved to obtain the three unknowns τ, l and $V(t)$. (The function $v(t)$ is determined by solving (3.7) with $u_n = u^{(1)}(v_n)$ in the region to the left of the leading front).

After a transient period, $v(t) \to 0$ and $V(t) \to V$ (a constant value), so that we have the simpler expressions

$$\tau = \int_0^V \frac{dv}{u^{(3)}(v) - Bv}\,, \tag{3.13}$$

$$\frac{dl}{dt} = \frac{c_-(0) - c_+(V)}{\epsilon}\,, \tag{3.14}$$

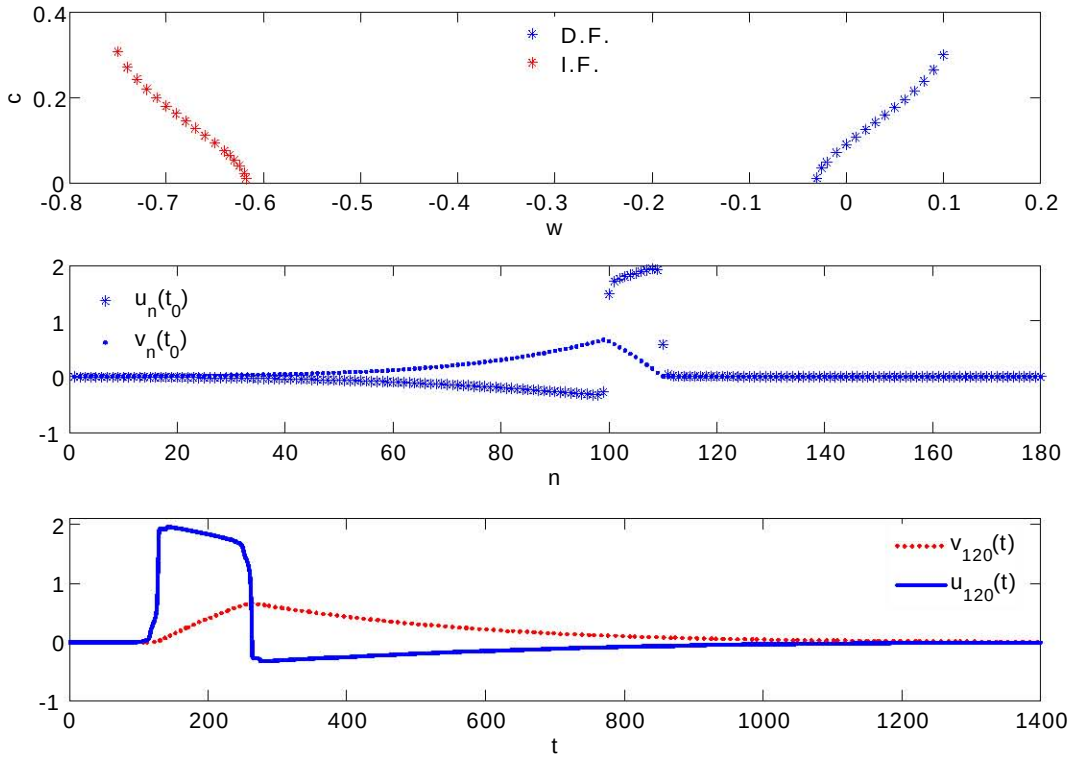

Figure 3-1 (a) Numerically obtained wave front velocity for (3.1) with $g(u) = u(u-a)(2-u) - w$, $d = 0.1$ and $a = B = 0.5$. The horizontal line graphically yields V^* such that $c_+(V^*) = c_-(0)$. **(b)** Profiles of the FHN pulse for $\epsilon = 0.003$. **(c)** Trajectories of one point, $u_{120}(t)$, $v_{120}(t)$, as the FHN pulse traverses it.

instead of (3.10) and (3.12), respectively. The number of points at the pulse top is now

$$l = \frac{c_-(0)\tau}{\epsilon} = \frac{c_-(0)}{\epsilon} \int_0^V \frac{dv}{u^{(3)}(v) - Bv} \,.$$

This equation yields V as a function of l. Then (3.14) becomes an autonomous differential equation for l that has a stable constant solution at $l = l^*$ such that $c_-(0) = c_+(V(l))$: At $l = l^*$, the right hand side of (3.14) has a slope $-[u^{(3)}(V) - BV]\, c'_+(V)/c_-(0) < 0$.

Recapitulating, for appropriate initial conditions, leading and trailing fronts of a pulse evolve until l reaches its stable value at which $c_-(0) = c_+(V(l^*))$ and (3.11) holds. To compute l^*, we

first determine $V^* = V(l^*)$ by using $c_-(0) = c_+(V(l^*))$. Then we calculate $\tau = \tau^*$ (which does not depend on ϵ!) from (3.13) and $l^* = c_-(0)\tau^*/\epsilon$. Our construction breaks down if the number of points between fronts falls below 1. This yields an upper bound for the critical value of ϵ above which pulse propagation fails: $\epsilon_c \sim c_-(0)\tau^*$.

To calculate the asymptotic length of the pulse tail, preventing the resulting length is infinity, we can calculate the time it takes for a solution $v(t)$ with $v(0) = V$ to reach a neighborhood of $v_* = 0$. we obtain

$$t = \int_v^V \frac{dv}{Bv - u^{(1)}(v)} \sim \int_{v_*}^V \left[\frac{1}{Bv - u^{(1)}(v)} - \frac{1}{(\eta)'_*(v - v_*)}\right] dv + \frac{1}{(\eta)'_*} \ln\left(\frac{V - v_*}{v - v_*}\right)$$

with $(\eta)'_* = d[Bv - u^{(1)}(v)]/dv|_{v=v_*} > 0$, and therefore

$$v(t) - v_* \sim (V - v_*)e^{-(\eta)'_*(t-T)}, \quad T = \int_{v_*}^V \left[\frac{1}{Bv - u^{(1)}(v)} - \frac{1}{(\eta)'_*(v - v_*)}\right] dv$$

for long times such that $v(t)$ is sufficiently close to v_* . The time needed for $v(t)$ to go from V to $v_* + (V - v_*)/e$ is then $T_* = T + 1/(\eta)'_*$. The tail length is approximately given by $M = c_-(0)T_*/\epsilon$.

The *figure 3-1* illustrates our construction. Setting $w = 0$, we find a velocity $c_-(0)$ of the DF. Then a horizontal line that intersects $c_-(w)$ at $w = 0$, as shown in *figure 3-1*(a), yields $c_+(w) = c_-(0)$ at $w = V^*$. Eq. (3.13) produces the pulse duration τ^* and (3.14) gives the pulse width l^* between its two fronts. The FHN pulse profile is shown in *figure 3-1(b)* and the trajectory of a single point traversed by the pulse is depicted in *figure 3-1(c)*.

3.3 $O(\epsilon)$ construction of the wave fronts comprising a pulse

3.3.1 Exact formula for the wave front profile

To correct the previous asymptotic theory of pulses, we need to improve the description of wave fronts. To this end, we use the fact that DF or IF profiles are monotonic functions of a variable $z = n - ct/\epsilon$, where c is the front velocity and we consider fronts moving from left to right ($c > 0$). Thus

$$u_n(t) = \mathcal{U}(z), \quad v_n(t) = \mathcal{V}(z),$$

with $\mathcal{U}'(z) > 0$ (resp. < 0) for IF (resp. DF). In either case, we can find

$$z = Z(U) \quad \text{which solves} \quad \mathcal{U}(z) = U.$$

Then the finite differences

$$D^{\mp}u_n \equiv \pm[u_n - u_{n\mp1}] = \pm[\mathcal{U}(z) - \mathcal{U}(z \mp 1)] = \pm[u_n - \mathcal{U}(Z(u_n) \mp 1),$$

$$D^{+}D^{-}u_n = u_{n+1} + u_{n-1} - 2u_n = \mathcal{U}(Z(u_n) + 1) + \mathcal{U}(Z(u_n) - 1) - 2u_n,$$

can be considered to be functions of u_n. To leading order as $\epsilon \to 0$, $\mathcal{U}(z) \sim \mathcal{U}^{(0)}(n - c^{(0)}t/\epsilon)$, $\mathcal{V}(z) = v$, as explained in the previous section. For an IF calculated with the leading order theory of section 3.2, *figure 3-2* (a) and (b) show the differences $D^{\pm}u_n$ and $D^{+}D^{-}u_n$ as functions of u_n. Note that these differences vanish for u_n on the nullcline $v = g(u_n)$.

Since the second difference $D^{+}D^{-}u_n$ is a function of u_n, we can derive from the equation for $v_n = \mathcal{V}(z)$:

$$-c\frac{dv_n}{dz} = \epsilon(u_n - Bv_n),$$

and from the equation for the wave front profile, $u_n = \mathcal{U}(z)$,

$$-c\frac{du_n}{dz} = d\,D^{+}D^{-}u_n + g(u_n) - v_n, \tag{3.15}$$

the following *exact* equation for v_n as a function of u_n:

$$\frac{dv_n}{du_n} = \epsilon\,\frac{u_n - Bv_n}{g(u_n) - v_n + d\,(D^{+}D^{-}u_n)(u_n)}.$$

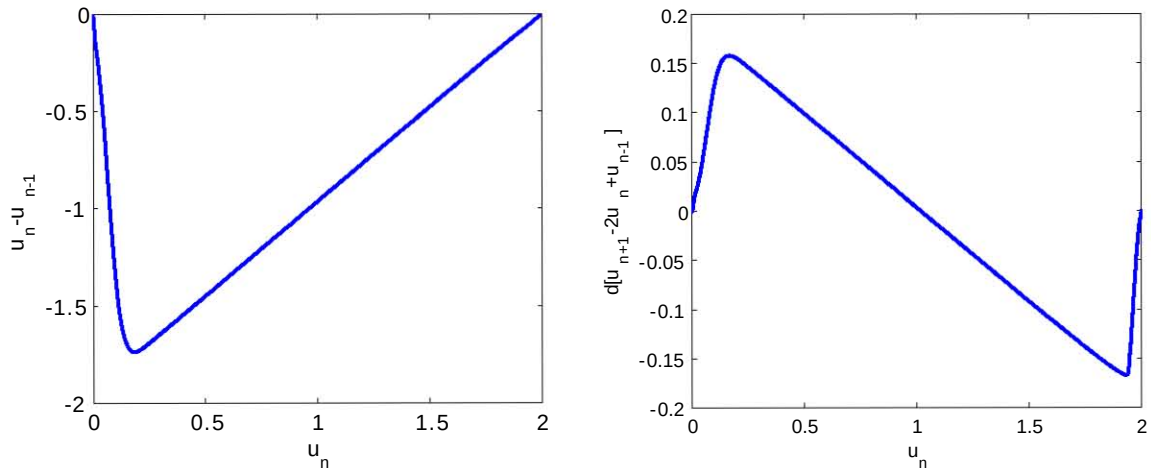

Figure 3-2 (a) Backward and forward differences as functions of u_n for a leading order DF at constant $v = 0$ in the interval (v_-, v_+). **(b)** Second order centered difference as a function of u_n for the same front. Parameter values as in *figure 3-1*.

3.3.2 Corrected decreasing front (leading front of a pulse)

Now we integrate this equation and iterate the result starting from the value $v_n(u_\infty) = v$ (corresponding to $t \to -\infty$ because $u_n(t) = \mathcal{U}(z)$, $z = n - ct/\epsilon$), thereby obtaining

$$v_n \sim v + \epsilon \int_{u_\infty}^{u_n} \frac{(u - B\,v)\,du}{g(u) - v + d\,\mathcal{D}^{(0)}(u)}, \tag{3.16}$$

up to terms of order ϵ^2. In (3.16), the leading order approximation to the second difference $(D^+D^-u_n)(u_n)$ has been denoted by $\mathcal{D}^{(0)}(u_n)$; cf. *figure 3-2*(b).

The starting point u_∞ is on the nullcline $v = g(u)$, and therefore it satisfies $g(u_\infty) = v$. This creates problems of convergence for the integral in Eq. (3.16) because the boundary condition $\mathcal{U}(\infty) = u_\infty$ seems to imply that the finite differences on this tail of the wave front are zero and therefore that the denominator in (3.16) would vanish.

We find a similar problem as $n \to -\infty$ and the final point of the wave front approaches the other nullcline. An easy way out is the case in which $v = v_*$ corresponds exactly to a uniform stationary solution (critical point). Then $u_\infty = u_*$, the value corresponding to the same critical point, the integrand in (3.16) has a finite limit as $u_n \to u_\infty$ and the integral converges. For $0 < B < B_1$, the only critical point is $u_* = v_* = 0$, so that we would have $u_\infty = 0$ for $v = 0$. For $B > B_1$, we have

two other possible critical points. If $v \neq v^*$, then we need to make sure that $\mathcal{D}^{(0)}(u_{-\infty}) \neq 0$ to avoid having a singular integrand at $u = u_\infty$.

Consider the case of only one critical point ($0 < B < B_1$). The leading front of a pulse is a decreasing front (DF) starting at the critical point $u_* = v_* = 0$ and ending on the third branch of the nullcline $v = g(u)$, whereas the trailing front is an increasing front (IF) that should join non-critical points on the first and third branches of the nullcline $v = g(u)$. For the DF, the integrand of (3.16) is not singular at the critical point $u_\infty = 0$ and the corrected wave front is the solution of the fast equation (3.15),

$$-c\,\frac{d\mathcal{U}}{dz} + v_n(\mathcal{U}) - g(\mathcal{U}) - d\,(D^+D^-u_n)(\mathcal{U}) = 0 \tag{3.17}$$

or, equivalently, the time-dependent version of this equation:

$$\frac{du_n}{dt} = d\,(u_{n+1} - 2u_n + u_{n-1}) + g(u_n) - v_n(u_n), \quad T = \epsilon\,(t - t_0)$$

($t_0 = 0$ for the DF and $t_0 = t_v$ for the IF explained below), with the boundary conditions:

$$u_n(-\infty) = \mathcal{U}(+\infty) = 0, \quad u_n(+\infty) = \mathcal{U}(-\infty) = u^{(3)}(v'), \quad v' > 0. \tag{3.18}$$

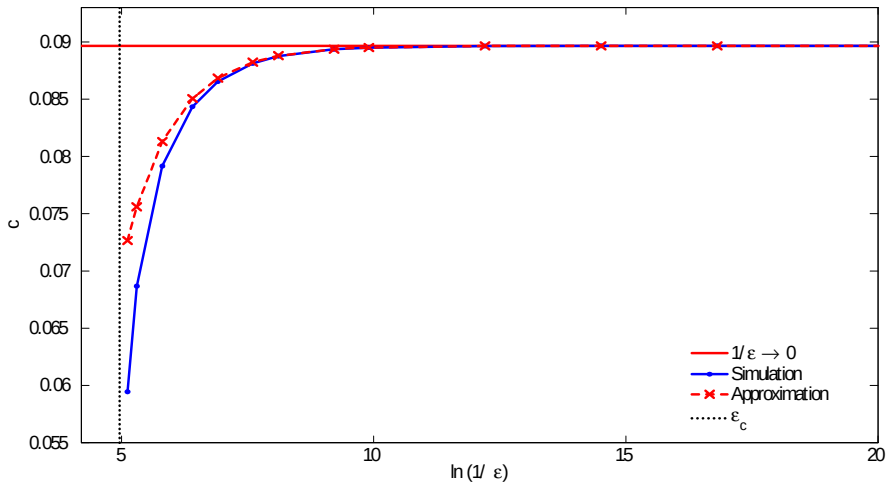

Figure 3-3 Velocity of the DF as a function of $-\ln\epsilon$ for a DF with $v_{-\infty} = 0$. For parameter values as in *figure 3-1*, we have marked with dots the critical value $\epsilon_c \approx 0.007$ above which no stable pulses are found.

In (3.18), the value $v' > 0$ is determined by solving (3.16) and (3.17) until the third branch of $g(u)$ is reached. The velocity of the DF is now a function of ϵ and *figure 3-3* shows that it is a much better approximation to the numerically calculated front velocity than that given by the leading order theory.

3.3.3 Corrected increasing front (trailing front of a pulse)

The case of the IF is more complicated: the integrand of (3.16) is now singular when u_∞ is on the third branch of the nullcline $v = g(u)$. To solve this problem, we first calculate the $O(\epsilon)$ correction to the slow scale equation (3.6) when u_n is on the third branch of the nullcline $v = g(u)$. The leading order approximation during the slow scale is $u_n = \Phi(v_n)$ ($\Phi(v_n) = u^{(3)}(v_n)$ for our IF). Inserting this function in (3.7), we get

$$\frac{dv_n}{dt} = \Phi(v_n) - Bv_n. \tag{3.19}$$

The $O(\epsilon)$ correction to the slow stage equations is obtained assuming that the discrete diffusivity is of order ϵ: $d(u_{n+1} + u_{n-1} - 2u_n) = \epsilon d' \mathcal{D}^{(0)}(u_n)$. Then we find $u_n(t;\epsilon) \sim u_n + \epsilon w_n^{(1)}$, $v_n(t;\epsilon) \sim v_n + \epsilon v_n^{(1)}$, with

$$\frac{dv_n^{(1)}}{dt} + Bv_n - w_n^{(1)} = 0, \tag{3.20}$$

$$g'(\Phi(v_n))w_n^{(1)} - v_n^{(1)} = \frac{\Phi(v_n) - Bv_n}{g'(\Phi(v_n))} - d'\mathcal{D}^{(0)}\Phi(v_n), \tag{3.21}$$

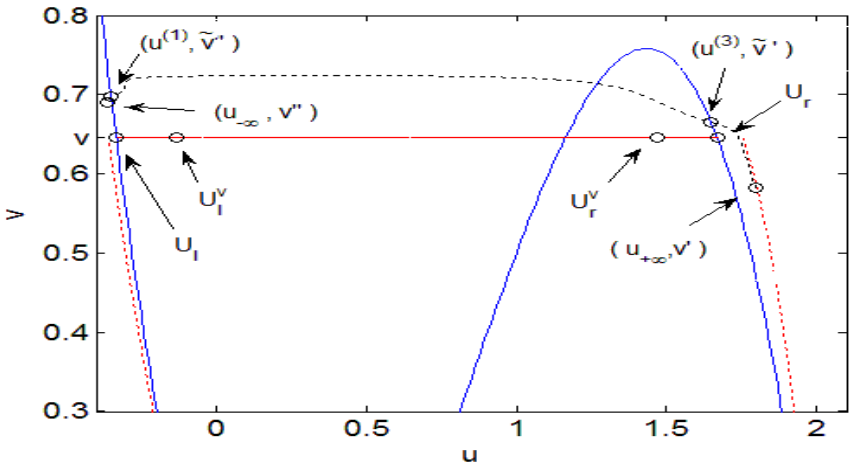

Figure 3-4 Sketch of the IF construction in the phase plane.

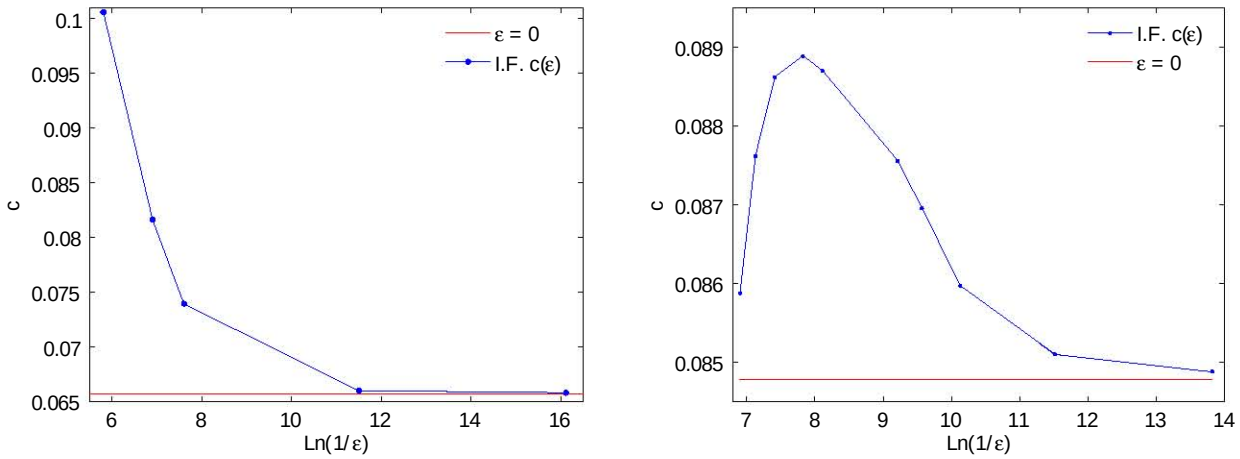

Figure 3-5 Wave front velocity as a function of $\ln 1/\epsilon$ for an IF **(a)** with a fixed $v_\infty = 0.63572$ and (b) with a fixed $V = 0.63586$.

where $\Phi(v) = u^{(3)}(V)$ on the third branch of the nullcline $v = g(u)$. Let $t = t_v$ be the time at which the zeroth order approximation (on the slow scale), $v_n(t_v)$, reaches the value v from which the zeroth order approximation to the IF would start on the fast scale: $u^{(3)}(V)$. We choose $u_\infty = u_n(t_v - 1/c; \epsilon)$, $V'(u_\infty) < V$. We now calculate U_r^v such that

$$\mathcal{D}^{(0)}(U_r^v) = u_{n+1}(t_v; \epsilon) + u_{n-1}(t_v; \epsilon) - 2u_n(t_v; \epsilon).$$

This U_l^v is in $[U_l, U_r]$ such that $\mathcal{D}^{(0)}(U_{l,r}) = 0$. For a fixed $u \in [u_n(t_v; \epsilon), u_n(t_v - 1/c; \epsilon)]$, t_u is such that $u_n(t_u; \epsilon) = u$. Then $\mathcal{D}^{(1)}(u) \equiv u_{n+1}(t_u; \epsilon) + u_{n-1}(t_u; \epsilon) - 2u_n(t_u; \epsilon)$. To each $u \in [u_n(t_v; \epsilon), u_n(t_v - 1/c; \epsilon)]$, we find $\mathcal{U}$ such that

$$\mathcal{D}^{(1)}(u) = \mathcal{D}^{(0)}(\mathcal{U}).$$

$\mathcal{U}$ is in the interval $[U_l^v, U_r^v]$, in which U_l^v is calculated in the same way as U_r^v except that we use the equations for the slow stage on the first branch of the nullcline $v = g(u)$ for which $t > t_v$. At $t = t_v+$ (immediately after the fast stage ends), the slow stage on the first branch of $v = g(u)$ starts at $v = V'$. *Figure 3-4* sketches the construction of the IF and shows the values $U_{l,r}^v$, $U_{l,r}$, V' and $u_{\pm\infty}$.

In the fast stage connecting $(u_{+\infty}, V')$ to $(u_{-\infty}, V'')$, we use an equation similar to (3.16),

$$v_n \sim V' + \epsilon \int_{u_\infty}^{u_n} \frac{(u - B\,v)\,du}{g(u) - v + d\,\mathcal{D}^{(1)}(u)}, \tag{3.22}$$

except that we have replaced $\mathcal{D}^{(1)}(u)$ instead of $\mathcal{D}^{(0)}(u)$ and $v_n \sim V'$ at leading order. The IF is a solution of (3.17) and (3.22) with boundary conditions

$$u_n(-\infty) = \mathcal{U}(+\infty) = u'_{+\infty}, \quad u_n(+\infty) = \mathcal{U}(-\infty) = u'_{-\infty}, \tag{3.23}$$

where

$$g(u'_{+\infty}) = v_n(u'_{+\infty}), \quad g(u'_{-\infty}) = v_n(u'_{-\infty}). \tag{3.24}$$

Here $u'_{+\infty} = u^{(3)}(v_n(u'_{+\infty}))$ is on the third branch of the nullcline $v = g(u)$, whereas $u'_{-\infty} = u^{(1)}(v_n(u'_{-\infty}))$ is on the first branch. The IF ends at a point $u_{-\infty}$ on the corrected first branch of the nullcline, namely the solution of (3.19), (3.20) and (3.21) with $\Phi(v) = u^{(1)}(v)$.

The velocity of the IF is a function of ϵ and *figure 3-5* shows that it is a much better approximation to the numerically calculated front velocity than that given by the leading order theory. For *figure 3-5*(b) we fix the V value. So, the starting point , $v_n(u_{+\infty})$, of the IF front have lower values as ϵ grows. When the value of $v_n(u_{+\infty})$ gets smaller, the IF front have less velocity. Therefore, in *figure 3-5* (b), a maximum in the IF front velocity is created.

3.4 $O(\epsilon)$ construction of pulses

How do we correct the pulse construction in Section 3.2 using our improved theory of wave fronts?

- The region of smooth variation in front of the pulse is as described in Section 3.2 with the corrections given by (3.20) and (3.21). In particular, u_n and v_n tend to 0 after a transient stage.

- To construct the leading and trailing wave fronts of the pulse, we have to use Eq. (3.17) instead of (3.8), together with (3.16) and boundary conditions (3.18) for the leading DF and (3.17) with (3.22) and (3.23) for the trailing IF. Assume the pulse moves from left to right. The leading wave front is a DF moving with speed $c_-(v)/\epsilon$ with $c_-(v) = c(a, B, v, \epsilon)$, $v = 0$, given by (3.17), (3.16) and boundary conditions (3.18). While 0 is the value at the initial potential u on the first branch of $g(u)$, v' is the recovery variable at the final point of the DF which is on the third branch of $g(u)$. The time it takes for a point to move from $(u^{(1)}(v), v)$ to $(u^{(3)}(v'), v')$ is of order ϵ and we can not ignore it when constructing the pulse. Eventually, $v = 0$, $v' > 0$.

- In the region between leading and trailing fronts, $u_n = u^{(3)}(v_n)$. On its far right, $v_n = v'$, where the DF ends. As we move towards the left, v_n increases until it reaches a certain value $\tilde{V}'$ corresponding to that in the trailing wave front.

- The trailing wave front is an IF moving with speed $c_+(V)/\epsilon$, with $c_+(V) = c(a, B, V, \epsilon)$ given by (3.17), (3.22) and boundary conditions (3.23). The recovery variables at the initial and final points of the IF are $\tilde{V}'$ and $\tilde{V}''$, respectively. Again the time it takes for a point to move from the third to the first branch of the nullcline $v = g(u)$ (on the IF) is of order ϵ and can not be ignored.

- The pulse tail is as described in section 3.2, except that its first point has a recovery variable $\tilde{V}''$ instead of V.

Equations (3.10) to (3.12) become

$$\tau = \int_{v'(t-\tau)}^{V(t)} \frac{dp}{u^{(3)}(p) - Bp}\,, \tag{3.25}$$

$$l = \frac{1}{\epsilon} \int_{t-\tau}^{t} c_-(v(t))\, dt\,. \tag{3.26}$$

$$\frac{dl}{dt} = \frac{c_-(v'(t)) - c_+(V(t))}{\epsilon}\,. \tag{3.27}$$

After the transient period, these equations become:

$$\tau = \int_{v'}^{\tilde{V}'} \frac{dv}{u^{(3)}(v) - Bv}\,, \tag{3.28}$$

$$l = \frac{c_-(0)\tau}{\epsilon} = \frac{c_-(0)}{\epsilon} \int_{v'}^{\tilde{V}'} \frac{dv}{u^{(3)}(v) - Bv}\,, \tag{3.29}$$

$$\frac{dl}{dt} = \frac{c_-(v') - c_+(V)}{\epsilon}\,. \tag{3.30}$$

Here v' is fixed, (3.29). $\tilde{V}'$ is fixed too with V and ϵ. This yields V as a function of l, and then (3.30) becomes an autonomous differential equation for $l(t)$. Its stable fixed point l^* and the corresponding time τ^* depend on ϵ because v' and $\tilde{V}'$ do. Except for this, the rest of the considerations made in section 3.2 apply.

3.5 Comparison with the results of direct numerical simulation

We have reconstructed the pulse profile in both the excitatory and the recovery variables using the zeroth and first order approximations for different values of ϵ. The results are presented in *figures 3-6* and *3-7*.

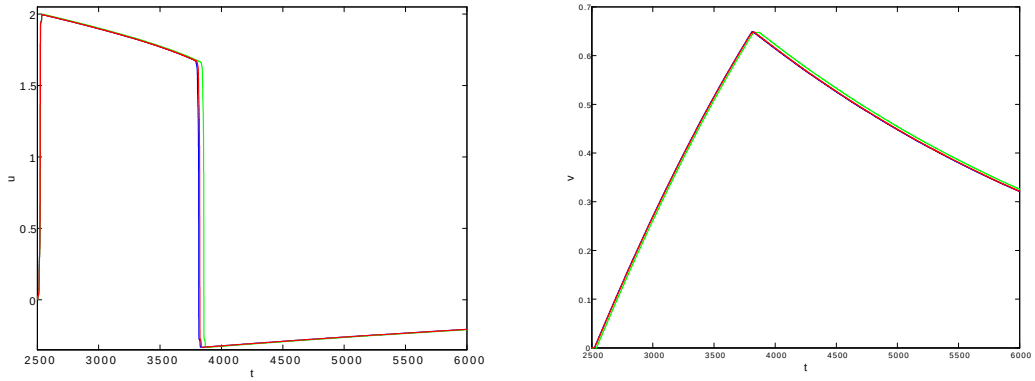

Figure 3-6 Comparison of the corrected asymptotic theory with the numerical solution for (a) $u(x,t)$, (b) $v(x,t)$. Here $\epsilon = 0.0003$, $d = 0.1$, $a = B = 0.5$.

For the parameter values in *figure 3-1*, $d = 0.1$, $a = B = 0.5$, $\epsilon_c \approx 0.007$. In *figure 3-6*, we show the pulse profiles for $\epsilon = 0.0003$ $(-\ln \epsilon = 8.11)$ and observe that the reconstruction of the pulse is already quite good for the leading zeroth order theory. The first order theory provides an even better approximation. *Figure 3-3* shows that the numerically calculated and approximated pulse velocities are quite close for this value of ϵ, so having a good reconstruction of the pulse for this value comes as no surprise.

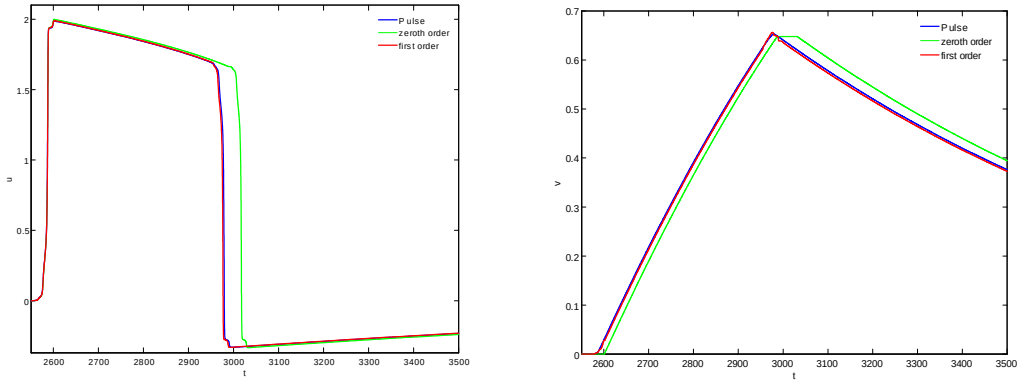

Figure 3-7 Comparison of the corrected asymptotic theory with the numerical solution for(a) $u(x,t)$, (b) $v(x,t)$. Here $\epsilon = 0.001$, $d = 0.1$, $a = B = 0.5$.

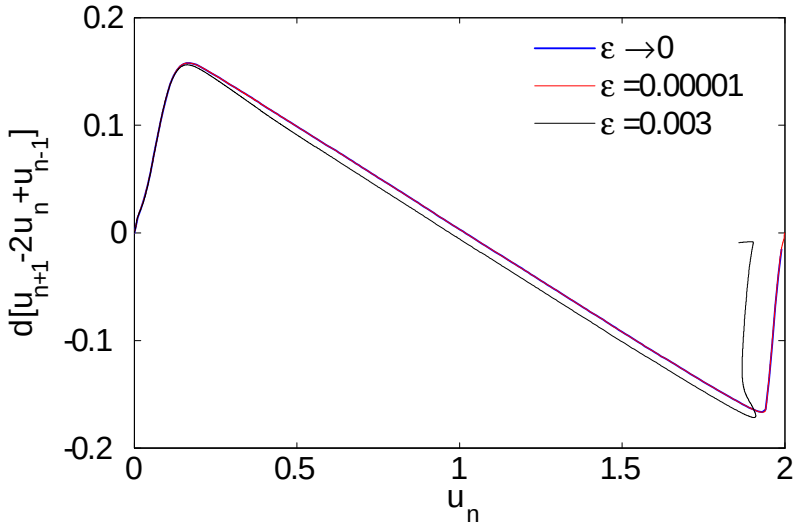

Figure 3-8 Comparison of the second order centered difference as a function of u_n for the same DF front with pulses with diferent ϵ

The value $\epsilon = 0.001$ $(-\ln \epsilon = 6.91)$ used in the reconstructions depicted in *figure 3-7* is closer to $\epsilon_c \approx 0.007$. *Figure 3-3* shows that the numerically calculated and approximated pulse velocities are not very close for this value of ϵ, and that the first order theory gives a better pulse velocity than the zeroth order theory (horizontal line in *figure 3-3*).

Then we can appreciate some differences between the zeroth order and first order reconstructions of the pulse in *figure 3-7* (a) and (b). The first order theory yields a better reconstruction and the differences with the numerically calculated pulse can be explained by the error in the calculation of the pulse velocity as observed in *figure 3-3*.

In the recostruction of a pulse profile, several errors are committed. The ϵ value, has the property of maximize or minimize these errors. We have seen some problems that can be solved by an $O(\epsilon^2)$ theory:

- The second finite differences, as we can see in *figure 3-8*, depends on ϵ values. For the DF, this problem is not as critical as we can think, because the front ends before $u^{(3)}$ of zeroth order theory is reached. But for the IF front, for bigger values of ϵ, the second finite differences have to be more precise. As long as the $\mathcal{D}^{(1)}(u)$ function is more similar to the pulse second finite differences, the trajectory of the IF front over the phase plane is more smooth.

- The unions between different regions are not smooth as we can wish, they have discontinuities in their slopes of the phase plane. This is due to several reasons.

  In the union of the DF with the peak region, the function $\mathcal{D}^{(0)}(u)$ is not continuous with the second differences $D^+D^-u_n$ of the peak.

  In addition; in the union of the IF with the peak and the tail region, the distance between the points $(u_{+\infty}, V')$ to $(u^{(3)}, \tilde{V}')$, and $(u^{(1)}, \tilde{V}'')$ to $(u_{-\infty}, V'')$ grows with ϵ value. As consequence, these three regions are not defined very well and a new theory have to be constructed.

- The trajectory over the phase plane, in the peak and the pulse tail regions, is not sufficiently close to the nullcline as ϵ grows. This implies that equations (3.28), (3.29) and (3.30) are no longer valid. Other solution have to be found with equations (3.20) and (3.21).

3.6 Conclusions

Spatially discrete excitable systems exhibit pulse solutions that can be constructed using matched asymptotic expansions which exploit the large separation of time scales in their dynamics (as measured by a small dimensionless parameter ϵ).

The pulse profile typically consists of slowly varying regions of the excitatory variable separated by sharp wave fronts. In the FitzHugh-Nagumo system, the velocity of a pulse is decided by the interaction between its leading and trailing fronts, but the leading order approximation often gives only a fair result when compared with direct numerical solutions.

We have shown how to find a better approximation to the wave fronts comprising the FHN pulse. Our approximation provides a pulse velocity that depends on ϵ and compares much better with the velocity obtained from numerical solutions. As a result, the reconstruction of the FHN pulse using the improved wave fronts also compares much better with the numerically obtained pulse.

Chapter 4

Weakly coupled photoexcited superlattices; the Physical Model

4.1 Introduction

In 1970, Esaki and Tsu [68] invented an artificial crystal, which they called a semiconductor superlattice (SL), in order to realize a device that exhibits Bloch oscillations. In the last decade, non-linear dynamical transport in semiconductor superlattices has witnessed a significant progress in the theoretical description as well as in the experimentally observed non-linear phenomena. The simplest mathematical models applied to a SL give rise to balance equations involving mesoscopic quantities such as the electric field, the electron density, the drift velocity, etc.

Weakly coupled SLs contain rather thick barriers separating the SL quantum wells, i.e. the barrier width is much larger than the typical electron wavelength inside the barrier. Therefore, a description of the electronic properties of weakly coupled SLs can be based on the subband structure of the corresponding isolated quantum well together with resonant tunnelling across the barrier of two adjacent wells.

Typical experiments of vertical charge transport use an undoped or doped SL of finite length placed in the central part of a diode (forming a p-i-n or n^+-n-n^+ structure) with respective contacts at either end of the diode. Depending on the bias condition, the SL configuration, the doping density, the photoexcitation, the temperature or other control parameters, the current through the SL and the electric field distribution inside the SL display a great variety of non-linear phenomena such as pattern formation, current self-oscillations, and chaotic behaviour.

In this chapter, weakly coupled superlattices are described by differential-difference equations. Therefore, weakly coupled superlattices exhibit a more complex dynamical behaviour than strongly coupled ones.

4.2 Temporal scales in the resonant sequential transport

In the regime of resonant sequential tunnel, are different temporal scales where the different physical phenomena related to the transport in photoexcited superlattices happen. To get a valid mathematical model, and to retain the physics of the experimental problem, first we have to analyze the most relevant scales, which are:

- **The dielectric relaxation time,** τ_{rd}: reflects the necessary average time in order to the charge fluctuations decline and obtain an electrical local neutrality. His order of magnitude can be obtained as the period of the superlattice divided by the average electronic velocity.

- **The tunneling time between neighboring quantum wells,** τ_t: defines the average time that an electron jumps from a quantum well to an other one, by tunnel effect helped by any type of scattering.

- **The intersubband *scattering* time,** τ_s: expresses the average time that an electron consumes in the jumping process from a subband with bigger energy to the first subband of the same quantum well.

- **The average recombination hole-electron time,** τ_r: indicates the average time that an excited electron consume in the recombination process with a hole . The order of magnitude of this time scale is indirectly proportional to the pumping intensity laser.

Numerically, the order of magnitude between the first three temporal scales can be expressed in the following relation:

$$\tau_s \ll \tau_t \ll \tau_{rd} \tag{4.1}$$

The expression (4.1), allows to suppose that the electrons only can occupy the first subband of every quatum well; And in addition, that in every instant of time we can assign to a every quantum

well a value of an electric field, $\tilde{F}_i$, and an 2D electron density ($\tilde{n}_i$) and hole density ($\tilde{p}_i$), without considering those electrons who in that instant can be tunneling from a well to other one.

The relation between the order of magnitude of τ_r with τ_{rd}, defines the different transport regimes which the superlattice can conduct, hence, the different charge waves that can manage to be observed; What we detail in the following chapters.

4.3 The tunnelling rate

We can consider the energy states of isolated quantum wells or subbands $\tilde{E}_\nu(\mathbf{k}_\perp) = \tilde{\mathcal{E}}_\nu + \hbar^2\mathbf{k}_\perp^2/(2m^*)$, where $\tilde{\mathcal{E}}_\nu$ is independent of k and m^* is the effective mass. First-order time-dependent perturbation theory indicates that the tunnelling rate through the ith barrier (from the μ subband of the ith well to the ν subband of the $(i+1)$th well) is given by Fermi's golden rule, assuming conservation of energy during tunnelling:

$$P_{i,i+1}^{\mu,\nu} = \frac{2\pi}{\hbar}\,|M_{i,i+1}^{\mu,\nu}|^2 \delta(\tilde{E}_\mu(k_{\perp,i}) - e\tilde{\phi}_i\tilde{l} - \tilde{E}_\nu(k_{\perp,i+1}) + e\tilde{\phi}_{i+1}\tilde{l}),$$

Here $\tilde{\phi}_i\tilde{l} = \sum_{n=0}^{i}\tilde{F}_n$ is the electric potential at the ith well. The matrix element $M_{i,i+1}^{\mu,\nu}$ can be calculated by means of the transfer Hamiltonian method (THM). Then

$$M_{i,i+1}^{\mu;\nu} = \frac{\hbar^2}{2m^*}\int_S (\Psi_i \nabla\Psi_{i+1}^* - \Psi_{i+1}^*\nabla\Psi_i)\cdot d\mathbf{S}, \tag{4.2}$$

In which $\Psi_i(\tilde{z}, \mathbf{x}_\perp)$ is the wave function of an isolated well with energy $\tilde{E}_\mu(\mathbf{k}_{\perp,i})$ and lateral momentum $\mathbf{k}_{\perp,i}$. The surface integral in equation (4.2) is over any lateral surface inside the ith barrier that is perpendicular to the growth direction. Choosing the plane at the end of the barrier, an elementary calculation yields

$$|M_{i,i+1}^{\mu,\nu}|^2 = \frac{\pi\hbar^4}{2m^{*\,2}}\,B_{i-1,i}B_{i,i+1}T_i\,\delta(\mathbf{k}_{\perp,i} - \mathbf{k}_{\perp,i+1}), \tag{4.3}$$

$$B_{i,i+1} = \frac{k_{i+1}}{w + \alpha_i^{-1} + \alpha_{i+1}^{-1}}, \tag{4.4}$$

$$T_i = \frac{16k_ik_{i+1}\alpha_i^2 e^{-2\alpha_i d_B}}{(k_i^2+\alpha_i^2)(k_{i+1}^2+\alpha_i^2)}. \tag{4.5}$$

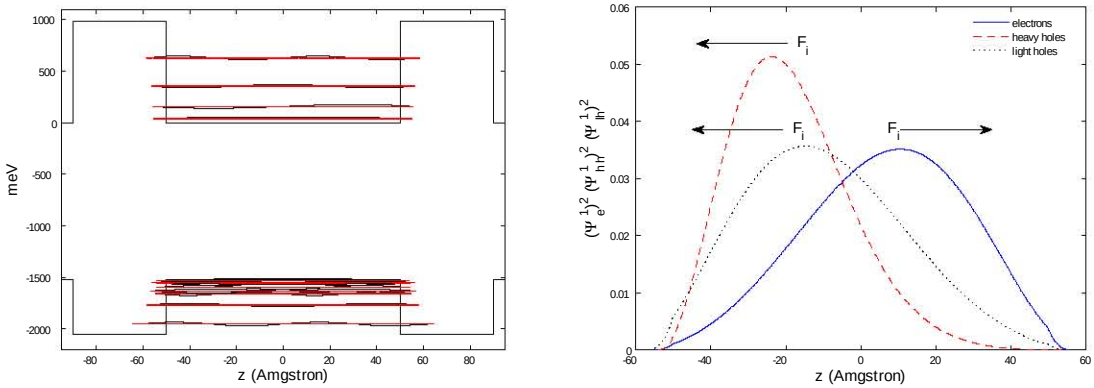

Figure 4-1 (a) Energy states of a isolated quantum well in a GaAs/AlAs(10/4) superlattice **(b)** Respectively, electrons, *heavy holes* and *light holes,* $\Psi^1_e(\tilde{z},\tilde{F}_i)^2$, $\Psi^1_{hh}(\tilde{z},\tilde{F}_i)^2$ and $\Psi^1_{lh}(\tilde{z},\tilde{F}_i)^2$ for the electric field corresponding to the second peak of the current.

Here k_i and α_i are the wave vectors at the ith well and barrier, respectively, while T_i is the transmission coefficient through the ith barrier.

To obtain the tunnelling current, we have to multiply $e\,P^{\mu,\nu}_{i,i+1}$ by a factor of 2 due to spin degeneracy and by the difference between the Fermi-Dirac distribution functions of both wells. Then, we sum over energies and states in both wells. When transforming the sums over the lateral momenta and energies into integrals, we should include broadened densities of states for both wells due to scattering.

To simplify matters, we can assume that the broadening functions do not depend on the lateral momentum. The result can be further simplified by noting that the lateral momentum is conserved according to equation (4.3) and that the integral over $\mathbf{k}_\perp$ affects only to the distribution functions. We have

$$\tilde{J}_{i\to i+1}=\frac{\hbar k_B\tilde{T}}{2m^*}\sum_{\nu=1}^{n_{max}}\int_0^\infty A_1(\tilde{\epsilon})\,A_\nu(\tilde{\epsilon}+e\tilde{F}_i\tilde{l})\,T_i(\tilde{\epsilon})\,\ln\left[\frac{1+e^{\frac{\mu_i-\tilde{\epsilon}}{k_B\tilde{T}}}}{1+e^{\frac{\mu_{i+1}-e\tilde{F}_i\tilde{l}-\tilde{\epsilon}}{k_B\tilde{T}}}}\right]d\epsilon. \tag{4.6}$$

In this formula, n_{max} is the number of subbands in the wells. The integral extends from the bottom of the ith well to infinity, and the bottom of the ith well is the origin of all the energies and the electrochemical potentials [70]. Then, μ_i and $\mu_{i+1}-e\tilde{F}_i\tilde{l}$ are the electrochemical potentials of wells i and $(i+1)$, respectively. μ_i is the *chemical potential* of the ith well referred to its bottom. It depends uniquely on the electron density $\tilde{n}_i$.

The broadening due to scattering is a Lorentzian function centred at the energy of the νth subband, whose width is proportional to the inverse of the scattering time:

$$A_\nu(\tilde{\epsilon}) = \frac{\gamma_\nu/\pi}{(\tilde{\epsilon} - \tilde{\mathcal{E}}_\nu)^2 + \gamma_\nu^2}.$$

Moreover, $\mathcal{T}_i(\tilde{\epsilon})$ is:

$$\mathcal{T}_i(\tilde{\epsilon}) = T_i(\tilde{\epsilon})\, B_{i-1,i}(\tilde{\epsilon})\, B_{i,i+1}(\tilde{\epsilon}),$$

and the wave vectors appearing in these formulas are:

$$\begin{aligned}
\hbar k_i &= \sqrt{2m^*\tilde{\epsilon}}\,, \quad \hbar k_{i+1} = \sqrt{2m^*[\tilde{\epsilon} + e(\tilde{L}_W + \tilde{L}_B)\tilde{F}_i]}, \\
\hbar\alpha_{i-1} &= \sqrt{2m^*\left[e\tilde{V}_b + e\left(\tilde{L}_B + \frac{\tilde{L}_W}{2}\right)\tilde{F}_i - \tilde{\epsilon}\right]}, \\
\hbar\alpha_i &= \sqrt{2m^*\left(e\tilde{V}_b - \frac{e\tilde{L}_W\tilde{F}_i}{2} - \tilde{\epsilon}\right)}, \\
\hbar\alpha_{i+1} &= \sqrt{2m^*\left[e\tilde{V}_b - e\left(\tilde{L}_B + \frac{3\tilde{L}_W}{2}\right)\tilde{F}_i - \tilde{\epsilon}\right]}.
\end{aligned} \tag{4.7}$$

Here, $\tilde{V}_b$ is the band offset of the $Al_xGa_{1-x}As/GaAs$ superlattice which depends on the Al content in the barrier. $\tilde{L}_B$ and $\tilde{L}_W$ is, respectively, the lenght of the barrier and the well.

The same type of arguments leading to equation (4.6) yield the following formulas for the tunnelling current through the first and last barrier of the SL:

$$\tilde{J}_{0\to1} = \frac{\hbar k_B\tilde{T}}{2\hbar}\sum_{\nu=1}^{n_{max}}\int_0^\infty A_\nu(\tilde{\epsilon})B_{0,1}(\tilde{\epsilon} - e\tilde{F}_0\tilde{l})T_0(\tilde{\epsilon})\ln\left[\frac{1+e^{\frac{\varepsilon_F + e\tilde{F}_0\tilde{l}-\epsilon}{k_B\tilde{T}}}}{1+e^{\frac{\mu_1-\epsilon}{k_B\tilde{T}}}}\right]d\tilde{\epsilon} \tag{4.8}$$

$$\tilde{J}_{N\to N+1} = \frac{\hbar k_B\tilde{T}}{2\hbar}\int_0^\infty A_1(\tilde{\epsilon})B_{N,N+1}(\tilde{\epsilon} + e\tilde{F}_N\tilde{l})T_N(\tilde{\epsilon})\ln\left[\frac{1+e^{\frac{\mu_N-\epsilon}{k_B\tilde{T}}}}{1+e^{\frac{\varepsilon'_F - e\tilde{F}_N\tilde{l}-\epsilon}{k_B\tilde{T}}}}\right]d\tilde{\epsilon} \tag{4.9}$$

In which $\epsilon = 0$ corresponds to the bottom of the first well in equation (4.8) and to the bottom of the Nth well in equation (4.9). ε_F and ε'_F are the Fermi energies of the injecting and the collecting regions, respectively.

The integrals in equations (4.6), (4.8), and (4.9) can be approximately calculated in the limit of a scattering broadening that is small compared to subband energies and chemical potentials, thereby yielding explicit formulas. For example, the formulas for the electron density and for the tunnelling current across an inner barrier are, [43]:

$$\tilde{n}_i = \frac{m^* k_B \tilde{T}}{\pi \hbar^2} \ln\left[1 + e^{\frac{\mu_i - \mathcal{E}_1}{k_B \tilde{T}}}\right], \tag{4.10}$$

$$\tilde{J}_{i\to i+1} = \frac{e\, v^{(f)}(\tilde{F}_i)}{\tilde{l}} \left\{\tilde{n}_i - \frac{m^* k_B \tilde{T}}{\pi \hbar^2} \ln\left[1 + e^{-\frac{e\tilde{F}_i \tilde{l}}{k_B \tilde{T}}} \left(e^{\frac{\pi \hbar^2 \tilde{n}_{i+1}}{m^* k_B \tilde{T}}} - 1\right)\right]\right\}, \tag{4.11}$$

$$v^{(f)}(\tilde{F}_i) = \sum_{\nu=1}^{n_{max}} \frac{\hbar^3 \tilde{l}}{2m^{*2}} \frac{(\gamma_1 + \gamma_\nu)\mathcal{T}_i(\tilde{\mathcal{E}}_1)}{(\tilde{\mathcal{E}}_1 - \tilde{\mathcal{E}}_\nu + e\tilde{F}_i\tilde{l})^2 + (\gamma_1 + \gamma_\nu)^2}. \tag{4.12}$$

Note that the *forward drift velocity* $v^{(f)}(\tilde{F}_i)$ is a sum of Lorentzians centred at the resonant field values $\tilde{F}_\nu = (\tilde{\mathcal{E}}_\nu - \tilde{\mathcal{E}}_1)/(e\tilde{l})$. The tunnelling current is a linear function of $\tilde{n}_i$, but it is a strongly nonlinear function of $\tilde{n}_{i+1}$. Moreover, $\tilde{J}_{i\to i+1} \sim e v^{(f)}(\tilde{F}_i)\tilde{n}_i/\tilde{l}$, for $\tilde{F}_i$ of the order of the first resonant value or larger. For such values, the resulting tunnelling current density has the same shape as assumed in the original *discrete drift model* [1, 69].

$$\tilde{J}_{i\to i+1} = \frac{v^{(f)}(\tilde{F}_i)}{\tilde{l}} \left(\tilde{n}_i - \tilde{n}_{i+1}\, e^{-\frac{e\tilde{F}_i \tilde{l}}{k_B \tilde{T}}}\right). \tag{4.13}$$

4.4 Model equations

The equations governing nonlinear charge transport in weakly coupled, undoped, photo-excited, type-I SLs are

$$\varepsilon\,(\tilde{F}_i - \tilde{F}_{i-1}) = e\,(\tilde{n}_i - \tilde{p}_i)\,, \quad i = 1, \ldots, N, \tag{4.14}$$

$$\varepsilon\,\frac{d\tilde{F}_i}{d\tilde{t}} + \tilde{J}_{i\to i+1} = \tilde{J}(t)\,, \quad i = 0, 1, \ldots, N, \tag{4.15}$$

$$\frac{d\tilde{p}_i}{d\tilde{t}} = \tilde{\gamma}(\tilde{I}) - \tilde{r}(\tilde{F}_i, \tilde{I})\,\tilde{n}_i \tilde{p}_i\,, \quad i = 1, \ldots, N. \tag{4.16}$$

In these equations, the tunneling current densities between the quantum wells (QWs) as well as between the SL and the contact regions are in the limit $k_B\tilde{T} \gg \pi\hbar^2\tilde{n}_{i+1}/m^* \approx \pi\hbar^2 N_D/m^*$. Therefore, we can approximate equation (4.11) by

$$\tilde{J}_{i\to i+1} = \frac{e\tilde{n}_i\tilde{v}(\tilde{F}_i)}{\tilde{l}} - e\tilde{D}(\tilde{F}_i)\frac{\tilde{n}_{i+1}-\tilde{n}_i}{\tilde{l}^2}\ , \tag{4.17}$$

$$\tilde{J}_{0\to 1} = \tilde{\sigma}\,\tilde{F}_0\ , \qquad \tilde{J}_{N\to N+1} = \frac{\tilde{n}_N}{N_D}\tilde{\sigma}\,\tilde{F}_N\ . \tag{4.18}$$

$$\tilde{v}(\tilde{F}_i) = v^{(f)}(\tilde{F}_i)\left(1 - e^{-\frac{e\tilde{F}_i\tilde{l}}{k_B\tilde{T}}}\right) \tag{4.19}$$

$$\tilde{D}(\tilde{F}_i) = v^{(f)}(\tilde{F}_i)\tilde{l}e^{-\frac{e\tilde{F}_i\tilde{l}}{k_B\tilde{T}}} \tag{4.20}$$

In which $v^{(f)}(\tilde{F}_i)$ is given by equation (4.12). The voltage bias condition is

$$\frac{1}{N+1}\sum_{i=0}^{N}\tilde{F}_i = \tilde{\phi} \equiv \frac{\tilde{V}}{\tilde{l}\,(N+1)}\ . \tag{4.21}$$

Here, ε, $\tilde{\sigma}$, N_D, $\tilde{n}_i$ and $\tilde{p}_i$ denote the average permittivity, the conductivity of the injecting contact, the doping density of the collecting contact, as well as the two-dimensional electron and hole densities of the ith period of the SL, respectively. Equation (4.14) corresponds to the averaged Poisson equation. Equation (4.15) denotes Ampère's law: the total current density $\tilde{J}(t)$ equals the sum of the displacement current density and $\tilde{J}_{i\to i+1}$, the electron tunneling current density across the ith barrier that separates the quantum wells i and $i+1$. Charge continuity is obtained by differentiating Eq. (4.14) with respect to time and using Eq. (4.15) in the result. Tunneling of holes is neglected so that only photogeneration and recombination of holes with electrons enter into Eq. (4.16).

Even for lower temperatures, the qualitative behavior of the solutions of the discrete drift-diffusion model is similar to one of the more general tunneling current models described in Ref. [10]. For $\tilde{D} = 0$ and a constant recombination coefficient $\tilde{r}$, Eqs. (4.14)–(4.17) describe the well known discrete drift model introduced in Ref. [1].

The indices $i = 0$ and $i = N+1$ represent the SL injecting and collecting contacts, and Eq. (4.15) holds for them with the phenomenological currents given by Eq. (4.18). The total current density follows from the voltage bias condition in Eq. (4.21)

$$\tilde{J}(t) = \frac{1}{N+1} \sum_{i=0}^{N} \tilde{J}_{i\to i+1} + \varepsilon \frac{d\tilde{\phi}}{d\tilde{t}} \, . \tag{4.22}$$

Photogeneration and recombination are given by $\tilde{\gamma}(\tilde{I}) = \tilde{I}\tilde{\alpha}_{\,3\mathrm{D}}(\hbar\omega_{\mathrm{exc}})\,\tilde{L}_w/(\hbar\omega_{\mathrm{exc}})$ and

$$\tilde{r}(\tilde{F},\tilde{I}) = \left(\frac{n_{\mathrm{ref}}}{n_{\mathrm{in}}\pi c}\right)^2 \int_0^\infty \frac{\omega^2 \tilde{\alpha}_{2\mathrm{D}}(\hbar\omega,\tilde{F})}{\exp(\frac{\hbar\omega}{k_B\tilde{T}})-1}\, d\omega \, , \tag{4.23}$$

respectively. Here $\tilde{I}$, ω_{exc}, n_{ref}, $n_{\mathrm{in}} \approx \tilde{\gamma} n_{\mathrm{ref}} \tilde{L}_w/c$, and c denote the photo-excitation intensity, the frequency of the exciting photon, the refractive index, the intrinsic carrier density, and the speed of light, respectively. $\tilde{\alpha}_{2\mathrm{D}}$ and $\tilde{\alpha}_{3\mathrm{D}}$ correspond to the two- (2D) and three-dimensional (3D) absorption coefficients. The 2D absorption coefficient is proportional to the square of the modulus of the electron-hole overlap integral for a constant electric field $\tilde{F}$ (cf. Ref. [16])

$$\begin{aligned} \tilde{\alpha}_{2D}(\omega,\tilde{F}) \;&=\; \alpha_0^{2D} \int_0^\infty \delta(\tilde{E}_{k_\parallel} + \tilde{E}_g - \hbar\omega + \tilde{E}_e^n(\tilde{F}) + \tilde{E}_h^m(\tilde{F}))\, d\tilde{E}_{k_\parallel} \\ &\quad \times \left| \int_{-l/2}^{l/2} \Psi_e^n(\tilde{z},\tilde{F}) \Psi_{hh}^m(\tilde{z},\tilde{F}) d\tilde{z} \right|^2 \, , \end{aligned} \tag{4.24}$$

where $\tilde{E}_g$ denotes the energy of the bandgap at the Γ point and Ψ_n as well as Ψ_h solve the stationary Schrödinger equation inside one SL period, $[-\tilde{l}/2, \tilde{l}/2]$, for the electrons and holes, respectively.

$$\left(-\frac{d}{d\tilde{z}}\left(\frac{\hbar^2}{2m^*(\tilde{z})}\frac{d}{d\tilde{z}}\right) + \tilde{V}(\tilde{z}) - e\tilde{F}\tilde{z}\right)\Psi(\tilde{z}) = \tilde{E}_z \Psi(\tilde{z}), \tag{4.25}$$

In this equation, the electric field $\tilde{F}$ is considered to be constant and $\Psi_{n,h}(\pm(\tilde{L}_w/2 + \tilde{l}_{p\pm})) = 0$, see *figure 4-1*, where the penetration length $\tilde{l}_{p\pm}$ solves the cubic equation

$$\tilde{l}_{p\pm} \sqrt{2m^* \left[\tilde{V} - e\tilde{F}\left(\tilde{l}_{p\pm} \mp \frac{\tilde{L}_w}{2}\right) - \tilde{E}_{n,h}\right]} = 1 \, ,$$

and therefore $\tilde{l}_{p\pm}$ depends self-consistently on the eigenvalue $\tilde{E}_{n,h}$. For a fixed value of $\tilde{I}$, the recombination coefficient decreases with increasing electric-field strength $\tilde{F}$, as depicted in *figure 4-2*.

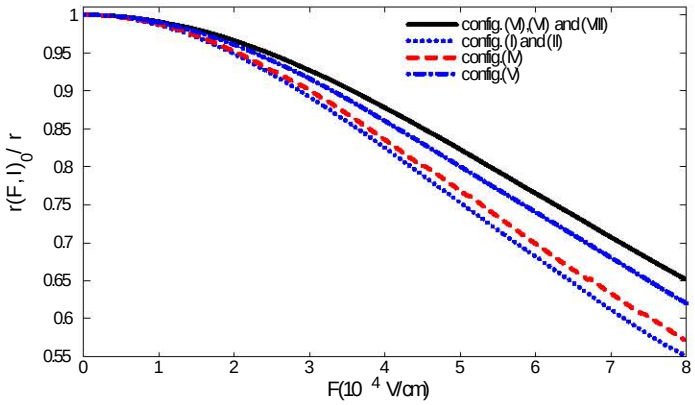

Figure 4-2 Recombination coefficient $\tilde{r}(\tilde{F},\tilde{I})/\tilde{r}(0,\tilde{I})$ vs electric field for the eight configurations listed in **table 4.1**.

4.5 Nondimensional equations

To study the model described by Eqs. (4.14)–(4.22), it is convenient to render them dimensionless. For a fixed value of the photo-excitation intensity $\tilde{I}$ and a constant electric field $\tilde{F}_i = \tilde{F}$, the stationary solution of Eq. (4.16) is $\tilde{n}_i = \tilde{p}_i = \sqrt{\tilde{\gamma}(\tilde{I})/\tilde{r}(\tilde{F},\tilde{I})}$. We use the maximum values $[n] = [p] = \sqrt{\tilde{\gamma}(\tilde{I})/\tilde{r}(0,\tilde{I})}$ to define typical values for $\tilde{n}_i$ and $\tilde{p}_i$. The field $\tilde{F}_M$ at the maximum of the drift velocity is a typical value of the field when there are self-sustained oscillations of the current (SSOC). Therefore, we adopt it as the field unit $[F] = \tilde{F}_M$. Similarly, $[v] = \tilde{v}_M$ and, therefore, $[J] = e[n]\tilde{v}_M/l$ and $[D] = l\tilde{v}_M$.

There are two possible time scales, the first one being $\tilde{t}_F = \varepsilon\tilde{F}_M/[J]$, which balances Maxwell's displacement current with the current density in Eq. (4.15), and the second one $\tilde{t}_n = [p]/\tilde{\gamma}(\tilde{I}) = 1/\sqrt{\tilde{\gamma}(\tilde{I})\tilde{r}(0,\tilde{I})}$, which balances both sides of Eq. (4.16). It is reasonable to choose the time unit as the longer of the two times $\tilde{t}_F$ and $\tilde{t}_n$.

We have chosen eight representative $GaAs/Al_xGa_{1-x}As$ SL configurations with 10 nm wells and 4 nm barriers. The configurations are I: $x = 0.25$ and $\tilde{I} = 120.5\ kW/cm^2$; II: $x = 0.25$ and $\tilde{I} = 302.69\ kW/cm^2$; III: $x = 0.3$ and $\tilde{I} = 120.5\ kW/cm^2$; IV: $x = 0.3$ and $\tilde{I} = 479.735\ kW/cm^2$; V: $x = 0.45$ and $\tilde{I} = 190.99\ kW/cm^2$;VI: $x = 1.0$ and $\tilde{I} = 30.27\ kW/cm^2$; VII: $x = 1.0$ and $\tilde{I} = 7.603\ kW/cm^2$; and VIII: $x = 1.0$ and $\tilde{I} = 76\ kW/cm^2$. We assume a circular cross section with a diameter of 160 μm, a photo-excitation intensity of 60 mW, a wavelength of 413 nm, and eight different beam diameters yielding the previously listed values of the laser intensity. For most of the cases listed in *table 4.1* $\tilde{t}_n > \tilde{t}_F$, and therefore we choose $[t] = \tilde{t}_n$. All scaled variables are listed in *table 4.1*:

config.	SL	$\tilde{I}$	$\tilde{n}$, $\tilde{p}$	$\tilde{F}$, ϕ	t	v	J	D	r	σ
		$\frac{\text{kW}}{\text{cm}^2}$	$\sqrt{\frac{\tilde{\gamma}(\tilde{I})}{\tilde{r}(0,\tilde{I})}}$ $\frac{10^{12}}{\text{cm}^2}$	$\tilde{F}_M$ $\frac{\text{kV}}{\text{cm}}$	$\frac{[n]}{\tilde{\gamma}(\tilde{I})}$ 10^{-11} s	$\tilde{v}_M$ $\frac{\text{km}}{\text{s}}$	$\frac{e[n]\tilde{v}_M}{\tilde{l}}$ $10^4\,\frac{\text{A}}{\text{cm}^2}$	$\tilde{l}\tilde{v}_M$ $10^{-2}\,\frac{\text{cm}^2}{\text{s}}$	$\tilde{r}(0,\tilde{I})$ $10^{-3}\,\frac{\text{cm}^2}{\text{s}}$	$\frac{e\tilde{v}_M[n]}{\tilde{F}_M\tilde{l}}$ $\frac{\text{A}}{\text{V cm}}$
I	$\mathcal{A}$	120.5	1.017	16.8	4.602	2.57	2.991	35.97	5.7	1.78
II	$\mathcal{A}$	302.69	4.0504	16.8	18.321	2.57	11.910	35.97	0.90026	7.0891
III	$\mathcal{B}$	120.5	1.016	16.0	8.75	1.42	1.652	19.89	5.689	1.0312
IV	$\mathcal{B}$	479.735	8.070	16.0	69.485	1.42	13.12	19.89	0.359	8.912
V	$\mathcal{C}$	190.99	2.022	15.20	84.34	0.312	0.7227	4.37	2.272	0.4754
VI	$\mathcal{D}$	30.27	0.2731	14.72	313.45	0.0057	8.28×10^{-4}	7.95×10^{-4}	90.7	5.62×10^{-4}
VII	$\mathcal{D}$	7.603	0.016	14.72	39.46	0.0057	$1.04{\times}10^{-4}$	7.95×10^{-4}	$1.43{\times}10^{3}$	$7.080{\times}10^{-5}$
VIII	$\mathcal{D}$	76	0.507	14.72	1248	0.0057	$3.29{\times}10^{-3}$	7.95×10^{-4}	14.37	$2.23{\times}10^{-3}$

Table 4.1 Units used to achieve a set of equations with dimensionless variables. The SL column details the aluminium content in the barrier. SL $\mathcal{A}$, $\mathcal{B}$, $\mathcal{C}$ and $\mathcal{D}$ have respectively $x = 0.25$, 0.3, 0.45 and 1.0 values. See appendix A.10

We now rewrite the model equations using dimensionless variables by defining $n_i = \tilde{n}_i/[n]$, $t = \tilde{t}/[t]$, ..., where $[n]$, $[t]$, etc. are the scales defined above and specified in *table 4.1*. Omitting hats over the variables, the nondimensional system of equations corresponding to Eqs. (4.14)–(4.22) read

$$F_i - F_{i-1} = (n_i - p_i)\nu \,, \tag{4.26}$$

$$\delta \frac{dF_i}{dt} + n_i v(F_i) - D(F_i)\,(n_{i+1} - n_i) = J(t) \,, \tag{4.27}$$

$$\frac{dp_i}{dt} = 1 - r(F_i)\, n_i p_i \,, \tag{4.28}$$

$$\sigma\, F_0 + \delta \frac{dF_0}{dt} = J \,, \qquad \sigma\alpha\, n_N F_N + \delta \frac{dF_N}{dt} = J \,, \tag{4.29}$$

$$\frac{1}{N+1} \sum_{i=0}^{N} F_i = \phi \,, \tag{4.30}$$

$$J = \frac{1}{N+1} \sum_{i=0}^{N} J_{i\to i+1} + \frac{d\phi}{dt} \,. \tag{4.31}$$

config.	α $\frac{[n]}{\tilde{N}_D}$	δ $\frac{\varepsilon\tilde{F}_M l\tilde{r}(0,\tilde{I})}{e\tilde{v}_M}$	ν $\frac{e[n]}{\varepsilon\tilde{F}_M}$	σ $\frac{\tilde{\sigma}\tilde{F}_M l}{e\tilde{v}_M[n]}$
I	0.9713	0.0037	8.446	1.0834
II	0.6944	5.91×10^{-4}	33.6228	1.0523
III	1	6.42×10^{-3}	8.876	1.080
IV	0.9779	4.05×10^{-4}	70.507	1.1074
V	1	1.09×10^{-2}	18.81	1.2980
VI	1.0146	22.3714	1.2721	1.2959
VII	2.34	354.25	0.1601	0.5625
VIII	1	3.55	5.065	1.3129

Table 4.2 Numerical values of the dimensionless parameters α, δ, ν and σ for the eight superlattice configurations listed in *table 4.1*

In these equations, there are four dimensionless parameters,

$$\delta = \frac{\varepsilon\tilde{F}_M l\tilde{r}(0,\tilde{I})}{e\tilde{v}_M}, \quad \nu = \frac{e[n]}{\varepsilon\tilde{F}_M}, \quad \alpha = \frac{[n]}{\tilde{N}_D} \equiv \frac{\sqrt{\tilde{\gamma}(\tilde{I})}}{\tilde{N}_D\sqrt{\tilde{r}(0,\tilde{I})}} ,$$

and the dimensionless conductivity $\tilde{\sigma}$, which is here simply denoted by σ. The values of the dimensionless parameters for the four SL configurations given in *table 4.1* are listed in *table 4.2*.

It is interesting to note that $\tilde{r}(0,\tilde{I}) \propto I^{-2}$ and $\tilde{\gamma}(\tilde{I}) \propto \tilde{I}$ so that $\nu \propto \tilde{I}^{3/2}$ and $\delta \propto \tilde{I}^{-2}$, i.e. ν increases with photo-excitation intensity, whereas δ decreases. The dimensionless parameter ν is a ratio of the carrier density scale determined by photogeneration and recombination to a density determined by scattering processes. The dimensionless parameter δ is a ratio of the time scales of dielectric relaxation and recombination [53]. These parameters depend on the laser intensity and the Aluminum content in the SL quantum barriers, $x \in (0,1]$. For high laser excitation, $\delta \ll 1$, whereas $\delta \gg 1$ for small laser excitation. The parameter ν can be of any order.

It is engrossing to depict the phase plane corresponding to spatially uniform solutions of Eqs. (4.26)–(4.28) with $n_i = p_i = p$, $F_i = F$

$$\delta\,\frac{dF}{dt} = J - p\,v(F), \quad \frac{dp}{dt} = 1 - r(F)\,p^2 \,. \tag{4.32}$$

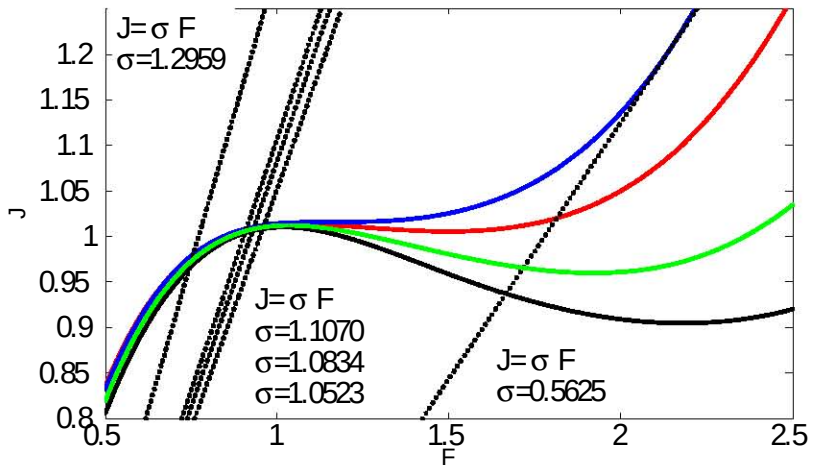

Figure 4-3 Local current density J vs electric field F. For a fixed value of the total current density J, there may be one or three zeros of $j(F)$-J depending on the Al content x. *SL* $\mathcal{A}$ (Blue) *SL* $\mathcal{B}$ (Red) *SL* $\mathcal{C}$ (Green) and *SL* $\mathcal{D}$ (Black)

Generically and for a fixed value of J, the nullclines $v(F)\,p = J$ and $r(F)\,p^2 = 1$ intersect in one or three fixed points, depending on the Al content x in the barriers. At these fixed points,

$$j(F) = J, \quad j(F) = \frac{v(F)}{\sqrt{r(F)}}\ . \tag{4.33}$$

The function $j(F)$ is depicted in *figure 4-3* for the SL configurations listed in *table 4.1*. The $v(F)$, $r(F)$ and $D(F)$ for the SL configurations listed in *table 4.1* are depicted in *figure 4-4*.

The calculations for arbitrary values of Aluminum content x show that for $0.45 \leq x \leq 1$, there are three fixed points of the system in Eq. (4.32), one on each of the three branches of $p = J/v(F)$, and the ratio of $(j_{\max} - j_{\min})$ to the average current $(j_{\max} + j_{\min})/2$ is sufficiently large. As we shall see in the following chapters, some nonlinear phenomena occurring in these SLs are quite similar to the ones observed in doped SLs: static electric-field domains with domain walls joining the stable branches of $p = J/v(F)$, SSOC due to the recycling of pulses formed by two moving domain walls having a high-field region between them, etc.

For $0 < x < 0.45$, $j(F)$ is either increasing for positive F (for $0 < x < 0.25$) or the ratio of $(j_{\max} - j_{\min})$ to the average current $(j_{\max} + j_{\min})/2$ is small (for $0.25 < x < 0.45$). For $0 < x < 0.25$, there is a unique fixed point at $F = F_*$, which, for an appropriate value of J, may be located on any of the three branches of $p = J/v(F)$.

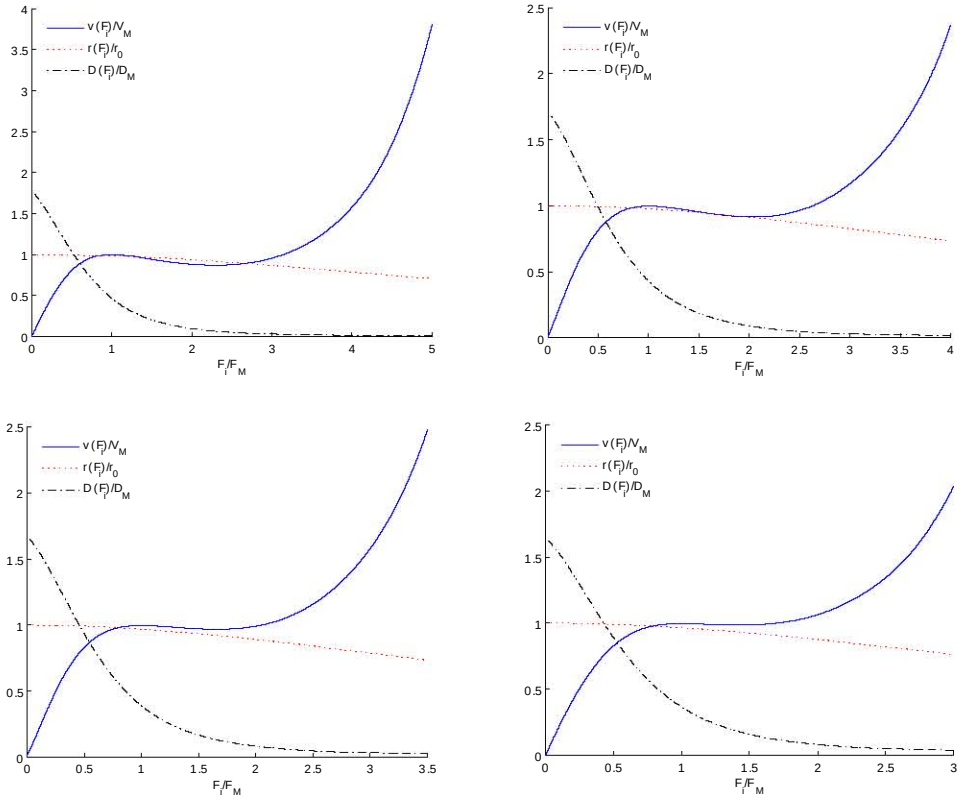

Figure 4-4: Nondimensional Drift velocity, diffusion and recombination as field functions for the superlattices (a) $SL\ \mathcal{D}(10/4)$,(b) $SL\ \mathcal{C}(10/4)$(c) $SL\ \mathcal{B}(10/4)$ and (d) $SL\ \mathcal{A}(10/4)$.

If the fixed point is located on one of the two stable branches of $p = J/v(F)$ for which $v(F)$ has a positive slope, the dynamical system of Eq. (4.32) is excitable, whereas it is oscillatory if the fixed point is located on the second branch of $p = J/v(F)$ with $v'(F_*) < -2\delta r(F_*) < 0$.

In an excitable dynamical system, an appropriate finite disturbance of the unique stable fixed point may cause a large excursion in phase space before returning to the stable state. When diffusion is added, the resulting excitable reaction-diffusion system may support a variety of wave fronts, pulses and wave trains.[12, 13, 14, 15] A dynamical system having an unstable fixed point and a stable limit cycle around it is oscillatory.

Again in the presence of diffusion, oscillatory systems may support different spatio-temporal patterns.[12, 15, 17] An undoped photo-excited SL with excitable or oscillatory dynamics exhibits quite unusual phenomena. Under dc current bias, it is possible to have pulses moving to the right or to the left and periodic wave trains. Under dc voltage bias, these pulses and wave trains may give rise to a variety of SSCOs. Similar phenomena are observed in the case $0.25 < x < 0.45$ for which

$j(F)$ has a shallow valley for a narrow interval of current densities. We will describe this phenomena in the next chapters.

4.6 Conclusions

The Nonlinear charge transport in weakly coupled photoexcited type-I superlattices, can be described mathematically with discrete convection-difusion equations . The Ampere law, charge continuity, Poisson and Ohms laws explain a rich dynamical behavior, including the formation of electric field domains, pinning of domains fronts, wave trains, self-sustained oscillations of the current, etc...

We have calculated the recombination coefficient as a function of the applied electric field for undoped, photo-excited, weakly coupled GaAs/$Al_xGa_{1-x}As$ SLs. Depending on the Al content x, the superlattice may have only one static domain for small x or two stable differentiated static domains for $0.45 < x \leq 1$.

The control of physical and technical parameters, such as the temperature, well width, barrier width and height, photoexcitation can be used to optimize the electron drift velocity function, as well as the electron-hole recombination function and electron difusion function, to select the dinamics we are interested on

Chapter 5

Wave fronts, pulses and wave trains in photoexcited superlattices

5.1 Introduction

The FitzHugh-Nagumo (FHN) model for nerve conduction is a classic example of an excitable medium [12, 52]. In its simplest form, it consists of two ordinary differential equations (ODE), one for the membrane voltage (the excitatory variable) and another for an ion concentration (the recovery variable). The voltage equation typically has a cubic source which also depends linearly on the recovery variable whereas the recovery equation is linear. The model has one stable stationary solution (fixed point) which is located in one of the branches of the cubic source and a finite disturbance from it may cause a large excursion in the phase plane before return to the fixed point is achieved.

This behavior is typical of an *excitable medium*. In the presence of diffusion in the equation for the excitatory variable, the FHN model has pulses and wave trains among its stable solutions [12, 52]. Adding a constant external current may push the fixed point of the FHN ODE to the second branch of the cubic source which renders it unstable. Then there is a stable limit cycle surrounding the fixed point and the FHN exhibits *oscillatory* behavior.

The diffusive FHN system then may have stable wave trains among its solutions and display synchronization phenomena [12]. Spatially discrete FHN systems model nerve conduction in myelinated fibers by simply replacing the diffusive term by a second order finite difference term. While the resulting discrete FHN system still has pulses and wave trains among its stable solutions [14], spatial

discreteness adds the possibility of pinning wave front solutions [12] and associated mechanisms for propagation failure of pulses [13].

Nonlinear charge transport in weakly coupled undoped type-I superlattices (SL) under laser photoexcitation is well described by spatially discrete drift-diffusion systems (DDDS) of equations [1, 2, 10]. SL are artificial crystals made by growing vertically layers of two different semiconductors, say Gallium Arsenide and Aluminum Gallium Arsenide. The difference in band gaps of these semiconductors cause the conduction band of the SL to resemble a succession of square wells and barriers for the electric potential. The Aluminum content in the barriers determines their height.

The DDDS consists of an equation for the electric field with a cubic-like nonlinear source and discrete convective and diffusive nonlinear terms coupled with an ODE for the density of holes. Electric field and carrier densities are constant within each period of the SL, thereby depending only on time and the discrete variable labeling the SL period.

Until recently, electron-hole recombination had been considered to be a constant, independent of the electric field [1]. The predicted nonlinear phenomena are quite similar to those observed in the much better known case of doped SL (in which the hole density is replaced by a constant doping density), namely the formation and dynamics of electric field domains, self-sustained oscillations of the current through voltage biased SL, chaos, etc [10].

Recently we have shown that including a field-dependent electron-hole recombination coefficient in the model has striking consequences [53]. At high laser intensity, it is possible to find only one stable electric field domain, not two as in the case of constant recombination coefficient [1]. Then, under dc voltage bias, periodic or chaotic self-sustained oscillations of the current may appear.

In this chapter, we construct relevant stable solutions of the discrete drift-diffusion system (DDS) of equations for dc current biased SL by means of asymptotic and numerical methods that extend and refine those used for the discrete FHN system [14, 13].

We find that pulses moving downstream with the electron flux can be described using matched asymptotic expansions based on separating the sharp leading and trailing wave fronts of the pulse from smoother regions outside them. Pulses moving upstream do so much more slowly and experience a saltatory motion in which intervals of slow change are separated by fast changes during which the pulse jumps to the previous SL period.

5.2 Wave fronts in a dc current biased photoexcited SL behaving as an excitable medium

Wave fronts and pulses of the electric field and carrier densities are key elements in the description of stable solutions of our model equations. We will start by describing these solutions on an infinite SL under constant current bias J in the limit of high laser excitation, $\delta \ll 1$, in which the dynamical behavior of the SL is richer [53]. In this section, we focus our attention on wave fronts and we deal with pulses in the next one.

5.2.1 Leading order construction of wave fronts

A wave front is a moving interface separating regions of smooth field variation on the time scale t. Inside the front, F_i varies rapidly on the time scale t/δ. Let us eliminate the electron density n_i by using (4.26) in system (4.26)–(4.29):

$$\begin{aligned} \delta \frac{dF_i}{dt} &+ v(F_i) \frac{F_i - F_{i-1}}{\nu} - D(F_i) \frac{F_{i+1} + F_{i-1} - 2F_i}{\nu} \\ &= J - v(F_i)p_i + D(F_i)\,(p_{i+1} - p_i), \end{aligned} \tag{5.1}$$

$$\frac{dp_i}{dt} = 1 - r(F_i)\,p_i \left(p_i + \frac{F_i - F_{i-1}}{\nu} \right), \tag{5.2}$$

In the regions where the field varies smoothly, we can set $\delta = 0$, $F_i = F_{i-1}$, $n_i = p_i$ in Eqs. (5.1) - (5.2), thereby obtaining the reduced problem

$$p_i v(F_i) = J, \tag{5.3}$$

$$\frac{dp_i}{dt} = 1 - r(F_i)\,p_i^2. \tag{5.4}$$

In the wave fronts that separate these regions, the electric field and the hole density vary rapidly as $F_i(t) = F(\xi)$, $p_i(t) = p(\xi)$, with $\xi = i - ct/\delta$. There, to leading order, Equations (5.1) and (5.2) yield

$$
\begin{aligned}
-c\,\frac{dF}{d\xi} &= J - \left[p + \frac{F(\xi) - F(\xi-1)}{\nu}\right] v(F(\xi)) \\
&+ D(F(\xi))\,\frac{F(\xi+1) + F(\xi-1) - 2F(\xi)}{\nu}, \qquad (5.5)
\end{aligned}
$$

$$
-c\,\frac{dp}{d\xi} = 0. \qquad (5.6)
$$

Thus p is a constant equal to the value $p_i(t)$ at the last point in the region of smooth variation before the front. Let $F^{(1)}(p) < F^{(2)}(p) < F^{(3)}(p)$ be the solutions of $J/v(F) = p$ for $v_{\min} < J/p < v_{\max}$, where the local maximum and minimum of the velocity $v(F)$ are reached at $(F_{\max}, v_{\max})$ and at $(F_{\min}, v_{\min})$, respectively (with $F_{\max} < F_{\min}$). Equation (5.5) has *increasing* front solutions (IFs) such that

$$
F_i(-\infty) = F(+\infty) = F^{(3)}(p), \quad F_i(+\infty) = F(-\infty) = F^{(1)}(p), \qquad (5.7)
$$

and *decreasing* front solutions (DFs) such that

$$
F_i(-\infty) = F(+\infty) = F^{(1)}(p), \quad F_i(+\infty) = F(-\infty) = F^{(3)}(p). \qquad (5.8)
$$

In *figure 5-1*, we show the nullclines $p = J/v(F)$ and $p = [r(F)]^{-1/2}$ for fixed J corresponding to (4.18), in a GaAs/AlAs SL. Depending on the parameters, the increasing function $p = [r(F)]^{-1/2}$ may intersect the cubic $p = J/v(F)$ in one, two or three critical points.

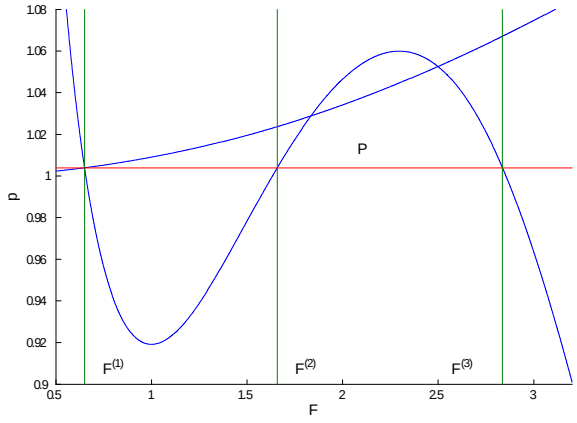

Figure 5-1: p–F phase plane exhibiting nullclines for fixed J and a wave front at constant p.

At least one critical point on the first or third branch of $p = J/v(F)$ makes our system behave as an excitable medium, whereas if there is only one critical point on the second branch of $p = J/v(F)$, our system has an oscillatory character, as we will see later.

In *figure 5-1*, we have also shown a horizontal line for a given constant value of p which joins the first and third branches of $p = J/v(F)$. This line corresponds to a wave front with fixed p as explained above. For sufficiently large ν, there are two critical values of the current density, J_{c1} and J_{c2}, so that IFs move to the right ($c > 0$) if $J < J_{c1}$, are pinned ($c = 0$) if $J_{c1} < J < J_{c2}$, and move to the left ($c < 0$) if $J > J_{c2}$. A similar picture holds for DFs. See *figure 5-2(b)*. Near the critical currents J_{ci} ($i = 1, 2$), the wave front profiles and their velocities can be approximately found by means of the theory of active QWs developed for doped SLs in [23] (see appendix A.7). In the limit $\nu \to 0+$, the equations for the fronts can be approximated by its continuum limit which is a first order hyperbolic PDE and the shock velocity gives a good approximation of the wave front velocity [23].

The theory we have just sketched holds in the limit as $\delta \to 0$ and we would expect that it also holds for sufficiently small positive values of δ. However, comparison of the front velocity given by the asymptotic theory and direct numerical simulation shows a remarkable difference even for quite small values of δ. For $\delta = 0.018$, the difference between the approximate and numerical velocities is about 0.06, which gives a relative error of 25%. This error is reduced to 2% for $\delta = 0.001$, but we would like to have an asymptotic theory which is better than this. How do we correct the simple wave front construction given above?

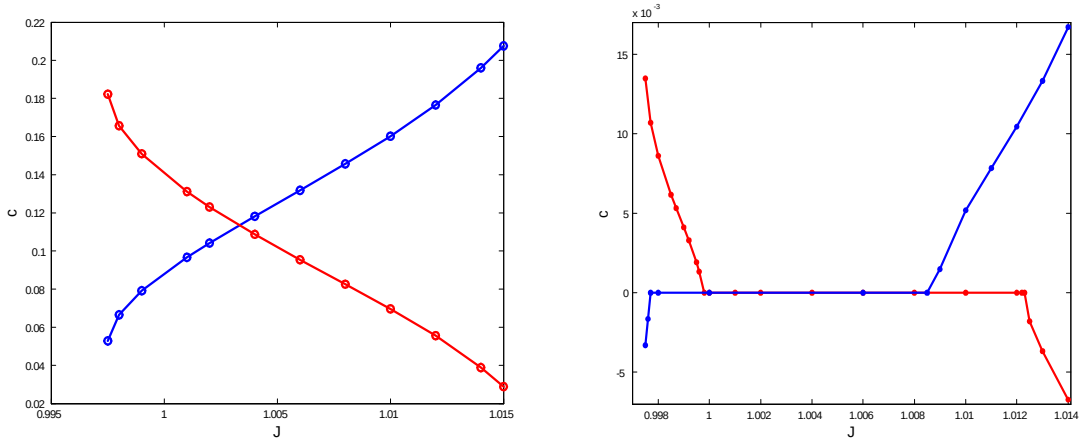

Figure 5-2 DF and IF dimensionless velocities as functions of dimensionless J for $x = 0.25$ and fixed p and ν. (a) $\nu = 8.45$, (b) $\nu = 330$. The DF (resp. IF) velocity is an increasing (resp. decreasing) function of J.

5.2.2 Corrected asymptotic theory of wave fronts

To correct the previous leading order theory of wave fronts, we use the fact that DF or IF profiles are monotone functions of a variable $\xi = i - ct/\delta$, where c is the front velocity. Thus

$$F_i(t) = \mathcal{F}(\xi), \quad p_i(t) = \mathcal{P}(\xi),$$

with $\mathcal{F}'(\xi) < 0$ (resp. > 0) for IF (resp. DF). In either case, we can find

$$\xi = \Xi(F) \quad \text{which solves} \quad \mathcal{F}(\xi) = F.$$

Then the finite differences

$$F_i - F_{i-1} = \mathcal{F}(\xi) - \mathcal{F}(\xi - 1) = F_i - \mathcal{F}(\Xi(F_i) - 1),$$

$$F_{i+1} + F_{i-1} - 2F_i = \mathcal{F}(\Xi(F_i) + 1) + \mathcal{F}(\Xi(F_i) - 1) - 2F_i, \tag{5.9}$$

can be considered to be functions of F_i. Therefore, we can derive from the equation for $p_i(\xi)$:

$$-c\frac{dp_i}{d\xi} = \delta\left[1 - r(F_i)p_i\left(p_i + \frac{F_i - F_{i-1}}{\nu}\right)\right],$$

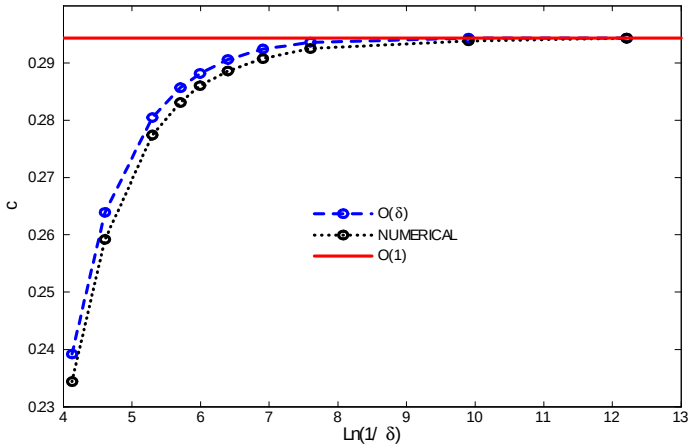

Figure 5-3 Comparison of the numerically obtained and asymptotic approximations to the DF velocity as a function of $\ln 1/\delta$. Parameter values are $x = 0.3$, $J = 1.006$, $\nu = 4.449$.

and from the equation for the wave front field profile, the following equation for p_i as a function of the field F_i:

$$\frac{dp_i}{dF_i} = \frac{\delta}{J} \frac{1 - r(F_i) p_i \left(p_i + \frac{F_i - F_{i-1}}{\nu} \right)}{1 - \left(p_i + \frac{F_i - F_{i-1}}{\nu} \right) \frac{v(F_i)}{J} + \frac{D(F_i)}{J} \left(p_{i+1} - p_i + \frac{F_{i+1} + F_{i-1} - 2F_i}{\nu} \right)}. \tag{5.10}$$

Now we integrate this equation and iterate the result starting from the value $p_i(F_0) = p$, thereby obtaining

$$\begin{aligned} & p_i \sim p \\ & + \frac{\delta}{J} \int_{F_0}^{F_i} \frac{\left[1 - r(F) p \left(p + \frac{F - \mathcal{F}(\Xi(F) - 1)}{\nu} \right) \right] dF}{1 - \left(p + \frac{F - \mathcal{F}(\Xi(F) - 1)}{\nu} \right) \frac{v(F)}{J} + \frac{D(F)}{J} \left(\frac{\mathcal{F}(\Xi(F) + 1) + \mathcal{F}(\Xi(F) - 1) - 2F}{\nu} \right)} \end{aligned} \tag{5.11}$$

up to terms of order δ^2.

The starting point F_0 should be selected so as to ensure convergence of the integral in Eq. (5.11). If $p = p_*$ corresponds exactly to a critical point, we can select F_0 as the field value of the same critical point, F_*. Then the integrand has a finite limit as $F \to F_0$ and the integral in Eq. (5.11) converges. If this is not the case, we need a nonzero value of the finite difference $F_0 - \mathcal{F}(\Xi(F_0) - 1)$ to get a nonzero value of the denominator in Eq. (5.10). We use the slow scale equation (5.3) to calculate $F_i = \Phi(p_i)$. Inserting this function in (5.4), we get

$$\frac{dp_i}{dt} = 1 - r(\Phi(p_i)) p_i^2. \tag{5.12}$$

We now solve this equation for an initial value $p_i(0) = p$, to obtain $p_i = p_i(t; p)$. Then $F_i(t) = \Phi(p_i(t; p))$. Using that F_i is a function of $i - ct/\delta$ in the wave front profile, we have $F_{i-1}(t = 0) = F_i(t = -\delta/c) = \Phi(p_i(-\delta/c; p))$. The equation

$$\mathcal{F}(\Xi(F_0) - 1) = \Phi \left(p_i \left(-\frac{\delta}{c}; p \right) \right),$$

determines F_0 as a function of p with $F_0 - \mathcal{F}(\Xi(F_0) - 1) \neq 0$.

Once we have determined p_i as a function of F_i by means of (5.11), we can solve the fast equation

$$-c\,\frac{dF_i}{d\xi} \quad + \quad \left(p_i(F_i) + \frac{F_i - F_{i-1}}{\nu}\right) v(F_i)$$
$$- \quad D(F_i)\left(p_{i+1}(F_{i+1}) - p_i(F_i) + \frac{F_{i+1} + F_{i-1} - 2F_i}{\nu}\right) = J, \tag{5.13}$$

with $F_i = F(\xi)$, $F_{i\pm1} = F(\xi \pm 1)$ and boundary conditions

$$F_i(-\infty) = F(+\infty) = F^{(3)}(p), \quad F_i(+\infty) = F(-\infty) = F^{(1)}(p'), \tag{5.14}$$

for the IFs and

$$F_i(-\infty) = F(+\infty) = F^{(1)}(p), \quad F_i(+\infty) = F(-\infty) = F^{(3)}(p'), \tag{5.15}$$

for the DFs. In (5.14), the value $p' \neq p$ is determined by solving (5.11) and (5.13) until the first branch of $J/v(F)$ is reached. Similarly, for a DF, p' is found by solving (5.11) and (5.13) until the third branch of $J/v(F)$ is reached.

The front velocity is now a function of δ and *figure 5-3* shows that it is a much better approximation to the numerically calculated front velocity than that given by the leading order theory.

In practice, it is easier to calculate directly the finite differences $\mp(F_i - F_{i\pm1})$ as functions of F_i.

5.3 Pulses moving downstream in an excitable SL

As we see in *figure 5-4* (a), a pulse moving downstream with positive velocity consists of regions of smooth field variation on the time scale t, separated by sharp interfaces in which F_i varies rapidly on the time scale t/δ. The same description can be done to the *figure 5-4* (c), but in this case, the stable solution is on the third branch. To find an asymptotic approximation to both pulses profiles, we first use the leading order description of its component wave fronts, according to which p_i is a constant independent of i inside the wave front.

We can now discuss different regions in the asymptotic description of a pulse with a stable solution on the first branch, recalling that the field profile is the mirror image of the motion of a QW, $F_i(t) = F(i - ct/\delta)$. The asymptotic description of a pulse with a stable solution on the third branch of $J/v(F)$ can be done in a similar way.

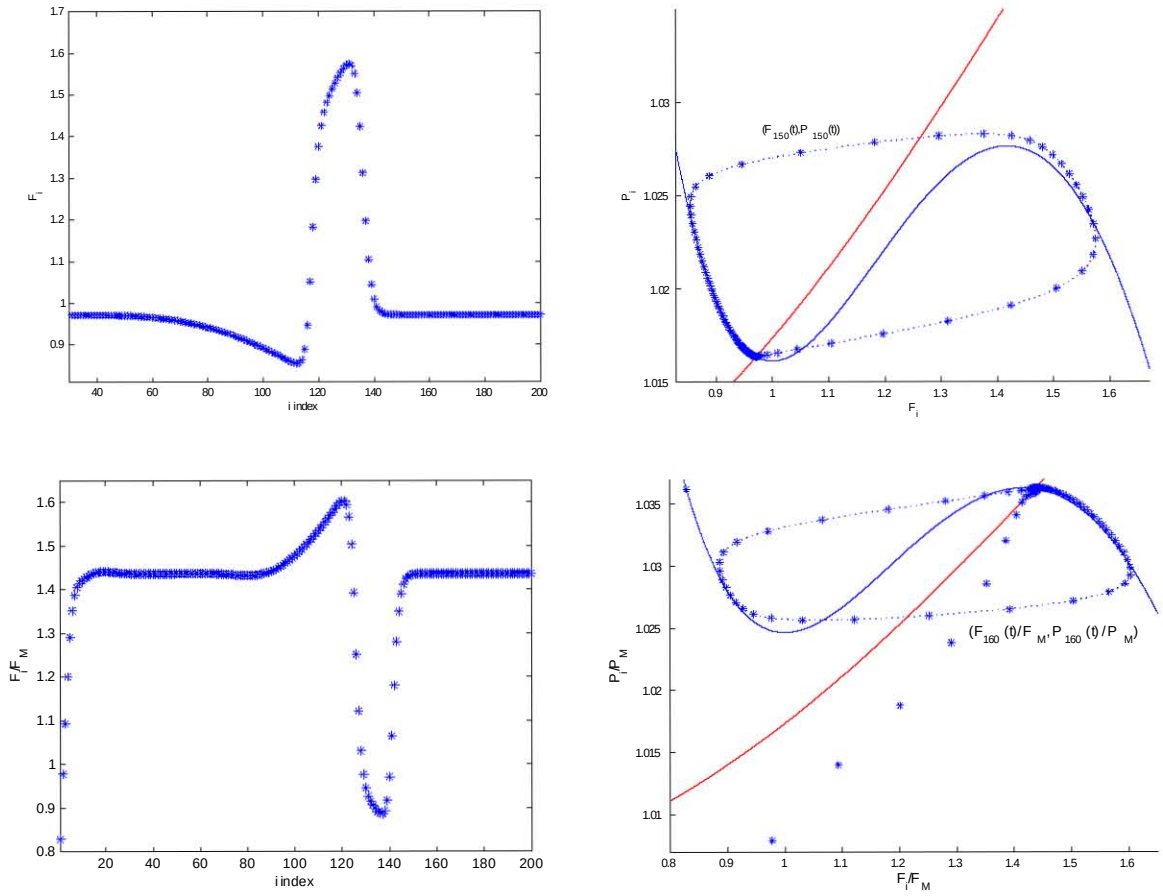

Figure 5-4 Numerically obtained field profile of pulses moving with positive speed for a SL $\mathcal{A}$ with, $\nu = 8.4456$, $\delta = 3.73 \times 10^{-3}$ (a) $J = 1.013$ and (c) $J = 1.0215$. (b) and (d) show the phase plane with the nullclines and the motion of a QW as the pulse traverses it. In (c) and (d) is also represented a stationary solution, see appendix A.3.

5.3.1 Only one critical point on the first stable branch of $J/v(F)$ (leading order theory)

First of all, we shall describe the pulses for values of J and ν such that there is one critical point, (F_*, p_*), located on the first branch of $J/v(F)$. There are no other critical points or, if they exist, they are located on the second branch of $J/v(F)$.

1. The region of smooth variation of F in front of the pulse is described by (5.3) and (5.4). In this region, $F_i = F^{(1)}(p_i)$, so that

$$\frac{dp_i}{dt} = 1 - r\left(F^{(1)}(p_i)\right) p_i^2,$$

and initial data evolve exponentially fast towards equilibrium, $F_i = F_*$, $p_i = p_*$.

2. The pulse leading edge. Let $p(t)$ be the value of p_i at the last point of the region in front of the pulse. Eventually, $p \to p_*$. At the leading edge, $F_i(t) = F(i - ct/\delta)$ is a DF moving towards the right with speed $C = c(J, \nu, p)/\delta$ measured in QWs per unit time t. The DF satisfies (5.5) with boundary conditions (5.8). It is convenient to call $c_-(p) = c(J, \nu, p)$. Eventually, $C \sim c_-(p_*)/\delta$, and F_i decreases from $F_i = F_{\max}$ to $F_i = F_*$ across the leading edge of the pulse.

3. Region between fronts: $F_i = F^{(3)}(p_i)$ and

$$\frac{dp_i}{dt} = 1 - r\left(F^{(3)}(p_i)\right) p_i^2.$$

There is a finite number of points in this region. On its far right, $p_i = p \to p_*$. As we move towards the left, p_i increases until it reaches a certain value $P(t)$ corresponding to that in the trailing wave front.

4. Trailing wave front: $p_i(t) = p(\xi) = P$, and $F_i(t) = F(\xi)$ is an IF satisfying (5.5) with boundary conditions (5.7). This front moves with speed $C = c(J, \nu, P)/\delta$ measured in QWs per unit time t. It is convenient to denote $c_+(P) = c(J, \nu, P)$. We shall indicate how to determine P below. Clearly, if the pulse is to move rigidly, we should have $c_+(P) = c_-(p_*)$ after a sufficiently long transient period.

5. Pulse tail. Again $F_i = F^{(1)}(p_i)$ and $dp_i/dt = 1 - r(F^{(1)}(p_i))\, p_i^2$. Sufficiently far to the left, $p_i = p_*$, $F_i = F_*$.

The number of QWs between wave fronts of the pulse can be calculated as follows [13]. Let τ be the delay between fronts, i.e. the time elapsed from the instant at which the leading front traverses the QW $i = I$ to the instant when the trailing front is at $i = I$. Clearly,

$$\tau = \int_{p(t-\tau)}^{P(t)} \frac{dp}{1 - r\left(F^{(3)}(p)\right)\, p^2}\,. \tag{5.16}$$

The number of QWs between fronts, $m(t)$, is

$$m = \frac{1}{\delta} \int_{t-\tau}^{t} c_-(p(t))\, dt\,. \tag{5.17}$$

On the other hand, the separation between fronts satisfies the equation

$$\frac{dm}{dt} = \frac{c_-(p(t)) - c_+(P(t))}{\delta}\,. \tag{5.18}$$

The three equations (5.16), (5.17) and (5.18) can be solved to obtain the three unknowns τ, m and $P(t)$. (The function $p(t)$ is determined by solving (5.4) with $F_i = F^{(1)}(p_i)$ in the region to the left of the leading front).

After a transient period, $p(t) \to p_*$ and $P(t) \to P$ (a constant value), so that we have the simpler expressions

$$\tau = \int_{p_*}^{P} \frac{dp}{1 - r\left(F^{(3)}(p)\right)\, p^2}, \tag{5.19}$$

$$\frac{dm}{dt} = \frac{c_-(p_*) - c_+(P)}{\delta}\,, \tag{5.20}$$

instead of (5.16) and (5.18), respectively. The number of points at the pulse top is now

$$m = \frac{c_-(p_*)\tau}{\delta} = \frac{c_-(p_*)}{\delta} \int_{p_*}^{P} \frac{dp}{1 - r(F^{(3)}(p))\, p^2}\,. \tag{5.21}$$

This equation yields P as a function of m. Then (5.20) becomes an autonomous differential equation for m that has a stable constant solution at $m = m^*$ such that $c_-(p_*) = c_+(P(m))$: At $m = m^*$, the right hand side of (5.20) has a slope $-[1 - r(F^{(3)}(J/P))\, P^2]\, c_+'(P)/c_-(p_*) < 0$.

Recapitulating, for appropriate initial conditions, leading and trailing fronts of a pulse evolve until m reaches its stable value at which $c_-(p_*) = c_+(P(m^*))$ and (5.21) holds. To compute m^*, we first determine $P^* = P(m^*)$ by using $c_-(p_*) = c_+(P(m^*))$. Then we calculate $\tau = \tau^*$ (which does not depend on δ!) from (5.19) and $m^* = c_-(p_*)\tau^*/\delta$. Our construction breaks down if the number

of QWs between fronts falls below 1. This yields an upper bound for the critical value of δ above which pulse propagation fails: $\delta_c \sim c_-(p_*)\tau^*$.

To calculate the asymptotic length of the pulse tail we cannot use Eq. (5.19) with $F^{(1)}$ replacing $F^{(3)}$ in that formula because the resulting time is infinity. However, we can calculate the time it takes for a solution $p(t)$ of Eq. (5.12) with $\Phi(p) = F^{(1)}(p)$ and $p(0) = P$ to reach a neighborhood of p_* . From that equation, we obtain

$$t = \int_p^P \frac{dp}{r(F^{(1)}(p))\,p^2 - 1} \sim \int_{p_*}^P \left[\frac{1}{r(F^{(1)}(p))\,p^2 - 1} - \frac{1}{(rp^2)'_*(p - p_*)}\right] dp + \frac{1}{(rp^2)'_*} \ln\left(\frac{P - p_*}{p - p_*}\right)$$

with $(rp^2)'_* = d[r(F^{(1)}(p))p^2]/dp|_{p=p_*} > 0$, and therefore

$$p(t) - p_* \sim (P - p_*)e^{-(rp^2)'_*(t-T)}, \qquad T = \left[\frac{1}{r(F^{(1)}(p))\,p^2 - 1} - \frac{1}{(rp^2)'_*(p - p_*)}\right] dp$$

for long times such that $p(t)$ is sufficiently close to p_* . The time needed for $p(t)$ to go from P to $p_*+(P-p_*)/e$ is then $T_* = T+1/(rp^2)'_*$. The tail length is approximately given by $M = c_-(p_*)T_*/\delta$.

5.3.2 Only one critical point on a stable branch of $J/v(F)$ (corrected theory)

How do we correct this pulse construction using our improved theory of wave fronts?

- The region of smooth variation in front of the pulse is as described above.

- On the other hand, we have to use Eq. (5.13) instead of (5.5), with boundary conditions (5.14) or (5.15), to construct the leading and trailing wave fronts of the pulse. Assume the pulse moves from left to right. The leading wave front is a DF moving with speed $c_-(p)/\delta$ with $c_-(p) = c(J, \nu, p, \delta)$ given by (5.13) and boundary conditions (5.15). While $p(t)$ is the value at the initial field on the first branch of $J/v(F)$, $p'(t)$ is the hole density at the final QW of the DF which is on the third branch of $J/v(F)$. The time it takes for a QW to move from $(F^{(1)}(p), p)$ to $(F^{(3)}(p'), p')$ is of order δ but we can not ignore it when constructing the pulse.

- In the region between leading and trailing fronts, $F_i = F^{(3)}(p_i)$. On its far right, $p_i = p' \to p'_*$, where we call p'_* the value of p' corresponding to $p = p_*$. As we move towards the left, p_i increases until it reaches a certain value $P(t)$ corresponding to that in the trailing wave front.

- The trailing wave front is an IF moving with speed $c_+(P)/\delta$, with $c_+(P) = c(J, \nu, P, \delta)$ given by (5.13) and boundary conditions (5.14). The hole densities at the initial and final QWs of the IF are P and P', respectively. The corresponding fields are $F^{(3)}(P)$ and $F^{(1)}(P')$, respectively. Again the time it takes for a QW to move from $(F^{(3)}(P), P)$ to $(F^{(1)}(P'), P')$ is of order δ but is not ignored.

- The pulse tail is as described above, except that its first QW has a hole density P' instead of P.

Equations (5.16) to (5.18) become

$$\tau = \int_{p'(t-\tau)}^{P(t)} \frac{dp}{1 - r\left(F^{(3)}(p)\right) p^2}\,, \tag{5.22}$$

$$m = \frac{1}{\delta} \int_{t-\tau}^{t} c_-(p(t))\, dt\,. \tag{5.23}$$

$$\frac{dm}{dt} = \frac{c_-(p'(t)) - c_+(P(t))}{\delta}\,. \tag{5.24}$$

After the transient period, these equations become (5.19) - (5.21) with p' instead of p_*. The rest of the considerations made above apply except that now τ^* depends on δ because p' does.

5.3.3 Two critical points on the stable branches of $J/v(F)$ for large photo-excitation intensities

In the case illustrated in *figure 5-5*, there is one critical point on each of the three branches of $J/v(F)$. Let (F_*, p_*) and (F^*, p^*) be the critical points on the first and third branches of $J/v(F)$, respectively. This case is very similar to that described before for the case of a sole critical point on the first branch.

However, now $c_-(p_*) \neq c_+(p^*)$ except for particular values of J. Therefore these pulses do not move rigidly in general: they will shrink and disappear or grow indefinitely. Regions 1 to 3 of the pulse in *figure 5-5*(a) are identical to those of the pulse with only one critical point, except that now $p \to p_*$, $P \to p^*$ and m either decays to zero or it grows indefinitely.

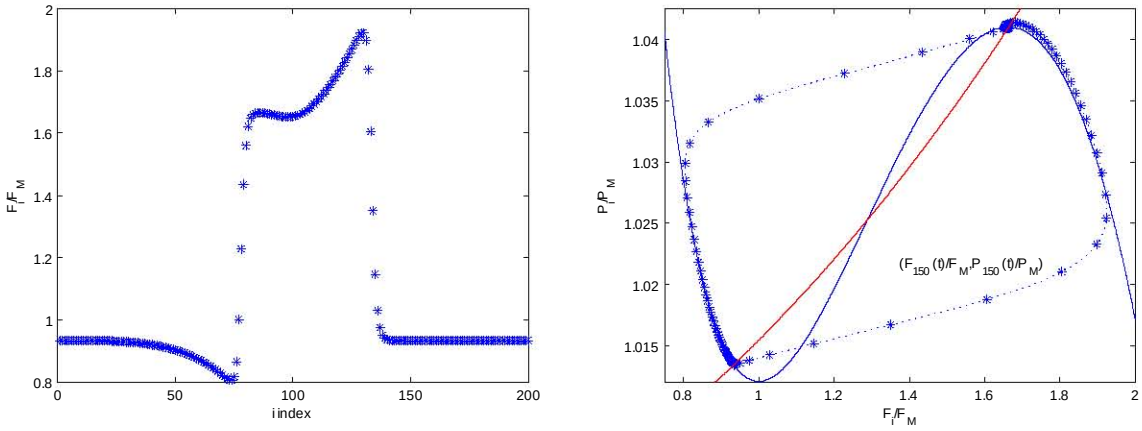

Figure 5-5 Numerically obtained field profile of pulses moving with positive speed for a configuration III with $J = 1.009$ (b) Phase plane showing the nullclines and the motion of the 150th QW as the pulse traverses it. Near the third branch stable solution, the QWs form a spiral to reach it

5.4 Wave trains moving downstream in a dc current biased photoexcited SL

For the spatially discrete FHN system, wave trains were constructed by A. Carpio using matched asymptotic expansions [14]. A similar construction can be carried out using our improved theory of wave fronts.

A wave train consists of a periodic profile $F(\xi)$, $p(\xi)$, $\xi = i - ct/\delta$, with period L and velocity c; cf. *figure 5-6 (b)* shows the passage of a wave train through a QW: starting at an unstable stationary state, trajectories in the phase plane evolve towards a stable limit cycle. *figure 5-6(a)* gives the corresponding field profile: a first smaller pulse triggers a periodic succession of equal pulses which become the wave train.

The wave train profiles can be reconstructed from a time periodic solution $F_i(t) = F(i - ct/\delta)$, $p_i(t) = p(i - ct/\delta)$, with time period $T = L\delta/c$ and velocity c. The spatial structure of the wave train at each fixed time t is given by $F_i(t) = F(i - ct/\delta)$ and $p_i(t) = p(i - ct/\delta)$. The points contained in a period satisfy $0 \leq i - ct/\delta \leq L$, that is, $ct/\delta \leq i \leq L + ct/\delta$. As time grows, the discrete points 'travel' along the continuous wave profile and are transferred from one period to the next. The number of integers i one can fit in an interval of length L is the integer part of L.

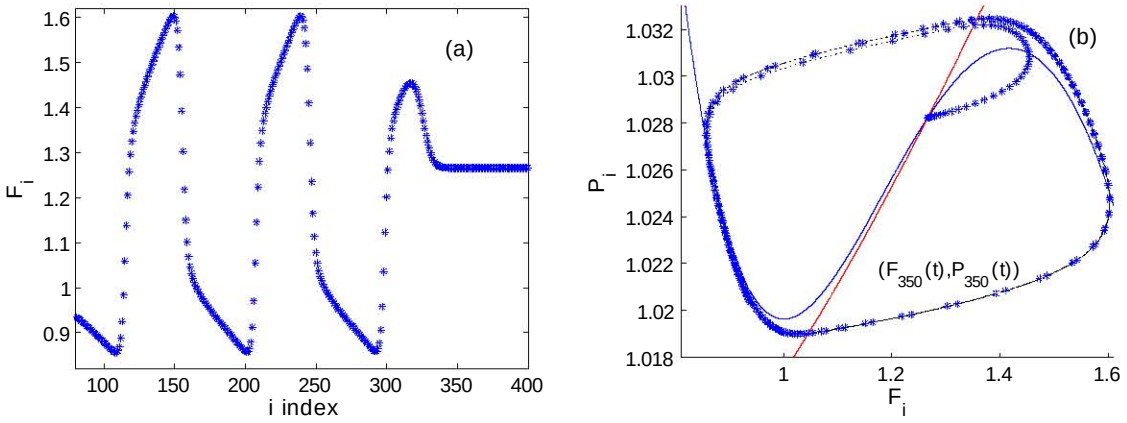

Figure 5-6 (a) Numerically obtained field profile of a pulse moving with positive speed followed by a wave train when there is only one critical point in the phase plane. Configuration I. (b) Phase plane showing the nullclines and the motion of the 350th QW as the pulse traverses it. $J = 1.009$.

Assuming positive speed, there are four stages in one time period of the wave trains $(F_i(T,\delta), p_i(T,\delta))$:

- Leading edge DF given by Eqs. (5.13) and (5.11), with boundary conditions (5.15). The DF velocity is $c_-(p)/\delta$ with $c_-(p) = c(J,\nu,p,\delta)$, where $p(t)$ is the value at the initial field on the first branch of $J/v(F)$ and $p'(t)$ is the hole density at the final QW of the DF, whose corresponding field is on the third branch of $J/v(F)$. The time it takes for a QW to move from $(F^{(1)}(p), p)$ to $(F^{(3)}(p'), p')$ is of order δ but we can not ignore it when constructing the train.

- In the peak region between leading and trailing fronts, $F_i = F^{(3)}(p_i)$. On its far right, $p_i = p'$. As we move towards the left, p_i increases until it reaches a certain value $P(t)$ corresponding to that in the trailing wave front. $P(t)$ will be calculated later. The duration of this stage is

$$T_p = \int_{p'}^{P} \frac{dp}{1 - r\left(F^{(3)}(p)\right) p^2} \,.$$

Note that T_p may become infinite if there is a fixed point (F^*, p^*) on the third branch of $J/v(F)$. In such a case, we may have wave trains only if $p < p^*$.

- The trailing wave front is an IF moving with speed $c_+(P)/\delta$, with $c_+(P) = c(J,\nu,P,\delta)$ given by (5.13) and boundary conditions (5.14). The hole densities at the initial and final QWs of the IF are P and P', respectively, and the corresponding fields are $F^{(3)}(P)$ and $F^{(1)}(P')$, respectively.

Again the time it takes for a QW to move from $(F^{(3)}(P), P)$ to $(F^{(1)}(P'), P')$ is of order δ and will not be ignored. For the wave train to move rigidly, we must have $c_-(p) = c_+(P) = c$. This condition gives P as a function of p.

- In the tail of the wave train, $F_i = F^{(1)}(p_i)$. On the far right of the tail region, $p_i = P'$ and p_i decreases until it reaches the value p. The duration of this stage is

$$T_t = \int_{P'}^{p} \frac{dp}{1 - r\left(F^{(1)}(p)\right)\, p^2}\,.$$

Note that T_t may become infinite if there is a fixed point (F_*, p_*) on the first branch of $J/v(F)$. In such a case, we may have wave trains only if $p > p_*$.

The previous construction of the wave train gives its velocity and period $T \sim T_p + T_t$ as functions of the parameter p. The spatial period L is the integer part of cT/δ. The number of QWs in the peak (resp. the tail) region is the integer part of $c_-(p)T_p/\delta$ (resp. $c_-(p)T_t/\delta$). Clearly our construction fails if the number of QWs in the peak region is smaller than one, i.e., if $c_-(p)T_p < \delta$. Thus, δ has to be larger than $c_-(p)T_p$.

5.5 Pulses moving upstream in a dc current biased photoexcited SL that behaves as an excitable medium

Numerical simulations of the complete model show pulses moving upstream, with negative velocity, both under dc current bias and under dc voltage bias. Although the field profile of these pulses is quite similar to that of downstream moving pulses (compare *figures 5-4(a)* and *5-7*), there are fundamental differences between them.

The velocity of these pulses is much smaller than that of downstream moving pulses and they cannot be approximated by one IF and one DF plus regions of slow variation of the electric field. In fact, *figure 5-2(b)* shows that, contrary to the case of wave fronts moving with positive velocity depicted in *figure 5-2*(a), it is not possible for a DF and an IF to move with the same negative velocity at a fixed J. Thus our construction of pulses in section 5.3 cannot describe pulses that move rigidly upstream with negative velocity.

The asymptotic construction of pulses moving rigidly with negative velocity under dc current bias is necessarily different from the case of downstream moving pulses. The rigid upstream motion of pulses is saltatory: there are periods in which the QWs move slowly on the pulse field profile separated by fast transitions, as shown in *figure 5-8(a)*.

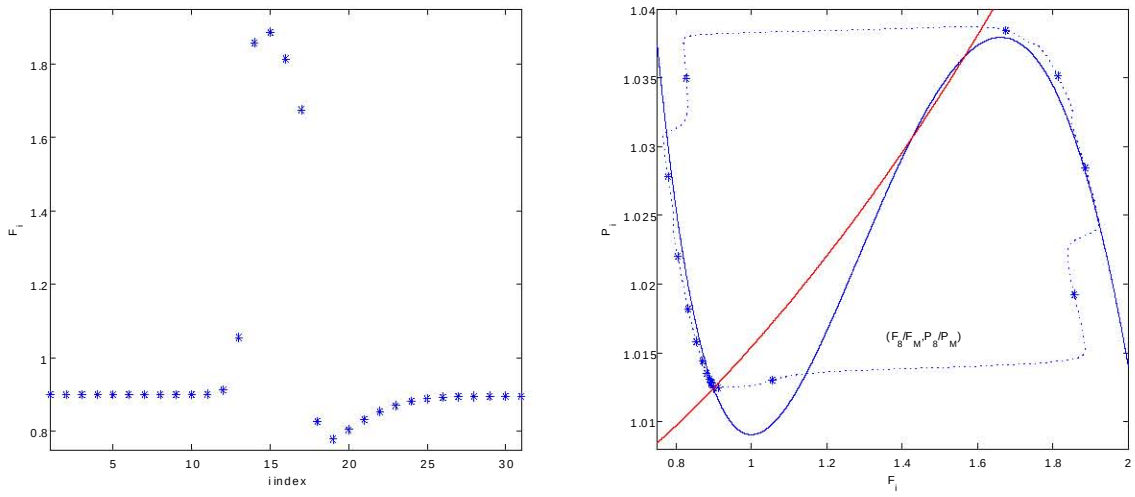

Figure 5-7(a) Numerically obtained field profile of a pulse moving with negative speed for SL $\mathcal{B}$, $J = 1.009$, $\nu = 70.5$, $\delta = 4.05 \times 10^{-4}$. (b) We show the phase plane with the nullclines and the motion of the 8th QW as the pulse traverses it. Here the laser intensity is 479,735 kW/cm^2.

Figure 5-8(b) shows that the hole density changes smoothly even at the fast transitions in the field profile. During the slow periods, the field and hole density at the QWs evolve according to the following equations:

$$\begin{aligned} & \left(p_i + \frac{F_i - F_{i-1}}{\nu}\right) v(F_i) - \left(p_{i+1} - p_i + \frac{F_{i+1} + F_{i-1} - 2F_i}{\nu}\right) D(F_i) \\ = \;& J, \end{aligned} \tag{5.25}$$

$$\frac{dp_i}{dt} = 1 - r(F_i)\, p_i \left(p_i + \frac{F_i - F_{i-1}}{\nu}\right), \tag{5.26}$$

which have been obtained setting $\delta = 0$ in (5.1) - (5.2). We have to solve Eq. (5.25) for the profile $\{F_i\}$ in terms of the instantaneous values of the $\{p_i\}$ and insert the result in (5.26). It turns out that there are several possible solutions corresponding to integer shifts of the pulse profile $i \to i + m$, $m = 0, \pm 1, \ldots$. The implicit function theorem establishes that, starting from an appropriate pulse-like initial condition, it is possible to find $F_i = F_i(\{p_j\})$, provided the Jacobian determinant corresponding to (5.25) is not zero.

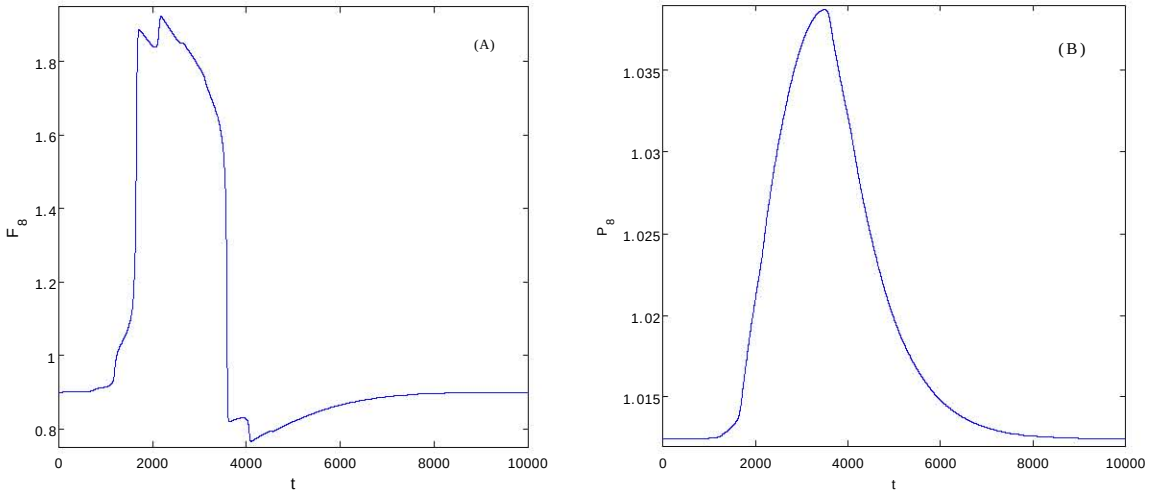

Figure 5-8(a) Numerically obtained field $F_8(t)$ of a pulse moving with negative speed for SL $\mathcal{B}$, $J = 1.009$, $\nu = 70.5$, $\delta = 4.05 \times 10^{-4}$. (b) Numerically obtained hole density $p_8(t)$ of the same pulse.

This condition holds until the QWs reach the points of abrupt field change in *figures 5-8(a)* or *5-7(b)* at times $t = t_a$. Then the Jacobian vanishes and the field values change according to

$$\begin{aligned} \frac{dF_i}{d\tau} &= J + \left(p_{i+1} - p_i + \frac{F_{i+1} + F_{i-1} - 2F_i}{\nu} \right) D(F_i) \\ &\quad - \left(p_i + \frac{F_i - F_{i-1}}{\nu} \right) v(F_i), \end{aligned} \tag{5.27}$$

with $\tau = (t - t_a)/\delta$ and $\{p_i\}$ frozen at their values at t_a given by (5.25) - (5.26). As explained before, the $\{F_i(\tau)\}$ tends as $\tau \to -\infty$ to the solution of (5.25) that is found at $t = t_a$, and it tends to the same profile shifted one step to the left: $i \to i - 1$ as $\tau \to +\infty$. Then another slow stage follows. The velocity of the pulse is approximately the reciprocal of the time one QW spends in the short interval of p between the abrupt long jump in F from the first branch of $J/v(F)$ to a value below that in the third branch of $J/v(F)$ and the abrupt short jump in F to the third branch of $J/v(F)$ which occurs for a somewhat higher value of p; cf. *figure 5-7(b)*.

As we can see in *figure 5-9*(a) the values of ν and δ modifies the velocity of the pulses. Independently of the value of the laser pumping intensity, the upstream pulses have a critical current, $J_c(\delta, \nu)$, in which they can be found in the SL. The variation of the velocity near this critical current is abrupt until δ is small enough. As long as δ grows, the velocity and the critical current grows too.

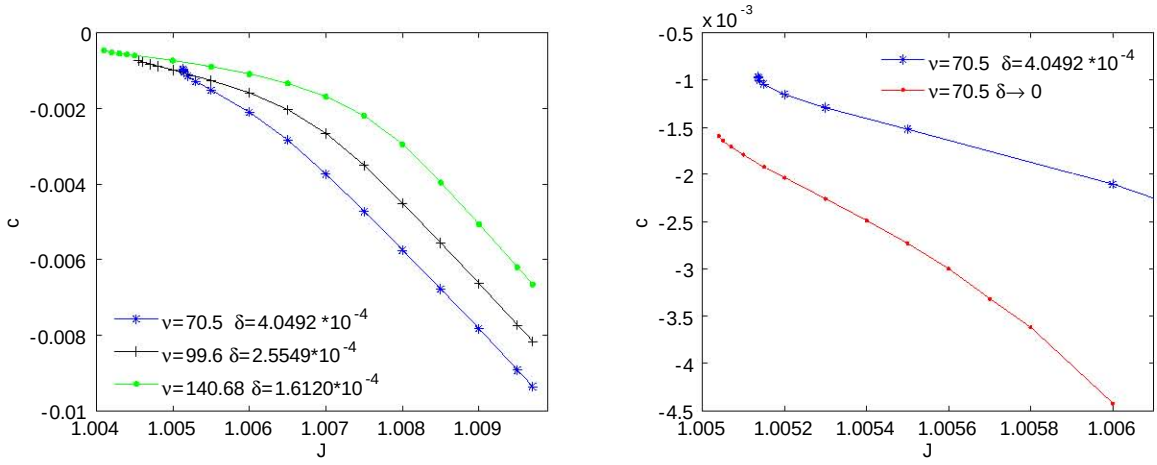

Figure 5-9 (a) Velocity of the upstream pulses vs current, for a SL $\mathcal{B}$ with different laser pumping intensities and (b) Velocity comparison with the theory of $\delta \to 0$

In *Figure 5-9*(b), fixing ν and supposing that they have the same temporal scale; we have compared the relation of the upstream pulse velocity and the J_c, with the value of the parameter $\delta = 1/\beta$. The difference between velocities is significantly big, so an asymptotic reconstruction of a pulse with this values will fail and this theory of first order must be enhanced.

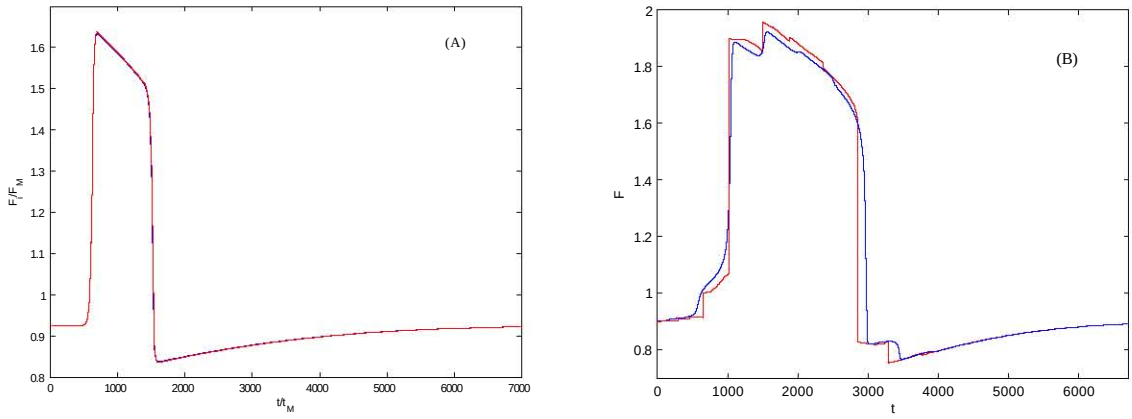

Figure 5-10 (a) Field reconstruction of an downstream pulse moving with positive speed for $J = 1.009$, $\nu = 70.5$, $\delta = 4.05 \times 10^{-4}$. (b) Field reconstruction of an upstream with negative speed for the same SL configuration.

5.6 Dipoles moving downstream in a SL with small photo-excitation intensities

With a small photo-excitation, the system (5.1) - (5.2) have a value of the parameter δ greater than 1. Now, the faster variables are the p_i and the slower variables are the F_i. Therefore, in the limit $\delta \longrightarrow \infty$, we can approximate that the variables p_i , come instantaneously to their unique stable stationary solutions, dependent on the electrical field profile.

$$p_i(F_i, F_{i-1}) = \frac{-(F_i - F_{i-1})/\nu + \sqrt{[(F_i - F_{i-1})/\nu]^2 + \frac{4}{r(F_i)}}}{2}, \tag{5.28}$$

So, for a fixed electrical field profile, the hole concentration is well defined, or in other words, the p_i are functions of $F_i - F_{i-1}$. Let be ΔF_i the difference $F_i - F_{i-1}$ and $\tau = \frac{1}{\delta}t = \beta t$ the new dimensionless time scale. The variation of the electric field over all the quantum wells is defined by:

$$\begin{aligned}\frac{dF_i}{d\tau} &= J - \frac{v(F_i)}{2}\left(\sqrt{(\Delta F_i/\nu)^2 + \frac{4}{r(F_i)}} + \Delta F_i/\nu\right) + \frac{D(F_i)}{2}\left(\frac{F_{i+1} + F_{i-1} - 2F_i}{\nu}\right) \\ &+ \frac{D(F_i)}{2}\left(\sqrt{(\Delta F_{i+1}/\nu)^2 + \frac{4}{r(F_{i+1})}} - \sqrt{(\Delta F_i/\nu)^2 + \frac{4}{r(F_i)}}\right)\end{aligned} \tag{5.29}$$

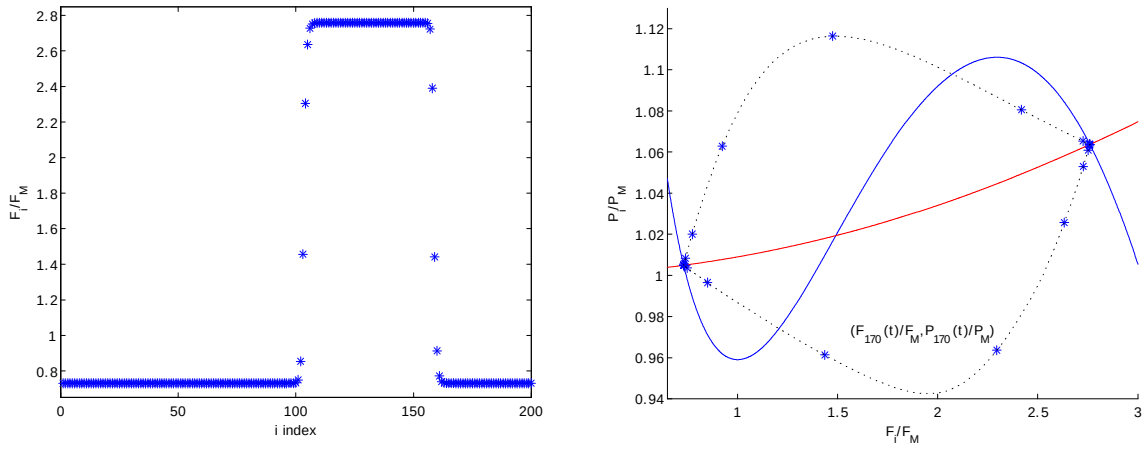

Figure 5-11 (a)Numerically obtained field profile of a dipole moving with positive speed for the configuration VIII with $J = 0.96$ (b) Phase plane showing the nullclines and the motion of the 150th QW as the pulse traverses it.

In *figure 5-11*, we have represented a dipole with three spatial field stable domains. There are three critical points which satisfy the condition $J = v(F)/\sqrt{r(F)}$. Let be U_1, U_2 and U_3 the electric field in these points, and the constants $P = \frac{J}{v(U_1)}$ and $P^{'} = \frac{J}{v(U_3)}$ the hole concentration in the two stable critical points.

Two types of dipoles can be observed in a SL. The difference between them, is the position of the fronts or the hole accumulation region in relation with the hole decumulation region, more close to the anode or to the cathode. For the dipole represented in *figure 5-11,* we distinguish four stages of the asymptotic reconstruction in which the SL quantum wells are in the dipole movement with positive velocity:

- **Decreasing front** (I).

  In this stage the variables F_i and p_i change their value, F_i from U_1 to reach U_3 and p_i from P to $P^{'}$ in the time interval $t \in [T_0\ T_1]$. Here $\Delta F_i \leq 0$, and as consequence there are a hole acumulation region given by (5.28)

  The decreasing front moves toward the contact with velocity $c_+(J)$, and is calculated in appendix A.8. With $s = i - c_+\tau$ the equation that describe the evolution of the electrical field profile in this stage is:

$$\begin{aligned} -c\frac{dF}{ds} &= J - \frac{v(F(s))}{2}\left[\sqrt{(\Delta F(s)/\nu)^2 + \frac{4}{r(F(s))}} + \Delta F(s)/\nu\right] \\ &\quad + \frac{D(F(s))}{2}\left[\frac{F(s+1) + F(s-1) - 2F(s)}{\nu}\right] \\ &\quad + \frac{D(F(s))}{2}\left[\sqrt{(\Delta F(s+1)/\nu)^2 + \frac{4}{r(F(s+1))}}\right] \\ &\quad - \frac{D(F(s))}{2}\left[\sqrt{(\Delta F(s)/\nu)^2 + \frac{4}{r(F(s))}}\right] \end{aligned} \tag{5.30}$$

  The boundary conditions are $F(\infty) = U_1$ and $F(-\infty) = U_3$

- **High electric field domain** (II).

  The values of F_i and p_i remain constant, a time $T_2 - T_1$, which depends on the initial number of wells between the fronts and the stage III velocity in the SL .

This stage can be described by the following equations:

$$\frac{dF_i(t)}{dt} = 0 \quad F_i(T_1) = U_3$$

$$\frac{dp_i(t)}{dt} = 0 \quad p_i(T_1) = P^{'}$$

- **Increasing front** (III).

  The values of F_i and p_i evolve in the time. F_i from U_3 to reach U_1 and p_i from $P^{'}$ to P in the time interval $t \in [T_3\ T_2]$. In this stage $\Delta F_i \geq 0$, and as consequence there are a hole decumulation region given by (5.28).

  The increasing front moves toward the contact with velocity $c_{-}(J)$ and is also described and calculated in the appendix **A.8**. Now, the boundary conditions used in (5.30) are $F(s = i - c_{-}t^{'} = -\infty) = U_3$ and $F(\infty) = U_1$

- **Low electric field domain** (IV).

  F_i and p_i remain constant, until they find another decreasing front. The following equations describe stage IV:

$$\frac{dF_i(t)}{dt} = 0 \quad F_i(T_3) = U_1$$

$$\frac{dp_i(t)}{dt} = 0 \quad p_i(T_3) = P$$

The fronts can have positive or negative velocities, and his value depends on the position of the two stable critical points and on his path in the phase plane. Nevertheless, we have not seen any dipole with a negative velocity.

In *figure 5-11*, the movement of the IF and DF produces an increase of the SL total voltage due to the fronts velocity difference. Except for particular values of J the velocity of both fronts is different. Therefore the dipoles do not move rigidly in general: they will shrink and disappear or grow indefinitely.

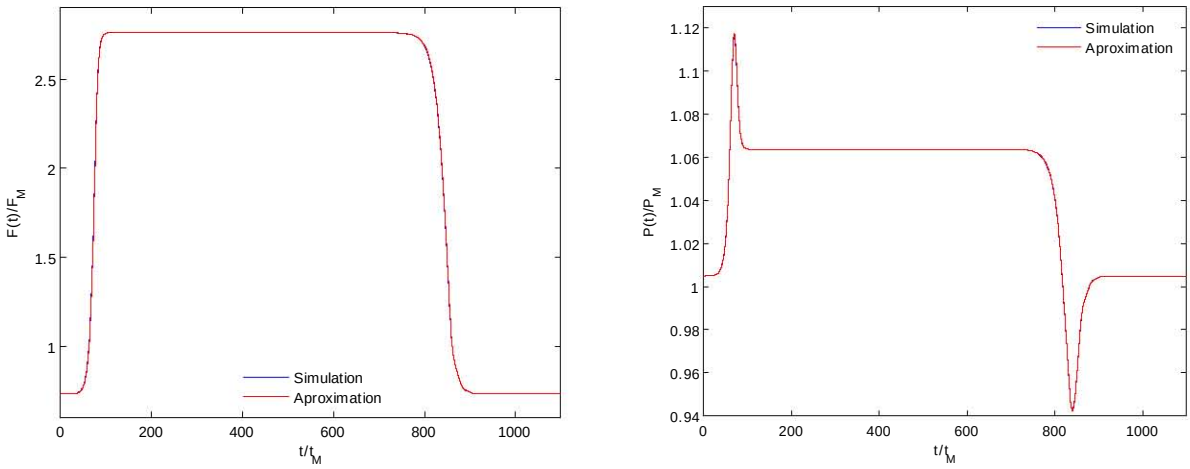

Figure 5-12 Asymptotic reconstruction of the (a) field and (b) hole concentration for the dipole represented in *figure 5-11*

5.7 Calculation of wave front velocity using the active well theory or the continuum limit

Wave fronts are solutions of (5.1) with time scale $\tau = t/\delta$ for a fixed value $p_i = p > 0$:

$$\frac{dF_i}{d\tau} + v(F_i)\left(p + \frac{F_i - F_{i-1}}{\nu}\right) - D(F_i)\,\frac{F_{i+1} + F_{i-1} - 2F_i}{\nu} = J, \tag{5.31}$$

which can be rewritten as

$$\frac{dF_i}{d\sigma} + v(F_i)\left(1 + \frac{F_i - F_{i-1}}{p\nu}\right) - D(F_i)\,\frac{F_{i+1} + F_{i-1} - 2F_i}{p\nu} = \frac{J}{p}, \tag{5.32}$$

with $\sigma = t/(p\delta)$. This equation is exactly that of a doped SL with dimensionless doping density and total current density $p\nu$ and J/p, respectively; cf. Eq. (9) of Ref. [23]. Depending on the value of $p\nu$, there is a current interval, $J_1 < J < J_2$, for which wave fronts fail to propagate and are pinned by the lattice. $J_2 - J_1$ increases with $p\nu$. Near the critical currents $J_i(p\nu)$ $(i = 1, 2)$, it is possible to construct the moving wave fronts and calculate their velocity using the theory of active QWs [23](see appendix A.8), which was proposed for general classes of spatially discrete nonlinear equations [36] and it works best for large values of $p\nu$. The approximate wave front velocity (in

the time scale σ) is proportional to $|J - J_c|^{1/2}$, where J_c is either J_1 or J_2, and the proportionality constant is given by Equations (19) - (21) of Ref. [23]. In the opposite limit $p\nu \to 0$, $p\nu i \to x$, (5.32) can be approximated by the hyperbolic equation

$$\frac{\partial F}{\partial \sigma} + v(F)\left(1 + \frac{\partial F}{\partial x}\right) = \frac{J}{p}. \tag{5.33}$$

SL wave fronts correspond to shock waves of (5.33) whose speed is given approximately by the equal area rule [23]

$$V(F_+, F_-) = \frac{\int_{F_-}^{F_+} \frac{v(F)}{v(F)+D(F)}\, dF}{\int_{F_-}^{F_+} \frac{1}{v(F)+D(F)}\, dF}.$$

Here F_- and F_+ are the values of the field before and after the shock wave, respectively. See [23] for details and for a better approximation of the wave front velocity.

5.8 Conclusions

In dc current bias, the spatially discrete system of our model exhibit pulse and front solutions that can be constructed using matched asymptotic expansions which exploit the large separation of time scales in their dynamics (measured by the dimensionless parameter δ).

With large photo-excitation, we have shown that the pulse profile typically consists of slowly varying regions of the excitatory variable separated by sharp wave fronts. As in the FitzHugh-Nagumo system, the velocity of a pulse is decided by the interaction between its leading and trailing fronts, but the leading order approximation often gives only a fair result when compared with direct numerical solutions. We have explained how to find a better approximation to the wave fronts. Our approximation provides a pulse velocity that depends on δ and compares much better with the velocity obtained from numerical solutions. As a result, the reconstruction of the pulses using the improved wave fronts also compares much better with the numerically obtained pulse.

Also, we have proved the existence of pulses with negative velocity, that resemble to the FHN pulses, and are quite different from other shown field profiles in the same large photo-excitation regime. We have made an asymptotic description that synthesize the behavior of these new pulses.

Finally, with small photo-excitation, we have described the dipole movement by the behavior of the DF and IF fronts. By the asymptotic reconstruction, we have seen that is not needed a better approximation of these fronts. But can be done with the same procedure shown with the high photo-excitation fronts.

Chapter 6

Photo-excited semiconductor superlattices as constrained excitable media: Motion of dipole domains and current self-oscillations

6.1 Introduction

Nonlinear charge transport in weakly coupled, undoped, photo-excited, type-I semiconductor superlattices (SLs) is well described by spatially discrete drift-diffusion equations. [1, 2] As in the much better known case of doped SLs, nonlinear phenomena include formation and dynamics of electric-field domains, self-sustained oscillations of the current through voltage-biased SLs, chaos, etc. Experimentally, the formation of static electric-field domains in undoped, photo-excited SLs was already reported many years ago. [3]

The first experimental observation of dynamical aspects of domain formation in undoped, photo-excited SLs such as self-sustained oscillations of the photo-current were reported by Kwok *et al.* [4] Due to the excitation condition, the oscillations were damped. Subsequently, undamped self-sustained oscillations of the photo-current in undoped SLs were observed for a type-II GaAs/AlAs [5] and for a direct-gap GaAs/AlAs SL. [6] Tomlinson *et al.* [7] reported the detection of undamped

photo-current oscillations in an undoped GaAs/$Al_{0.3}Ga_{0.7}As$ SL, where the transport is governed by resonant tunnelling between Γ states.

The evolution from a static state at low carrier densities to an oscillating state at higher carrier densities was demonstrated in an undoped, photo-excited SL by increasing the photo-excitation intensity. [8] An investigation of the bifurcation diagrams for undoped, photo-excited SLs showed the existence of a transition between periodic and chaotic oscillations. [9] For a detailed review of the nonlinear static and dynamical properties of doped and undoped superlattices, see Ref.[10].

Previous theoretical studies of undoped photo-excited SLs, including studies of bifurcation and phase diagrams, [11] are based on a discrete drift model having a constant recombination coefficient. [1] So far, there have been no reports on considering field-dependent recombination or the fact that the time scale of the electron-hole dynamics depends strongly on the optical excitation intensity.

However, the consequences of including these effects for the dynamics of electric-field domains can be striking. In dc voltage bias, we incorporate into the previously studied discrete model the dependence of the electron-hole recombination on the electric field and on the photo-excitation intensity using a straightforward model that takes into account the overlap integral between the electron and hole wave functions.

At high photo-excitation intensities, it is possible to find only one stable electric-field domain, not two as in the case of a constant recombination coefficient. [1] In this case, self-sustained oscillations of the current (SSOC) may appear under dc voltage bias. The field profile during SSOC can exhibit nucleation of dipole waves inside the sample, the splitting of one wave into two, and the motion of the resulting waves in opposite directions. Some of these dipole waves resemble the pulses in excitable reaction-diffusion systems such as the FitzHugh-Nagumo model for nerve conduction [12, 13, 14, 15] and are quite different from field profiles for a constant recombination coefficient. [1, 2, 10]

In an excitable dynamical system, an appropriate finite disturbance of the unique stable fixed point may cause a large excursion in phase space before returning to the stable state. When diffusion is added, the resulting reaction-diffusion system may support wave fronts, pulses, and wave trains. It is also possible to find SL configurations at high photo-excitation intensities for which there exist no stable electric-field domains.

In these cases, there are SSOC, whose corresponding field profiles are wave trains, comprising a periodic succession of dipole waves. These cases are similar to wave trains in oscillatory media such as those appearing in the FitzHugh-Nagumo model in the presence of a sufficiently large external current. [12, 15]

6.2 dc voltage-biased superlattice for small photo-excitation intensities

The behavior of a dc voltage-biased SL is quite different depending on its Al content and photo-excitation intensity. For an Al content smaller than 25%, $j(F)$-J in Eq. (4.33) has a single zero for any value of J, and the only stable states of the SL are stationary ones unless the photo-excitation intensity is sufficiently large (cf. next section).

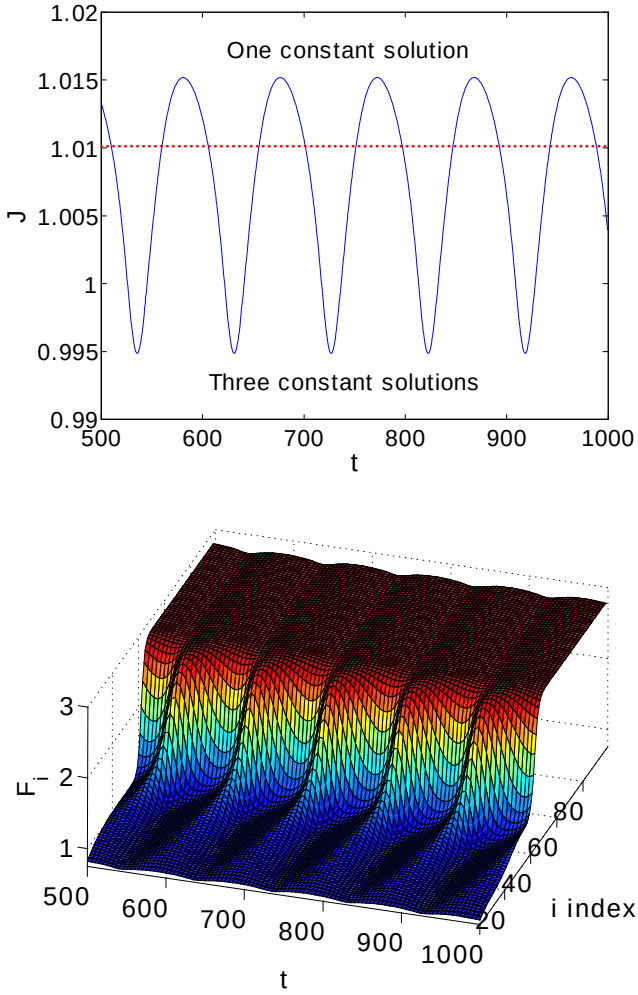

Figure 6-1 (top) Current vs time and field distribution vs time (bottom) displaying SSCOs due to monopole recycling at the injecting contact. The injecting contact conductivity and the bias are $\sigma = 1.2959$ and $V = 2.0416236$, respectively. The other parameter values correspond to configuration VI in *table 4.1* and are $N = 99$, $\delta = 22.35636$, $\alpha = 1.0146$, $\nu = 1.27214$ and Al content $x = 1$.

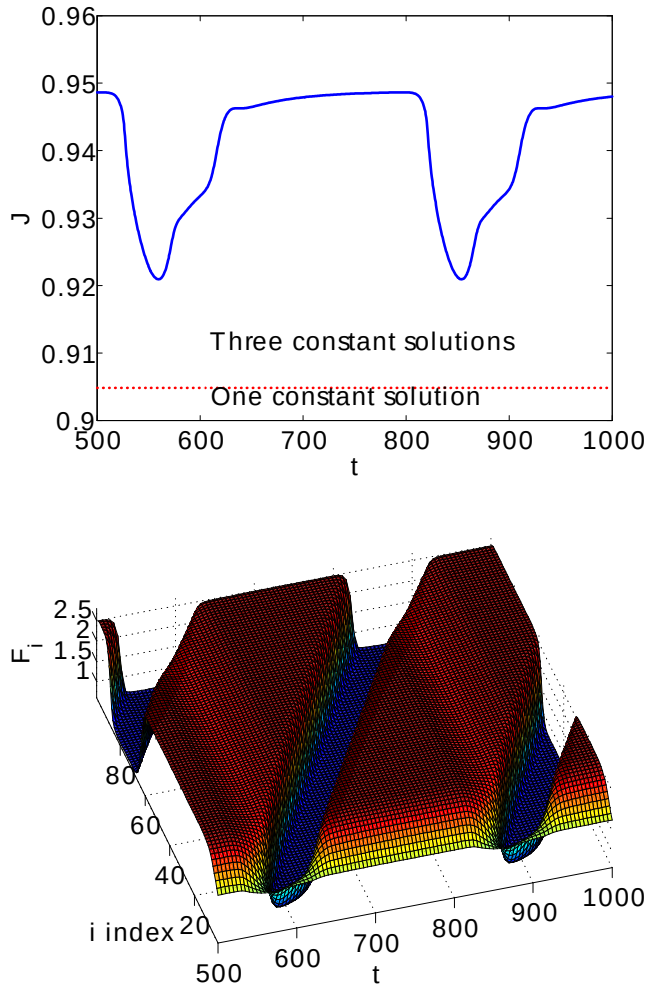

Figure 6-2 (a) Current vs time and (b) field distribution vs time displaying SSCOs due to dipole recycling at the injecting contact. The injecting contact conductivity and the bias are $\sigma = 0.5625$, $\alpha = 2.3374$ and $V = 2.05148375$, respectively. The other parameter values are the same as the ones used for *figure 6-1* corresponding to configuration VI in *table 4.1*.

Let us assume that the Al content is larger than 45% so that $j(F)$-J in Eq. (4.33) may have three zeros for an appropriate range of J values. In this case, the undoped SL behaves similarly to an n-doped SL [10]. Here, the most interesting limit is that of small photo-excitation intensity, i. e., $\delta \gg 1$.

In this limit, $\beta = \delta^{-1} \ll 1$, the equation (5.29) is similar to the one describing the electric field in a doped SL, but now there are drift and diffusion terms which are nonlinear in the differences $F_i - F_{i-1}$. Under dc voltage bias, there are SSOC mediated by pulses of the electric field. The

current density varies on a slow time scale, whereas the electric-field profile consists of a varying number of wave fronts joining the stable constant solutions of Eq. (5.29) at the instantaneous value of the current. [10]

Depending on the conductivity of the injecting contact σ, there are different types of SSOC due to the periodic generation of dipoles or monopoles at the injecting contact. If the curve σF intersects the bulk current-field characteristic curve $j(F)$ before its maximum (cf. *figure. 4-3*), SSCOs due to recycling and motion of charge monopole waves (moving charge accumulation layers) appear as shown in *figure. 6-1*. If σF intersects $j(F)$ after its maximum (cf. *figure. 4-3*), SSCOs due to recycling and motion of dipole waves are obtained, as depicted in *figure 6-2*. We have indicated in *figures. 6-1* and *6-2* whether there are one or three uniform and time-independent (constant) solutions of Eq. (4.32), solving $p\,v(F) = J$ and $r(F)\,p^2 = 1$ for the instantaneous value of the current density $J = J(t)$ during the SSOC.

6.3 dc voltage-biased superlattice for large photo-excitation intensities

If $0 < x < 0.25$, the phase plane in Eq. (4.32) may have only one fixed point located on any branch of the nullcline $p = J/v(F)$. For small photo-excitation intensities, the only stable state is a stationary one. However, for sufficiently large photo-excitation intensities, an infinite, dc current-biased SL may exhibit pulses moving downstream or upstream and also wave trains moving downstream.[18]

The counterpart of these stable solutions for a dc voltage-biased SL is very interesting and different from anything observed in an n-doped SL. Our simulations correspond to SLs with different Al contents, whose current-field characteristics $j(F)$ and injecting contact curve $j = \sigma F$ are shown in *figure 4-3*. In all cases, SSCOs appear for an average bias roughly in the region of negative differential resistance (NDR), where $j'(F) < 0$ (e.g., σ=0.5625 in *figure 4-3*).

When the conductivity of the injecting contact is such that σF intersects $j(F)$ near the maximum thereof, it is possible to have SSCOs that are quite different from the ones appearing in n-doped SLs. For an injecting contact conductivity $\sigma = 1.05231$ (cf. *figure 4-3*), pulses (charge dipoles) may be triggered at the injecting contact, move toward the receiving contact, and cause SSCOs as shown in *figure 6-3*. For all the instantaneous values of $J(t)$ during these SSCOs, there is only one constant solution of Eq. (4.32): most of the times this solution is on the second NDR branch of $j(F)$. Only when $J(t)$ is near its maximum value, the constant solution is on the third branch of $j(F)$.

For a constant current density, the constant solution of Eq. (4.32) is on the NDR branch, which implies that the system is oscillatory and that periodic wave trains are possible. The realization of wave trains for a long dc-biased SL are displayed in *figure 6-3*: at any time during SSOC, there are only two fully developed pulses present in this SL. These pulses experience variations in their shape and velocity when they are generated or arrive at the contacts, but longer SLs allow for realizations of wave trains, in which more pulses exist simultaneously inside the SL.

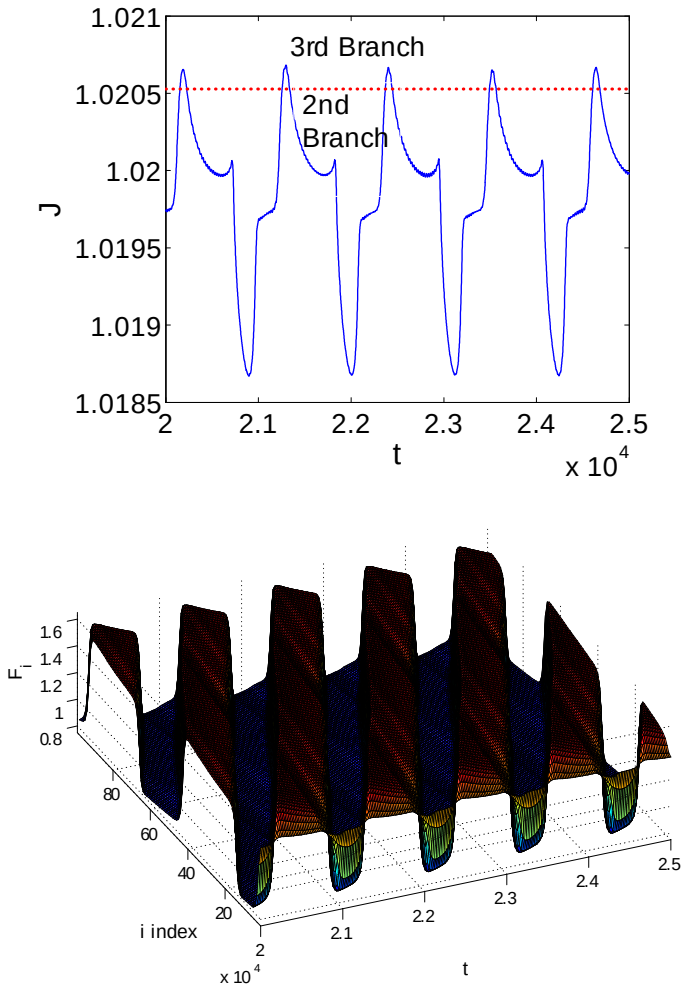

Figure 6-3 Current vs time (top) and field distribution vs time (bottom) displaying dipole-mediated bulk SSCOs for an injecting contact conductivity $\sigma = 1.05231$ and $x = 0.25$ (cf. *figure. 4-3*). These oscillations correspond to having a finite wave train. The other parameter values correspond to configuration II in *table 4.1* and are $N = 99$, $\nu = 33.62275$, $\delta = 5.91 \times 10^{-4}$, $V = 1.22732$, and $\alpha = 0.6944$.

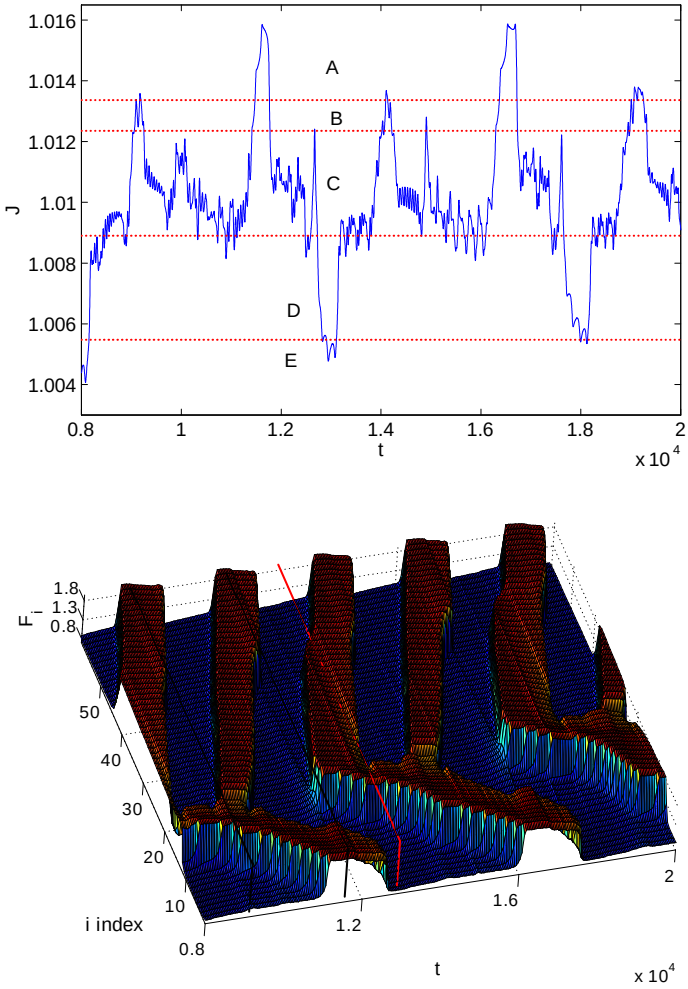

Figure 6-4 Current vs time (top) and field distribution vs time (bottom) displaying dipole mediated bulk SSCOs for an injecting contact conductivity $\sigma = 1.107$ (cf. *figure. 4-3*). The other parameter values correspond to configuration IV in *table 4.1* and are $N = 61$, $\nu = 70.50677$, $\delta = 4.069 \times 10^{-4}$, $V = 1.269848$, and $\alpha = 0.9779$.

In the previous example, pulses always move downstream, from left to right. For slightly larger conductivity of the injecting contact ($\sigma = 1.107$ in *figure 4-3*), *figure 6-4* shows that two pulses are formed inside the SL and move with opposite velocities toward the contacts. These pulses are similar to the ones constructed above for the case of dc current bias (with positive or negative velocity), except that the current changes slowly with time during the self-oscillation and the pulses accommodate their form to the instantaneous value of the current. Note that the pulses are triggered inside the SL, not at the injecting contact.

A pulse moving with positive speed has a long trailing region, in which the field increases as we move away from the pulse. However, there is a depletion layer near the injecting contact, in which the field decreases as we move away from the injecting contact. In a long, but finite SL, a local maximum is formed inside the SL, when the decreasing field near the contact meets the increasing field in the trailing region of the exiting pulse with positive speed. The current increases as the exiting pulse is absorbed by the receiving contact, until it surpasses a critical value. In this case, the local maximum of the field profile inside the SL is split, and two new pulses are created.

The pulse closer to the injecting contact moves toward it with negative speed whereas the other pulse moves toward the receiving contact with positive speed. The upward moving pulse reaches the injecting contact and is absorbed there before the downward moving pulse arrives at the other contact. In this case, the field profile close to the injecting contact is quasi-stationary, and a local maximum of the field is formed when we match this region with the trailing region of the downward moving pulse. After the critical value of the current is reached, another pulse pair is nucleated, and the same process is periodically repeated.

It is interesting to evaluate in some detail the process of nucleation and disappearance of pulses during these SSCOs. In the current vs time diagram in *figure 6-4*, we distinguish different regions depending on the number of constant solutions of Eq. (4.32) that exist for the corresponding instantaneous value of $J(t)$.

- In region A, there is only one constant solution on the third branch of $j(F)$.

- In region B, there is one constant solution on the third branch and two on the second branch of $j(F)$.

- In region C, there are three constant solutions, one on each branch of $j(F)$, whereas two of these solutions are on the second branch and one of the first branch of $j(F)$, if $J(t)$ is in region D.

- There is only one constant solution located on the first branch of $j(F)$, if $J(t)$ is in region E.

For a constant voltage bias, a pulse moving upstream may be generated only if $J(t)$ surpasses a critical value (1.007454), which is located in region D. Once generated, the upstream moving pulses persist for any instantaneous value of the current density. These SSOC are apparently weakly chaotic: we have calculated the corresponding Lyapunov exponents and found that there is a single positive exponent with a rather small value of 7.9×10^{-6}.

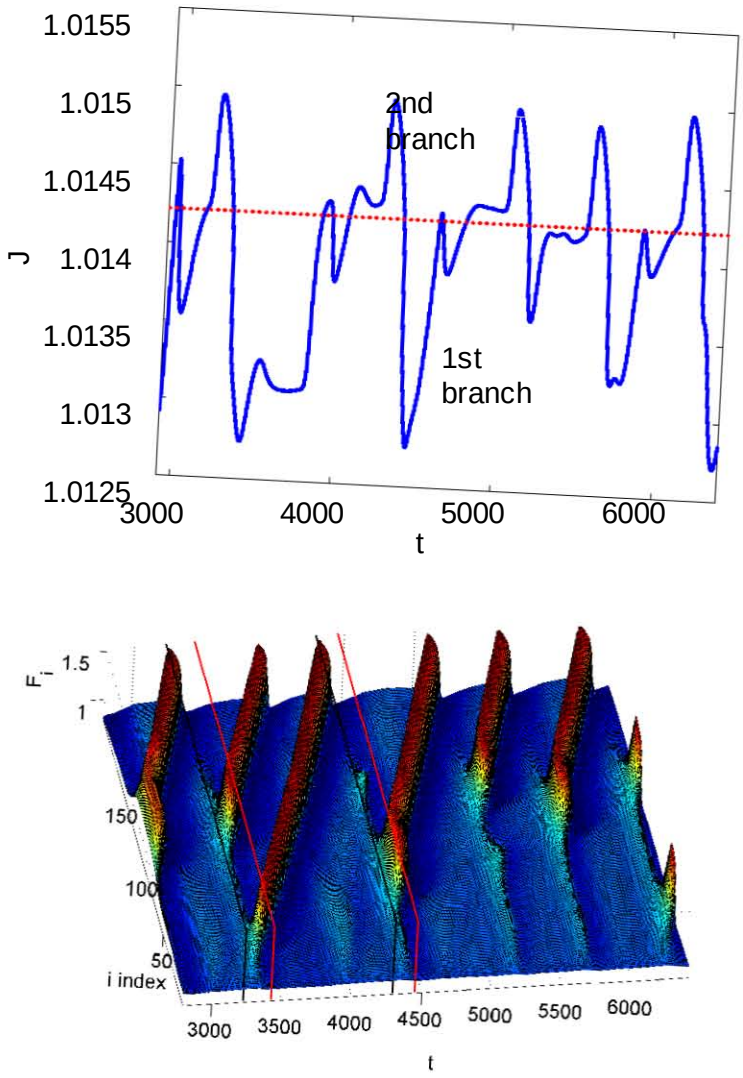

Figure 6-5 Current vs time (top) and field distribution vs time (bottom) displaying dipole-mediated bulk SSCOs for an injecting contact conductivity $\sigma = 1.083425$ (cf. *figure 4-3*). The other parameter values correspond to configuration I in *table 4.1* and are $N = 199$, $\nu = 8.44566$, $\delta = 3.7287 \times 10^{-3}$, $V = 1.00417485$, and $\alpha = 0.9713$.

We have also observed SSCOs mediated by dipole waves that nucleate alternatively at two different QWs of the SL as shown in *figure 6-5*. During these SSCOs, there is only one constant solution of Eq. (4.32) for any instantaneous value of $J(t)$. This solution is either on the first or the second branch of $j(F)$. At about $t = 3232$, where $J(t)$ reaches its global maximum, two dipole waves are nucleated at two different QWs. They become fully developed pulses and move with positive speed toward the receiving contact.

When the first one arrives there, the current increases so that the corresponding constant solution of Eq. (4.32) is on the second branch of $j(F)$. In this case, a small dipole wave is nucleated at the local field maximum, where the tail of the first dipole meets the depletion layer near the injecting contact. The small dipole wave never grows into a fully developed field pulse, and it continues advancing, until the old large dipole wave disappears at the receiving contact. At this time (about 4296), a large current spike appears, and a new dipole wave is formed closer to the injecting contact than the small dipole.

$J(t)$ decreases abruptly, while the small dipole disappears, and the newly created dipole reaches a large size and moves toward the receiving contact. Shortly afterward, a new current spike marks the creation of another small dipole. This small dipole travels toward the receiving contact, and it grows only when the only existing large pulse reaches the receiving contact and disappears. A small dipole formed closer to the injecting contact does not grow, until the large pulse reaches the receiving contact and disappears without triggering a new dipole wave. In this case, the corresponding pulse is close to the receiving contact. When it reaches the contact and disappears into it, two new dipoles are simultaneously triggered and become fully developed.

A scenario similar to the one previously described follows, marked again by a large current spike. The situation is not repeated exactly: there are small differences in the QWs at which pulses are nucleated, differences in the size and lifetimes of the small dipoles, etc. These oscillations also seem to be weakly chaotic, in which the greater Lyapunov exponent is small and positive.

If the injecting contact conductivity is smaller so that the contact current σF intersects $j(F)$ on the NDR branch thereof, there appear standard SSCOs due to repeated dipole pulse nucleation at the injecting contact and motion toward the receiving contact.

6.4 The nucleation process and the wave generation, phase plane.

The SSCOs not only depends on the contact conductivity, *Al* content in the barriers and photo-excitacion. Other factors like voltage are implied too. As we can see in *figure 6-6 (a)* and *(b),* if the length of the SL is duplicated, preserving the voltage value, the time between current peaks is seemingly duplicated. But for the values exposed in the *figure 6-6 (c)*, if the length of the SL is duplicated, the time between peaks seemingly don´t change by the dipole generation process. Also in *figure 6-6 (c)* the shape of the SSCOs are afected by the interaction between the two fronts of the dipole, in the dc voltage bias condition (4.22). In any case, with small photo-excitation the shape of the current amplitude is modified if the length of the SL is duplicated.

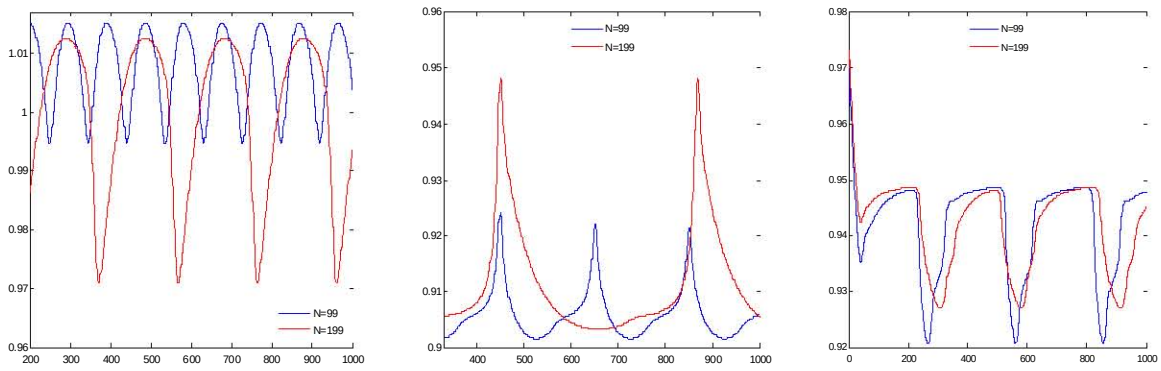

Figure 6-6 SL **(I)** Comparison of the current oscillations for the configuration VI with $\alpha\sigma = 1.3148$ **(a)** (monopole) $V = 2.0416236$ $\sigma = 1.2959366$ **(b)** $V = 2.0416236$ $\sigma = 0.359206$ (monopole) and **(c)** $\sigma = 0.5624996$ $\mathbf{V}$ =2.05148375 (dipole)

With large photo-excitation, the current behavior is even more complex due to the fast changes in the QWs electric field and due to the movement of the different allowed types of waves inside the SL. Now, let assume a conductivity in the anode, $\sigma_2 = \alpha\sigma_1 \neq \frac{v(F_N)}{p_N F_N \sqrt{r(F_N)}}$, and in the cathode, $\sigma_1 = \sigma \neq \frac{v(F_0)}{\sqrt{r(F_0)F_0}}$.

These values of the conductivity generate a holes accumulation regions (or decumulation) in the QWs near to the contacts. Furthermore, these charge profiles are the instantaneous stationary solutions for a fixed current; And with the theory described in the appendix A.3 can be approximated.

When a critical value of the current is reached in (6.1), the charge accumulation regions near to the two contacts can generate a new pulse or monopole. Sometimes, as in *figure 6-5*, after reached this critical current, the pulse can not be created because other pulse are generated inside the SL. In this case, a nucleation point (*NP*) is generated instead. This *NP* moves toward the receiving contact, and when a critical current is reached again in the SL, can generate a new pulse. In *figure 6-5,* during the nucleation process, there are a competition between the contacts and the *NP*s to create a new pulse.

The union of an upstream pulse tail with a downstream pulse tail is a *NP* which can nucleate two other new pulses when a critical current is reached. Also in the *figure 6-4* we can see how an upstream pulse can also generate a downstream pulse, splitting itself.

Basically, the generation of waves pulses and monopoles depend on the temporal function of the current given by the dc voltage bias condition exposed in (4.22). Now we can express this condition by the equation:

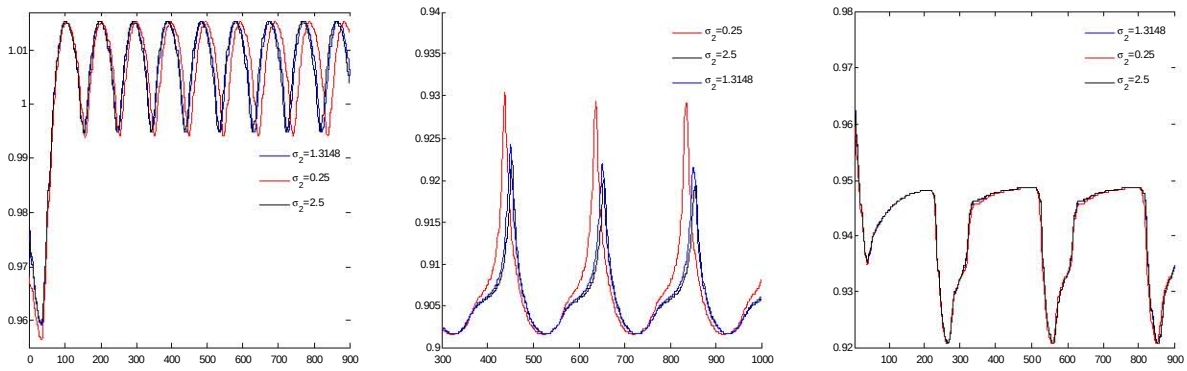

Figure 6-7 SSCOs of the SLs with a configuration VI photo-excitation, the other parameters are $N = 99$ **(a)** $V = 2.0416236$, $\sigma_1 = 1.2959366$ **(b)** $V = 2.0416236$, $\sigma_1 = 0.359206$ and **(c)** $\sigma_1 = 0.5624996$ **V** =2.05148375

$$J(t) = \frac{1}{N+1}[\sum_{i=1}^{N-1} \begin{pmatrix} v(F_i(t))(\frac{F_i(t)-F_{i-1}(t)}{\nu} + p_i(t)) \\ -D(F_i(t))(p_{i+1}(t) - p_i(t) + \frac{F_{i+1}(t)+F_{i-1}(t)-2F_i(t)}{\nu}) \end{pmatrix}$$
$$+\sigma_1 F_0 + \sigma_2 F_N(t) n_N(t)] \tag{6.1}$$

Let's analyze all the parameters and variables inside the equation (6.1):

- **The number of QWs**, $N + 1$.

  The SL current change if the hole and electric field profiles change too. The magnitude of this variation depends on the length of the SL. For small SLs, fast changes in the electric field profile generate current peaks. Instead, for huge SLs this current variations are more smooth.

  The QWs number allows the coexistence of wave trains and different pulses types inside the SL. All these charge waves interact between them, on their generation, on their movement across the SL and on their destruction in the contacts. In any case, to observe SSCOs, the size of the SL have to be bigger than the length of the monopoles fronts or the pulses which are principally fixed by the photo-excitation value.

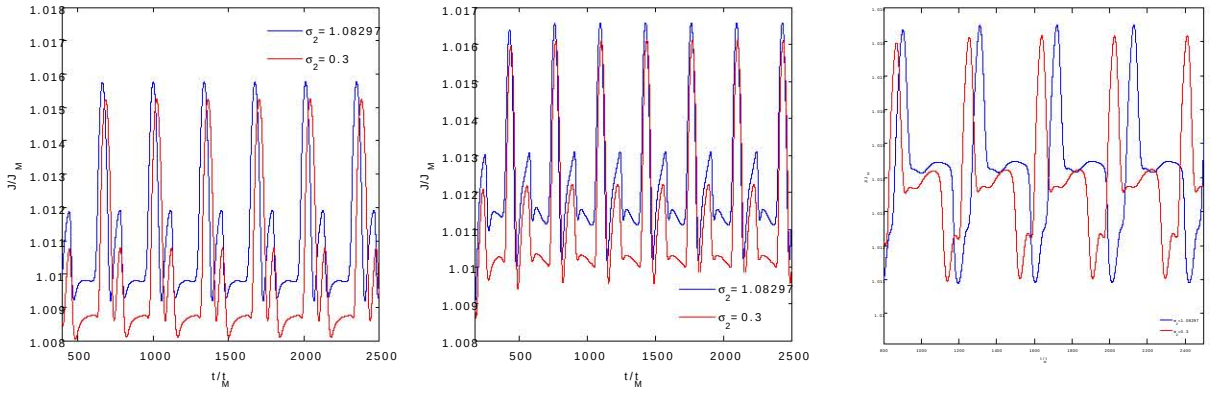

Figure 6-8 SSCOs of the SLs with a configuration III photo-excitation, the other parameters are $\sigma_1 = 1.1073976327$ **N** =61 **(a) V** =1.211998 **(b) V** =1.269848 **(c) V** =1.47123253

- **Dimensionless photo-excitation parameters, ν and δ.**

  δ is not explicit in (6.1). But as we have seen in previous chapters, δ and ν determine the size and the velocities of the fronts and of the pulses. So, is implicit in the SL allowed field profiles, and in his variations.

  When δ have very small values; The fronts are constituted by few wells, and these ones, in the front displacement, change abruptly their electrical field. Therefore, the front displacement generate peaks in the current values to compensate the possible voltage variation. The peaks number can indicate us how many wells have change in their brunch position.

  The ν value emphasize the QW electrical field differences in the SL current value. As the difference of electrical field is placed principally in the SL fronts, the ν value point out the fronts relevancy in (6.1).

- **The drift velcity**, $v(F_i)$

  This is an important function that determines many relevant aspects in (6.1). Drift velocity define the electrical field domains values, the critical current to allow the upstream pulses in the SL, the front profiles and velocities, etc.

  Let´s remark on the importance of this function, with the **diffusion function** $D(F_i)$, in the length of the stationary solutions near the contacts (see appendix A.3). When there can not be a stationary solution in any of both contacts, there is generated a dynamical solution, a pulse or monopole. Being defined a critical current value.

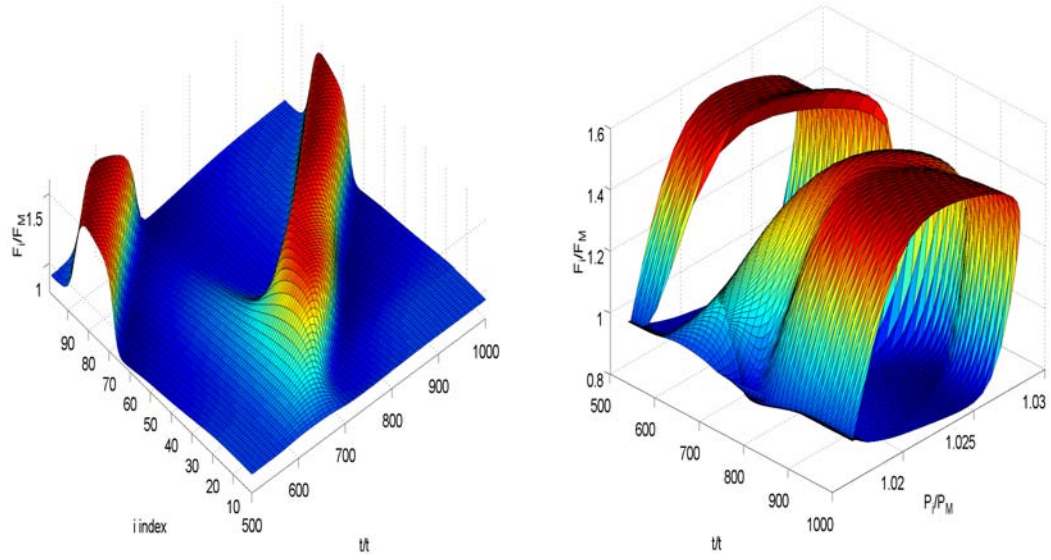

Figure 6-9 SL configuration I the other parameters are **V** =1.00417485 **N** =99
(a) Electric field profile versus time and well index (b) Phase plane versus time.

- **The cathode conductivity,** σ.

  This is a fundamental value to obtain the length of the stacionary solution near the cathode. This length, change at the same time as (6.1) changes. In other words, the σ value, defines the position of the first point of nucleation (or the initial front of a SSCO), and the inner QWs region of the SL far away from the contact. The length of these inner wells define the distance that the pulses have to cross to reach the anode, and as consequence the SSOCs frecuencies and their applied voltage interval in the SL.

- **The anode conductivity,** $\alpha\sigma = \sigma_2$.

  This value modifies the amplitude of the SSCO and displaces a certain quantity towards higher values of the current, see *figure 6-8* and *6-7*. The shape of the oscillation also changes, but lightly. This behavior is due to the movement of the stationary solution of the N quantum well, when the current changes. If F_N rises in value, the electric field of the stationary profile near the anode grows too and therefore, the effective applied voltage to the inner wells is lower.

In addition, these values are capable of regulating the creation of new pulses, see *figure 7-2(a)*.

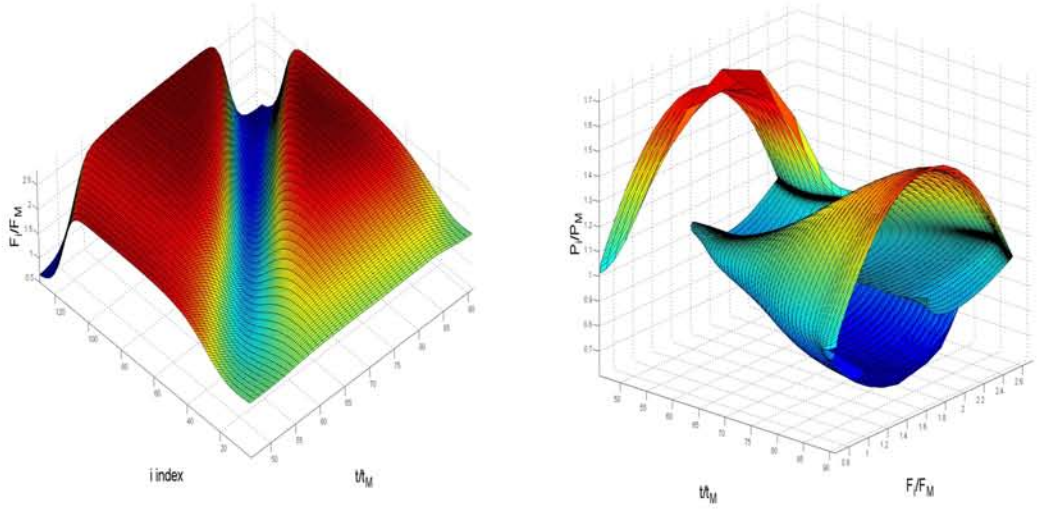

Figure 6-10 SL configuration VII the other parameters are **N = 130 V** =2.05148375
(a) Electric field profile versus time and well index (b) Phase plane versus time.

- **The electric field profiles and the QWs holes concentration profiles.**

  By the equation (6.1) the SL is forced to fulfill the following condition, *in any instant of time the sum of the electric field profile is a constant proportional to the voltage.* So, if the electric field is fixed, in some way the QWs hole concentration too. In addition, if any charge acumulation region disappears for reaching to any contact, then the SL is forced to create it again.

+ With small photo-excitation, the dynamic solutions are the monopoles and dipoles. In most cases, when any front type reach the anode, the stationary solutions near the cathode generate it again.

  In the *figure 6-10* is represented the dipole movement in the phase plane. Initialy, only a DF is moving through the SL and a dipole is starting to be created in the cathode. When the DF disappear in the anode, the evolution of the dipole is quickly enhanced.

  The new dipole contains two new fronts, an IF and a DF, and therefore two regions of hole accumulation and hole deccumulation which are represented in the phase plane as arcs. The arcs height, grows as long as the time passes and the two fronts evolves to have the same velocity.

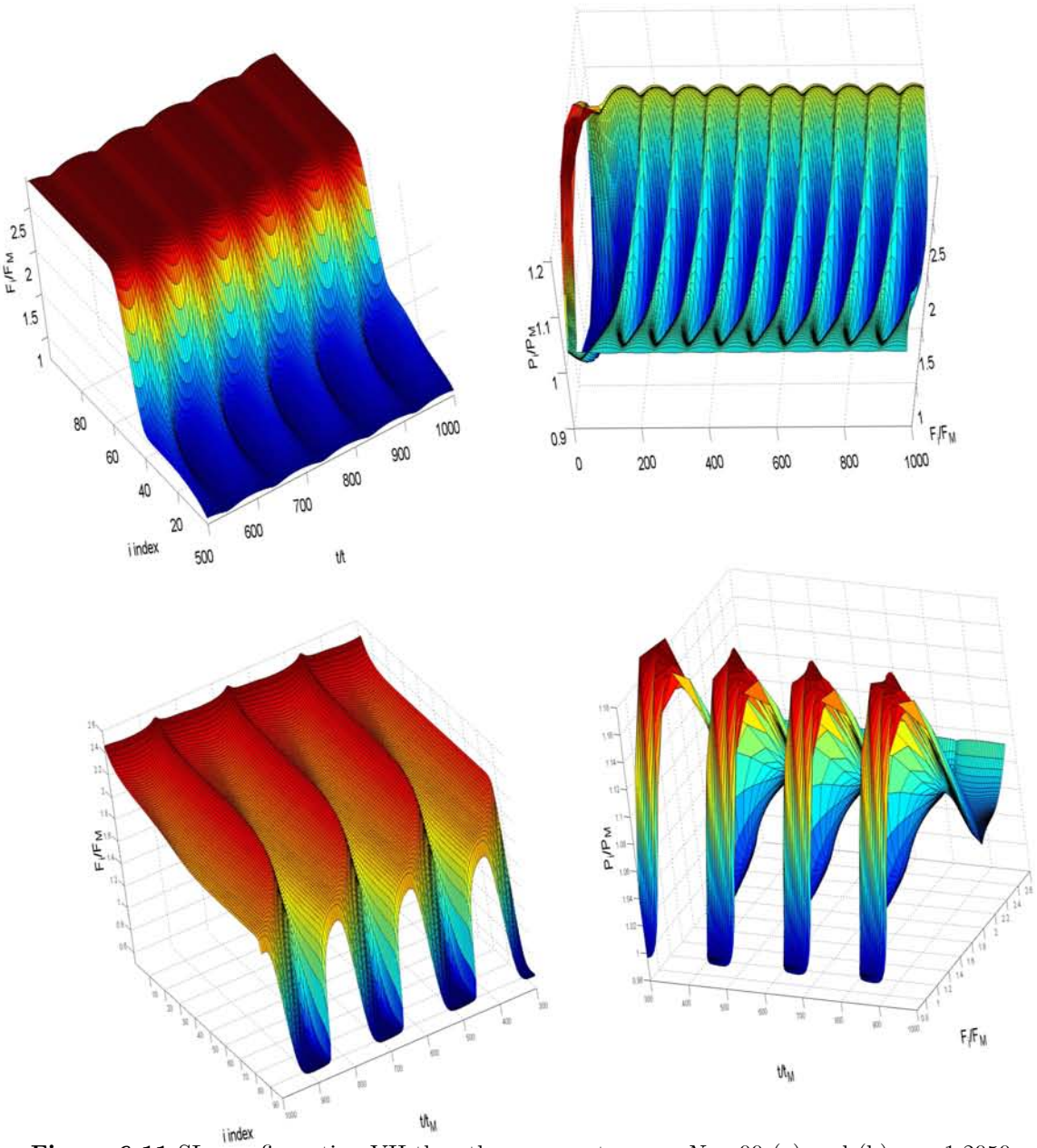

Figure 6-11 SLs configuration VII the other parameters are $N = 99$ (a) and (b) $\sigma = 1.2959$ $V = 2.0416236$ $\alpha = 1.0146$ (c) and (d) $V = 2.05148375$, $\sigma = 0.5624996$ $\alpha = 2.3374$ (a) and **(c)** Electric field profile versus time and well index (b) and (d) Phase plane versus time.

Finally, the dipole reaches the anode. The first front that disappears is the IF. At this moment, the stationary solution of the cathode starts to generate a new dipole. A period of the SSCOs has been completed.

Initially there is a dipole in the *figure 6-11(b)* as a initial hole and electric field profile. With the experiment selected conductivity, the cathode only can generate IFs. Therefore, the dipole disappears, and the SSCOs are generated by the IF evolution.

The movement of the IF implies that the voltage decreases, as a consequence the field domains are increased to compensate this voltage decrease. The IF never reaches the anode and as consequence the deccumulation hole concentration is also created and destroyed inside the SL.

In the *figure 6-11(c)* and *(d)* is represented an electric field profile which correspond to a DF profile oscillation. Due to the voltage condition, most of the time, the DF have not complete in his construction. This can be seen in the phase plane evolution, when the front is complete the hole accumulation region is well defined by an arc in the phase plane, *figure 6-11(d)*.

\+ With large photo-excitation, the dynamic solutions are extremely very complex.

The anode and the cathode can generate charge waves. The pulses can split up and generate two new pulses. The wave fronts can change his movement direction over the SL. The NPs, small variations of the electric field domains, move over the SL and can generate a new pulses inside the SL. The fast variation of the electric field in a single QW, makes peaks in the current. With wave trains, there are pulses profiles interactions in the (6.1) current calculation. And so on.

In a simple case, represented in the *figure 6-9,* the destruction of a pulse by having reached the anode, produces a new charge accumulation region near the cathode. The union between the tail of the old pulse and the stationary solution of the contact create a NP which after some time generate a new complete pulse.

As we can see in *figure 6-9(b),* the initial fronts of the pulse don´t have the same velocity, because the surface of the phase plane change with time. After some time the pulse is well defined and finally reaches to the anode. Starting again the pulse creation - destruction process, which explains basically the SSOCS with large photo-excitation.

6.5 Conclusions

The generation of monopoles, dipoles and pulses in the dc voltage bias, depends on the temporal electric field profiles and on photo-excitation. The contact conductivity is a key value to select the SSCO shape.

In the dc voltage biased SL under weak photoexcitation may exhibit self-sustained oscillations of the current due to repeated nucleation of a charge monopole or dipole waves at the injecting contact and their motion toward the collector. For high photo-excitation intensities, the walls separating electric field domains are mostly pinned, and self-sustained oscillations of the current occur only in narrow voltage intervals.

For small x among other unusual phenomena, there may appear weakly chaotic SSOC due to dipole dynamics in dc-voltage-biased SLs for high photo-excitation intensities, during which nucleated dipole waves can split in two oppositely moving dipoles. These dipoles are pulses of the electric field with shapes and behavior similar to pulses in excitable media, where a sufficiently large disturbance about the unique stable domain may induce them.

For other parameter values, the unique static domain is unstable, and the underlying dynamics is oscillatory so that wave trains formed by succession of pulses give rise to self-sustained oscillations of the current.

Chapter 7

Chaotic dynamics under constant voltage bias.

7.1 Introduction

The *chaos* definition, found in bibliography [48], says:

> **Chaos** is *aperiodic long-term behavior* in a *deterministic* system that exhibits *sensitive dependence on initial conditions*.

To find and measure the chaos existence, we are going to use as possible indicator the Lyapunov exponents. A Lyapunov exponent, λ, of a dynamic system as (A.1)-(A.5), it is a quantity that characterizes the separation radius of two initial paths infinitesimal nearby. This means, that two paths in the phase plane with a initial vector separation δ_0, diverge or converge, during a time horizon, a certain quantity expressed by:

$$\begin{aligned} ||\delta(t)|| &= ||\delta_0|| e^{\lambda t} \\ t_{horizon} &\sim O\left(\frac{1}{\lambda} \ln \frac{a}{||\delta_0||}\right) \end{aligned}$$

Where a is a measure of our tolerance for our initial trajectory. Then, our prediction becomes intolerable when $||\delta(t)|| \geq a$, and this occurs after a time $t_{horizon}$ [48].

The strange attractors have the responsibility of this trajectory disturbance. This behavior can be measured as function of λ, and can show a sensitive dependence to the initial conditions. This means that if λ has a negative value, the dynamic system will tend to his own initial trajectory, in spite of any perturbation of his variables. On the other hand, if λ has a positive value, a small variation of the trajectory, it will mean an important variation of the initial SL behavior. The Lyapunov exponents depends on which trajectory and on the starting point of this trajectory. So we should average over many points on the same trajectory if we want to obtain a right value of λ.

Now cosider the, $2N+1$ dimensional space of the vector ($F_j(t)$ $j=0,..N$, $P_k(t)$ $k=1,...N$), of the system (A.1)-(A.5) at dc voltage bias. To know the infinitesimal paths near of our real trajectory, as well as his deviations for small perturbations, we have to solve the following linearized system:

$$\begin{aligned}
\frac{d\hat{e}_0}{dt} &= \Lambda - \sigma_1 \hat{e}_0 \qquad (7.1)\\
\frac{d\hat{e}_i}{dt} &= \Lambda - dv(F_i)(p_i + \frac{F_i - F_{i-1}}{\nu})\hat{e}_i - v(F_i)(\hat{e}_{i+N} + \frac{\hat{e}_i - \hat{e}_{i-1}}{\nu}) \\
&\quad + dD(F_i)(p_{i+1} - p_i + \frac{F_{i+1} + F_{i-1} - 2F_i}{\nu})\hat{e}_i + D(F_i)(\hat{e}_{i+N+1} - \hat{e}_{i+N} + \frac{\hat{e}_{i+1} + \hat{e}_{i-1} - 2\hat{e}_i}{\nu}) \\
\frac{d\hat{e}_N}{dt} &= \Lambda - \sigma_2(\frac{F_N - F_{N-1}}{\nu} + p_N)\hat{e}_N - \sigma_2 F_N[\hat{e}_{2N} + \frac{\hat{e}_N - \hat{e}_{N-1}}{\nu}]; \\
\beta\frac{d\hat{e}_{i+N}}{dt} &= -dr(F_i)p_i(p_i + \frac{F_i - F_{i-1}}{\nu})\hat{e}_i - r(F_i)p_i(\hat{e}_{i+N} + \frac{\hat{e}_i - \hat{e}_{i-1}}{\nu}) - r(F_i)(p_i + \frac{F_i - F_{i-1}}{\nu})\hat{e}_{i+N}
\end{aligned}$$

Here, $i = 1,..,N$ and $\hat{e}_i$ is the perturbative vector of the electrical field and hole concentration, and Λ have the next expresion:

$$\begin{aligned}
\Lambda &= \frac{1}{N+1}[\sum_{i=1}^{N-1} \begin{pmatrix} dv(F_i)(P_i + \frac{F_i - F_{i-1}}{\nu})\hat{e}_i + v(F_i)(\hat{e}_{i+N} + \frac{\hat{e}_i - \hat{e}_{i-1}}{\nu}) \\ -dD(F_i)(P_{i+1} - P_i + \frac{(F_{i+1} + F_{i-1} - 2F_i)}{\nu})\hat{e}_i \\ -D(F_i)(\hat{e}_{i+1+N} - \hat{e}_{i+N} + \frac{\hat{e}_{i+1} + \hat{e}_{i-1} - 2\hat{e}_i}{\nu}) \end{pmatrix} \\
&\quad + \sigma_1\hat{e}_0 + \sigma_2\hat{e}_N(p_N + \frac{F_N - F_{N-1}}{\nu}) + \sigma_2 F_N(\hat{e}_{2N} + \frac{\hat{e}_N - \hat{e}_{N-1}}{\nu})] \qquad (7.2)
\end{aligned}$$

The systems (7.1)-(7.2) and (A.1)-(A.5), have $4N+2$ diferential ecuations. These systems must be integrated simultaneously to obtain the greater Lyapunov exponent, $\lambda_{\max}$, which indicate the chaos degree in our SL. Depending on the initial values of β and ν, the different equations of the system (7.1)-(7.2) will be more or less correlated between them.

If we denote $||\hat{e}_i(\tau)||$ as the euclidean norm of the vector $\hat{e}_i$ in the time τ , the Lyapunov's maximum coefficient is defined by the expression:

$$\lambda_{\max} = \lim_{\tau \to \infty} \frac{1}{\tau} \ln \frac{||\hat{e}_j(\tau)||}{||\hat{e}_j(0)||} \quad j = 0, ..2n \tag{7.3}$$

In order to avoid an *overflow* of the computer, the perturbation vectors must be re-normalized. Therefore, we have used the *Benettin's et all* algorithm, [49],[50]:

$$\lambda_{\max} = \lim_{k \to \infty} \frac{1}{kT_d} \sum_{j=1}^{k} \ln ||d_j|| \tag{7.4}$$

Where d_j is the growth vector of of the perturbation during the jth period of renormalization T_d.

While the system (7.1)-(7.2), (A.1)-(A.5) is integrated forward in time, the vectors $\hat{e}_i^{(n)}(\tau)$ tend to line up in the direction of the greatest growth. Therefore, the perturbations will need to be renormalized from time to time to prevent overflow. So we have to use the Gram-Schmidt orthonormalization procedure to separate the vectors into orthogonal components.

The choice of the renormalization period, as well as the choice of the initial vectors $\hat{e}_j(0)$, are crucial factors in order to get the correct solution and to avoid certain catastrophes. In the work of Alan WOLF et all, [51], we can find that the principal reasons of the intrinsic error in the Lyapunov exponent calculus are:

- Insufficient renormalization periods.

- To the own value of the exponent of lyapunov and to the renormalization time:

$$\frac{\Delta\lambda_{\max}}{\lambda_{\max}} = \frac{Cte}{\lambda_{\max} T_d}$$

In our case, in order to reduce these errors, we must have in mind that the renormalization period must be greater or with the same order of the adimensional parameter β.

In addition, the not correlation of the differential equations of the system (7.1)-(7.2) can confuse us, in the calculation of the maximum Lyapunov exponent. To avoid this problem, we have to put all the initial base of vectors $\hat{e}_j(0)$ in the system (7.1)-(7.2).

7.2 Experiments

The calculus of the $2N + 1$ Lyapunov exponents is very complex due to the elapsed time to obtain them, and due to the "*CPU*" consumption. To look and find possible chaotic solutions, is more suitable to use the Foürier discret Transform (*figure 7-1 (b), figure 7-2 (b) and figure 7-3 (b)*) or the Poincaré's current maps (*figure 7-1 (f), figure 7-2 (f) and figure 7-3 (e)*).

Whenever the Foürier discrete Transform of the current show a great quantity frequencies, or Poincaré's maps are excessively complex. We can predict a possible chaotic system, that later can be confirmed, by the measuring of the Lyapunov exponents.

By different simulations and with the method before exposed, we measure the Lyapunov exponents of two SLs with different compositions and photo-excitation.

- In the SL with less photoexcitation and with SSCOs produced by the monopole oscillation, $\beta \lll 1$ (*figure 7-1),* we don´t find any evidence of chaos, being $\lambda_{\max}$ = -0.002855.

  The number of current frequencies observed, is relatively small in comparison with other simulations. This fact, can also be found in the shape of the Poincaré's map.

- In the SL with more photo-excitation $\beta \ggg 1$. With oscillations of current produced by different pulses with positive speed as with negative speed (*figure 7-2 and 7-3),* we found evidence of chaos.

  In the SL represented in *figure 7-2,* we find ten positive Lyapunov exponents, among all of them, the maximum value is $\lambda_{\max} = 8.353 \cdot 10^{-6}$.

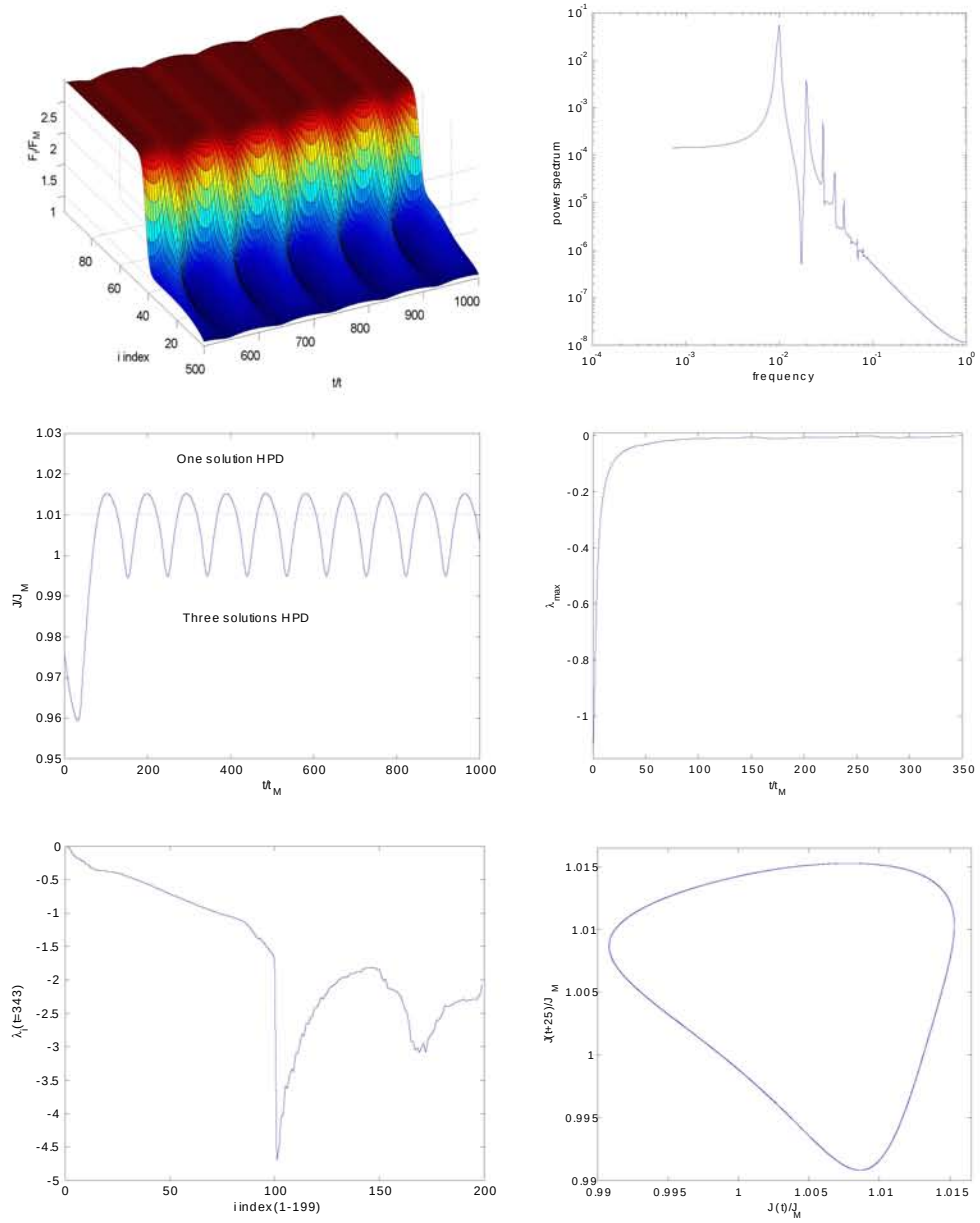

Figure 7-1 SL configuration VI the other parameters value are **V** =1.00417485 and **N** =99 **(a)** Electrical field depending on time and the well number **(b)** Current Spectrum of frequencies (Foürier discret Transform) **(c)** $J(t)$ **(d)** Maximum Exponent of Lyapunov $\lambda_{\max}(t)$ **(e)** Lyapunov exponents represented in function on his vector $\hat{e}_i$ **(f)** Map of the current density for a given frequency.

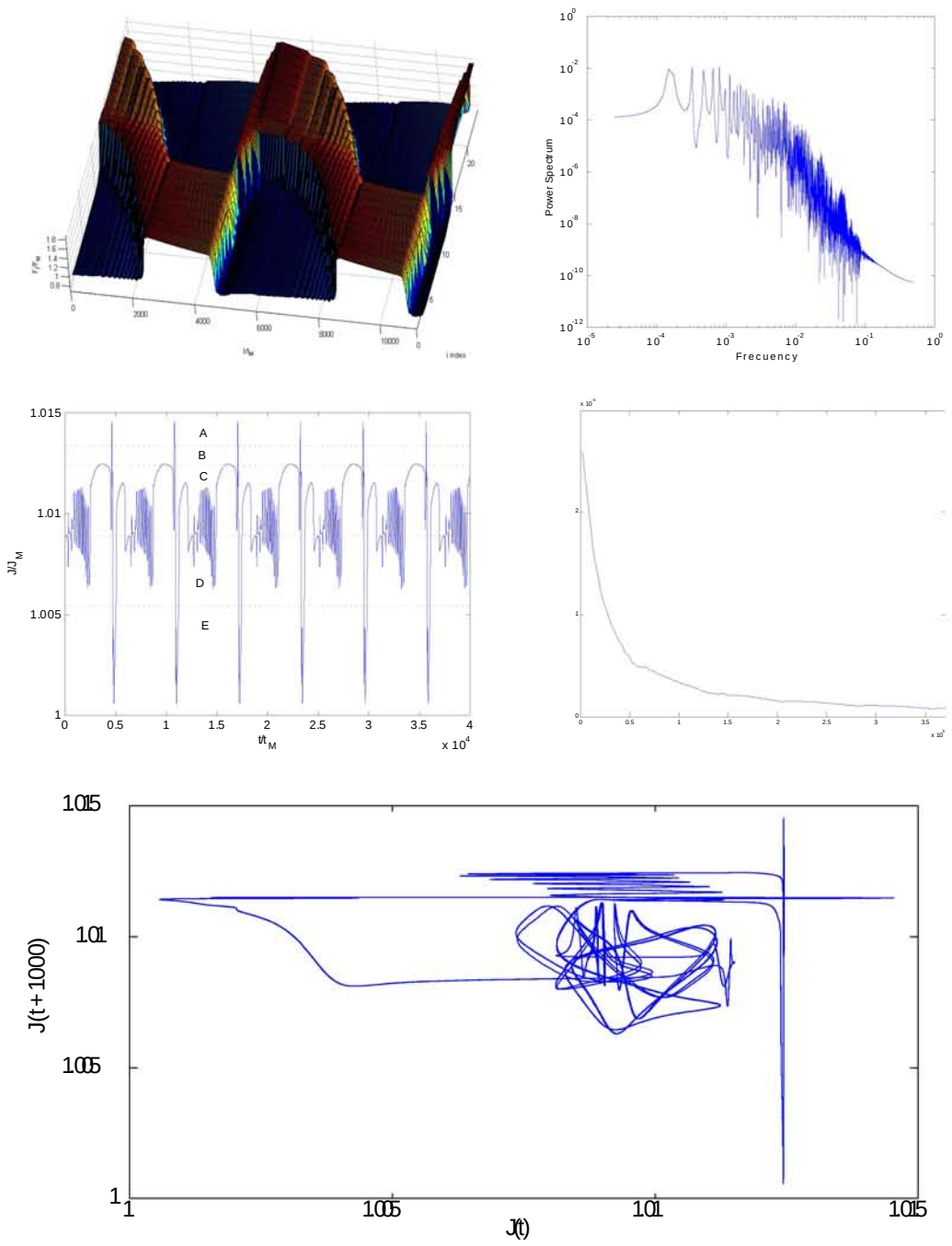

Figure 7-2 SL configuration IV the other parameters value are $\mathbf{V}$ =1.23724 and $\mathbf{N} = \mathbf{24}$ **(a)** Electrical field depending on time and the well number **(b)** Current Spectrum of frequencies (Foürier discret Transform)**(c)** $J(t)$ **(d)** Maximum Lyapunov exponent $\lambda_{\max}(t)$ **(e)** Map of the current density for a given frequency.

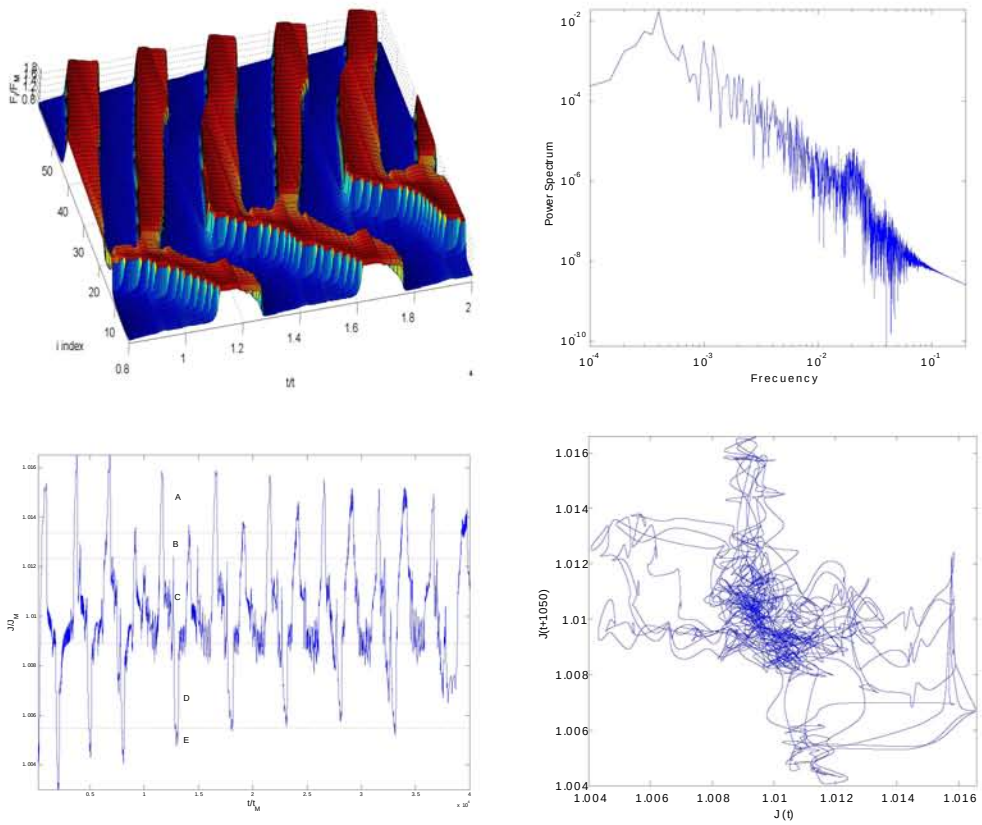

Figure 7-3 SL configuration IV the other parameters value are $\mathbf{V}$ =1.269848 and $\mathbf{N} = \mathbf{61}$ **(a)** Electrical field depending on time and the well number **(b)** Current Spectrum of frequencies (Foürier discret Transform) **(c)** $J(t)$ **(d)** Map of the current density for a given frequency.

7.3 Conclusions

In dc and ac voltage bias, spatio-temporal chaos is expected to occur in weakly coupled superlattices under appropriate values of photoexcitation and temperature. We don´t show any experiment in ac voltage bias. But is easy to predict that the modification of the dc voltage bias SSCOs type with a time dependence can allow more chaos in our model equations.

This chaos can be explain by the rich dynamic properties in a SL with large photoexcitation, and small NDC region. The SL as an oscillatory and excitation media, the possibility to develop waves with distinct velocity sign, the movement and the interaction between different charge waves and nucleation points makes a complex mathematical system which the chaos can be found.

Chapter 8

Global conclusions

In this section we review the main results of this work and outline some problems which are still awaiting their solutions.

There are many interesting physical and mathematical problems associated with superlattice transport. The physics of sequential tunneling in weakly coupled photo-excited type-I superlattices was treated in this PhD Thesis. The FitzHugh-Nagumo system have been studied and analyzed to introduce, in the following chapters, the charge wave transport in large photo-excited type-I superlattices.

The FitzHugh-Nagumo pulse solution can be reconstructed mathematically, using matched asymptotic expansions which exploit the time scales differences in his dynamics. The wave fronts velocities depends on ϵ parameter and can be obtained with our front approximation which eliminates the discrete form of the FHN equations. Our reconstruction of the FHN pulse compares much better with the numerically obtained pulse.

The Ampere law, charge continuity, Poisson and Ohm´s law constitute the Nonlinear charge transport model in weakly coupled photoexcited type-I superlattices. This model depends on electron drift velocity, difusion and electron-hole recombination. Depending on the barrier Aluminium content and other physical parameters such as temperature. This functions allows a rich dynamical behavior, including the formation of electric field domains, pinning of domains fronts, self-sustained oscillations of the current, etc..

In dc current bias, with large photo-excitation, the spatially discrete system of our model exhibit wave trains, pulses and fronts solutions with similarities to the FHN solutions. With the same procedure used on the FHN system, the pulses and the fronts can be reconstructed as a function

of SL photo-excitation. Our approximation compares much better with the velocity obtained from numerical solutions. Also, we found and explained a new type of pulse with negative velocity. We have made an asymptotic reconstruction of these new pulses that could be improved with a next order theory.

With small photo-excitation, the fronts solutions are quite different to those in large photoexcitation. We have described the fronts behavior and we have made an asymptotic reconstruction of them.

In dc voltage bias, have been described and analyzed the different generation processes of pulses and monopoles, as well as his movement and destruction in the SL. The value of the contacts conductivity, the photo-excitation, the barrier Ga content and the number of QWs in the SL are important keys to obtain the frequency and amplitude of the SSCOs. Under small photoexcitation, the SL may exhibit SSOCs due to repeated nucleation of a charge monopole or dipole waves at the injecting contact and their motion toward the collector. For high photo-excitation intensities, the pulses, fronts and wave trains nucleation-movement and destruction processes have a rich dynamical behavior.

We have found the existence of small chaos in dc voltage bias and we have measured it. With large photo-excitation is more easily to find chaotic SSOCs. The SL as an oscillatory and excitation media, the possibility to develop waves with distinct velocity sign, the movement and the interaction between different charge waves and nucleation points makes a complex mathematical system. We could not find chaos with small photo-excitation. In ac voltage bias, we predict more chaotic behavior in weakly coupled photo-excited type-I superlattices

In the appendices we extend the used mathematical and physcal theory. In addition, we show different ways to nondimensionalize the model and we study the stationary solutions which explain the domain formation, pinning, multistability...

8.1 Open problems and future work.

There are many interesting problems associated with superlattice transport, which couldn´t be addressed here. Also, the work exposed in this PhD Thesis opens a great quantity of questions. The following examples can be our upcoming work lines:

- *Ac voltage bias,* $V(t)$. In this point, we expect similar SSOCs to the already seen in previous chapters, but now with a new extra frequencies due to the voltage variation.

- *Ac voltage bias, dc voltage bias and dc current bias with a temporal photo-excitation intensity, $I(t)$.* There are many interesting phenomena in the semiconductor response to the THz photo-excitation intensity. The scales used in our nondimensional model depend on the photoexcitation and the recombination functions. These functions, depend on the laser intensity which now have a temporal dependence.

  Therefore a new set of nondimensional equation is needed. With these new equations, what happens to the front velocity, the Sl domains, etc?. [75].

- *Dc voltage bias in SL with different diffusion and velocity functions* (by a temperature gradient in the SL or by the barriers shape height and width modulation). The spatial variation of the transport dynamics, might select the position of a nucleation point or the emision point of a quantum cascade laser. [76].

- *A SL model for three different spatial photo-excitation and transport regimes, Wannier-Stark hopping - Secuential tunneling and again Wannier-Stark hopping.* To study the possible quantum cascade laser amplification, tunability and emision oscillations.

- *Photo-excitation function with an electric field dependence, $\tilde{\gamma}(\tilde{I}, \tilde{F}_i, \omega_{exc})$.* The field dependence of photo-excitation is described in *figure A.6-1*. We expect, by the modulation of the pumping laser excitation frequence, the creation of new electric field domains between the two peaks of the current. With this new domains we expect new types of pulses in the SL and probably more chaos.

- *Sequential tunneling in photo-excited $Al_xGa_{1-x}As/GaAs$ type II SLs.* With these SLs, there are several factors in our model that have to change. The first interesting point is due to the electron - hole recombination function, which now, not only it depends on the electrical field of the electrons QW. A different electrical field have to be taken into account in the electrons barriers where the holes are situated. In addition, now the lighter carrier charge is the hole, $m^{*X}_{e(AlAs)} = 1.3\ m_e$ and $m^{*\Gamma}_{hh(GaAs)} = 0.377\ m_e$. So, the main contribution to the current is made by the holes

  These considerations will generate other pulses and other dynamics that have not been described in this phD thesis.

- *Extension and modification of the exposed model.* It could be interesting to introduce other factors in the equation (4.25), like a magnetic external field, Coulomb Blockade, etc... and other physical phenomena like the consideration in our model of the dependence in the intensity absorption with the depth of the SL and like the quantum hall effect.

- Upstream pulse $O(\epsilon)$ *theory.* For a better approximation of these waves with negative velocity.

- *Numerical bifurcations continuation.* Changing the values of the parameters N, J, V, σ and α ; and by qualitative changes in the eigenvalues of the linearized system (4.26)-(4.31), it is possible to find the points where are the Hopf bifurcations, Saddle-Node, etc... In this way, can be obtained the bifurcation diagrams and the the stability of the solutions which can be useful to find chaotic SSCOs.

Appendix A

APPENDICES

A.1 Appendix: Other nondimensional equations of the model

For a better numerical treatment, always is advisable to render the system (4.14)–(4.22) dimensionless. The process to nondimensionalize the model equations is not unique. In some sections of this PhD Thesis, we have changed the temporal scale for the equations (4.26)–(4.31). Being $\delta t' = t$ the new time scale, and $\beta = 1/\delta$, the new constant which relates some of the physical temporal scales. This change remains the dependence with the pumping intensity laser and give us the following system of equations:

$$\frac{dF_i(t')}{dt'} = J - v(F_i)(\frac{F_i - F_{i-1}}{\nu} + p_i) + D(F_i)(\frac{F_{i+1} - 2F_i + F_{i-1}}{\nu} + p_{i+1} - p_i) \quad \text{(A.1)}$$

$$\beta\frac{dp_i(t')}{dt'} = 1 - r(F_i))(\frac{F_i - F_{i-1}}{\nu} + p_i)p_i \quad \text{(A.2)}$$

$$\frac{1}{N+1}\sum_{i=0}^{N} F_i(t') = V(t') \quad \text{(A.3)}$$

$$\frac{dF_0(t')}{dt'} = J(t') - \sigma F_0(t') \quad \text{(A.4)}$$

$$\frac{dF_N(t')}{dt'} = J(t') - \frac{\sigma F_N(t')(\frac{F_N - F_{N-1}}{\nu} + p_N)}{N_D} \quad \text{(A.5)}$$

In other sections of this PhD Thesis, for our convenience, we use another scales for all the variables of our system. In the following table are resumed:

$\tilde{F}$	$\tilde{v}$	$\tilde{n}_i$ $\tilde{p}_i$	$\tilde{\gamma}$	$\tilde{t}$	$\tilde{J}$	$\tilde{D}$	$\tilde{\Phi}$	$\tilde{\sigma}$
V/cm	cm/s	cm^{-2}	cm^2s^{-1}	ns	A/cm^{-2}	cm^2/s	V	$AV^{-1}cm^{-1}$
$\tilde{F}_M$	$\tilde{v}_M$	$\frac{\varepsilon\tilde{F}_M}{e}$	$\frac{\tilde{r}\left(0,\tilde{I}\right)\varepsilon^2\tilde{F}_M^2}{e^2}$	$\frac{l}{\tilde{v}_M}$	$\frac{\varepsilon\tilde{F}_M\tilde{v}_M}{l}$	$\tilde{l}\tilde{v}_M$	$N\tilde{F}_M\tilde{l}$	$\frac{\varepsilon\tilde{v}_M}{l}$

Which give us the following nondimensional system of equations, [46]:

$$\frac{dF_i(t)}{dt} = J - v(F_i)(F_i - F_{i-1} + p_i) + D(F_i)(F_{i+1} - 2F_i + F_{i-1} + p_{i+1} - p_i) \quad (A.6)$$

$$\beta\frac{dp_i(t)}{dt} = \gamma - r(F_i)(F_i - F_{i-1} + p_i)p_i \quad (A.7)$$

$$\frac{1}{N}\sum_{i=1}^{N} F_i(t) = V(t) \quad (A.8)$$

$$\frac{dF_0(t)}{dt} = J(t) - \sigma F_0(t) \quad (A.9)$$

$$\frac{dF_n(t)}{dt} = J(t) - \frac{\sigma F_n(t) n_n}{N_D} \quad (A.10)$$

Where here, the new value of the dimensionless parameter β is

$$\beta = \frac{\tilde{r}\left(0,\tilde{I}\right)\tilde{l}\varepsilon\tilde{F}_M}{e\tilde{v}_M}$$

The main distinction, between the system (A.1)–(A.5) and (A.6)–(A.10), we can find it in the dependence with the photo-excitation. In (A.1)–(A.5) almost all scales depends on pumping intensity laser, instead in (A.6)–(A.10) only the parameters γ and β gets this dependence. In addition, in (A.1)–(A.5) the value of the electric field differences decreases with photo-excitation.

But these nondimensional systems are not always advisable; what happens when the intensity of the laser depends on the $\tilde{z}$ direction, due to a physical calibration of the experiment or due to the existence of several lasers focused on different lighting domains of the superlattice?

The first step is to assign a different intensity to each quantum well, $\tilde{I}_i$. So, if we use the same method to obtain the nondimensional system (A.6)–(A.10), we only have to change some parameters $\gamma \longrightarrow \gamma_i$ and $\beta \longrightarrow \beta_i$ where $i = 0, .., N$. This new theory are developed in A.6.

A.2 Appendix: Modulate parameters in $Al_xGa_{1-x}As/GaAs$ superlattices

The whole dynamics generated in a SL depends strongly on the shape of the diffusion, drift velocity and recombination functions. For that reason, we must do an analysis of the different experimental parameters which they depend. In order to fit the problem to a certain shape of the functions $D(F)$, $v(F)$ and $r\,(F)$, to select a specific dynamic of the SL which we are interested.

- The *aluminium content* $Al_xGa_{1-x}As/GaAs$ in the SL, determines the *height of the barriers*, and as consequence fixes the number of energetic allowed levels in the quantum well. With high barriers the penetration length of the electrons and holes wave functions in their barriers is small. With less penetration length of the charge carriers wave functions, the $\tilde{r}(\tilde{F})$ function shape decreases more slowly with the electrical field.

- For lower *barrier heights,* the first maximum value of the electrons drift velocity, $\tilde{v}_M$, is bigger. This means, that it is possible to obtain small δ values with small values of ν in a SL with small aluminium content.

- Both the *barrier thickness* and the *well thickness* determine the maximums position of the drift velocity in relation to the electrical field. But is the *barriers thickness* value which determine principally the first drift velocity maximum. And as consequence the value relation between the dimensionless ν and δ parameters.

- The *frequency* and the *pumping laser intensity* regulate the equilibrium population of the free charge carrier and as consequence the scales of our system. They also describe with the δ and ν dimensionless parameters, the importance in our system of the differences on QWs electrical field; and finally in what transport regime is the SL. The laser *frequency* can modify the $\gamma\,(F)$ function, if $\hbar\omega_{exc}$ is close to the $GaAs$ bandgap value.

- As the *quantum well thickness* gets smaller, the QW energy levels $\tilde{E}_e^1(F)$ and $\tilde{E}_e^2(F)$, are more separated between them. As a first consequence, the second peak of the current increase his position in relation with the electrical field $\tilde{F}$. In relation with the electron-hole recombination fuction; if the QW length is decreased, his shape have less decrease with the dimensional electric field value.

- With more *temperature,* the scattering times changes; and for a fixed energy band width, the diffusion function decreases slower with the electrical field, (4.20), and in addition, the first

peak of $\tilde{v}(\tilde{F})$ is placed lightly in a greater value of the electrical field (4.19). The second peak of the dimensional drift velocity have a greater values, but the nondimensional $v(F)$ second peak is placed in lower values of F. As consequence the minimum between $v(F)$ peaks too.

- If the value of the *effective electron mass* gets higher, due to an aluminium content in the electron QW layer, the difference between $\tilde{E}_e^1(F)$ and $\tilde{E}_e^2(F)$ QW energy levels are lower. Therefore the drift velocity, $\tilde{v}(\tilde{F})$, have lower values and his peaks are situated more closely. The electron-hole recombination decrease faster with electric field.

- Due to the fact that the holes do not contribute, in a great way, to the total SL current, the *hole effective mass* only contributes in the variation of the recombination function, in the same terms seen in the previous paragraph.

- The energy level broadening by the different scattering processes, fixes the width of the $v(F)$ peaks. As consequence the position and the value of the minimum between these peaks. The QW scattering time also modifies lightly the position of the first maximum of the dimensional drift velocity.

- For QWs with bigger values of the electrons energy levels, and as consequence with electrons wave functions having more penetration length in the barrier, the recombination function decrease more fastly.

A.3 Appendix: Stationary solutions in dc current bias.

This section is focused on the global stationary solutions of the the convection-diffusion model given by the system (4.26)-(4.31). Though the model is simple, the not linear drift velocity function, and the high number of freedom degrees that presents this system of equations, generate a great variety of solutions in dc current bias.

The stable stationary solutions for an $Al_xGa_{1-x}As/GaAs$ generic superlattice in dc current bias, can be summarized in three types:

- Homogeneous electrical field profiles or more commonly known as electric domains. These domains can be stable or unstable.

- Regions of quantum wells with charge accumulation or charge decumulation, produced by the nearness of the contacts.

- Increasing, or decreasing electrical field profiles that join two stable domains which in other sections we call them pinned fronts.

The value of the QWs electrical field and hole concentration, which are in a specific domain, is defined in the phase plane by the nullclines intersection of the system (4.26)–(4.31):

$$\begin{aligned} N_1 &= \{(F,P) : p = J/v(F)\} \\ N_2 &= \{(F,P) : p = \sqrt{1/r(F)}\}. \end{aligned} \tag{A.11}$$

For each value of the current, the nullcline position N_1 changes in the phase plane, and as consequence the domains number in the SL. The stability of these domains depend on the branch in which the nullclines N_1 and N_2 have an intersection.

To find all the possible stationary profiles in a $Al_xGa_{1-x}As/GaAs$ SL, it is necessary to to solve numerically the following system of equations:

$$\begin{aligned} 0 &= J - v(F_i)(p_i + \frac{F_i - F_{i-1}}{\nu}) + D(F_i)(p_{i+1} - p_i + \frac{F_{i+1} + F_{i-1} - 2F_i}{\nu}), \\ 0 &= 1 - r(F_{i+1})(p_{i+1} + \frac{F_i - F_{i-1}}{\nu})p_{i+1}. \end{aligned} \tag{A.12}$$

where F_0, F_N y p_N are defined by the contacts conductivity in the resolution of (4.29).

The resolution of (A.12) give a great quantity of stationary solutions, stable or unstable solutions without distinction. In order to find the stationary stable profiles is more advisable the map function:

$$F_{i-1} = f(F_i, \nu, J) \qquad i = 2, 3, ..., N \tag{A.13}$$

where:

$$\begin{aligned} f(F_i, \nu, J) &\equiv F_i - \frac{\nu J}{v(F_i)} + \frac{\nu v(F_i)}{J r(F_i)} \\ P_i(F_i) &= \frac{v(F_i)}{J r(F_i)} \end{aligned} \tag{A.14}$$

The intersection of (A.13) with the line $F_{i-1} = F_i$ (*figure* ***A.3****-1(a)*), gives from one to three stationary homogeneous solutions, which indicate the possible electrical field domains in the SL, $F^{(1)}$, $F^{(2)}$ y $F^{(3)}$ with its corresponding holes concentrations calculated with equation (A.14).

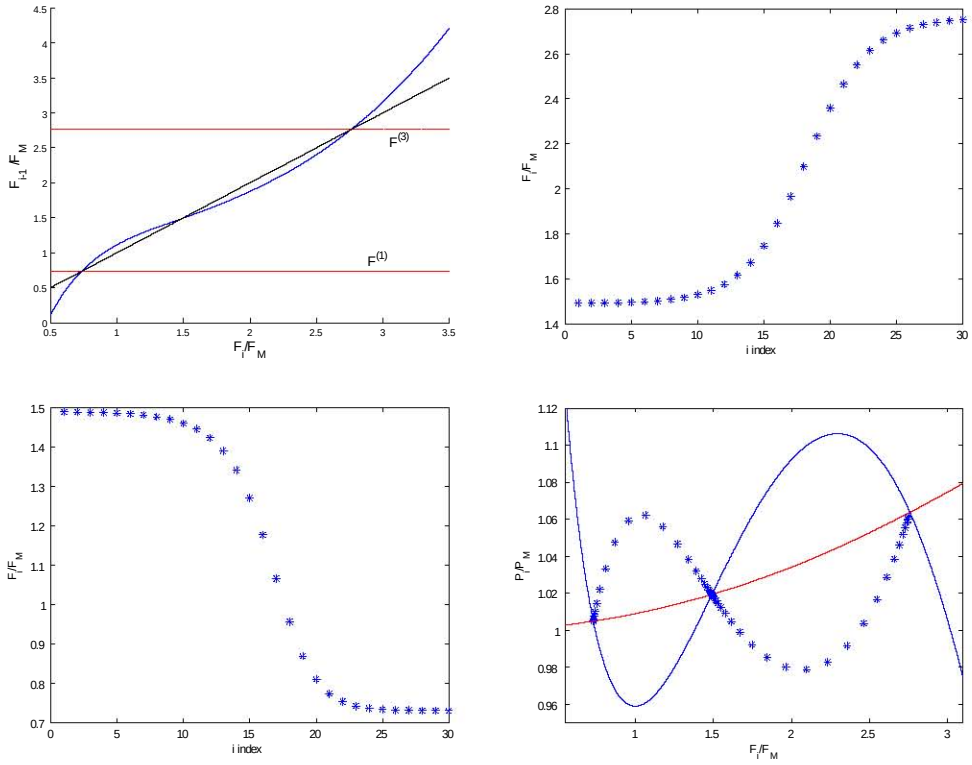

Figure A.3-1(a) $f(F_i, \nu = 1.1,\, J = 0.96)$ **(b)** Stationary electric field profile for a SL $\mathcal{D}$ with $N = 30$ and $F_N \approx F^{(1)}(J = 0.96)$ **(c)** Idem but with $F_N \approx F^{(3)}(J = 0.96)$ **(d)** The (b) and (c) electric field profiles plotted in the phase plane.

As we can see in the *figure* ***A.3-1 (d)***, the stationary profiles draw a path in the phase plane, and this path have a direct relation with the area of the homogeneous system nullclines. The union of the stable domains, $F^{(1)}$ and $F^{(3)}$, by a stationary profile, only it is possible, if the minimum of the map function is lower to $F^{(1)}$ value, or, if the maximum of the map function is greater to $F^{(3)}$.

The map function is also useful to estimate the critical value of $F_0 = \frac{J}{\sigma_1}$, for which the contact can generate pulses. In the *figure* ***A.3-2 (c)*** we can observe that if $F_0 > \max(f(F_i, \nu, J))$, does not exist any possible stationary profile between the contact and the low field domain, and the SL contact would generate fronts every certain interval of time.

In a similar way, in the *figure* ***A.3-2 (d)*** we can observe that if $F_0 < \min(f(F_i, \nu, J))$, does not exist any stationary profile between the contact and $F^{(3)}$. If we analyze the *figure* ***A.3-2(a) and (b)***, we can highlight the appearance of stacionary profiles that join $F^{(3)}$ with $F^{(1)}$, or vice versa, which start in a certain range of values of J and ν. For greater values of the parameter ν, more stationary profiles joining the stable domains are possible.

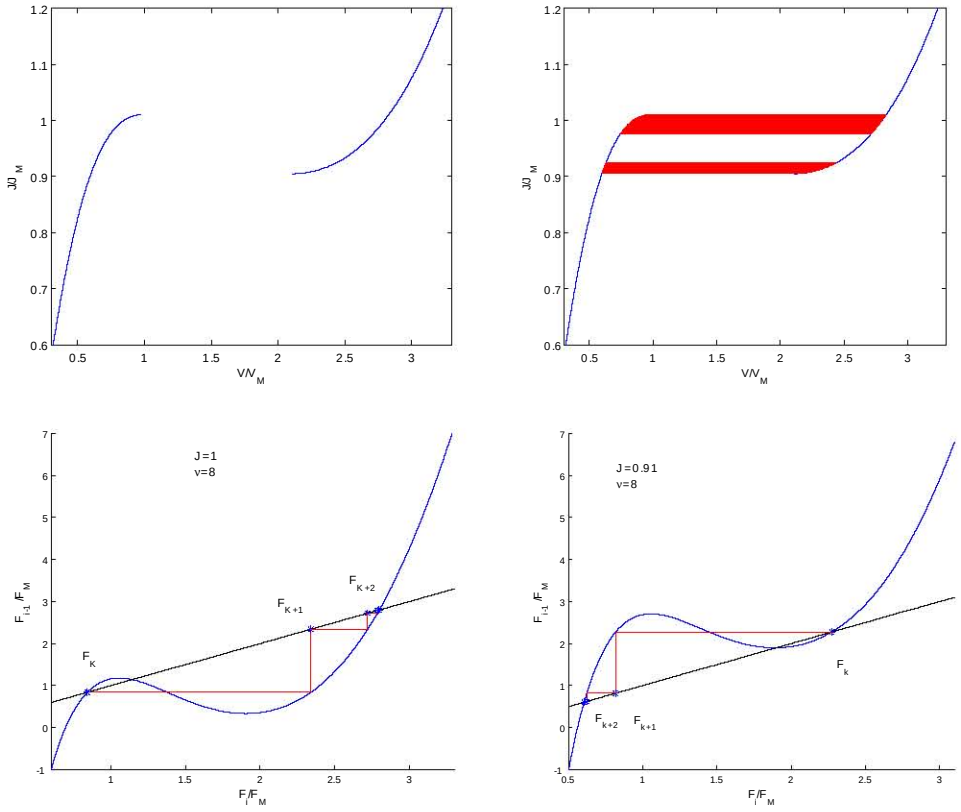

Figure A.3-2 SL $\mathcal{D}$ **(a)** and **(b)** Current versus voltage in a infinite SL with $\nu = 1$ and $\nu = 8$, respectively. Stable domains $F^{(1)}$ and $F^{(3)}$ (Blue) and stacionary profiles joining the high and low electric field domains, or vice versa (Red) **(c)** and **(d)** Stationary profiles between stable domains calculated with (A.13).

The relation between the values ν and δ determine the pumping intensity range in which the dynamic solutions can exist, and the type of these solutions. The fact of having big values of ν implies the appearance of stationary profiles of electrical field in the SL, between the anode and the cathode, or between the domains and the contacts. The number of quantum wells, N, is a crucial value.

The SL $\mathcal{D}$ and SL $\mathcal{C}$ have small values of $\tilde{v}_M$, which indicates that ν is big for small values of δ. For that reason these SLs are ideal to find dynamic solutions with low intensity laser. In contrast, the SL $\mathcal{A}$ and SL $\mathcal{B}$ have small values of ν with small values of δ, so we can find pulses with a high intensity laser.

A.4 Appendix: Photoluminescence

The experimental evidence of pulses, waves trains and domains in a superlattice, can be obtained by the spectrum of photoluminescence, which measures the light emited frequencies by the electron-hole recombination process, by unit of time, [45].

If an external current and a photo-excitation intensity is applied into to the superlattice, two photo-emission peaks can appear in the photo-luminescence spectrum (PLS). These phenomena can be explained by the stark effect. The energy bands of the QWs change his values with the electric field. So, the QWs with a bigger electrical field, due to the electron-hole recombination, have a less energy photo-emission in comparison with those QWs that have less electrical field.

The contribution of all the quantum wells generate the PLS. The presence of two peaks in the PLS involves the existence of two domains or pulses in the superlattice. If we want to distinguish between a mobile front or a pulse, we have to analyze the spatial spectrum or the temporal spectrum of the photo-luminescence

The ideas exposed in the previous paragraph, are expressed in the following formula, which relates the PLS to the charge carriers density and the electrical field applied to every well, [47]:

$$I_{pl}(\hbar\omega) = \sum_{i=1}^{N} \tilde{r}(\tilde{F}_i)\tilde{n}_i\tilde{p}_i\Delta(\hbar\omega - \Omega\,(F_i))$$

Where, $\Delta(\mu)$ is a lorenzian function, witch contains the contributon of $\Omega\,(F)$ to the PLS with energy $\hbar\omega$, [44], [16]. $\Omega\,(F)$ has been obtained by numerical simulation of the Schrödinger ecuation for a quantum well of a superlattice $Al_xGa_{1-x}As/GaAs$ (10/4).

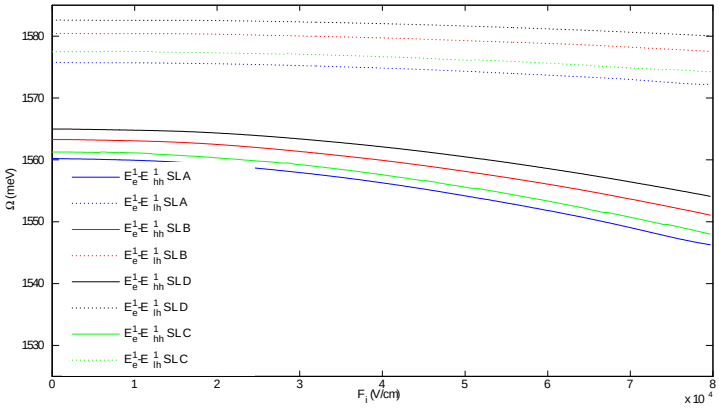

Figure A.4-1 $\Omega(\tilde{F}_i) = \tilde{E}^1_e - \tilde{E}^1_{hh}$ and $\Omega(\tilde{F}_i) = \tilde{E}^1_e - \tilde{E}^1_{lh}$ for a SL $\mathcal{A}$, $\mathcal{B}$, $\mathcal{C}$ and $\mathcal{D}$

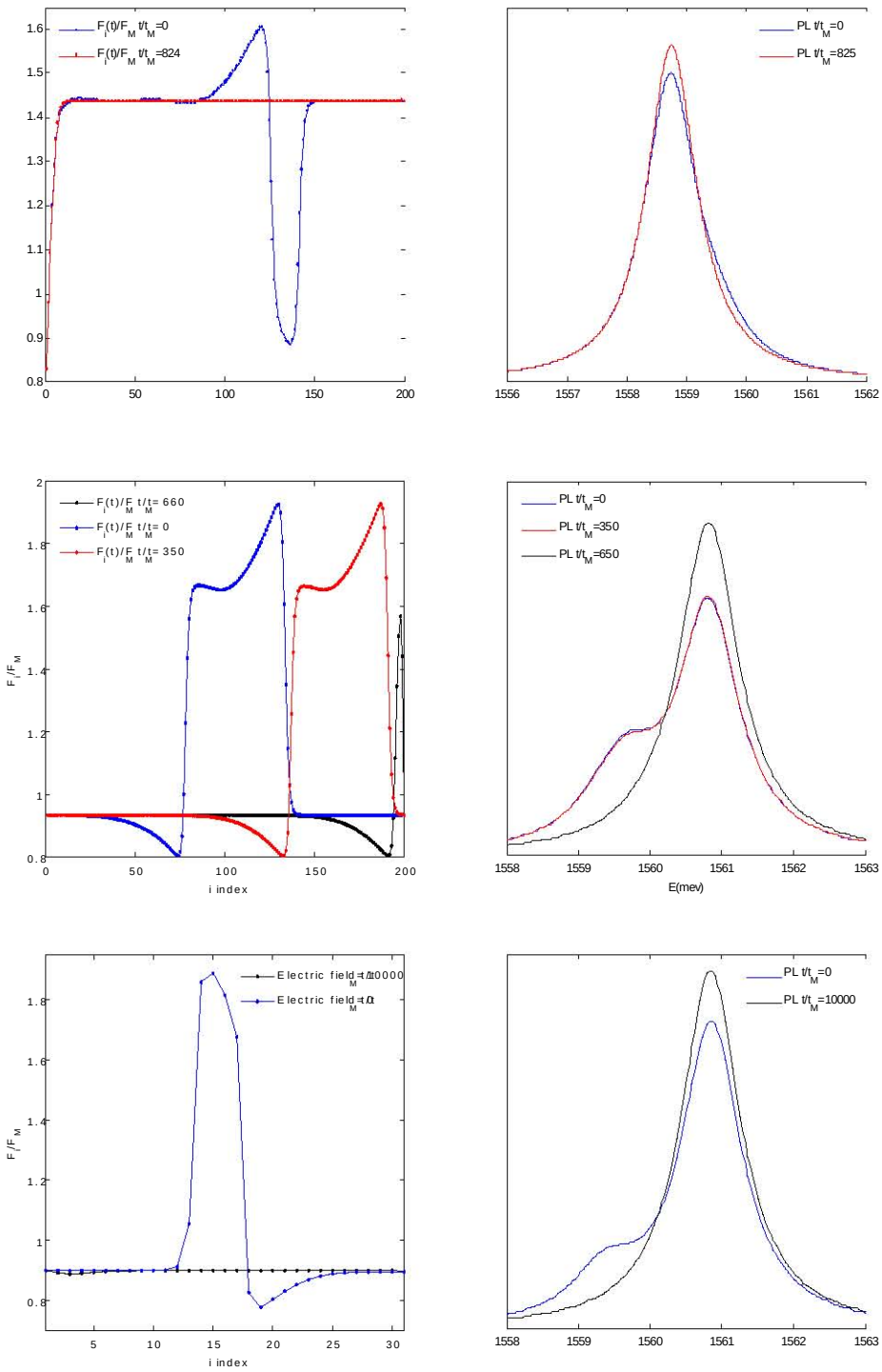

Figure A.4-2 (b)(d)(f)$I_{pl}(\hbar\omega, t)$, for diferent F_i profiles contained in (a)(c)(e) (e) Pulse with c<0 (a) and (c) Pulses with c>0

A.5 Appendix: Unstable pulses at the first current peak

If the temperature is changed, as a external parameter to the SL, with low photo-excitation and dc current bias, other types of pulses in the first current peak can be obtained mathematically. With extremely low temperatures in the SL ($\tilde{T} = 1.4\ ^oK$), the diffusion term in equation (A.6) can be neglected. Now, the dinamical solutions of the SL can be described by the following equation:

$$\frac{dF_i}{dt} = J - \frac{v(F_i)}{2}\left(\sqrt{\left(\frac{F_i - F_{i-1}}{\nu}\right)^2 + \frac{4}{r(F_i)}} + \frac{F_i - F_{i-1}}{\nu}\right) \tag{A.15}$$

The electric field domains can be found solving $J = v(F)/\sqrt{r(F)}$. This section is focused to the SL dinamical solutions which have the first two homogeneous solutions, $F^{(1)}$ (stable) and $F^{(2)}$ (unstable).

As the term of the diffusion is not considered, the wells placed in the second homogeneous solution (saddle-node) are removed very slowly from his unstable solution. In that way, we are able to find similar profiles to the represented in the *figure A.5-1*. Increasing and decreasing fronts that can travel through an infinte SL for a long time period.

In the *figure A.5-1*, the IF and the DF travel with different velocities, decreasing, in this case, the applied voltage to the SL. The three parameters (J, β, ν) fix the fronts velocities in the first current peak and, therefore, the voltage variation.

The relation between photo-excitation and the electric field difference, $\mathcal{K}=\frac{F_i - F_{i-1}}{\nu}$, indicates how the phase plane change for a single QW. As we can see in *figure A.5-2*, the saddle-node appears in the QW phase plane for some $\mathcal{K}$ values. Allowing or not, the QW movement from the first branch to the second branch, or vice versa.

In the dc voltage bias, the pulses described with this theory are forced to be transformed in others that develop between two stable solutions. In the same way as we have seen and described in other sections.

As in the dc voltage bias, there can not be seen SSCOs related to these pulses; and, in dc current bias, the IF and DF are difficult to maintain in the SL because they collapse. These unstable pulses and fronts can be considered a rarety of the SLs.

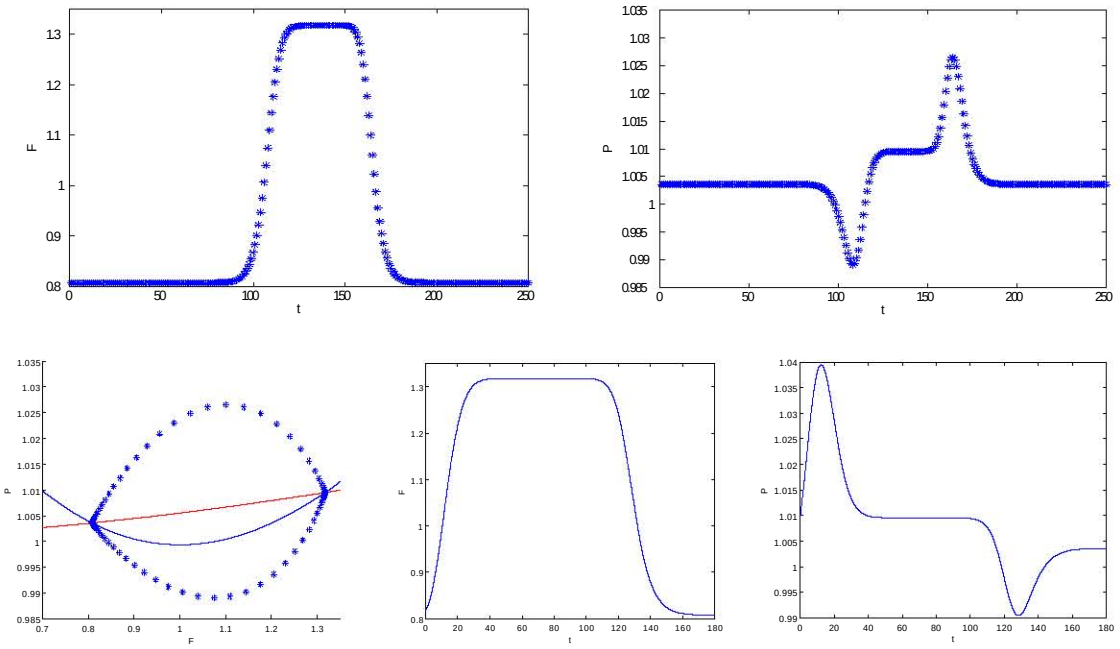

Figure A.5-1 F_i and P_i profiles. **(a)(b)** spatially represented **(c)** in the phase plane and **(d)(e)** temporal profile of the 140th QW. The used parameters are ($J = 1$, $\nu = 1$, $\beta = 0.05$).

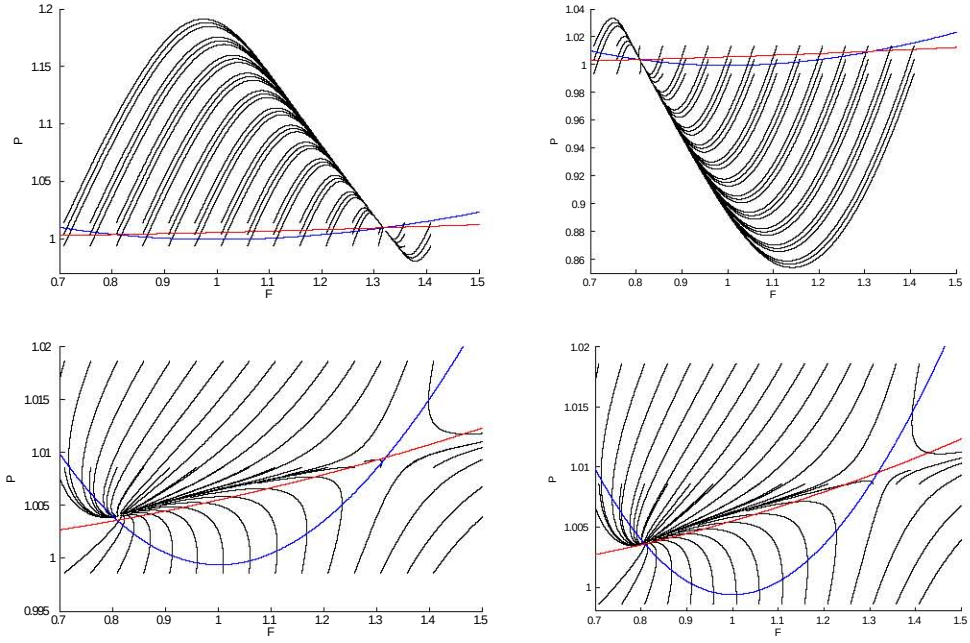

Figure A.5-2 Paths Skecth in the phase plane for a QW situated in a **(a)** DF **(b)** IF of a SL with $N = 2$.**(c)** and **(d)** idem, but for a $\mathcal{K}$ and β values where fronts are pinned.

A.6 Appendix: Heterogeneous illuminated Superlattices

The task of describing the behavior of all heterogeneous illuminated Superlattices is excessively complex. The principal reason of this complexity, can be argued by the great quantity of SL combinations. Different spatial regions, which can be illuminated by different types of lasers or by different intensities for example. We will try to synthesize the problem.

Our first step, to describe this problem, is to fix the frequency of the laser pumping intensity. We choose a great laser frequency in order to eliminate the electrical field dependence of the parameter γ, see *figure A.6-1*. The second necessary step, consists in taking into account an effective intensity for each quantum well in the system (A.6)–(A.10). So, γ and β which depends on $\tilde{I}$, now have to depend on the well number of the SL. We denote them as $\gamma_i(\tilde{I}_i)$ and $\beta_i(\tilde{I}_i)$.

The experiments done in dc current bias, which are annexed in the movies section *A.11*, show that the pulses that cross the SL, are transformed during the SL time scale and depending on the region in which they are moving. Increasing or diminishing temporarily the voltage of the SL according to the region value of β_i .

If a moving pulse, that is trying to change of ilumination region, is unable to excite the following region, it disappears from the SL. This can happen because we need a bigger pulse trying to enter in the following region or simply an appropriate J, γ_i and β_i values in which we could find fronts or pulses.

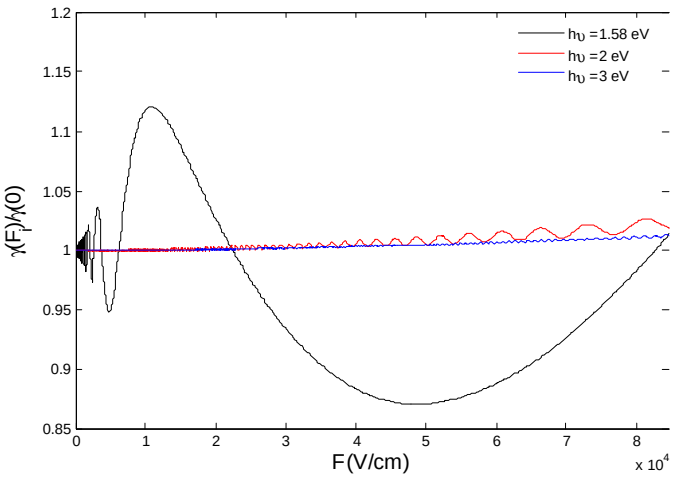

Figure A.6-1 electric field dependence of $\tilde{\gamma}(\tilde{F}_i, \hbar\omega_{exc})/\tilde{\gamma}(0, \hbar\omega_{exc})$ for an AlAs/GaAs(4/10) SL photoexcited with different frequencies.

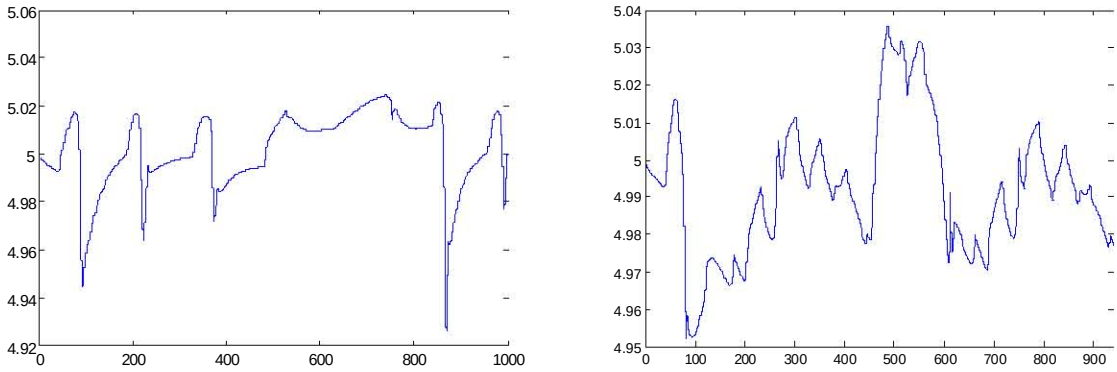

Figure A.6-2 SSCOs, $J(t)$, in a SL with a constant voltage $V = 1.42798$ and $\gamma = 24$, whith two lighting domains **(a)** $\beta_{i=1...250} = 200$ and $\beta_{i=251...500} = 0.01$ **(b)** $\beta_{i=1,...,250} = 0.01$ and $\beta_{i=251,...,500} = 200$

For our convenience, let us assume in the SL a central region with $\frac{dp_i}{dt} \approx 0$, due to an extremely high ilumination or due to other physical experimental configuration. So, the holes concentration in this zone can be considered constant, for a long period of time which is greater than the experiment time.

When the regions with $\frac{dp_i}{dt} = 0$, do not satisfy with the condition $P_- < p_i(t = 0) < P_+$, these regions will stop any pulse that tries to enter them. Being P_- and P_+, respectively, the minimum and the maximum of the nullcline for a fixed J. In addition, if the initial position in the phase plane satisfy the condition $(F_i, p_i(t = 0)) > (F_{threshold}, P_{threshold})$, periodically this region would generate pulses of the first branch. On the other hand, if this region have the condition $(F_i, p_i(t = 0)) < (F'_{threshold}, P'_{threshold})$ fulfilled, would periodically generate pulses of the third branch.

The solutions in dc voltage bias depend on the different composition of the illuminated regions as the variation of the current value. This fact was proved when we change the position of two different lighting domains in a SL, one lighting domain with $\beta \lll 1$ and the other lighting domain with $\beta \ggg 1$. The behavior that we observed was very different in both SL, see *figure A.6-2.*

In dc voltage bias a SL, with a sufficiently big central region, which have a constant initial hole concentration, can be obtained a reconstruction of the SSCOs of a smaller SL. This fact can be explained because the total current has relation with the oscillations produced in the different illuminated regions. As we can see in the *figure A.6-3,* the effect of this central region in the total current graph is very small. But this affirmation can take us into a mistake, because, as we explained before, in dc current bias this central region can generate new pulses in the neighboring region. The values taked in *figure A.6-3* avoid this problem.

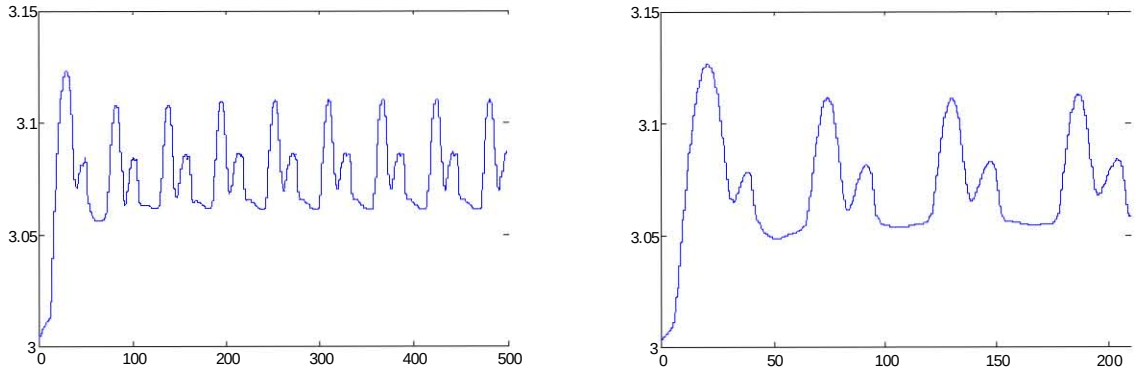

Figure A.6-3 SSCOs, $J(t)$, in a SL with $\frac{dp_{i=71:100}}{dt} = 0$, $N = 171$ and two initial pulses constructed with the parameters $J = 3$ $\beta = 200$ $\gamma = J^2$ and a constant voltage in the SL (a) 1.2371 ($p_{i=71:100}(t = 0) = 3.4$) and (b) 1.2072 ($p_{i=71:100}(t = 0) = 3.6$).

If we consider the symmetric SLs with a intermediate region of great ilumination, we have to take into account that the SSCOs only depends on the total voltage of the SL. If the regions have different initial electric profiles, the SL tend to regenerate the initial pulses at the same instant of time, and as consequence is obtained a similar SSCOs of a smaller SL, *figure A.6-5 (a) and (b).*

Now, if we consider the non-symmetric SLs with a central region of great illumination, the SSCOs only depends on the voltage too, but now there is a lack of coordination from the different ilumination regions to the SSCOs contribution, *figure A.6-5 (c)* and *(d).* The SL regenerate the pulses at the same instant of time, but the path length of these pulses is different. This is the explanation of the two peaks in each SSCO period in the *figure A.6-5(d)*.

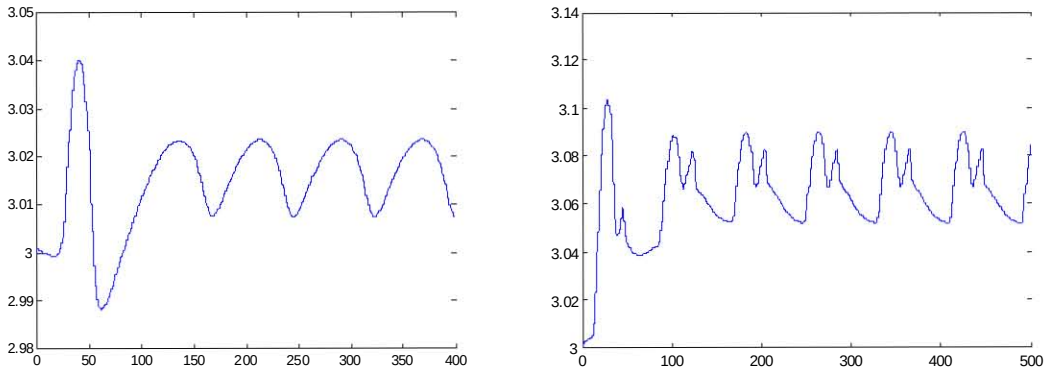

Figure A.6-4 $J(t)$ in a SL with $\frac{dp_{i=101:130}}{dt} = 0$, $p_{i=101:130} = 3.6$ and two initial pulses constructed with the parameters(a) $J = 3$, $\beta_{i=1:100} = 200$, $\gamma_{i=1:100} = J^2$, $\beta_{i=131:230} = 0.01, \gamma_{i=131:230} = 0.96J^2$ (b) $J = 3$, $\beta = 200$, $\gamma_{i=1:100} = J^2$, $\gamma_{i=131:187} = 1.1J^2$ and an applied voltage (a) 1.13957 y (b) 1.0594

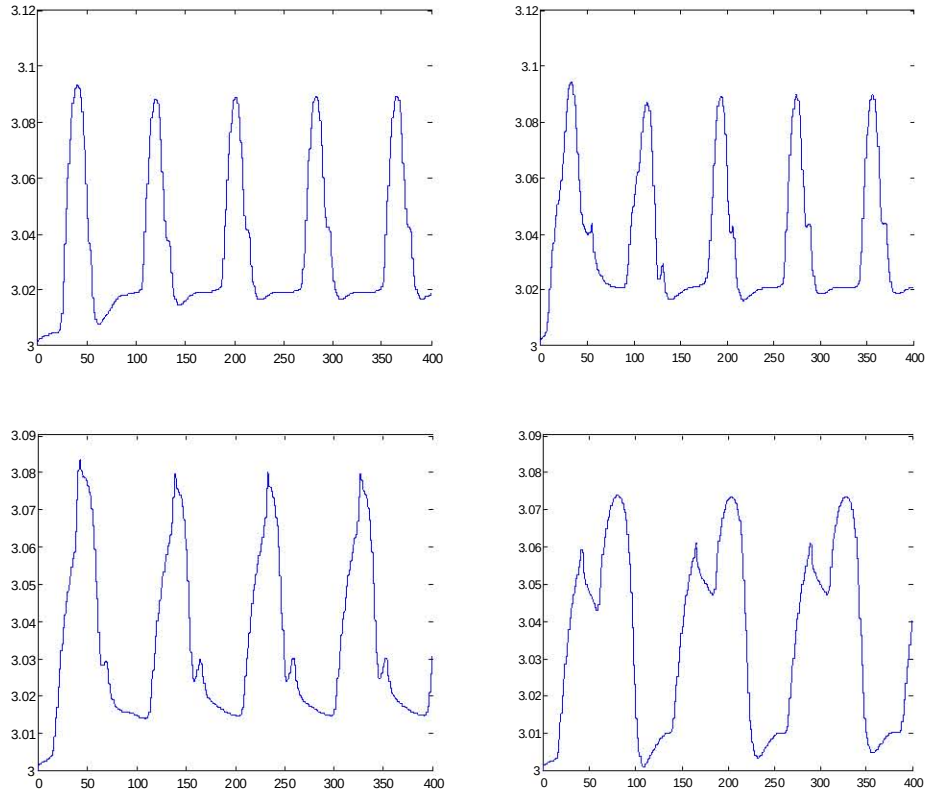

Figure A.6-5 $J(t)$ in a SL with $\frac{dp_{i=101:130}}{dt} = 0$, $N = 230$, $p_{i=101:130}(t = 0) = 3.6$ and two initial pulses constructed with the parameters $J = 3$, $\beta = 200, \gamma = J^2$ and an applied voltage(a) 1.06287(b) 1.0687 (c) 1.03268, $N = 260$ and (d) 1.005, $N = 290$

The SSCO initial shape diference between *figure A.6-5(a)* and *figure A.6-5(b)* is due to the initial conditions. As they have a similar voltage, this implies that they also have a similar SSCO shape.

When are used two distinct regions with different β values and a intermediate region with a constant hole concentration, in the SL takes place a redistribution of the total voltage between these two regions. So, the SL is forced to generate pulses only in one lighting domain, *figure A.6-4*. This situation, is is due to the voltage conservation and due to the existence of two lighting domains with different speed to regenerate pulses.

A.7 Appendix: Large photo-excitation, Fronts

In the limit $\delta \longrightarrow 0$ of the Eq. system (4.26)–(4.29). Between the two critical currents, J_{c1} and J_{c2} the wave fronts in fail to propagate and are pinned. Therefore, the field profile is a stationary front, $F_i = F_i(J, \nu)$. Near these critical currents the wave fronts profiles loses continuity and the voltage variation is like stair shape. The depinning transition from stationary fronts to moving wave fronts is a global saddle-node bifurcation.

For sufficiently large ν and J close to a critical current, the moving front is led by the behavior of a single well, the *active well*.

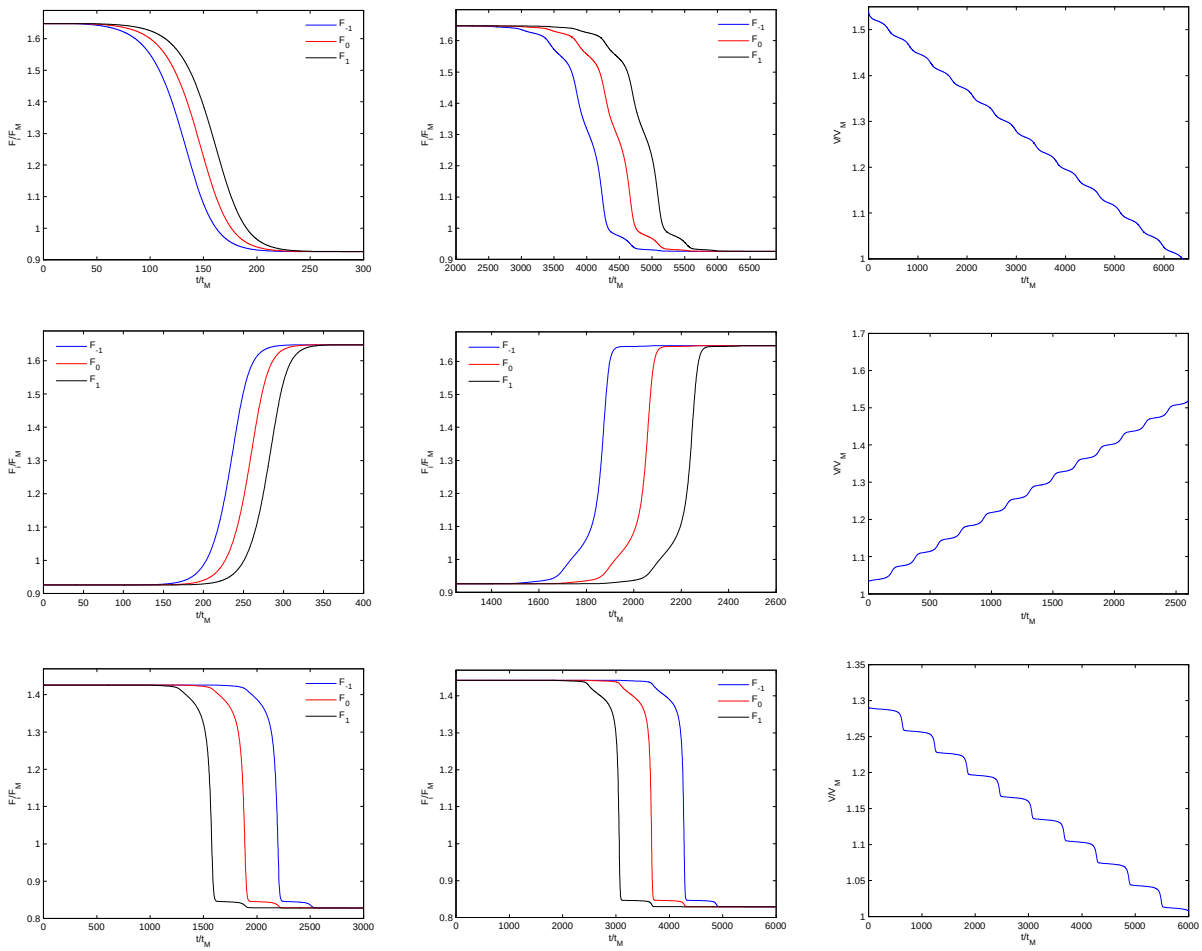

Figure *A.7-1* SL $\mathcal{A}$**(a)** IF$(c > 0)$ $J = 1.01$ $\nu = 8.44566$ **(b)** and **(c)** IF$(c > 0)$, $J = 1.01$ $\nu = 40$ $N = 20$ **(d)** DF$(c > 0)$ $J = 1.01$ $\nu = 40$ **(e)** and **(f)** DF.$(c > 0)$, $J = 1.01$ $\nu = 330$ $N = 20$ **(g)** F.D.$(c < 0)$ $J = 0.9975$ $\nu = 330$ **(h)** and **(i)** F.D.$(c < 0)$, $J = 0.9976$ $\nu = 330$ $N = 420$.

A.7.1 Theory of wave fronts pinning, with an active well.

Let us call F_0 the electric field at the *active well*. In the limit $\delta \longrightarrow 0$, p is a constant. Before the active well jumps and if the *active well* is in an IF; $F_i = U_1$ for $i < 0$ and $F_i = U_3$ for $i > 0$. Thus Eq. (A.1) becomes respectively for the IF and the DF:

$$\begin{aligned}
\frac{dF_0}{dt} &= J - v(F_0)(\frac{F_0 - U_1}{\nu} + p) + D(F_i)(\frac{U_3 - 2F_0 + U_1}{\nu}) \\
\frac{dF_0}{dt} &= J - v(F_0)(\frac{F_0 - U_3}{\nu} + p) + D(F_i)(\frac{U_3 - 2F_0 + U_1}{\nu})
\end{aligned}$$

For a fixed p value, this equations has three stationary solutions for $J_{c1} < J < J_{c2}$, two stable and one unstable. At the critical currents, two of these solutions coalesce forming a saddle node.

If we denote the electrical field of the *active well* as $F_0(t) = F_0(J_c) + \varphi(t)$, near these critical currents and fixing U_1 and U_3 as a constants. The previous equations, up to terms of order $|J - J_c|$, becomes:

$$\frac{d\varphi(t)}{dt} = \alpha(U_1) \cdot |J - J_c| + \Delta(U_1) \cdot \varphi(t)^2 \tag{A.16}$$

Equation (A.16) has the outer solution:

$$\varphi(t) = \sqrt{\frac{\alpha(U_1) \cdot |J - J_c|}{\Delta(U_1)}} \tan(\sqrt{\alpha(U_1) \cdot \Delta(U_1) \cdot |J - J_c|}(t - t_0)) \tag{A.17}$$

Where the coefficients $\alpha(U_1)$ and $\Delta(U_1)$ for the DF are given by:

$$\begin{aligned}
\alpha(U_1) &= 1 - \frac{v(F_0)}{v(U_1)} \\
2\Delta(U_1) &= -\frac{v''(F_0)J_c}{v(U_1)} - v''(F_0)(\frac{F_0 - U_3}{\nu}) - \frac{2}{\nu}v'(F_0) - \frac{4}{\nu}D'(F_0) + \\
&\quad + D''(F_0)(\frac{U_1 + U_3 - 2F_0}{\nu})
\end{aligned}$$

and for the IF these coefficients are given by the following expressions:

$$\begin{aligned}
\alpha(U_1) &= 1 - \frac{v(F_0)}{v(U_1)} \\
2\Delta(U_1,\nu) &= -\frac{v''(F_0)J_c}{v(U_1)} - v''(F_0)(\frac{F_0-U_1}{\nu}) - \frac{2}{\nu}v'(F_0) - \frac{4}{\nu}D'(F_0) + \\
&\quad + D''(F_0)(\frac{U_1+U_3-2F_0}{\nu})
\end{aligned}$$

When the solution begins to blow up, the outer solution (A.17) is no longer a good approximation. The equation (A.17) is very small most of the time, but it blows up when the argument of the tangent function approaches to $\pm\pi/2$. The outer solution is valid in the time interval $(t-t_0) \sim \pi/\sqrt{\alpha(U_1)\cdot\Delta(U_1)\cdot(J-J_c)}$. The reciprocal of this time interval yields an approximation for the wave front velocity which depends on J and U_1,[58]:

$$|c(J,U_1)| = \frac{\sqrt{\alpha(U_1)\cdot\Delta(U_1)\cdot(J-J_c)}}{\pi} \tag{A.18}$$

With the same procedure, but now, fixing p as a constant in the relation $v(U_1)p = J$, and considering up to terms of order $|J-J_c|^2$. We can get another front velocity approximation which depends on J and p :

$$|c(J,p,\nu)| = \frac{\sqrt{\alpha(p)\cdot\Delta(p)\cdot(J-J_c) + \varsigma(p)\cdot\Delta(p)\cdot(J-J_c)^2}}{\pi} \tag{A.19}$$

where the coefficients $\alpha(p)$, $\Delta(p)$ and $\varsigma(p)$ for de DF are:

$$\begin{aligned}
\alpha(p,\nu) &= 1 + \frac{D(F_0)}{pv'(U_1)\nu} + \frac{D(F_0)+v(F_0)}{pv'(U_3)\nu} \\
2\Delta(p,\nu) &= -v''(F_0)p - v''(F_0)(\frac{F_0-U_3}{\nu}) - \frac{2}{\nu}v'(F_0) - \frac{4}{\nu}D'(F_0) \\
&\quad + D''(F_0)(\frac{U_1+U_3-2F_0}{\nu}) \\
\varsigma(p,\nu) &= \frac{-v(F_0)v''(U_3)}{\nu p^2 v'(U_3)^3} - \frac{D(F_0)v''(U_3)}{\nu p^2 v'(U_3)^3} - \frac{D(F_0)v''(U_1)}{\nu p^2 v'(U_1)^3}
\end{aligned}$$

and for the IF:

$$\begin{aligned}
\alpha(p,\nu) &= 1+\frac{v(F_0)+D(F_0)}{\nu p v'(U_1)}+\frac{D(F_0)}{\nu p v'(U_3)} \\
2\Delta(p,\nu) &= -v''(F_0)p - v''(F_0)(\frac{F_0-U_1}{\nu}) - \frac{2}{\nu}v'(F_0) - \frac{4}{\nu}D'(F_0) + \\
&\quad + D''(F_0)(\frac{U_1+U_3-2F_0}{\nu}) \\
\varsigma(p,\nu) &= \frac{-v(F_0)v''(U_1)}{\nu p^2 v'(U_1)^3} - \frac{D(F_0)v''(U_3)}{\nu p^2 v'(U_3)^3} - \frac{D(F_0)v''(U_1)}{\nu p^2 v'(U_1)^3}
\end{aligned}$$

If we want a more precise way to obtain the fronts velocities, is advisable to take more active wells in the front description instead of taking more order terms, $|J-J_c|^n$. This theory is described in the following section.

A.7.2 Theory of wave fronts pinning, with several active wells.

The wave front profile obey $F_i(t) = F(i-ct)$, where $i = -L-1, ..., M+1$ are the indices of the *active wells*. Here, an approximation for the IF have to be done $F_{-L-1} = U_1$, $F_{M+1} = U_3$, and vice versa for the DF. The system of equations for all the *active wells* is given by the following expression:

$$\frac{dF_i(t)}{dt} = J - v(F_i)(p_i + \frac{F_i - F_{i-1}}{\nu}) + D(F_i)(\frac{F_{i+1}+F_{i-1}-2F_i}{\nu})$$

This equations system can be expressed by a matrix form $\frac{dF}{dt} = G(F,J)$; which at $J = J_c$, this system have as stationary solution F_{-L},..., F_M.

Let us now construct the front profile after depinnig near the critical currents, $F_i(t) = F_i(J_c) + \varphi_i(t)$. Where $\varphi_i(t)$ can be obtained solving:

$$\begin{aligned}
\frac{d\varphi}{dt} &= G(F_0,J_c) + \frac{dG(F_0,J_c)}{dF}\varphi + \frac{dG(F_0,J_c)}{dJ}(J-J_c) \\
&\quad + \frac{1}{2}\frac{d^2G(F_0,J_c)}{dF^2}\varphi^2 + o(\varphi^3) + o(J^2) + o(\varphi J)
\end{aligned} \tag{A.20}$$

The $\frac{dG(F_0,J_c)}{dF}$ matrix have L+M eigenvalues plus a smallest eigenvalue with a left and right eigenvectors, fulfilling $\Psi\Phi = 1$. With a similar procedure in [59], (A.20) can be approximated to the normal form of a saddle-node bifurcation. But now, in the front velocity approximation,(A.18), the coefficients $\alpha(U_1)$ and $\Delta(U_1)$ are:

$$\begin{aligned}
\alpha(U_1) &= \sum_{i=-L}^{M} \Psi_i - \frac{\Psi_i v(F_i)}{v(U_1)} \\
2\Delta(U_1,\nu) &= \sum_{i=-L}^{M} [\Phi_i^2 \begin{pmatrix} -\frac{v''(F_i)J_c}{v(U_1)} - v''(F_i)(\frac{F_i - F_{i-1}}{\nu}) - \frac{2}{\nu}v'(F_i) \\ -\frac{4}{\nu}D'(F_i) + D''(F_i)(\frac{F_{i+1}+F_{i-1}-2F_i}{\nu}) \end{pmatrix} \\
&\quad + \Phi_i\Phi_{i+1}\left(\frac{2}{\nu}D'(F_i)\right) + \Phi_i\Phi_{i-1}\left(\frac{2}{\nu}v'(F_i) + \frac{2}{\nu}D'(F_i)\right)]\Psi_i
\end{aligned}$$

And if we consider a constant p and the $o(J^2)$, The coefficients $\alpha(p)$, $\varsigma(p)$ and $\Delta(p)$ required in (A.19) are:

$$\begin{aligned}
\alpha(p,\nu) &= \sum_{i=-L}^{M} \Psi_i + \frac{v(F_{-L}) + D(F_{-L})}{\nu p v'(F_{-L-1})}\Psi_{-L} + \frac{D(F_M)}{\nu p v'(U_{M+1})}\Psi_M \\
2\Delta(p,\nu) &= \sum_{i=-L}^{M} [\Phi_i^2 \begin{pmatrix} -v''(F_i)p - v''(F_i)(\frac{F_i - F_{i-1}}{\nu}) - \frac{2}{\nu}v'(F_i) \\ -\frac{4}{\nu}D'(F_i) + D''(F_i)(\frac{F_{i+1}+F_{i-1}-2F_i}{\nu}) \end{pmatrix} \\
&\quad + \Phi_i\Phi_{i+1}\left(\frac{2}{\nu}D'(F_i)\right) + \Phi_i\Phi_{i-1}\left(\frac{2}{\nu}v'(F_i) + \frac{2}{\nu}D'(F_i)\right)]\Psi_i \\
\varsigma(p,\nu) &= \frac{-v(F_{-L})v''(F_{-L-1})}{\nu p^2 v'(F_{-L-1})^3}\Psi_{-L} - \frac{D(F_{-L})v''(F_{-L-1})}{\nu p^2 v'(F_{-L-1})^3}\Psi_{-L} \\
&\quad - \frac{D(F_M)v''(F_{M+1})}{\nu p^2 v'(F_{M+1})^3}\Psi_M
\end{aligned}$$

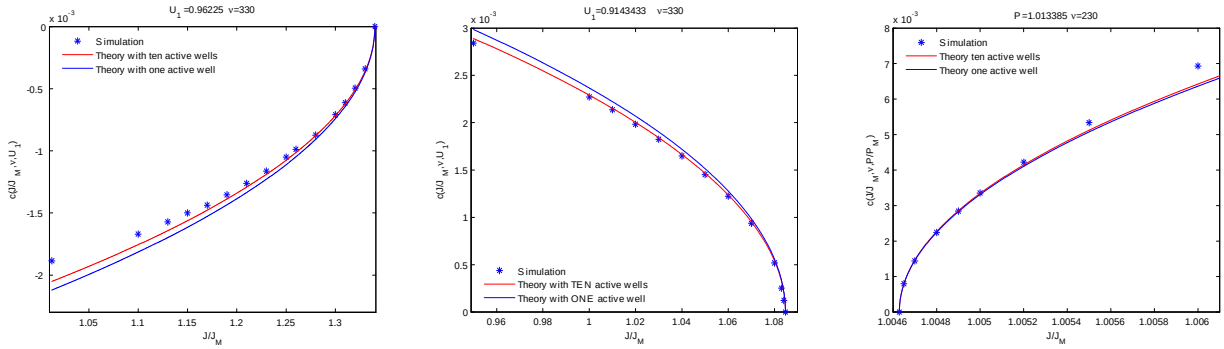

Figure *A.7-2* **(a)SL** $\mathcal{A}$ $c(J,U_1,\nu)$ IF **(b)** $c(J,U_1,\nu)$ DF and **(c) SL** $\mathcal{B}$ $c(J,P,\nu)$ DF

A.8 Appendix: Small photo-excitation, Fronts

In the limit $\delta \longrightarrow \infty$, the fronts are also pinned between two critical currents, J_{c1} and J_{c2}. Near these critical currents the electric and the hole fronts profiles loses their continuity and the voltage variation is like stair shape, see *figure A.8-1*.

For sufficiently large ν and J close to a critical current, the moving front is also led by the behavior of a single well, the *active well*.

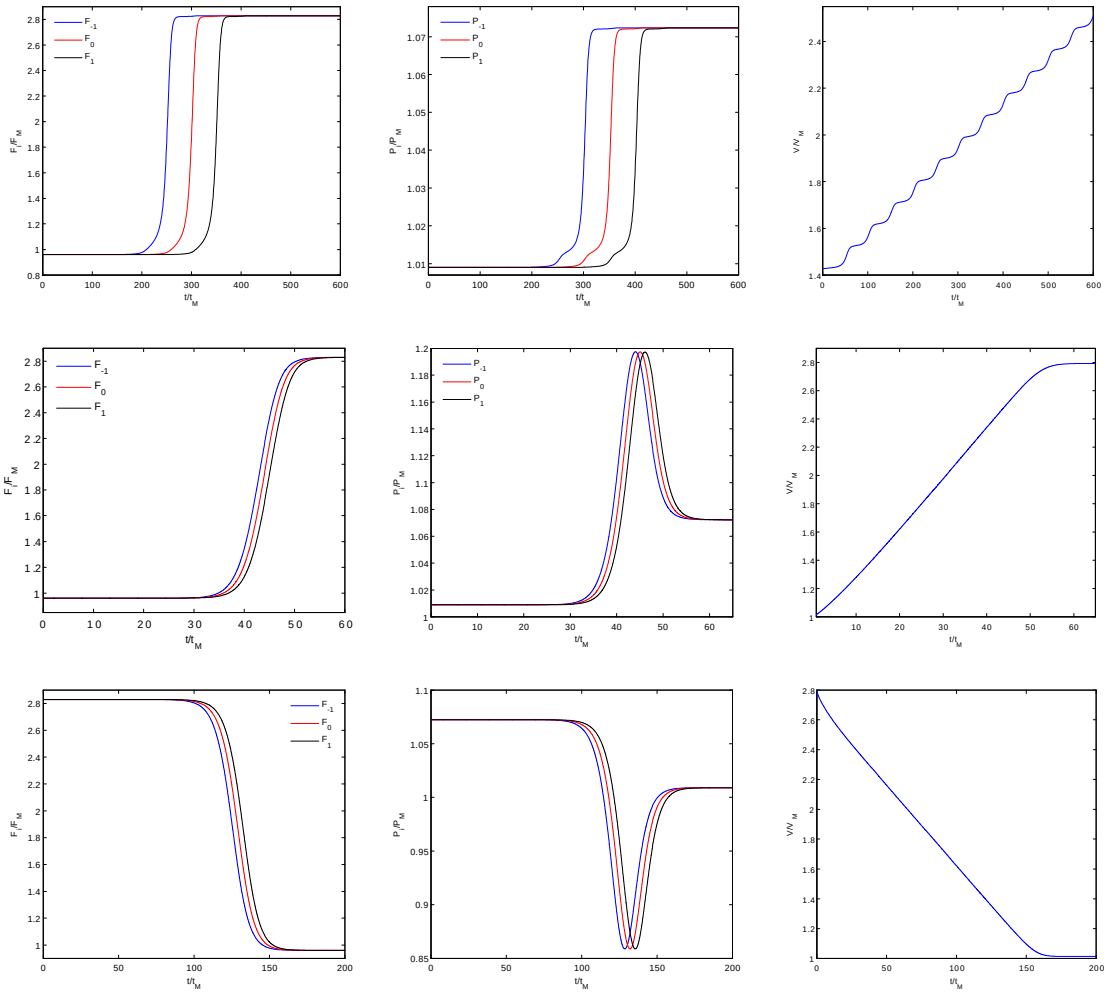

Figure A.8-1 SL $\mathcal{D}$(a), (b), (c) DF J = 1.01 $\nu = 330$ $N = 30$ **(d),(e),(f) DF J = 1.01** $\nu = 0.75$ $N = 50$ **(g),(h),(i) IF J = 1.01** $\nu = 0.75$ $N = 50$

A.8.1 Theory of domain fronts pinning, with an active well.

Let us call now, F_0 the electric field at the *active well*, U_1 the lower electric domain and U_3 the higher electric domain. The equations for the IF and DF with one *active well* are*:*

$$\begin{aligned}\frac{dF_0}{dt} &= J-\frac{v(F_0)}{2}\left(\sqrt{\left(\frac{F_0-U_1}{\nu}\right)^2+\frac{4}{r(F_0)}}+\frac{F_0-U_1}{\nu}\right)+\frac{D(F_0)}{2}\left(\frac{U_3+U_1-2F_0}{\nu}\right)\\ &+\frac{D(F_0)}{2}\left(\sqrt{\left(\frac{U_3-F_0}{\nu}\right)^2+\frac{4}{r(U_3)}}-\sqrt{\left(\frac{F_0-U_1}{\nu}\right)^2+\frac{4}{r(F_0)}}\right)\end{aligned} \tag{A.21}$$

$$\begin{aligned}\frac{dF_0}{dt} &= J-\frac{v(F_0)}{2}\left(\sqrt{\left(\frac{F_0-U_3}{\nu}\right)^2+\frac{4}{r(F_0)}}+\frac{F_0-U_3}{\nu}\right)+\frac{D(F_0)}{2}\left(\frac{U_3+U_1-2F_0}{\nu}\right)\\ &+\frac{D(F_0)}{2}\left(\sqrt{\left(\frac{U_1-F_0}{\nu}\right)^2+\frac{4}{r(U_1)}}-\sqrt{\left(\frac{F_0-U_3}{\nu}\right)^2+\frac{4}{r(F_0)}}\right)\end{aligned} \tag{A.22}$$

From the homogeneous system of (5.29), we can reach to the following expression:

$$\begin{aligned}\frac{dU_1}{dJ} &= \left[\frac{r(U_1)}{v'(U_1)r(U_1)^{1/2}-\frac{1}{2}r(U_1)^{-1/2}r'(U_1)v(U_1)}\right]\\ \frac{dU_3}{dJ} &= \left[\frac{r(U_3)}{v'(U_3)r(U_3)^{1/2}-\frac{1}{2}r(U_3)^{-1/2}r'(U_3)v(U_3)}\right]\end{aligned}$$

If we repeat the seen process of the previous appendix. Now, for the DF, $\alpha(U_1)$ and $\Delta(U_1)$ can be obtain with the following expressions:

$$\begin{aligned}\alpha(U_1,\nu) &= 1-\frac{v(F_0)}{2}m^{-1/2}\frac{dm}{dJ}+\frac{v(F_0)}{2\nu}\frac{dF_L}{dJ}+\frac{D(F_0)}{2\nu}\left(\frac{dU_3}{dJ}+\frac{dU_1}{dJ}\right)\\ &+\frac{D(F_0)}{2}\left(n^{-1/2}\frac{dn}{dJ}-m^{-1/2}\frac{dm}{dJ}\right)\end{aligned} \tag{A.23}$$

$$\begin{aligned}2\Delta(U_1,\nu) &= -\frac{1}{2}v''(F_0)\left(2m^{\frac{1}{2}}+\frac{F_0-F_L}{\nu}\right)-v'(F_0)\left(m^{\frac{-1}{2}}\frac{dm}{dF_0}+\frac{1}{\nu}\right)\\ &-\frac{1}{2}v(F_0)\left(-\frac{1}{2}m^{\frac{-3}{2}}\left(\frac{dm}{dF_0}\right)^2+m^{\frac{-1}{2}}\frac{d^2m}{dF_0^2}\right)-\frac{2}{\nu}D'(F_0)\\ &D''(F_0)\left(\frac{U_3+U_1-2F_0}{2\nu}\right)+D''(F_0)\left(n^{\frac{1}{2}}-m^{\frac{1}{2}}\right)+D'(F_0)\left(n^{\frac{-1}{2}}\frac{dn}{dF_0}-m^{\frac{-1}{2}}\frac{dm}{dF_0}\right)\\ &+D(F_0)\left(-\frac{1}{4}n^{\frac{-3}{2}}\left(\frac{dn}{dF_0}\right)^2+\frac{1}{2}n^{\frac{-1}{2}}\frac{d^2n}{dF_0^2}+\frac{1}{4}m^{\frac{-3}{2}}\left(\frac{dm}{dF_0}\right)^2-\frac{1}{2}m^{\frac{-1}{2}}\frac{d^2m}{dF_0^2}\right)\end{aligned} \tag{A.24}$$

For simplicity in the previous equations; we have denote $m(F_0,\nu)$, $n(F_0,\nu)$, $\frac{dm}{dJ}$ and $\frac{dn}{dJ}$ as:

$$\begin{aligned} F_L &= U_3 \\ m(F_0,\nu) &= \frac{(F_0-U_3)^2}{4\nu^2} + r(F_0)^{-1} \\ n(F_0,\nu) &= \frac{(U_1-F_0)^2}{4\nu^2} + r(U_1)^{-1} \\ \frac{dm}{dJ} &= -\frac{(F_0-U_3)}{2\nu^2}\cdot\frac{dU_3}{dJ} \\ \frac{dn}{dJ} &= \left[\frac{(U_1-F_0)}{2\nu^2} - r(U_1)^{-2}r'(U_1)\right]\cdot\frac{dU_1}{dJ} \end{aligned}$$

The $\alpha(U_1,\nu)$ and $2\Delta(U_1)$ equations for the IF, are the same, (A.23) and (A.24). But, we have to change some values inside them. This values are:

$$\begin{aligned} F_L &= U_1 \\ m(F_0,\nu) &= \frac{((F_0-U_1))^2}{4\nu^2} + r(F_0)^{-1} \\ n(F_0,\nu) &= \frac{(U_3-F_0)^2}{4\nu^2} + r(U_3)^{-1} \\ \frac{dn}{dJ} &= \left[\frac{(U_3-F_0)}{2\nu^2} - r(U_3)^{-2}r'(U_3)\right]\cdot\frac{dU_3}{dJ} \\ \frac{dm}{dJ} &= -\frac{(F_0-U_1)}{2\nu^2}\cdot\frac{dU_1}{dJ} \end{aligned}$$

The coefficients $\alpha(U_1)$ and $\Delta(U_1)$, facilitates the first approximation of the fronts velocities in the Eq (A.18). If we want a better approximation we must use more active wells in the front profile.

A.8.2 Theory of domain fronts pinning, with several active wells.

As we have explained in the previous appendix, with the coefficients $\alpha(U_1)$ and $\Delta(U_1)$, we can obtain the fronts velocities near the critical currents J_c, *figure A.8-2*.

To obtain the value of this coefficients, we need an initial electric field profile F_i, which are close to the critical current. The number of active wells is defined by the electric field profile which $i=-L,....,M$. For the IF, $F_{-L-1}=U_1$ and $F_M=U_3$. For the DF, $F_{-L-1}=U_3$ and $F_M=U_1$.

Here, the expressions for $\alpha(U_1,\nu)$ and $2\Delta(U_1,\nu)$ are:

$$\begin{aligned}\alpha(U_1,\nu) &= \sum_{i=-L}^{M}\Psi_i + \frac{D(F_{-L})}{2\nu}\Psi_{-L}\frac{dF_{-L-1}}{dJ} + \frac{D(F_M)}{2\nu}\Psi_M\frac{dF_M}{dJ} \\ &-\frac{D(F_{-L})}{4}M(F_{-L},F_{-L-1},\nu)^{-1/2}\Psi_{-L}\frac{dM(F_{-L},F_{-L-1},\nu)}{dJ} \\ &+\frac{D(F_M)}{4}N(F_{M+1},F_M,\nu)^{-1/2}\Psi_M\frac{dN(F_{M+1},F_M,\nu)}{dJ} \\ &-\Psi_{-L}\frac{v(F_{-L})}{2}\left[\frac{1}{2}M(F_{-L},F_{-L-1},\nu)^{-1/2}\frac{dM(F_{-L},F_{-L-1},\nu)}{dJ} - \frac{1}{\nu}\frac{dF_{-L-1}}{dJ}\right]\end{aligned} \tag{A.25}$$

$$\begin{aligned}2\Delta(U_1,\nu) &= \sum_{i=-L}^{M}[\Phi_i^2\begin{pmatrix} -\frac{1}{2}v_i''(M^{\frac{1}{2}}+\frac{F_i-F_{i-1}}{\nu}) - v_i'(\frac{1}{2}M^{\frac{-1}{2}}\frac{dM}{dF_i}+\frac{1}{\nu}) \\ -\frac{1}{2}v_i(-\frac{1}{4}M^{\frac{-3}{2}}\left(\frac{dM}{dF_i}\right)^2+\frac{1}{2}M^{\frac{-1}{2}}\frac{d^2M}{dF_i^2}) - \frac{2}{\nu}D_i' \\ D_i''(\frac{F_{i+1}+F_{i-1}-2F_i}{2\nu}) + \frac{1}{2}D_i''(N^{\frac{1}{2}}-M^{\frac{1}{2}}) \\ +D_i'(\frac{1}{2}N^{\frac{-1}{2}}\frac{dN}{dF_i} - \frac{1}{2}M^{\frac{-1}{2}}\frac{dM}{dF_i}) \\ +\frac{1}{2}D_i(-\frac{1}{4}N^{\frac{-3}{2}}\left(\frac{dN}{dF_i}\right)^2+\frac{1}{2}N^{\frac{-1}{2}}\frac{d^2N}{dF_i^2}+\frac{1}{4}M^{\frac{-3}{2}}\left(\frac{dM}{dF_i}\right)^2-\frac{1}{2}M^{\frac{-1}{2}}\frac{d^2M}{dF_i^2}) \end{pmatrix} \\ &+\Phi_i\Phi_{i+1}\begin{pmatrix}\frac{D_i'}{\nu}+\frac{1}{2}D_i'N^{-\frac{1}{2}}\frac{dN}{dF_{i+1}}+\frac{1}{2}D_iN^{-\frac{1}{2}}\frac{d^2N}{dF_idF_{i+1}} \\ -\frac{1}{4}D_iN^{-\frac{3}{2}}\frac{dN}{dF_{i+1}}\frac{dN}{dF_i}\end{pmatrix} \\ &+\Phi_i\Phi_{i-1}\begin{pmatrix}-v_i'(\frac{1}{2}M^{-\frac{1}{2}}\frac{dM}{dF_{i-1}}-\frac{1}{\nu})+\frac{D_i'}{\nu}+D_i'(-\frac{1}{2}M^{-\frac{1}{2}}\frac{dM}{dF_{i-1}}) \\ -v_i(-\frac{1}{4}M^{-\frac{3}{2}}\frac{dM}{dF_i}\frac{dM}{dF_{i-1}}+\frac{1}{2}M^{-\frac{1}{2}}\frac{d^2M}{dF_idF_{i-1}}) \\ +D_i(\frac{1}{4}M^{-\frac{3}{2}}\frac{dM}{dF_i}\frac{dM}{dF_{i-1}}-\frac{1}{2}M^{-\frac{1}{2}}\frac{d^2M}{dF_idF_{i-1}})\end{pmatrix} \\ &+\Phi_{i+1}\Phi_{i+1}\left(+\frac{1}{2}D_i(-\frac{1}{4}N^{-\frac{3}{2}}\left(\frac{dN}{dF_{i+1}}\right)^2+\frac{1}{2}N^{-\frac{1}{2}}\frac{d^2N}{dF_{i+1}^2})\right) \\ &+\Phi_{i-1}\Phi_{i-1}\begin{pmatrix}-\frac{1}{2}v_i(-\frac{1}{4}M^{-\frac{3}{2}}\left(\frac{dM}{dF_{i-1}}\right)^2+\frac{1}{2}M^{-\frac{1}{2}}\frac{d^2M}{dF_{i-1}^2}) \\ +\frac{1}{2}D_i(\frac{1}{4}M^{-\frac{3}{2}}\left(\frac{dM}{dF_{i-1}}\right)^2-\frac{1}{2}M^{-\frac{1}{2}}\frac{d^2M}{dF_{i-1}^2})\end{pmatrix}]\Psi_i\end{aligned} \tag{A.26}$$

$$\begin{aligned}M(F_i,F_{i-1},\nu) &= (\frac{F_i-F_{i-1}}{\nu})^2+4r(F_i)^{-1} \\ N(F_{i+1},F_i,\nu) &= (\frac{F_{i+1}-F_i}{\nu})^2+4r(F_{i+1})^{-1}\end{aligned}$$

Where Ψ and Φ, are respectively the left and the right eigenvectors of the smallest eigenvalue of the $\frac{dG(F_0,J_c)}{dF}$ matrix, [59].

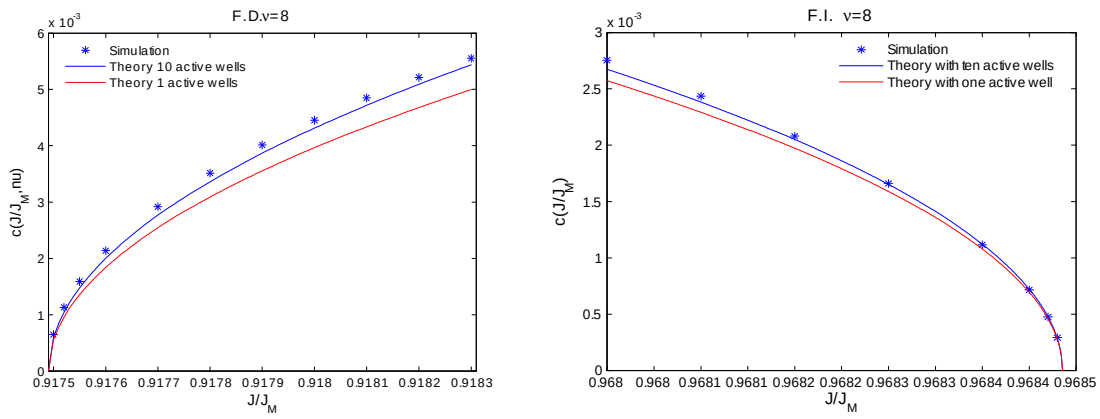

Figure A.8-2 SL $\mathcal{D}$ **(a)** $c(J, \nu = 8)$ for the DF **(b)** $c(J, \nu = 8)$ for the IF.

A.9 Appendix: Graphics and other numerical simulations

In this appendix we summarize some numeric experiments which are interesting to extend the photo-excited SLs theory at dc current bias and dc voltage bias. Let's begin with the numerical simulations in dc current bias:

- In *figure A.9-1* is represented a DF and IF. There are three spatial stable domains in the SL $\mathcal{D}$. The value of β is greater than 1, but with the temporal front motion represented in *figure A.9-1(d)(e)* and *(f)* we can conclude that IF and DF are like $\beta \longrightarrow 0$ fronts theory. The bigger variation of $p_i(t)$ is in the front time period. The voltage is increased in SL because the IF have $c < 0$ and DF $c > 0$. Finally the two fronts collapse because with their movement they "crash" inside of the SL.

- In *figure A.9-2* is also represented a DF and IF, but now the three spatial stable domains in the SL $\mathcal{D}$ are changed. Therefore the IF and the DF positions are also changed. The paths in the phase plane of the IF and DF are the same of the previous simulation (*A.9-1*). The IF still have $c < 0$ and the DF still have $c > 0$. As consequence, in the beginning, the voltage grows in the SL, and finally, the fronts reach to the contacts and the voltage is constant.

- A dipole is represented in *figure A.9-3*. The higher electric field domain is between the two fronts. The IF and the DF have a positive velocities. Initially, the voltage is increasing due to the fronts velocities difference. Finally, the voltage is decreasing due to the IF velocity and because the DF have reached the contact.

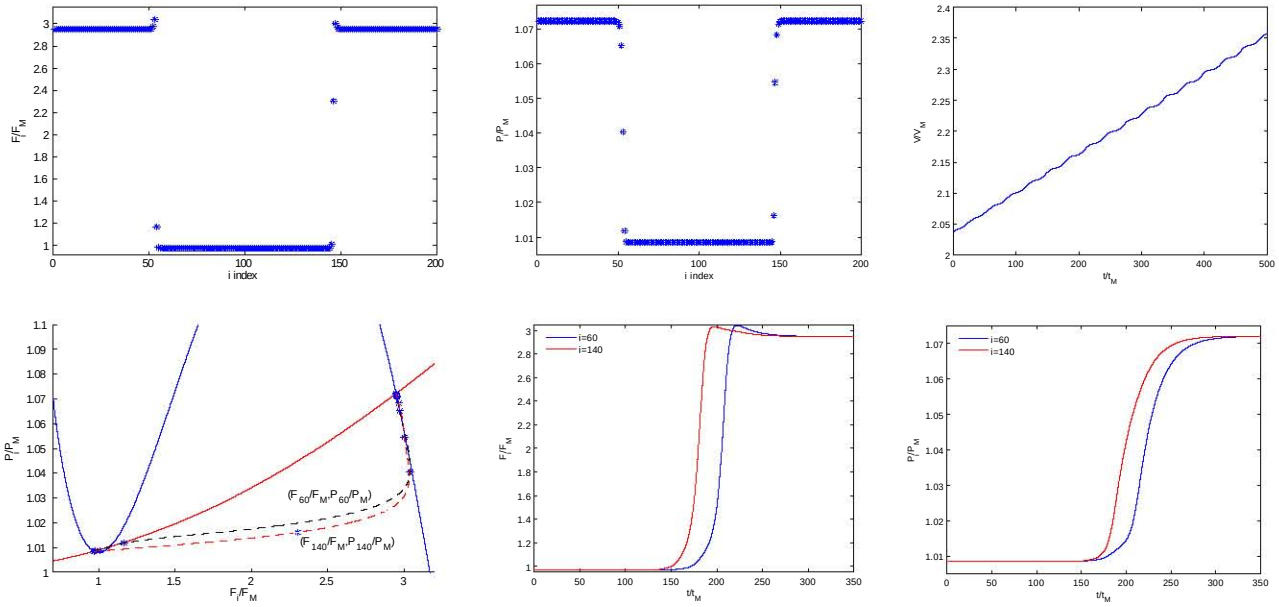

Figure A.9-1 (a)(b) Numerically obtained field and hole profile for a SL $\mathcal{D}$ with $J = 1.009,\ \nu = 226.22$ and $\beta = 44.73$. **(c)** V(t) **(d)** Phase plane showing the nullclines and the motion of two QWs. **(e)(f)** $F_i(t)$ and $P_i(t)$ for the IF and DF.

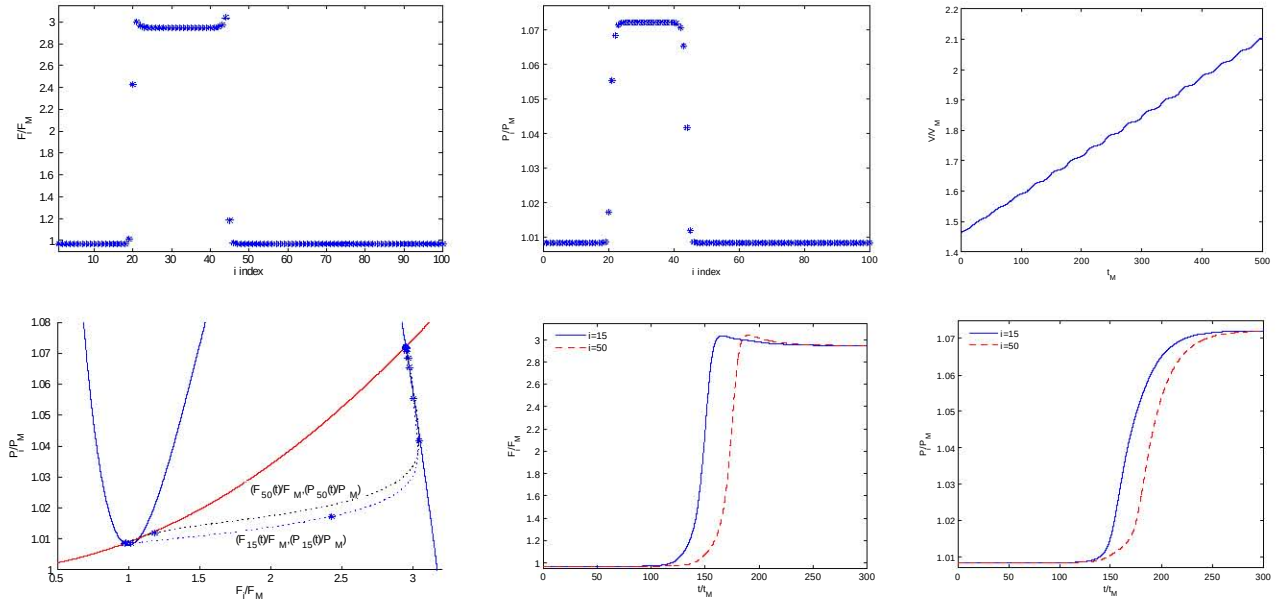

Figure A.9-2(a)(b) Numerically obtained field and hole profile for a SL $\mathcal{D}$ with $J = 1.009,\ \nu = 226.22$ and $\beta = 44.73$.**(c)** V(t) **(d)** Phase plane showing the nullclines and the motion of two QWs. **(e)(f)** $F_i(t)$ and $P_i(t)$ for the IF and DF.

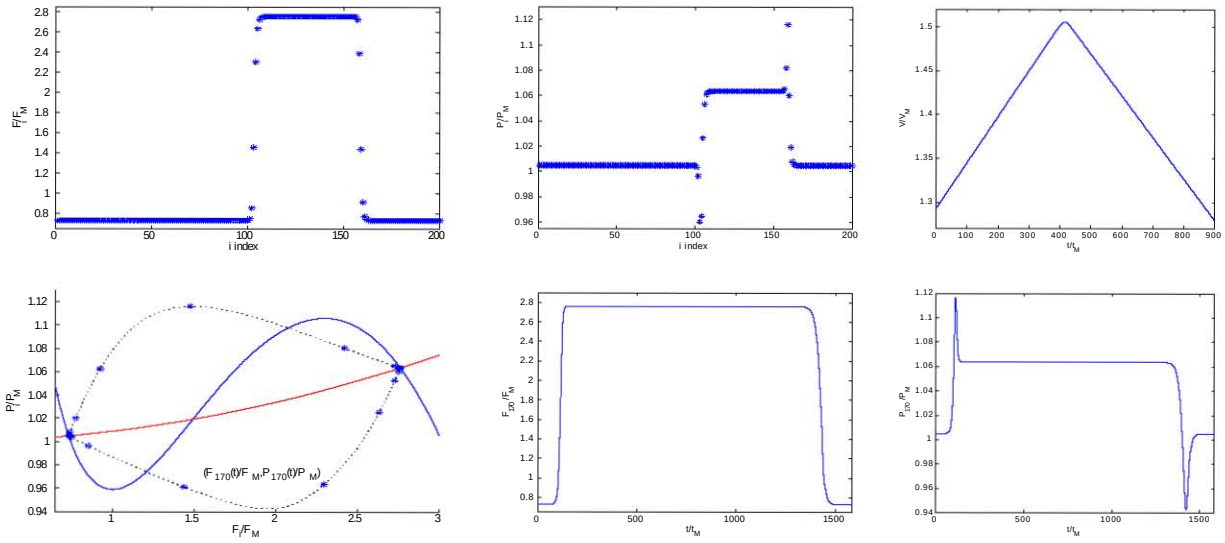

Figure A.9-3 (a)(b) Numerically obtained field and hole profile for a SL $\mathcal{D}$ with $J = 0.96$, $\nu = 5.0645$ and $\beta = 0.282$ **(c)** V(t) **(d)** Phase plane showing the nullclines and the motion of two QWs. **(e)(f)** $F_i(t)$ and $P_i(t)$ for the IF and DF.

- A pulse with a critical point on the third branch is represented in the *figure A.9-4*. This figure is an extension of the numerical simulation exposed in the *figure 5-4(c)(d)*. It is interesting to show how is the pulse tail ending, *figure A.9-4(e)*. The spiral profile (marked with asterisks) is not complete because the pulse is still close to the contact and also the stationary profile is attempting to reach the third homogeneous solution. The path of temporal profile, in the phase plane, of the 160th QW is clearly a spiral. Initially, the voltage is constant due to the similar velocities of the IF and DF. When the IF reach the contact, the voltage is increased. Finally, both fronts reach the contant an the only contribution to voltage is the tail profile variation.

- The *figure A.9-5* is an extension of the numerical simulation exposed in the *figure 5-6.* Is represented an initial SL wave train. Also is represented the stationary profile near the contact which is going to create a new pulse of the wave train. This stationary profile can´t reach the unique critical point of the homogeneous system (A.1)–(A.2) and join the tail (or the peak) solution of the nearest pulse. The voltage value is oscillatory due to the contact pulse creation process and due to the pulse destruction process. The amplitude difference in *figure A.9-5(c)* is due to the shape of the first pulse which reach the contact.

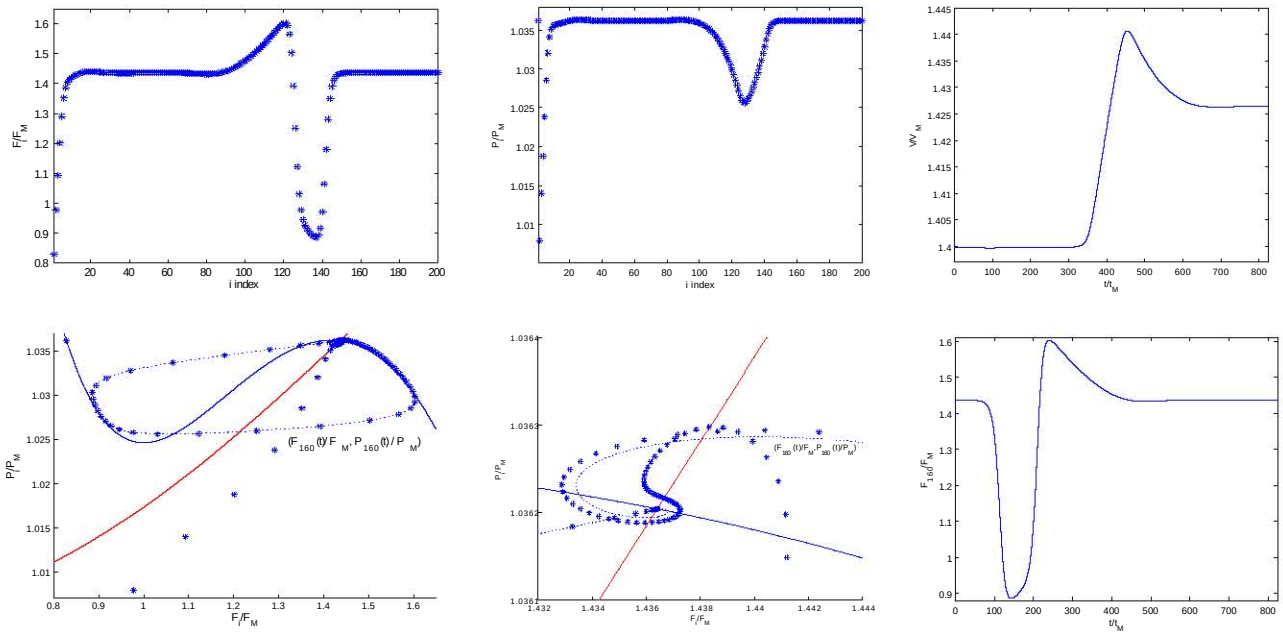

Figure A.9-4 (a)(b) Numerically obtained field and hole profile for a SL $\mathcal{A}$ with $J = 1.0215$, $\nu = 8.44565$ and $\beta = 268.1876$ **(c)** V(t) **(d),(e)** Phase plane showing the nullclines and the motion of the 160th QW. **(f)** $F_{160}(t)$.

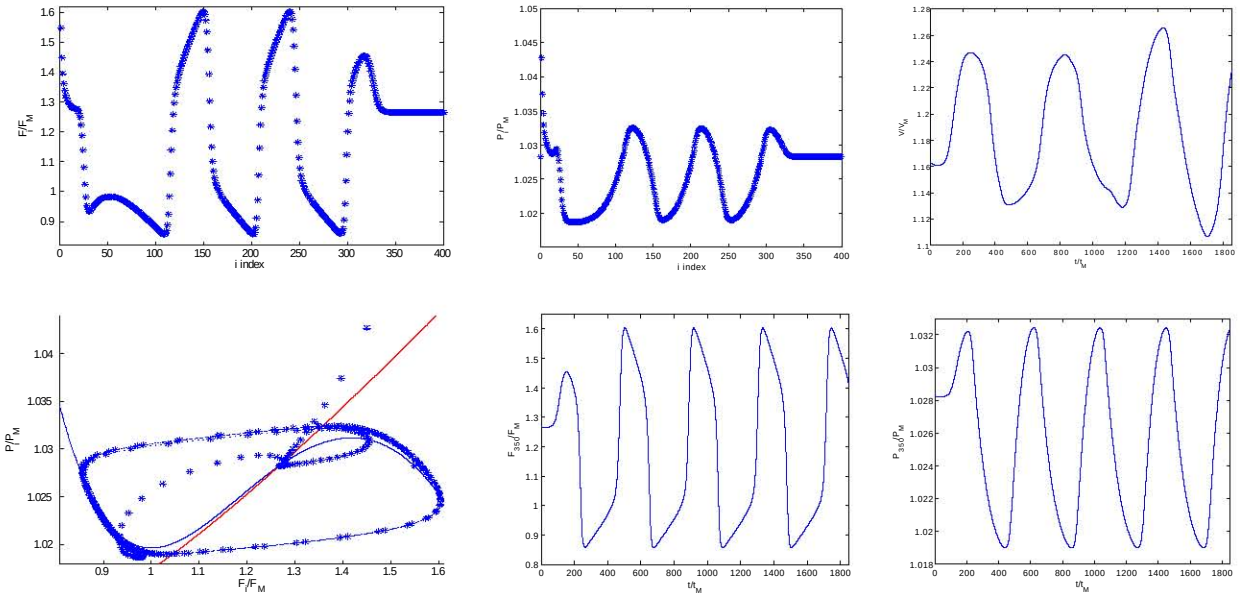

Figure A.9-5 (a)(b) Numerically obtained field and hole profile for a SL $\mathcal{A}$ with $J = 1.0165$, $\nu = 8.44565$ and $\beta = 268.1876$ **(c)** V(t) **(d)** Phase plane showing the nullclines and the motion of the 350th QW **(e)** $F_{170}(t)$ **(f)** $P_{170}(t)$.

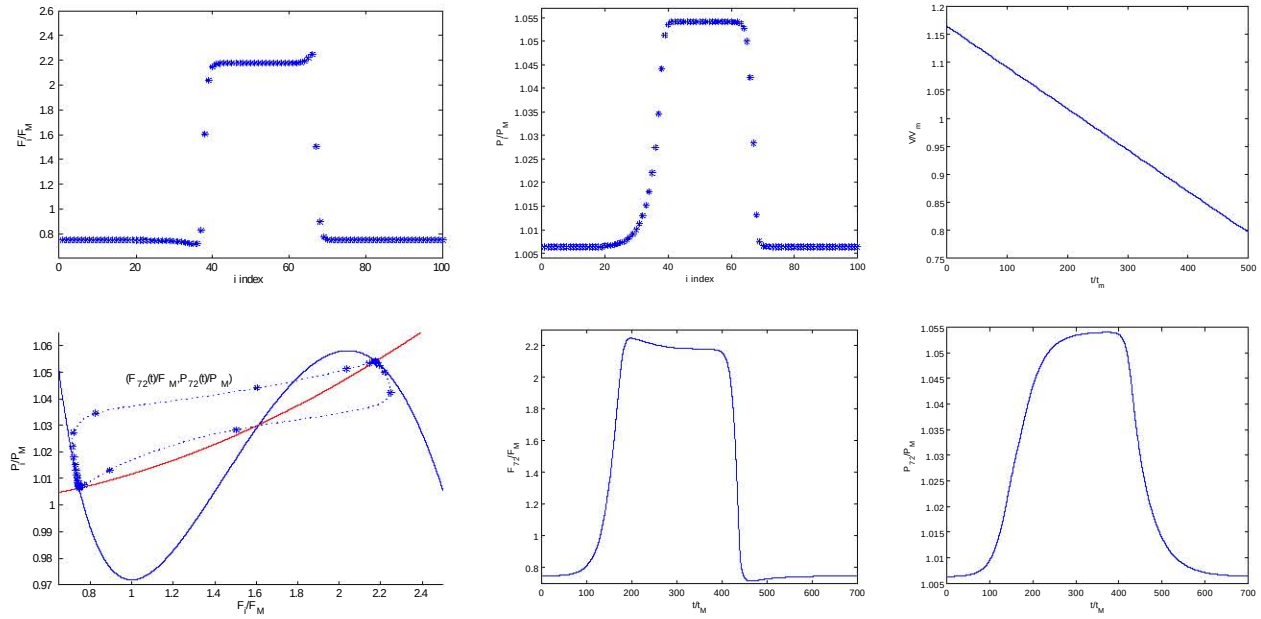

Figure A.9-6 (a)(b) Numerically obtained field and hole profile for a SL $\mathcal{C}$ with $J = 0.97$, $\nu = 18.81$ and $\beta = 91.35$ **(c)** V(t) **(d)** Phase plane showing the nullclines and the motion of the 150th QW **(e)** $F_{150}(t)$ **(f)** $P_{150}(t)$.

- In the *figure A.9-6*, the velocity of the IF is positive and greater than the DF velocity, as consequence the voltage is decreasing in the SL. The DF trayectory over the phase plane is sinuous because is near a critical current. The initial pulse of this simulation don´t reach the contact due to the front velocity difference.

- The *figure A.9-7* and *figure A.9-6* represent a numerical pulse profiles with two stable critical points. The main difference between these pulses are the behavior near the high field domain. In *figure A.9-7*, there is a spiral profile in the third branch near the homogeneous critical point.

- In the *figure A.9-8*, is represented an upstream pulse with negative velocity. The shape of the voltage figure have two stages. In the first stage, the QWs of the SL change fastly their electric profile. Finally, in the second stage the variation of the electric field profile is small, so the voltage variation is not sharp as in the previous stage.

- The asymptotic reconstruction of the two pulses in *figure A.9-9* are precise due to the big value of photoexcitation. But the main difference between *figure A.9-9(a)* and *(c)* is in the IF position. In *figure A.9-9(c)* The IF starts on the second stable homogeneous solution. Instead the figure *A.9-9(a)* there are only one stable homogeneous solution.

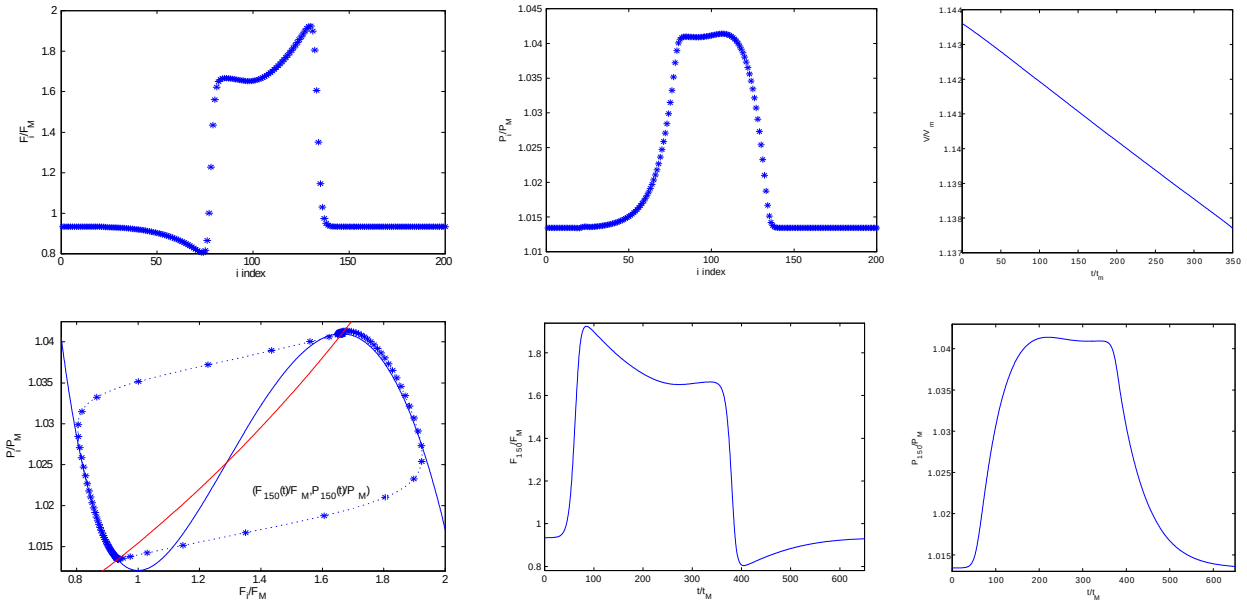

Figure A.9-7 (a)(b) Numerically obtained field and hole profile for a SL $\mathcal{B}$ with $J = 1.009$, $\nu = 8.876$ and $\beta = 155.822$ **(c)** V(t) **(d)** Phase plane showing the nullclines and the motion of the 150th QW **(e)** $F_{150}(t)$ **(f)**$P_{150}(t)$.

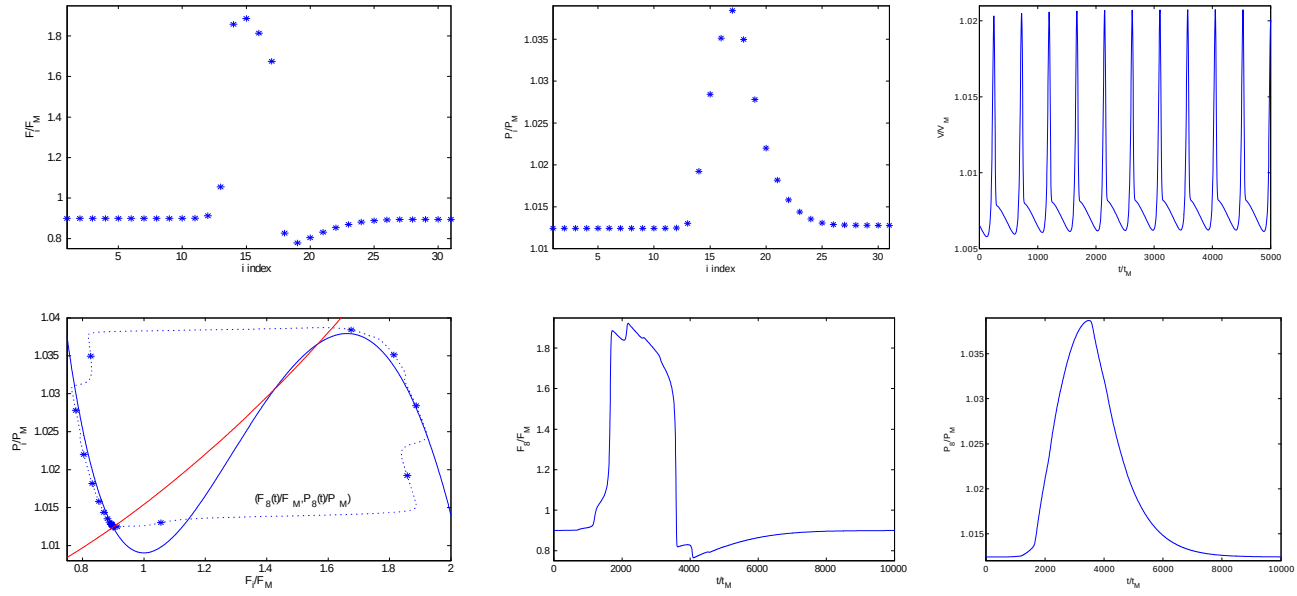

Figure A.9-8 (a)(b) Numerically obtained field and hole profile for a SL $\mathcal{B}$ with $J = 1.006$, $\nu = 70.5$ and $\beta = 2469.6$ **(c)** V(t) **(d)** Phase plane showing the nullclines and the motion of the 8th QW **(e)** $F_8(t)$ **(f)** $P_8(t)$.

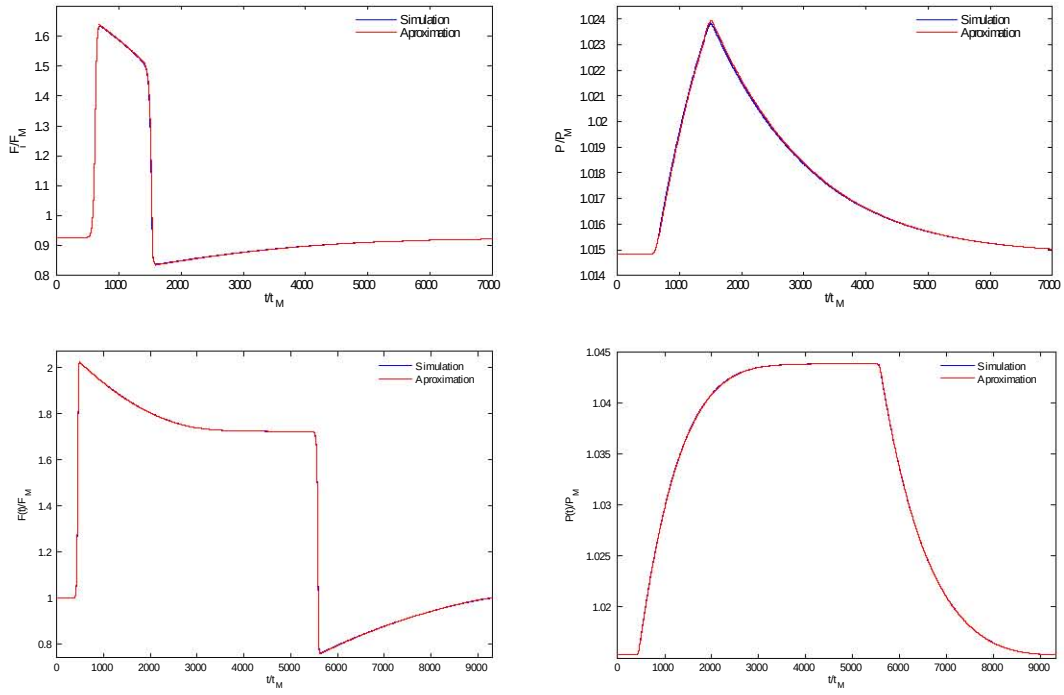

Figure A.9-9 Asymptotic reconstruction of the (a)(c) field and (b)(d) hole concentration (a)(b) for a SL $\mathcal{A}$ with the parameters $J = 1.01$, $\beta = 4250.486$ and $\nu = 67.086$. (c)(d) for a SL $\mathcal{B}$ with the parameters $J = 1.01$, $\beta = 2469.60459$ and $\nu = 70.5$.

The following figures are some of the numerical simulations, in dc voltage bias, which we have studied and we have considered interesting to notice in the content exposed in the chapter 6:

- In the *figure A.9-10,* is represented a SL $\mathcal{A}$ SSCOs mediated by a single pulse. Initially, when the pulse is starting to be regenerated in the contact, the instantaneous value of the current places the unique homogeneous solution of Eq 4.32 on the second branch. The QWs located in the tail SL structure, change their electric field trying to reach the third branch. After the sharp variation of the current, some of the QWs are located in the regenerated pulse and others QWs returns to the first branch.

- The values of the simulation parameters are the same in the *figure A.9-10* and in the *figure A.9-11* with the exception of the σ_1 conductivity. The shape of the both SSCOs are similar but ligthly greater in the *figure A.9-10.* The stationary profile near the contact is greater in *figure A.9-11.*

- In the *figure A.9-12,* is represented a SL $\mathcal{B}$ SSCOs mediated by a single pulse. The stationary solution close to the contact and the tail pulse structure makes a NP. When the stationary

solution close to the contact, is deformed in the phase plane due to the current variation, the NP starts the creation of the new pulse. The QWs near the NP travels over the phase plane but they never reach the third branch. Until the initial pulse is more far away from the contact the pulse is not complete in the phase plane. See the *figure A.9-12(c).*

- The values of the simulation parameters are the same in the *figure A.9-12* and in the *figure A.9-13* with the exception of the σ_1 conductivity. The shape of the both SSCOs are similar but have some differences. $J(t)$ of the *figure A.9-13* have lower values and is more smooth in the pulse propagation period inside the SL.

- In the *figure A.9-14*, there are initially two fronts moving in the opposite directions. The DF is fastly pinned due to the current variation. The shape of the current is like a "down staircase" due to the IF movement which only have one active well.

- *Figure A.9-15, figure A.9-16 and figure A.9-17* have the same simulation parameters, that *figure A.9-12 and figure A.9-13* have, with the exception of the σ_1 conductivity and the QW number N. The shape of SSCOs is different but they have similarities. The position of the NP is regulated by the contact conductivity, in the *figure A.9-15* the NP is around the middle of the SL.

- The pinning of the IF in dc voltage bias is represented in *figure A.9-18.* Initially the IF have positive velocity, but as time goes on the velocity is reduced to zero. The β parameter is greater than 1, but the hole profile is like the $\beta \longrightarrow 0$ fronts.

- In the figures *A.9-19* and *A.9-20,* there are upstream and downstream pulses. Due to the instantaneous $J(t)$ value, the upstream pulses can be nucleated or not.

- The homogeneous solution of Eq 4.32, in *figure A.9-22*, is in the second branch most of the time. There are two pulses inside the SL, they change their velocity and their height due to the pulse creation-destruction process.

- The SSCOs of the *figure A.9-23* have a lot of sharp peaks due to the movement of the pulse fronts. When the DF reach the anode, the IF change its velocity until a new pulse is generated in the cathode.

- In *figure A.9-25,* is represented a SL $\mathcal{A}$ SSCOs mediated by a two pulses of the first branch. When one pulse reach the anode, other pulse is starting to be generated in the cathode. During the elapsed time in the new pulse generation, the central pulse expands himself to compensate the loss of voltage.

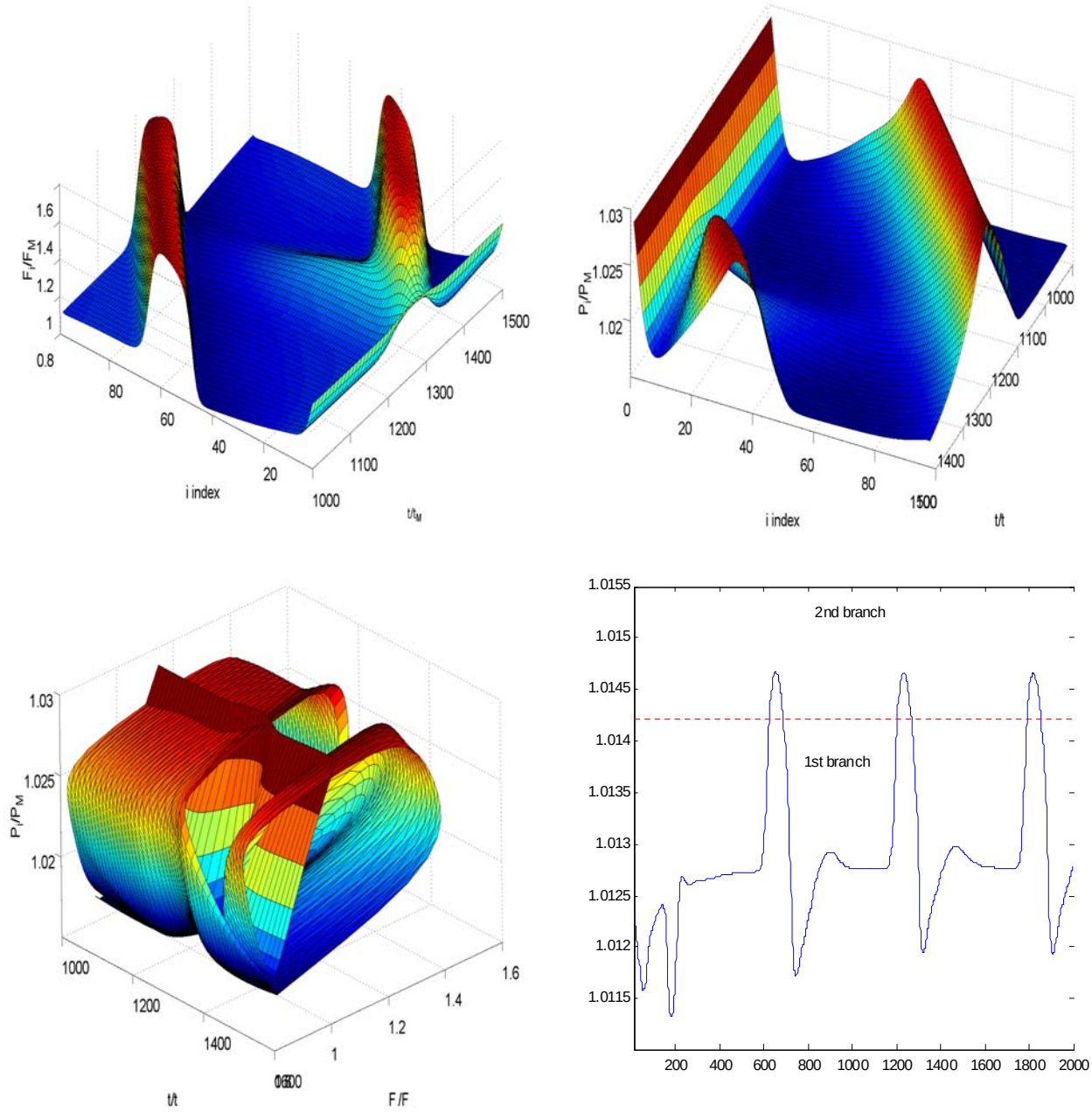

Figure A.9-10 SL $\mathcal{A}$ with parameters $\mathbf{V}$ =1.00417, $\beta = 268.18757$, $\nu = 8.44565$, $\sigma_2 = 1.05231$, $N = 99$ and $\sigma_1 = 0.83413$.(a) $F_i(t)$(b) $P_i(t)$(c) $P(F,t)$(d) $J(t)$.

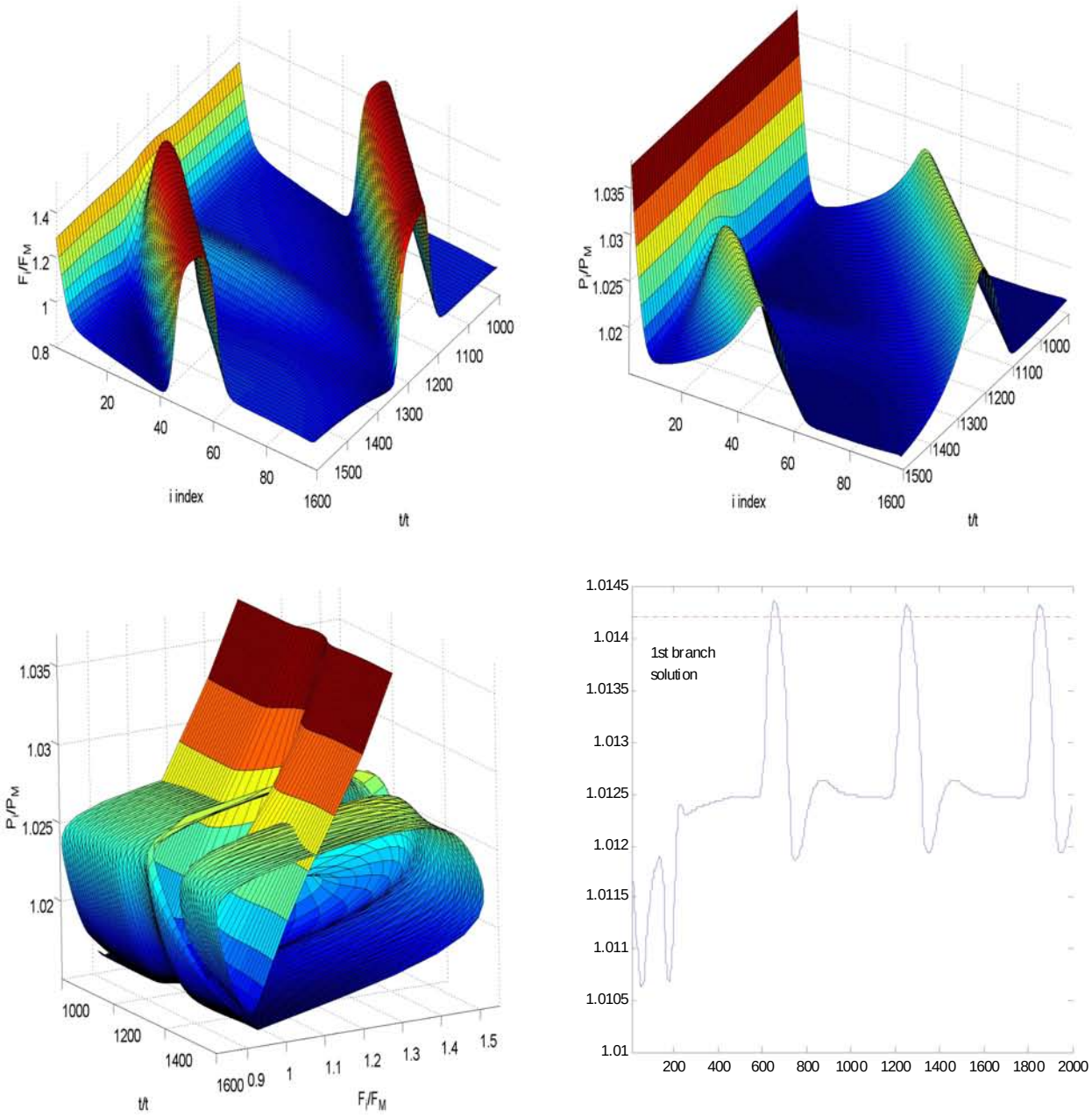

Figure A.9-11 SL $\mathcal{A}$ with parameters $\mathbf{V}$ =1.00417, $\beta = 268.18757$, $\nu = 8.44565$, $\sigma_2 = 1.05231$, $\mathbf{N}$ =99 and $\sigma_1 = 0.73075$.(a) $F_i(t)$ (b) $P_i(t)$ (c) $P(F,t)$ (d)$J(t)$.

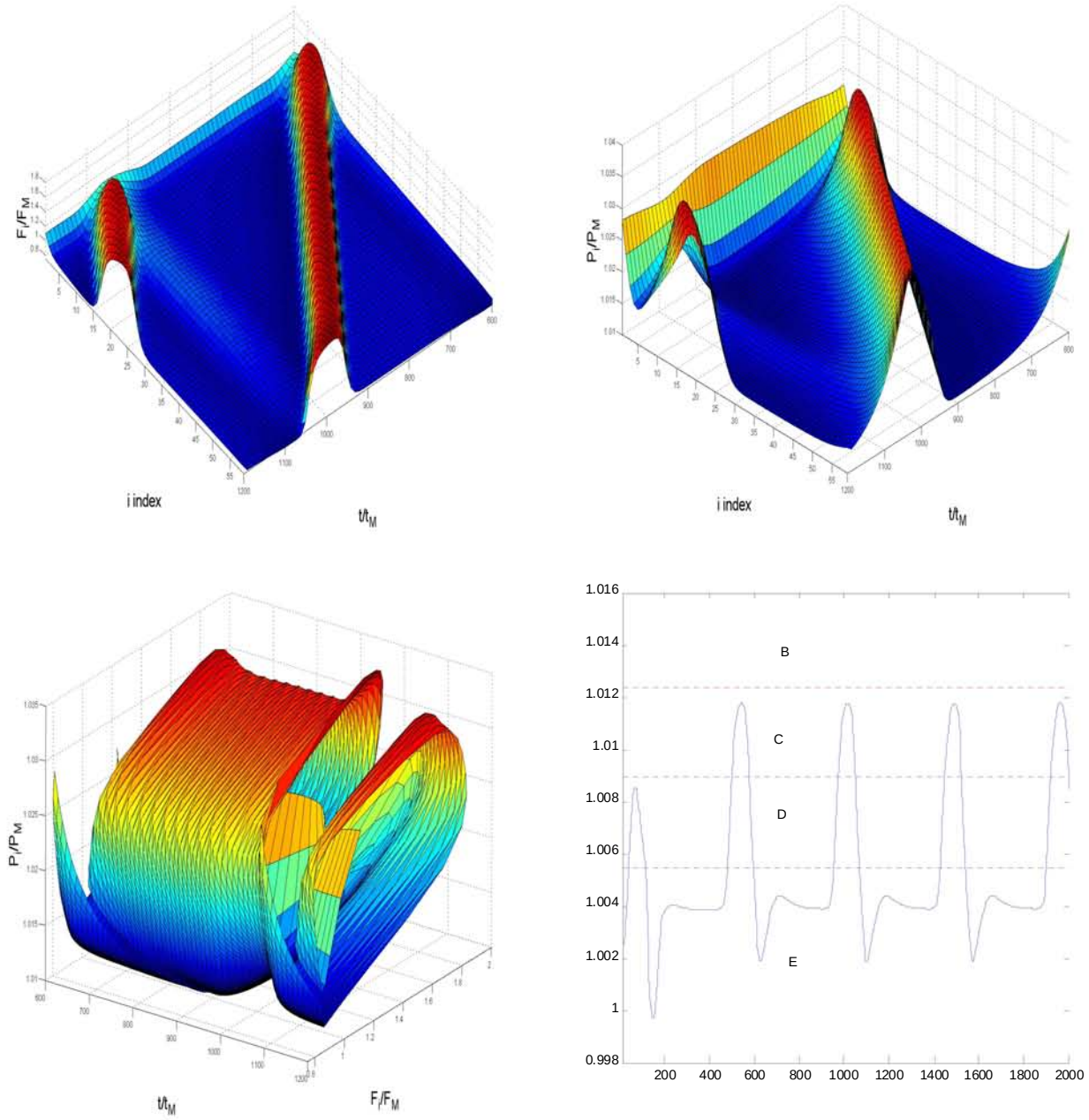

Figure A.9-12 SL $\mathcal{B}$ with parameters $\mathbf{V}$ =1.009998, $\beta = 155.82152$, $\nu = 8.87628$, $\sigma_1 = 0.79632$, $\sigma_2 = 1.08297$ and $\mathbf{N}$ =61.(a) $F_i(t)$ (b) $P_i(t)$ (c) $P(F,t)$ (d) $J(t)$.

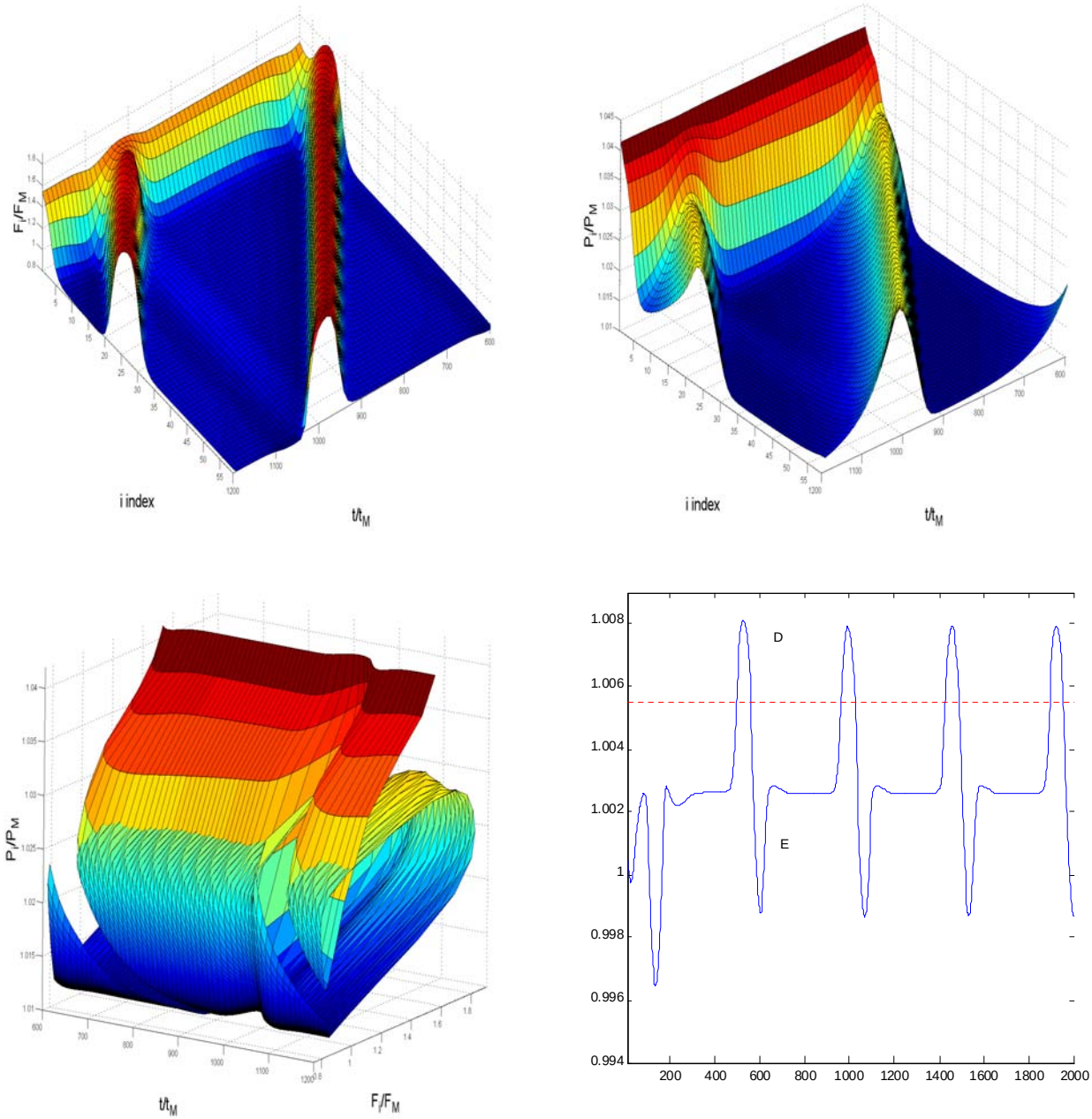

Figure A.9-13 SL $\mathcal{B}$ with parameters $\mathbf{V}$ =1.009998, $\beta = 155.82152$, $\nu = 8.87628$, $\sigma_2 = 1.08297$, $\mathbf{N}$ =61 and $\sigma_1 = 0.62168$.(a) $F_i(t)$ (b) $P_i(t)$ (c) $P(F,t)$ (d) $J(t)$.

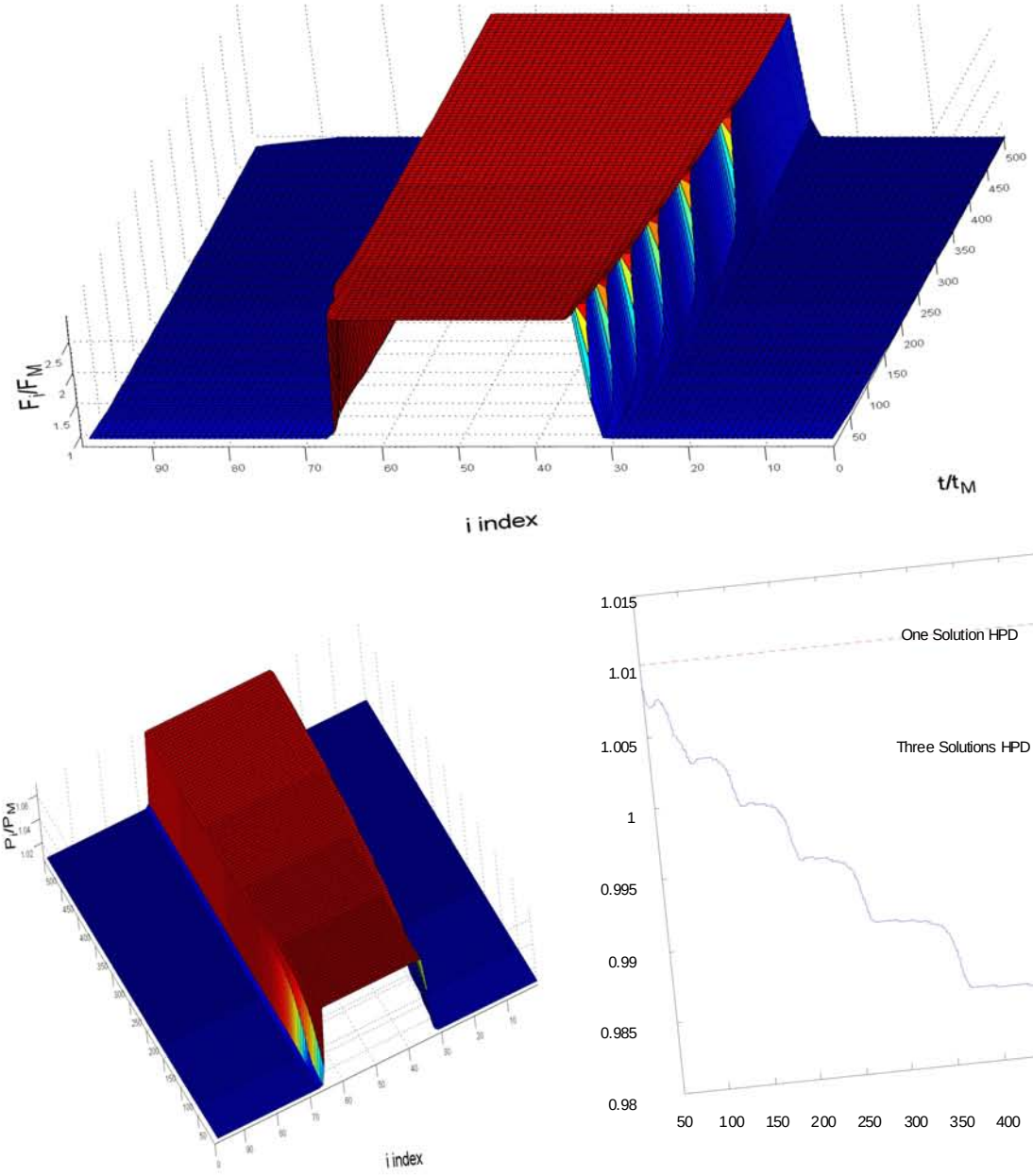

Figure A.9-14 SL$^{1M}\mathcal{D}$ with parameters $N = 100$, $\beta = 70.8989$, $\nu = 319.549$, $\sigma_2 = 1.31483$, $\sigma_1 = 1.2959$ and $\mathbf{V}$ =1.56435.(a) $F_i(t)$ (b) $P_i(t)$ (c) $J(t)$.

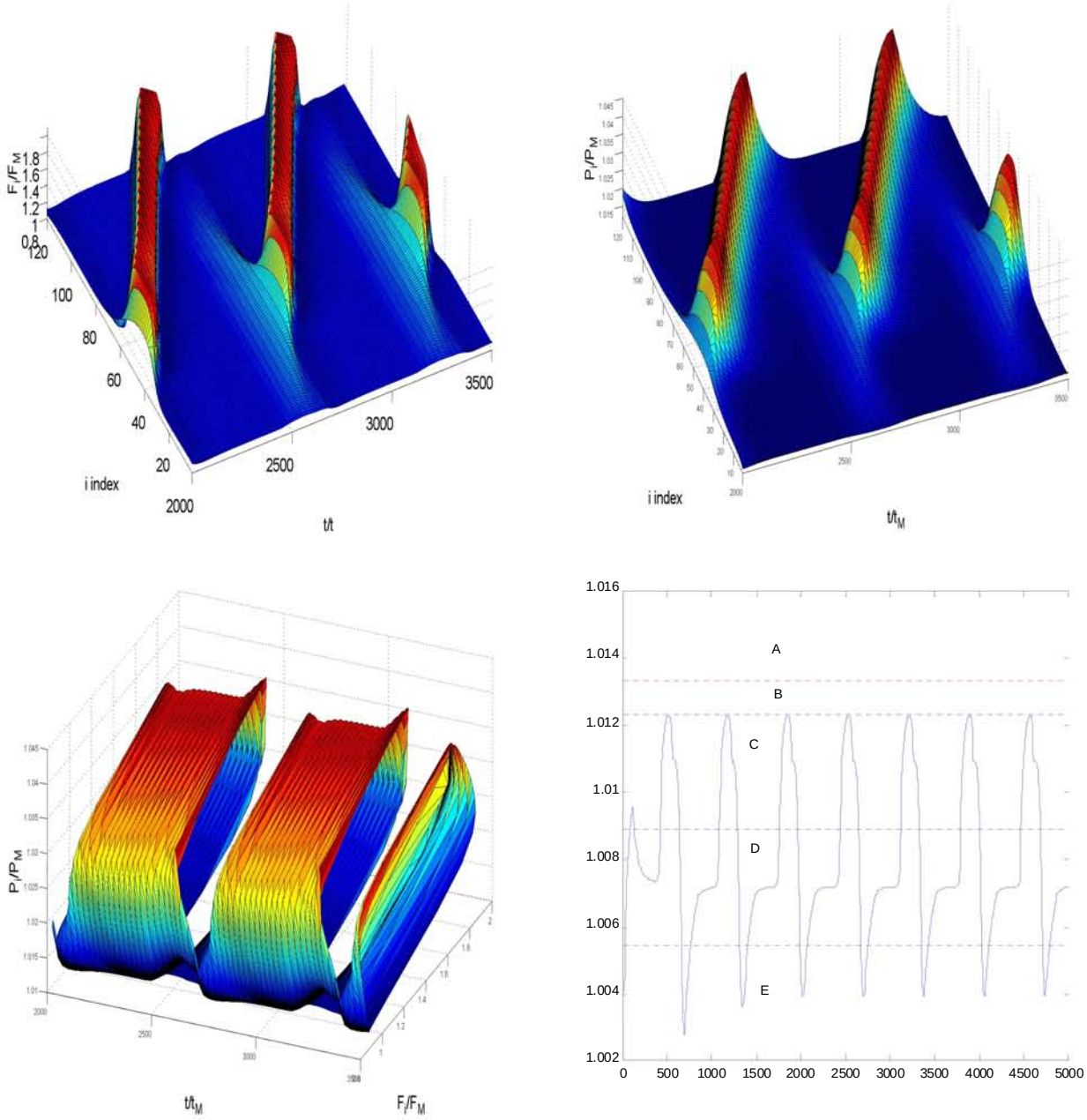

Figure A.9-15 SL $\mathcal{B}$ with parameters $\mathbf{V}$ =1.009998, $\beta = 155.82152$, $\nu = 8.87628$, $\sigma_2 = 1.08297$, $\mathbf{N}$ =123 and $\sigma_1 = 1.107398$ (a) $F_i(t)$ (b) $P_i(t)$ (c) $P(F,t)$ (d)$J(t)$

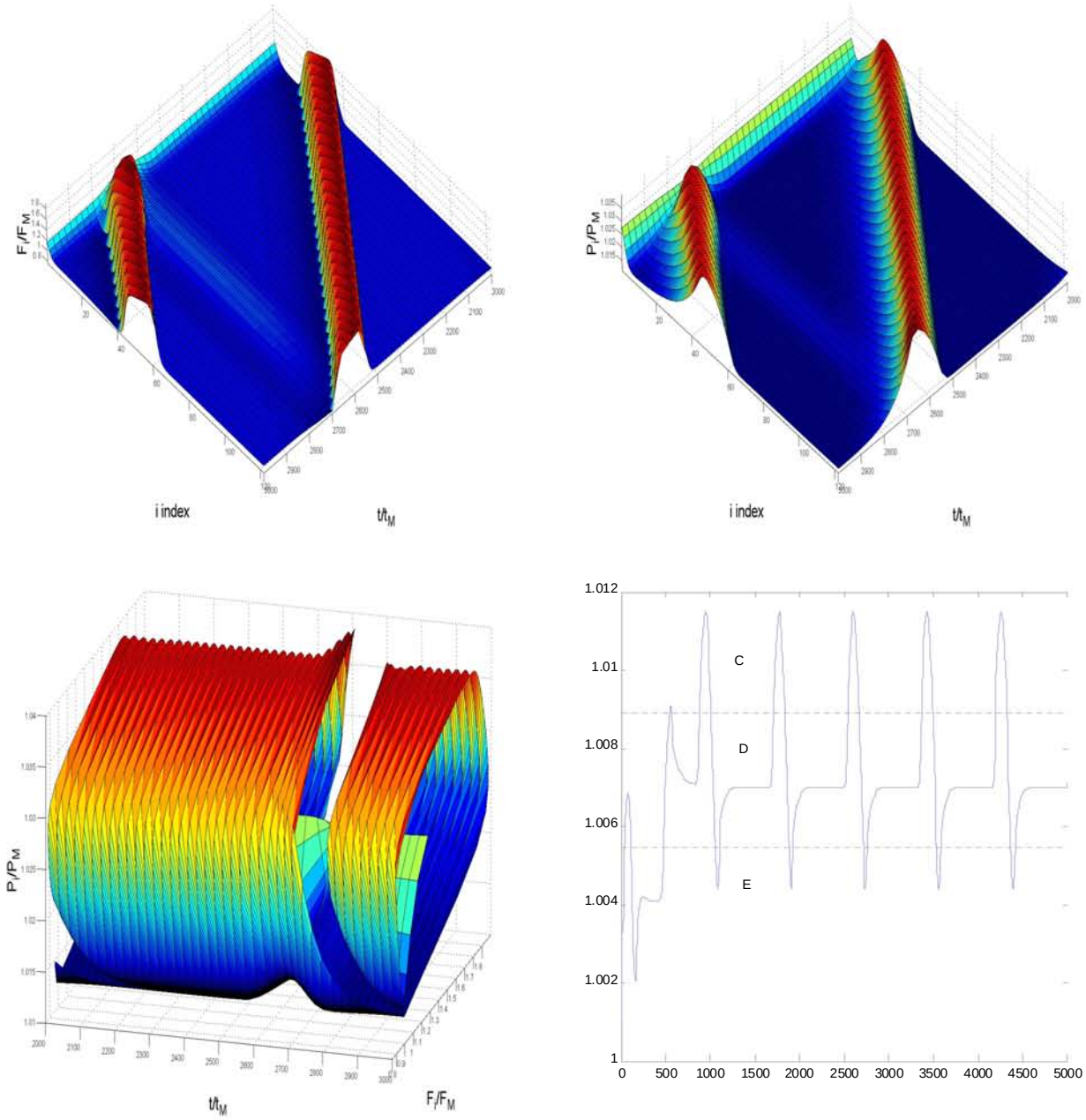

Figure A.9-16 SL $\mathcal{B}$ with parameters $\mathbf{V}$ =1.009998, $\beta = 155.82152$, $\nu = 8.87628$, $\sigma_2 = 1.08297$, $\mathbf{N}$ =123 and $\sigma_1 = 0.79632$.(a) $F_i(t)$ (b) $P_i(t)$ (c) $P(F,t)$ (d) $J(t)$.

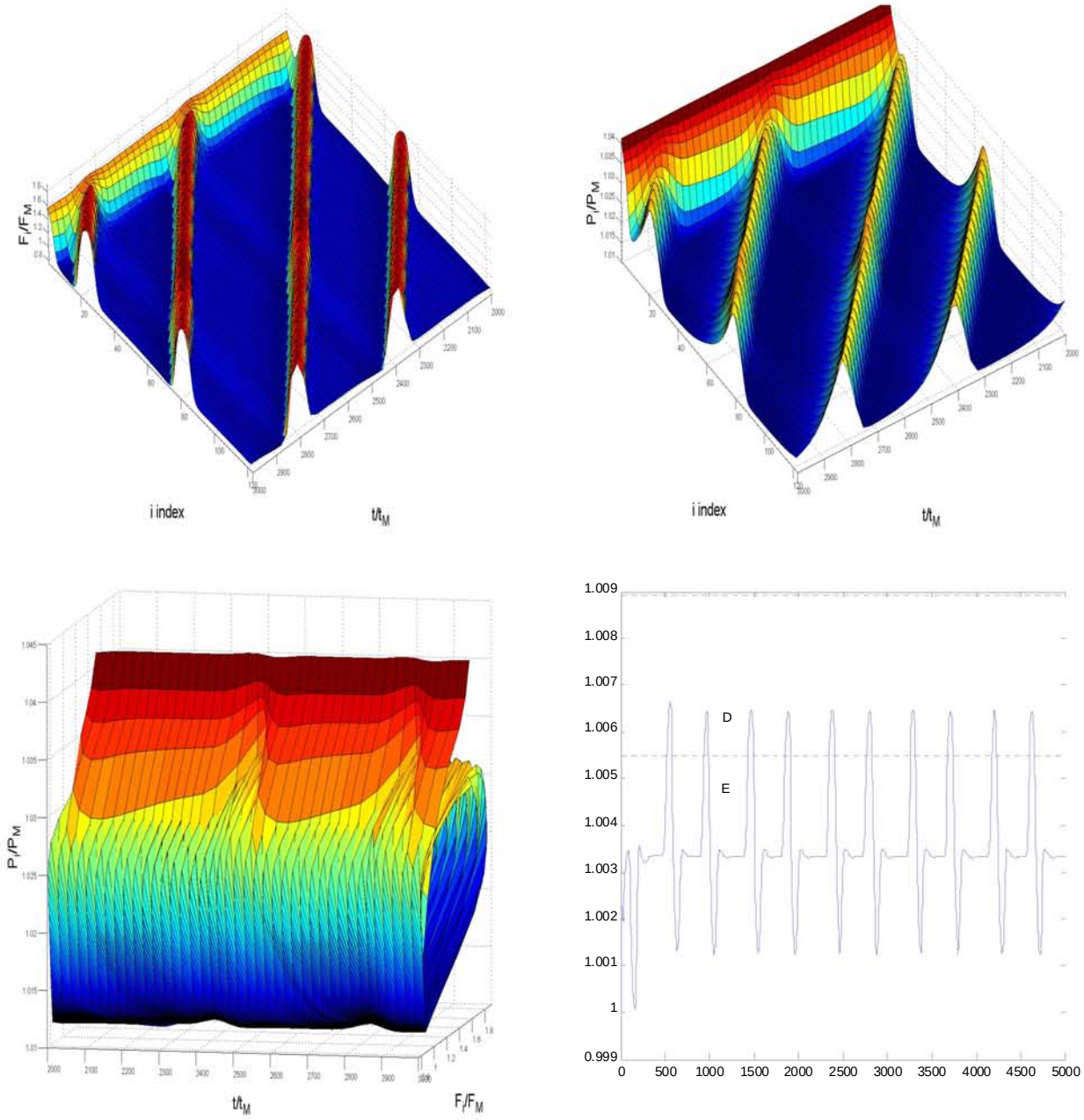

Figure A.9-17 SL $\mathcal{B}$ with parameters $\mathbf{V}$ =1.009998, $\beta = 155.82152$, $\nu = 8.87628$, $\sigma_2 = 1.08297$, $\mathbf{N}$ =123 and $\sigma_1 = 0.62168$.(a) $F_i(t)$ (b) $P_i(t)$ (c) $P(F,t)$ (d) $J(t)$.

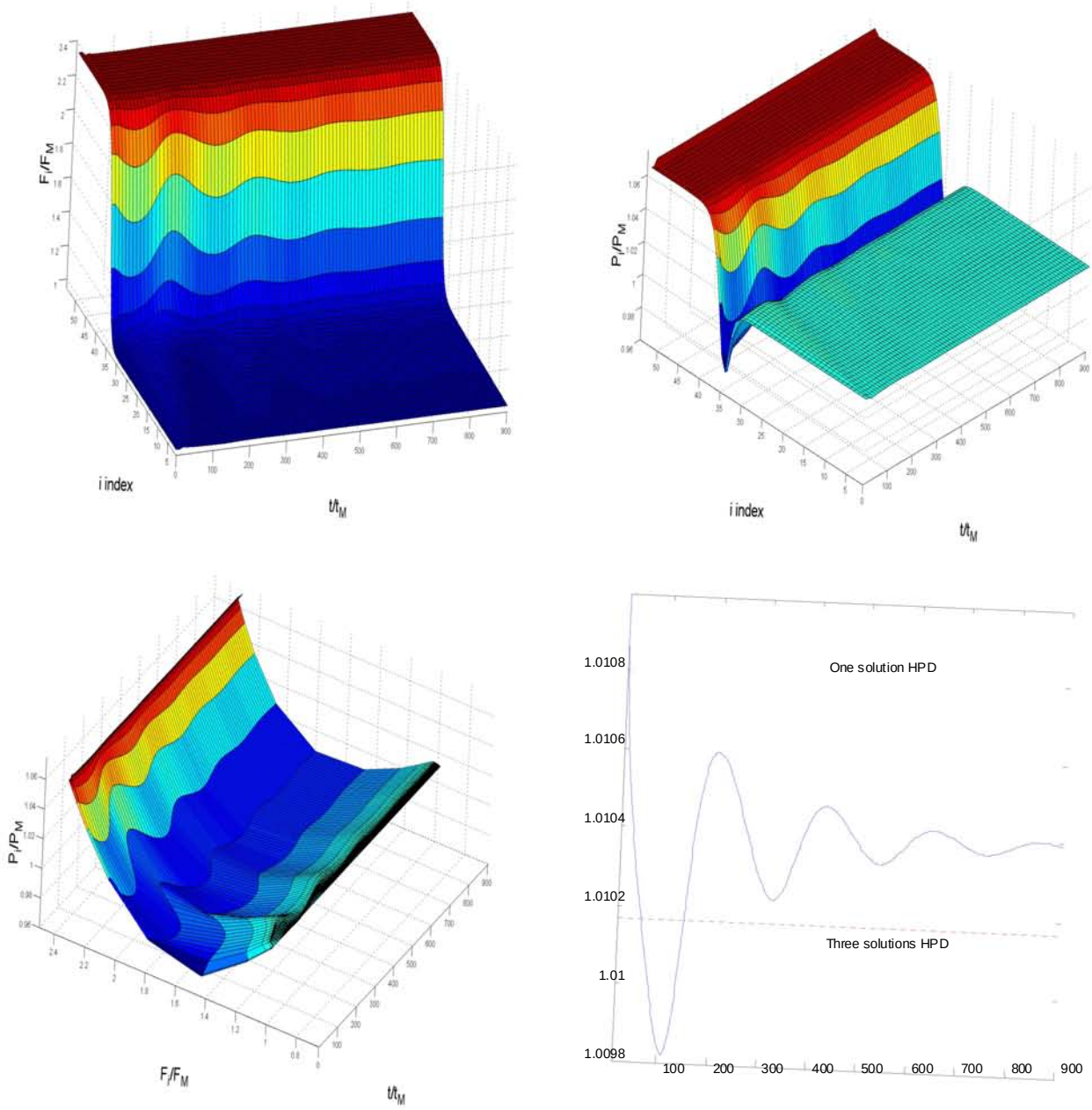

Figure A.9-18 SL $\mathcal{C}$ with parameters $\mathbf{N} = \mathbf{55}$, $\beta = 7.5985$, $\nu = 2.9138$, $\mathbf{V}$ =1.47276, $\sigma_1 = 1.0264$ and $\sigma_2 = 1.00429$.(a) $F_i(t)$ (b) $P_i(t)$ (c) $P(F,t)$(d) $J(t)$.

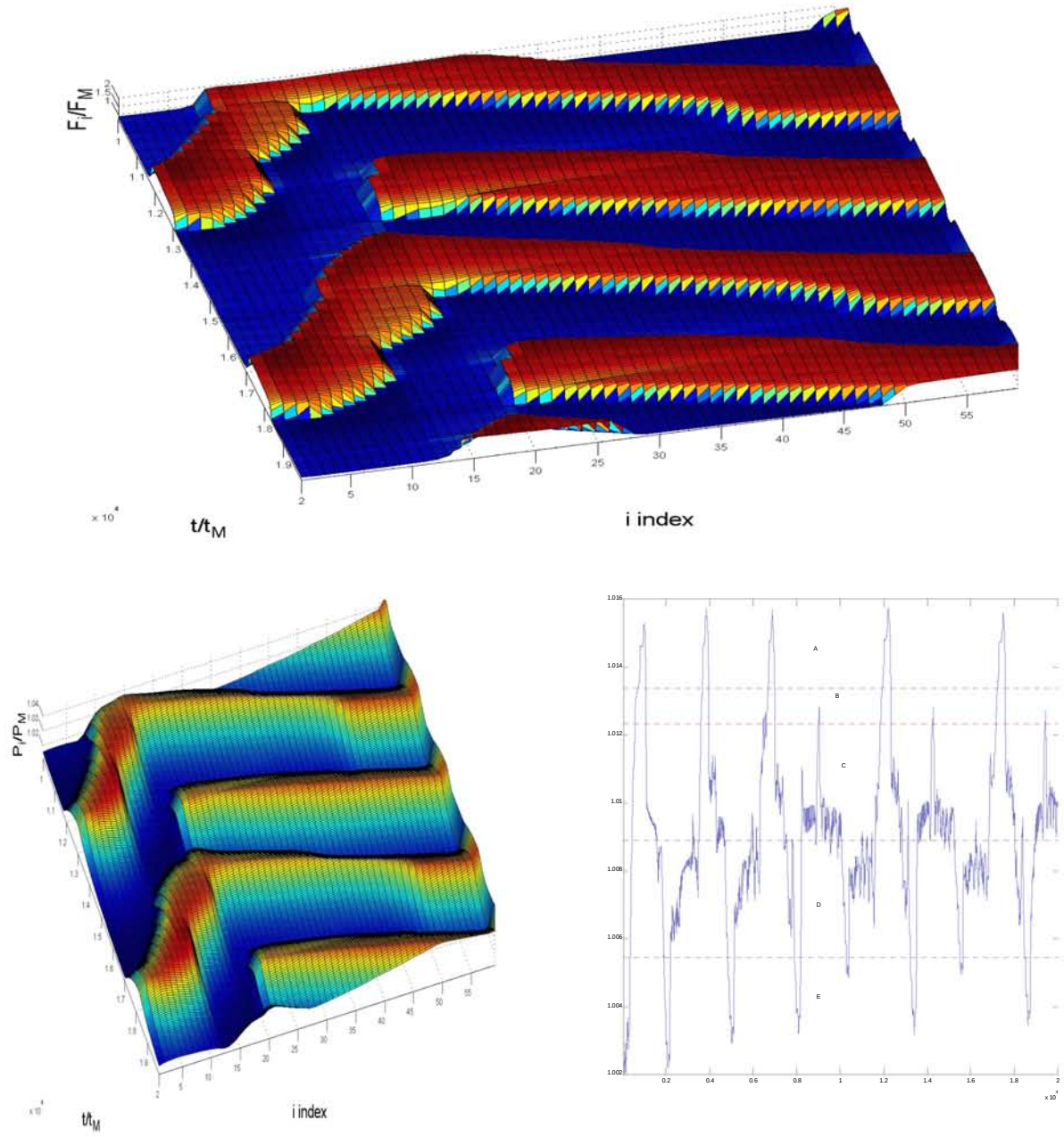

Figure A.9-19 SL $\mathcal{B}$ with parameters $\beta = 2469.6$, $\nu = 70.50677$, $\mathbf{V}$ =1.26985, $\sigma_1 = 1.107398$, $\sigma_2 = 0.3$ and $\mathbf{N} = \mathbf{61}$.(a) $F_i(t)$ (b) $P_i(t)$ (c)$J(t)$.

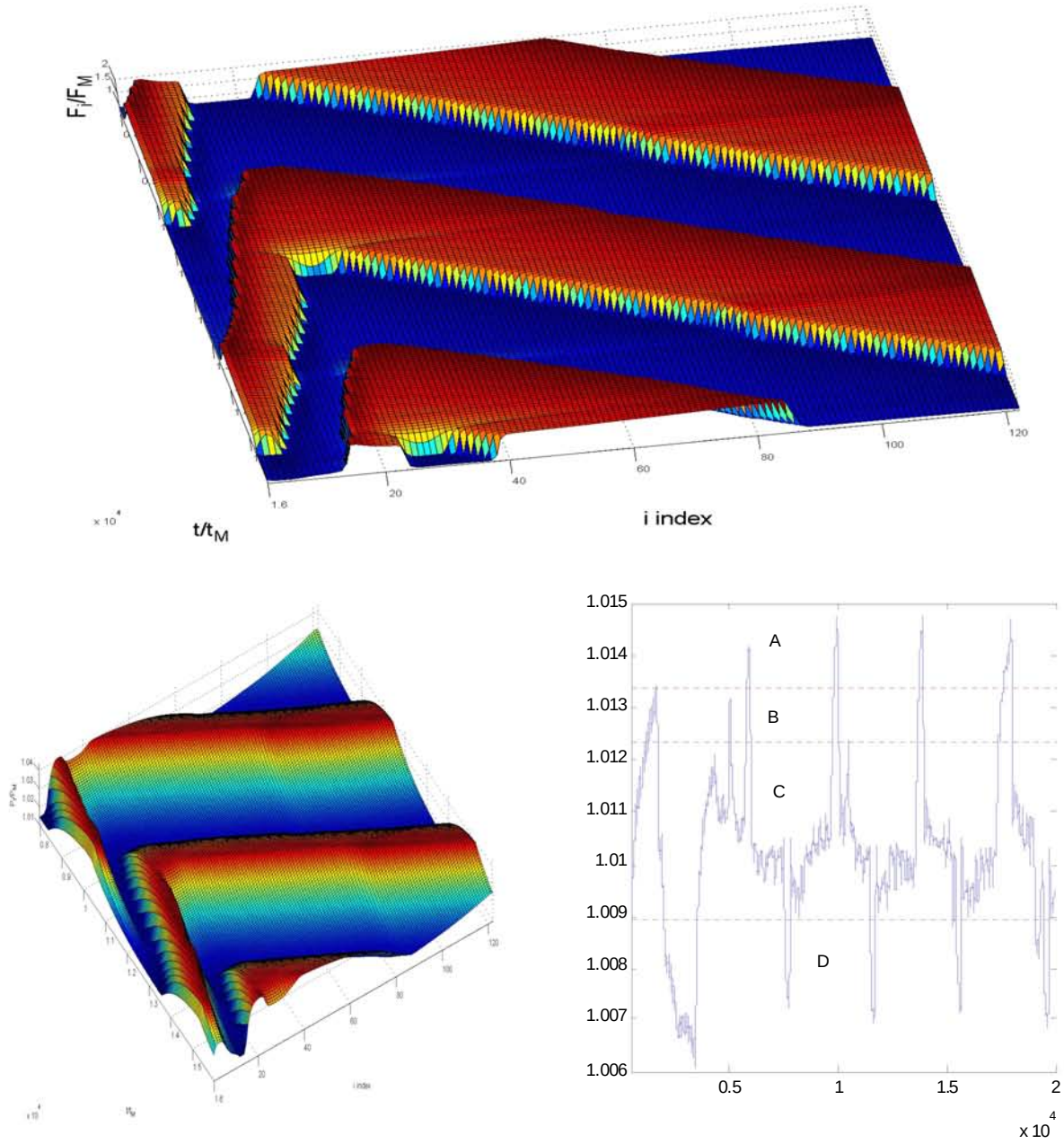

Figure A.9-20 SL $\mathcal{B}$ with parameters $\beta = 2469.6$, $\nu = 70.50677$, $\mathbf{V}$ =1.26985, $\sigma_1 = 1.107398$, $\sigma_2 = 1.08297$ and $\mathbf{N} = \mathbf{123}$.(a) $F_i(t)$ (b) $P_i(t)$ (c) $J(t)$.

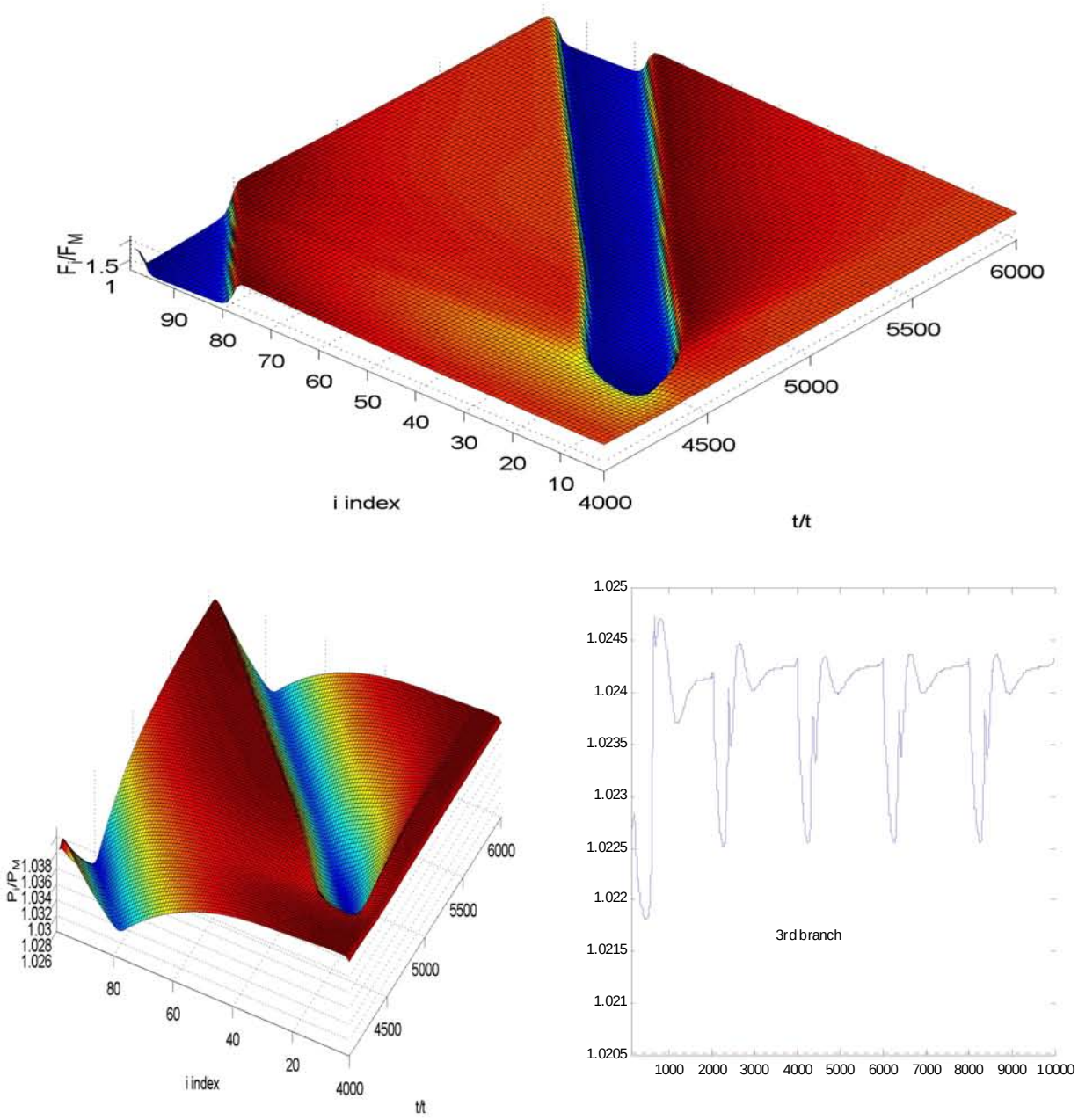

Figure A.9-21 SL$\mathcal{A}$ with parameters $N = 99,\ \beta = 1692.1491,\ \nu = 33.62275,\ \sigma_1 = 1.05231,$ $\sigma_2 = 0.73075$ and $\mathbf{V}$ =1.35479.(a) $F_i(t)$(b) $P_i(t)$ (c) $J(t)$.

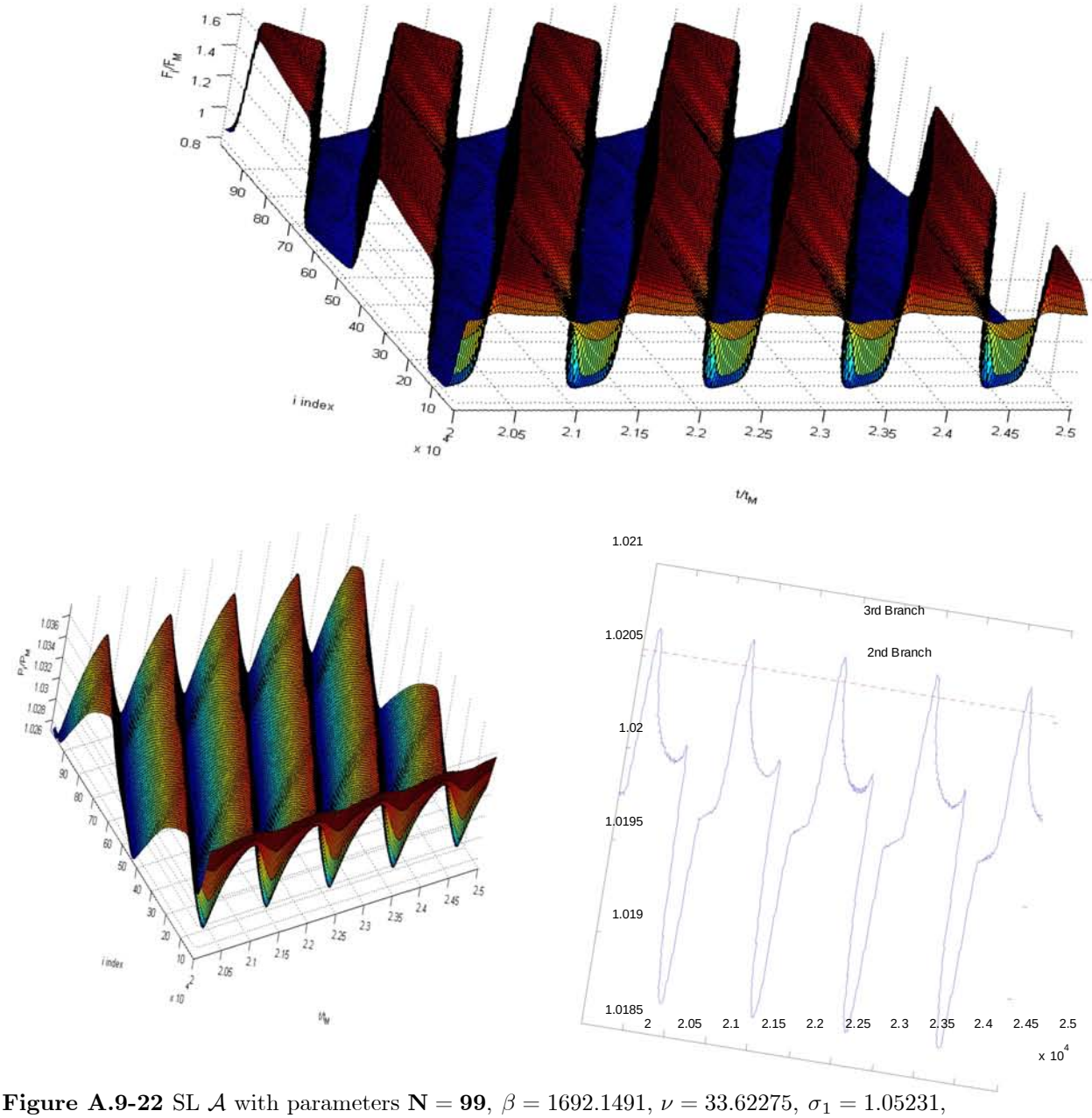

Figure A.9-22 SL $\mathcal{A}$ with parameters $\mathbf{N} = \mathbf{99}$, $\beta = 1692.1491$, $\nu = 33.62275$, $\sigma_1 = 1.05231$, $\sigma_2 = 0.73075$ and $\mathbf{V}$ =1.22732. (a) $F_i(t)$ (b) $P_i(t)$ (c) $J(t)$.

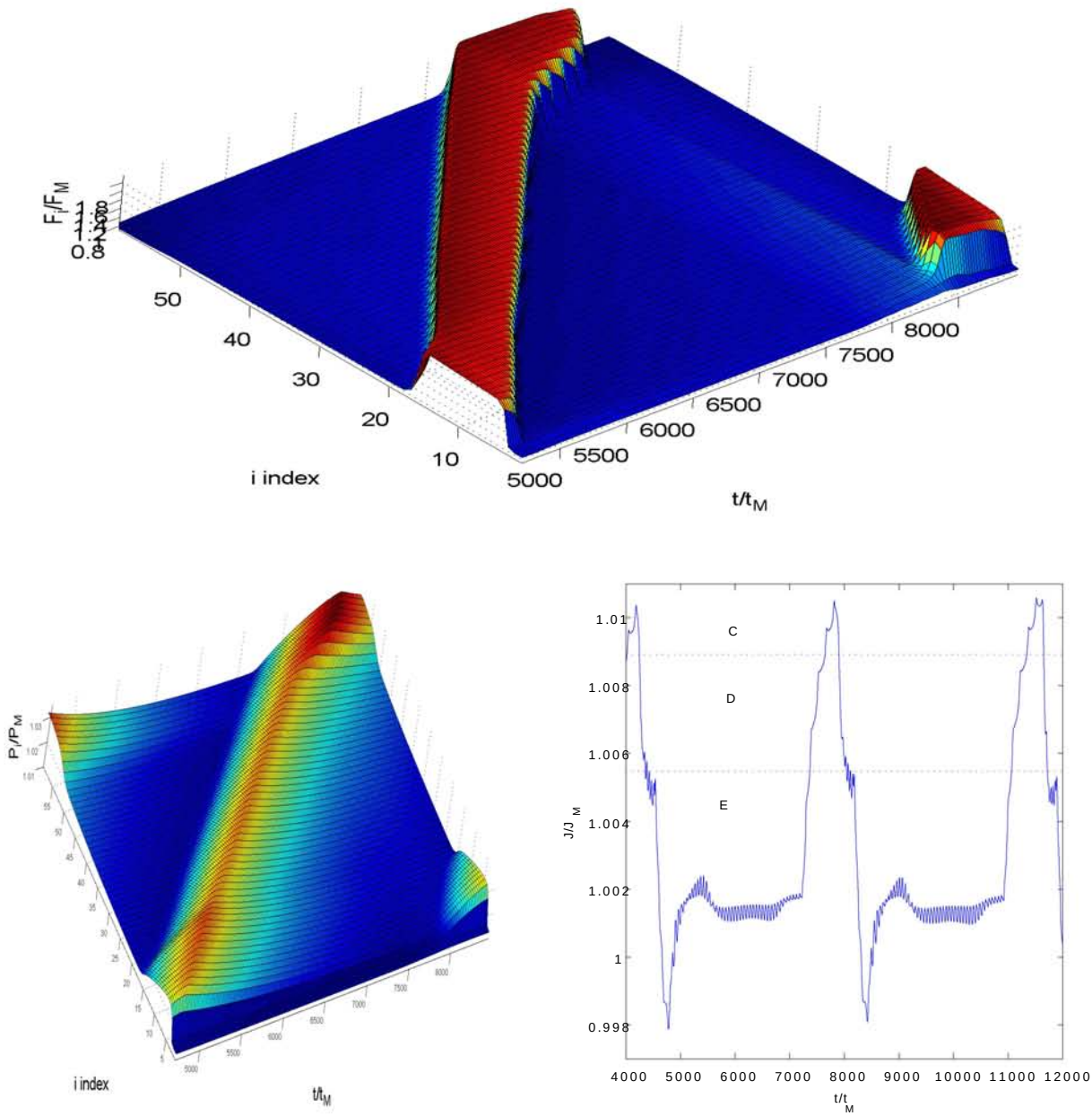

Figure A.9-23 SL $\mathcal{B}$ with parameters $\mathbf{V}$ =1.009998, $\beta = 2469.6$, $\nu = 70.5$, $\sigma_2 = 1.08297$, $\mathbf{N}$ =61 and $\sigma_1 = 1.107398$.

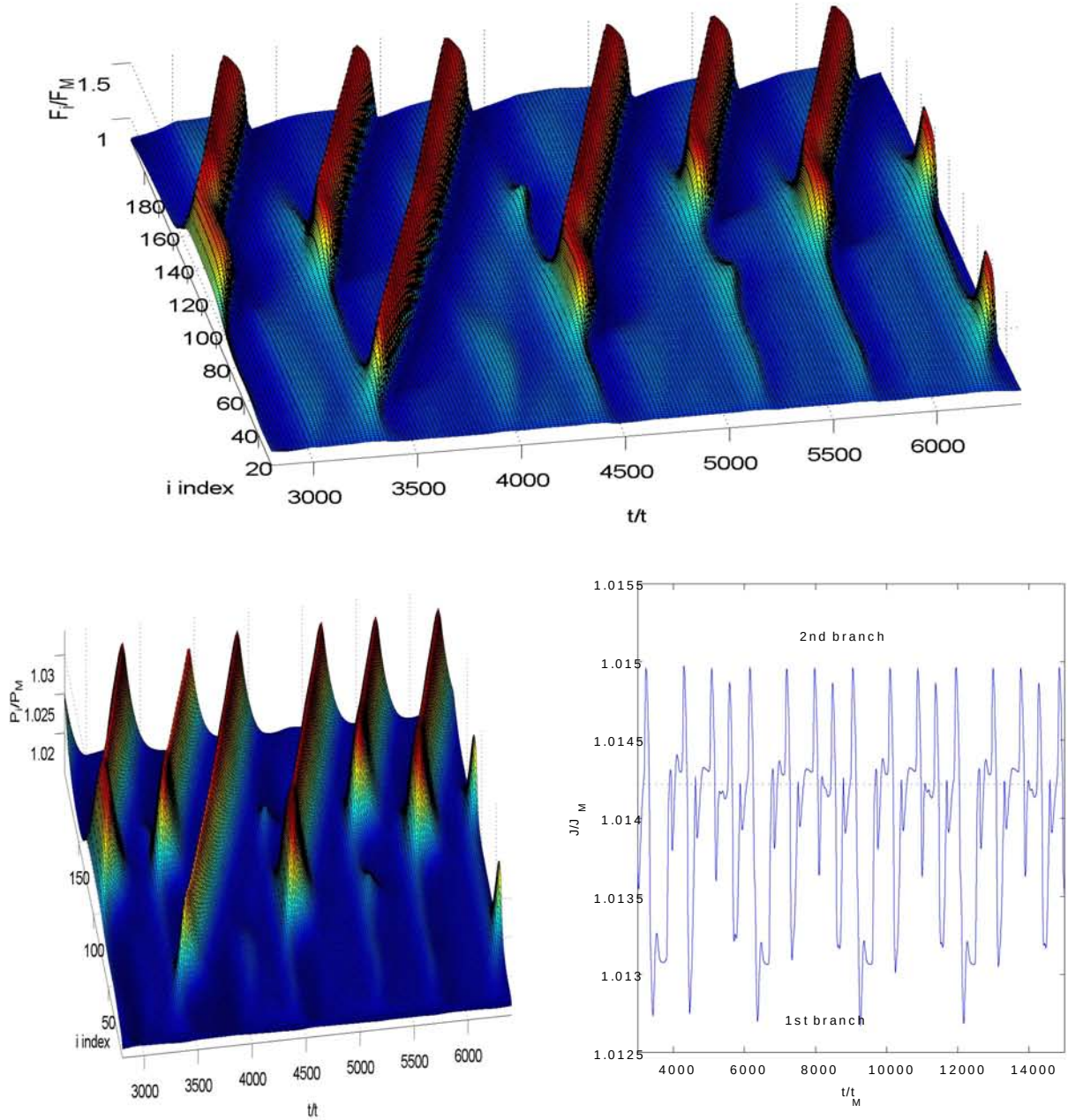

Figure A.9-24 SL $\mathcal{A}$ with parameters $\mathbf{V}$ =1.00417, $\beta = 268.18757$, $\nu = 8.44566$, $\sigma_2 = 1.05231$, $\mathbf{N}$ =199 and $\sigma_1 = 1.08343$

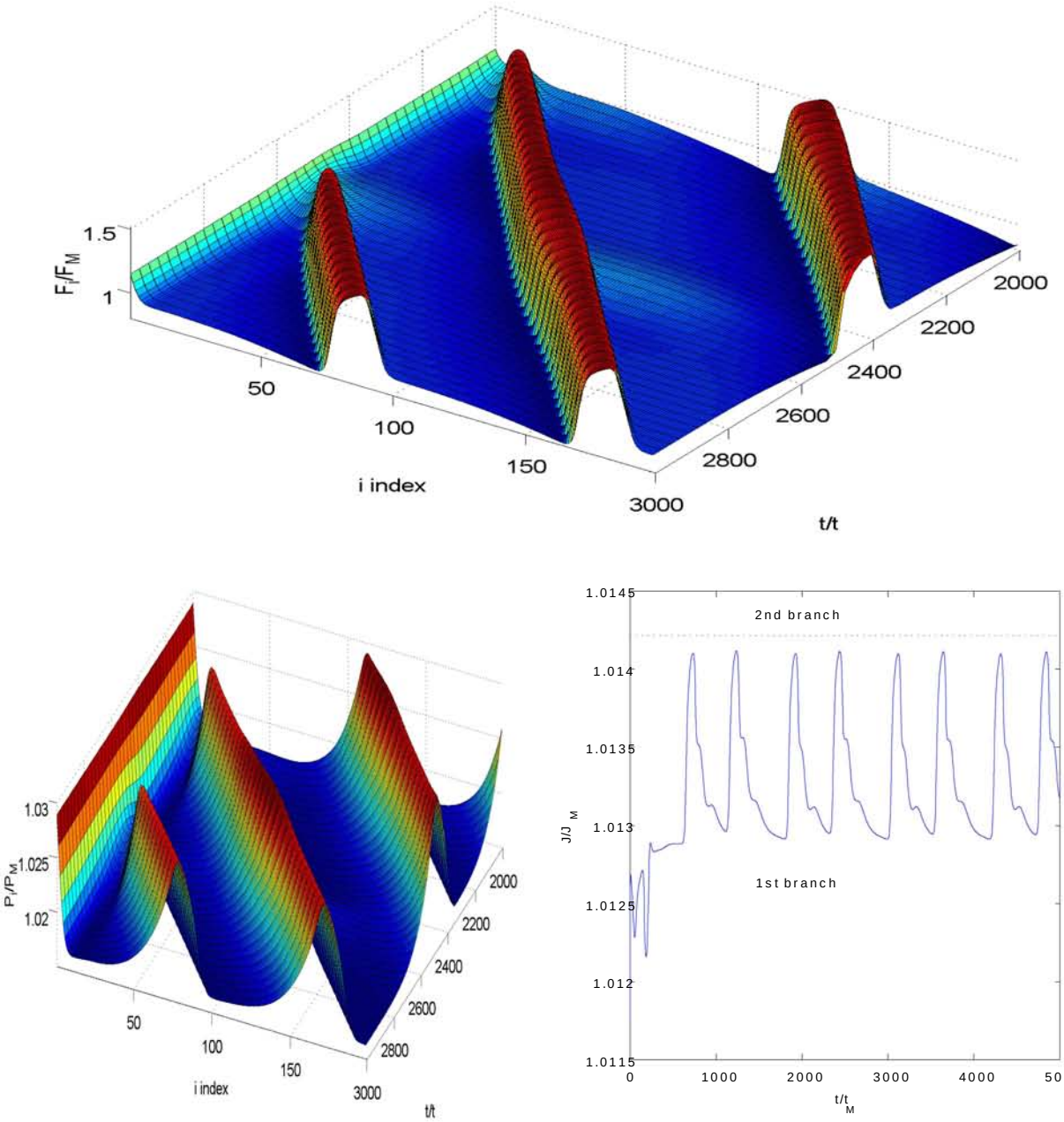

Figure A.9-25 SL $\mathcal{A}$ with parameters $\mathbf{V}$ =1.00417 $\beta = 268.18757$ $\nu = 8.44566$ $\sigma_2 = 1.05231$ $\mathbf{N}$ =199 and $\sigma_1 = 0.83413$

A.10 Appendix: Data

In this section we summarize some important data which are used in this work.

Fundamental constants

quantity	*Símbol*	*Value*
elemental charge	e	$1.60219 \cdot 10^{-19}\ As$
Electron Mass	m_e	$9.1056 \cdot 10^{-31}\ kg$
Dielectric constant of the vacuum	ε_0	$8.8.8542 \cdot 10^{-12}\ As/Vm$
Planck´s constant	$\hbar$	$1.05459 \cdot 10^{-34}\ Js$
Bolzmann´s constant	k_b	$1.38062 \cdot 10^{-23}\ J/K$
Velocity of light	c	$2.99793 \cdot 10^{8}\ ms^{-1}$

Other used parameters

Superlattices

SL $\mathcal{D}$	$AlAs/GaAs$	4nm / 10 nm
SL $\mathcal{C}$	$Al_{0.45}Ga_{0.55}As/GaAs$	4nm / 10 nm
SL $\mathcal{B}$	$Al_{0.3}Ga_{0.7}As/GaAs$	4nm / 10 nm
SL $\mathcal{A}$	$Al_{0.25}Ga_{0.75}As/GaAs$	4nm / 10 nm

Energy levels of the quantum wells

$\tilde{E}^{1-\Gamma}_{e(\mathcal{D})}(0) = 37.87\ meV$ $\tilde{E}^{2-\Gamma}_{e(\mathcal{D})}(0) = 152.51\ meV$ $\tilde{E}^{1-\Gamma}_{hh(\mathcal{D})}(0) = -1.527\ meV$
$\tilde{E}^{1-\Gamma}_{e(\mathcal{A})}(0) = 33.77\ meV$ $\tilde{E}^{2-\Gamma}_{e(\mathcal{A})}(0) = 126.29\ meV$ $\tilde{E}^{1-\Gamma}_{hh(\mathcal{A})}(0) = -1.526\ meV$
$\tilde{E}^{1-\Gamma}_{e(\mathcal{C})}(0) = 36.25\ meV$ $\tilde{E}^{2-\Gamma}_{e(\mathcal{C})}(0) = 143.27\ meV$ $\tilde{E}^{1-\Gamma}_{hh(\mathcal{C})}(0) = -1526.89\ meV$
$\tilde{E}^{1-\Gamma}_{e(\mathcal{B})}(0) = 34.67\ meV$ $\tilde{E}^{2-\Gamma}_{e(\mathcal{B})}(0) = 133.38\ meV$ $\tilde{E}^{1-\Gamma}_{hh(\mathcal{B})}(0) = -1526.59\ meV$
$\tilde{E}^{1-X}_{e(\mathcal{D})}(0) = 143.92\ meV$ $\tilde{E}^{1-X}_{e(\mathcal{A})}(0) = 386.82\ meV$ $\tilde{E}^{1-X}_{e(\mathcal{C})}(0) = 319\ meV$
$\tilde{E}^{1-X}_{e(\mathcal{B})}(0) = 369.93\ meV$

Energy gap

$E^{\Gamma}_{g(AlAs)} = 3.030\ eV$ $E^{\Gamma}_{g(Al_{0.25}Ga_{0.75}As)} = 1.897\ eV$ $E^{\Gamma}_{g(GaAs)} = 1.519\ eV$
$E^{\Gamma}_{g(Al_{0.45}Ga_{0.55}As)} = 2.198\ eV$

Dielectric Constants

$\varepsilon_{(Al_{0.45}Ga_{0.55}As)} = 11.787\ \varepsilon_0 \quad \varepsilon_{(AlAs)} = 10.06\ \varepsilon_0 \quad \varepsilon_{(Al_{0.25}Ga_{0.75}As)} = 12.415\ \varepsilon_0$
$\varepsilon_{(GaAs)} = 13.2\ \varepsilon_0$

Efective Masses

$m^{*\Gamma}_{e(Al_{0.45}Ga_{0.55}As)} = 0.10435\ m_e \quad m^{*\Gamma}_{e(GaAs)} = 0.067\ m_e \quad m^{*\Gamma}_{e(AlAs)} = 0.15\ m_e$
$m^{*X}_{e(AlAs)} = 1.3\ m_e \quad m^{*\Gamma}_{hh(AlAs)} = 0.478\ m_e \quad m^{*X}_{e(GaAs)} = 1.1\ m_e$
$m^{*\Gamma}_{hh(Al_{0.25}Ga_{0.75}As)} = 0.4023\ m_e \quad m^{*\Gamma}_{hh(GaAs)} = 0.377\ m_e \quad m^{*\Gamma}_{lh(AlAs)} = 0.208\ m_e$
$m^{*\Gamma}_{e(Al_{0.25}Ga_{0.75}As)} = 0.0878\ m_e \quad m^{*X}_{e(Al_{0.25}Ga_{0.75}As)} = 1.25\ m_e \quad m^{*\Gamma}_{lh(GaAs)} = 0.0905\ m_e$

Conduction and valence bands offset

$\Delta E_v^{(\mathcal{D})\Gamma} = 529\ meV \quad \Delta E_c^{(\mathcal{D})\Gamma} = 982\ meV$
$\Delta E_v^{(\mathcal{A})\Gamma} = 132.25\ meV \quad \Delta E_c^{(\mathcal{A})\Gamma} = 245.5\ meV$
$\Delta E_v^{(\mathcal{C})\Gamma} = 238.05\ meV \quad \Delta E_c^{(\mathcal{C})\Gamma} = 441.9\ meV$
$\Delta E_v^{(\mathcal{B})\Gamma} = 158.7\ meV \quad \Delta E_c^{(\mathcal{B})\Gamma} = 294.6\ meV$

The first maximum of the current

$\tilde{v}_M^{(\mathcal{D})} = 568.2\ cm/s \quad \tilde{F}_M^{(\mathcal{D})} = 1.47 \cdot 10^4\ V/cm$
$\tilde{v}_M^{(\mathcal{A})} = 256923\ cm/s \quad \tilde{F}_M^{(\mathcal{A})} = 1.68 \cdot 10^4 V/cm$
$\tilde{v}_M^{(\mathcal{C})} = 31227\ cm/s \quad \tilde{F}_M^{(\mathcal{C})} = 1.52 \cdot 10^4\ V/cm$
$\tilde{v}_M^{(\mathcal{B})} = 142058\ cm/s \quad \tilde{F}_M^{(\mathcal{B})} = 1.60 \cdot 10^4\ V/cm$

Other data

$\tilde{T} = 200\ ^oK \quad \tilde{w} = 100\ \mathring{A} \quad \tilde{d} = 40\ \mathring{A}$

A.11 Appendix: CD Relation of Figures and movies.

FIGURE	DESCRIPTION	FILE
Figure 6-2	$F(t,i)$	CD:\movies\movie1.avi
Figure 6-2	$P(t,i)$	CD:\movies\movie2.avi
Figure 6-6 **(a)**	$F(t,i)$	CD:\movies\movie3.avi
Figure 6-6 **(b)**	$F(t,i)$	CD:\movies\movie4.avi
Figure 6-6 **(c)**	$F(t,i)$	CD:\movies\movie5.avi
Figure 6-9	$F(t,i)$	CD:\movies\movie6.avi
Figure 6-9	$P(t,i)$	CD:\movies\movie7.avi
Figure 6-10	$F(t,i)$	CD:\movies\movie8.avi
Figure 6-10	$P(t,i)$	CD:\movies\movie9.avi
Figure 6-11(a)	$F(t,i)$	CD:\movies\movie10.avi
Figure 6-11(a)	$P(t,i)$	CD:\movies\movie11.avi
Figure 6-11(c)	$F(t,i)$	CD:\movies\movie12.avi
Figure 6-11(c)	$P(t,i)$	CD:\movies\movie13.avi
Figure 7-2	$F(t,i)$	CD:\movies\movie14.avi
Figure 7-3	$F(t,i)$	CD:\movies\movie15.avi
Figure 7-3	$P(t,i)$	CD:\movies\movie16.avi
Figure A.6-2 **(a)**	$F(t,i)$	CD:\movies\movie17.avi
Figure A.6-2 **(a)**	$P(t,i)$	CD:\movies\movie18.avi
Figure A.6-2**(b)**	$F(t,i)$	CD:\movies\movie19.avi
Figure A.6-2**(b)**	$P(t,i)$	CD:\movies\movie20.avi
Figure A.6-3**(a)**	$F(t,i)$	CD:\movies\movie21.avi
Figure A.6-3**(a)**	$P(t,i)$	CD:\movies\movie22.avi
Figure A.6-3**(b)**	$F(t,i)$	CD:\movies\movie23.avi
Figure A.6-3**(b)**	$P(t,i)$	CD:\movies\movie24.avi
Figure A.6-4	$F(t,i)$	CD:\movies\movie25.avi
Figure A.6-4	$P(t,i)$	CD:\movies\movie26.avi
Figure A.6-5**(a)**	$F(t,i)$	CD:\movies\movie27.avi
Figure A.6-5**(a)**	$P(t,i)$	CD:\movies\movie28.avi
Figure A.6-5**(b)**	$F(t,i)$	CD:\movies\movie29.avi

FIGURE	**DESCRIPTION**	**FILE**
Figure A.6-5**(b)**	$P(t,i)$	CD:\movies\movie30.avi
Figure A.6-5**(c)**	$F(t,i)$	CD:\movies\movie31.avi
Figure A.6-5**(c)**	$P(t,i)$	CD:\movies\movie32.avi
Figure A.6-5**(d)**	$F(t,i)$	CD:\movies\movie33.avi
Figure A.6-5**(d)**	$P(t,i)$	CD:\movies\movie34.avi
Figure A.9-10	$F(t,i)$	CD:\movies\movie35.avi
Figure A.9-10	$P(t,i)$	CD:\movies\movie36.avi
Figure A.9-11	$F(t,i)$	CD:\movies\movie37.avi
Figure A.9-11	$P(t,i)$	CD:\movies\movie38.avi
Figure A.9-12	$F(t,i)$	CD:\movies\movie39.avi
Figure A.9-12	$P(t,i)$	CD:\movies\movie40.avi
Figure A.9-13	$F(t,i)$	CD:\movies\movie41.avi
Figure A.9-13	$P(t,i)$	CD:\movies\movie42.avi
Figure A.9-16	$F(t,i)$	CD:\movies\movie43.avi
Figure A.9-16	$P(t,i)$	CD:\movies\movie44.avi
Figure A.9-17	$F(t,i)$	CD:\movies\movie45.avi
Figure A.9-17	$P(t,i)$	CD:\movies\movie46.avi
Figure A.9-18	$F(t,i)$	CD:\movies\movie47.avi
Figure A.9-18	$P(t,i)$	CD:\movies\movie48.avi
Figure A.9-20	$F(t,i)$	CD:\movies\movie49.avi
Figure A.9-20	$P(t,i)$	CD:\movies\movie50.avi
Figure A.9-22	$F(t,i)$	CD:\movies\movie51.avi
Figure A.9-22	$P(t,i)$	CD:\movies\movie52.avi
Figure A.9-23	$F(t,i)$	CD:\movies\movie53.avi
Figure A.9-23	$P(t,i)$	CD:\movies\movie54.avi
Figure A.9-24	$F(t,i)$	CD:\movies\movie55.avi
Figure A.9-24	$P(t,i)$	CD:\movies\movie56.avi
Figure A.9-25	$F(t,i)$	CD:\movies\movie57.avi
Figure A.9-25	$P(t,i)$	CD:\movies\movie58.avi

A.12 Resumen en castellano

La comprensión del comportamiento de las superredes semiconductoras es esencial para el diseño y la fabricación de estos dispositivos nanoelectrónicos, que actualmente son utilizados en la ciencia y en la industria como osciladores de alta frecuencia, láseres de cascada cuántica, fotodetectores, monitorización de la polución, diagnóstico y control de la combustión y la catálisis en la industria de la automoción, etc..

Esta tesis se centra principalmente en la descripción y en el estudio del transporte de carga mediante el mecanismo de *Túnel Resonante Secuencial* de las superredes $Al_xGa_{1-x}As/GaAs$ fotoexcitadas tipo I, bajo los regímenes de voltaje y corriente constante. La configuración de los parámetros externos e intrínsecos de la superred, puede generar una dinámica rica en distintos patrones y comportamientos. Además, el proceder de las ondas de carga y la variación del campo eléctrico en estas superredes es muy similar a las soluciones descritas en el sistema de ecuaciones de FitzHugh-Nagumo, por lo que en esta tesis también abordamos dicho sistema para poder aplicar más tarde nuestros resultados.

A continuación se resume el contenido de todos los capítulos y anexos de esta tesis, explicando las aportaciones originales del trabajo, la metodología empleada y alguna de las conclusiones alcanzadas.

En el capítulo 2 introducimos los conceptos básicos y necesarios para comprender la física de las superredes que se desarrolla en esta tesis. Mediante la estructura de bandas de los semiconductores diferenciamos entre superredes tipo I y tipo II, y también, entre las superredes fuerte o débilmente acopladas. Describimos los diferentes regímenes de transporte y tratamos cómo el campo eléctrico y el acoplamiento entre pozos vecinos determinan cuál es el principal régimen de transporte en la superred.

Mediante la ecuación de Bolzman, la ecuación de schrödinger, la regla de oro de Fermi y otros métodos, deducimos la velocidad y la difusión de los portadores de carga; además introducimos también el concepto de conductancia diferencial negativa.

Dada su importancia, se decriben los principales métodos de *scattering* en una superred, y se resaltan aquellos procesos que pueden ser regulados mediante la composición y mediante la construcción de la superred.

El tercer capítulo está enfocado al estudio de las soluciones del sistema de ecuaciones de FitzHugh-Nagumo (**FHN**). Se ha constatado que en este sistema, la velocidad y los perfiles de los pulsos son modificados por el valor del parámetro ϵ.

Por ende, en este capítulo se desarrolla un método para obtener una mejor aproximación de los distintos tipos de frentes de onda. Además se incluye dentro de esta nueva aproximación, la corrección de orden ϵ con el que se mejora la descripción de las *colas* y los *picos* de estos pulsos.

Utilizando métodos asintóticos corregidos se ha reconstruido numéricamente diferentes pulsos y se ha comprobado que con la nueva mejora de la descripción de los frentes, las reconstrucciones se ajustan mucho mejor a la forma de los pulsos **FHN**. Algunos métodos y técnicas empleadas en esta sección son también utilizados en los capítulos posteriores.

En el cuarto capítulo se introduce el modelo físico para las superredes $Al_xGa_{1-x}As/GaAs$ tipo I, no dopadas y fotoexcitadas que conducen mediante el régimen de *transporte resonante secuencial*. En él, se tiene en cuenta los órdenes de magnitud de las escalas temporales de los diferentes procesos físicos relacionados con el transporte y la creación-destrucción de pares electrón-hueco.

Estas consideraciones proporcionan una nueva relación de ecuaciones adimensionales discretas del modelo, las cuales permiten describir diferentes dinámicas en la superred, en función de la velocidad media de los portadores de carga y la intensidad de la fotoexcitación.

Los procesos cuánticos en el transporte, están desarrollados e introducidos en el término de la corriente del modelo. Además, se ha reflejado el hecho de que la recombinación de pares electrón-hueco decrece con el campo eléctrico aplicado, lo cual, aporta necesariamente una nueva visión de las distintas dinámicas del transporte de carga en la superred.

Mediante simulación numérica de la ecuación de schrödinger se han obtenido para cuatro superredes distintas, la función de recombinación, velocidad y difusión en función del campo eléctrico aplicado a un pozo cuántico. Modificando la fotoexcitación, se han obtenido ocho configuraciones distintas para estas superredes.

El contenido de aluminio en las barreras de la superred repercute en la forma y en el valor de la función de la velocidad de los portadores de carga. Lo cual se ve reflejado en los distintos parámetros adimensionales del modelo y en la curva característica corriente-voltaje asociada a cada superred.

En el quinto capítulo se describen los distintos frentes, pulsos y trenes de onda que se pueden desarrollar en las superredes $Al_xGa_{1-x}As/GaAs$ tipo I, fotoexcitadas y bajo la condición de corriente constante. Se distinguen dos tipos de soluciones, en los dos rangos de fotoexcitación:

-*Alta iluminación láser ($\delta \to 0$):* en el cual se representan los frentes, los pulsos de velocidad negativa, los pulsos con una y dos soluciones homogéneas estables, y por último los trenes de onda.

-*Baja iluminación láser ($\delta \to \infty$):* en el que se describen los frentes y los dipolos.

En el límite de alta fotoexcitación o alta iluminación láser, se presenta y se desarrolla la teoría corregida de los frentes de onda. Se calcula y se compara su velocidad con respecto a esta nueva teoría, obteniendo unos buenos resultados.

Se presenta la teoría que explica la dinámica de los pulsos con velocidad negativa y mediante reconstrucciones asintóticas se demuestra sus diferencias con respecto a los pulsos de medio excitable. Se analiza la velocidad de estos nuevos pulsos con respecto a los parámetros adimensionales δ y ν.

En el límite de baja fotoexcitación, se analiza la dinámica de los dos tipos de frentes y mediante una reconstrucción asintótica, demostramos esta aproximación.

En el capítulo 6 describimos, en ambos regímenes de iluminación láser, las estructuras dinámicas y estáticas existentes en las superredes $Al_xGa_{1-x}As/GaAs$ tipo I, fotoexcitadas y bajo la condición de voltaje constante. Analizamos la forma y las frecuencias de las oscilaciones autosostenidas de la corriente en función de parámetros modulables como el voltaje, la resistividad de los contactos, el número de pozo cuánticos, etc..

Finalmente, en el capítulo 7, obtenemos y resolvemos el sistema de ecuaciones necesarias para poder estudiar mediante los coeficientes de Lyapunov, el caos en las soluciones obtenidas del modelo bajo la condición de voltaje constante.

Dada la complejidad en la resolución de dicho sistema, primero se realiza un estudio mediante el análisis de frecuencias y centros atractores, para indicarnos la posibilidad de un sistema caótico. Demostramos la existencia de caos en el régimen de alta iluminación láser y apreciamos un comportamiento estable en el rango de baja iluminación láser.

En el apéndice A.1, se calculan y se describen tres nuevas formas de adimensionalizar el modelo físico expuesto en el cuarto capítulo de la presente tesis. Las cuales, son utilizadas en algunos de los siguientes anexos.

En el segundo apéndice, se analiza los diferentes parámetros que repercuten en la forma y en el valor de las funciones de velocidad, difusión y recombinación electrón-hueco del modelo.

Las soluciones estacionarias del modelo desarrollado en la presente tesis son estudiadas en el apéndice A.3. Aquí, se muestra la relación corriente-voltaje dependiente de cada superred $Al_xGa_{1-x}As/GaAs$ y además se demuestra su relación con la potencia de fotoexcitación. Los perfiles estacionarios de campo eléctrico entre el ánodo y el cátodo, y entre los dominios y los contactos, son obtenidos, justificados y explicados mediante la intensidad de la fuente fotoexcitadora.

A continuación, en el siguiente apéndice (A.4) detallamos y analizamos el proceso de la fotoluminiscencia en las superredes. Utilizando varios perfiles de carga y campo eléctrico de ondas,

obtenemos el espectro temporal de la fotoluminiscencia y descubrimos su importancia a la hora de detectar experimentalmente las soluciones dinámicas descritas en secciones anteriores.

En el quinto apéndice, son descritos mediante simulación numérica los frentes y los pulsos que se pueden desarrollar en el primer pico de la corriente. Se demuestra que dichos pulsos sólo se pueden observar bajo la condición de corriente constante, con baja fotoexcitación y cuando el término de la difusión es despreciable.

En el apéndice A.6 se introduce el problema de las superredes no homogéneamente iluminadas. En primer lugar se analiza la dependencia con el campo eléctrico de la función generación pares electrón-hueco con respecto a la frecuencia de excitación de un láser ($\gamma(F_i,\hbar\omega_{exc})$).

Utilizando una adimensionalización adecuada e iluminando de manera heterogénea diferentes regiones de una superred, observamos los efectos producidos en la corriente, bajo la aplicación de la condición de voltaje constante sobre dicha superred. Como consecuencia, se analizan y se explican los efectos de las discontinuidades en la iluminación.

En los dos siguientes apéndices (A.7 y A.8), se describen las dinámicas de los frentes en los regímenes de alta y baja fotoexcitación. Se definen las corrientes críticas para las cuales los frentes se anclan y pasan a ser una solución estacionaria del sistema. Mediante la teoría de los pozos "activos" se obtienen las expresiones que permiten aproximar la velocidad de ambos tipos de frentes cerca de las corrientes críticas. Se demuestra que la aproximación de la velocidad mejora cuando se consideran más pozos activos en la descripción de un frente.

Finalmente en el apéndice A.9, mediante diferentes simulaciones numéricas representadas en las distintas figuras anexadas, se desarrolla con más profundidad los procesos relacionados con las oscilaciones autosostenidas de la corriente y los diversos frentes y ondas observados bajo la condición de corriente constante.

Bibliography

[1] L. L. Bonilla, J. Galán, J. A. Cuesta, F. C. Martínez, and J. M. Molera, Phys. Rev. B **50**, 8644 (1994).

[2] L. L. Bonilla, in *Nonlinear Dynamics and Pattern Formation in Semiconductors and Devices*, edited by F.-J. Niedernostheide. Page 1. Springer, Berlin, 1995.

[3] H. T. Grahn, H. Schneider, and K. von Klitzing, Phys. Rev. B **41**, 2890 (1990).

[4] S. H. Kwok, T. B. Norris, L. L. Bonilla, J. Galán, J. A. Cuesta, F. C. Martínez, J. M. Molera, H. T. Grahn, K. Ploog, and R. Merlin, Phys. Rev. B **51**, 10171 (1995).

[5] M. Hosoda, H. Mimura, N. Ohtani, K. Tominaga, T. Watanabe, K. Fujiwara, and H. T. Grahn, Appl. Phys. Lett. **69**, 500 (1996).

[6] N. Ohtani, M. Hosoda, and H. T. Grahn, Appl. Phys. Lett. **70**, 375 (1997).

[7] A. M. Tomlinson, A. M. Fox, J. E. Cunningham, and W. Y. Jan, Appl. Phys. Lett. **75**, 2067 (1999).

[8] K. J. Luo, S. W. Teitsworth, H. Kostial, H. T. Grahn, and N. Ohtani, Appl. Phys. Lett. **74**, 3845 (1999).

[9] N. Ohtani, N. Egami, K. Fujiwara, and H. T. Grahn, Solid-State Electron. **42**, 1509 (1998).

[10] L. L. Bonilla and H. T. Grahn, Rep. Prog. Phys. **68**, 577 (2005).

[11] A. Perales, L. L. Bonilla, M. Moscoso, and J. Galán, Int. J. Bifurcations and Chaos **11**, 2817 (2001).

[12] J. P. Keener and J. Sneyd, *Mathematical Physiology* (Springer, New York, 1998).

[13] A. Carpio and L. L. Bonilla, SIAM J. Appl. Math. **63**, 619 (2003).

[14] A. Carpio, Physica D **207**, 117 (2005).

[15] L. L. Bonilla and S. W. Teitsworth, *Nonlinear wave methods for charge transport* (Wiley, New York).

[16] H. T. Grahn, *Introduction to Semiconductor Physics* (World Scientific, Singapore, 1999).

[17] Y. Kuramoto, *Chemical oscillations, waves and turbulence* (Dover, New York, 2003).

[18] J. I. Arana, L. L. Bonilla, and H. T. Grahn, *Wave fronts,pulses and wave trains in photoexcited superlattices behaving as excitable or oscillatory media*, unpublished.

[19] J. Frenkel and T. Kontorova, *On the theory of plastic deformation and twinning*, J. Phys. USSR **13**, 1-10 (1938).

[20] A. Carpio and L.L. Bonilla, *Edge dislocations in crystal structures considered as traveling waves of discrete models*. Phys. Rev. Lett. **90**, 135502 (2003).

[21] J. W. Cahn, *Theory of crystal growth and interface motion in crystalline materials*, Acta Metallurgica **8** (1960), 554–562.

[22] L. L. Bonilla, *Theory of nonlinear charge transport, wave propagation and self-oscillations in semiconductor superlattices*, J. Phys. Condensed Matter **14** (2002), R341–R381.

[23] A. Carpio, L. L. Bonilla, and G. Dell'Acqua, *Wave front motion in semiconductor superlattices*, Phys. Rev. E **64**, 036204 (2001).

[24] L. L. Bonilla and S. W. Teitsworth, *Nonlinear wave methods for charge transport*, Wiley, Weinheim, 2010.

[25] G. Grüner, The dynamics of charge-density waves, Rev. Modern Phys. **60** (1988), 1129–1181.

[26] A. C. Scott, The electrophysics of a nerve fiber, Rev. Modern Phys. **47** (1975), 487–533.

[27] A. R. A. Anderson and B. D. Sleeman, W*ave front propagation and its failure in coupled systems of discrete bistable cells modelled by FitzHugh-Nagumo dynamics*, Internat. J. Bifur. Chaos Appl. Sci. Engrg. **5** (1995), 63–74.

[28] J. P. Keener and J. Sneyd, *Mathematical Physiology*, Springer, New York, 1998, Chapter 9.

[29] B. Zinner, *Existence of traveling wavefront solutions for the discrete Nagumo equation*, J. Differential Equations **96** (1992), 1–27.

[30] D. Hankerson and B. Zinner, *Wave fronts for a cooperative tridiagonal system of differential equations*, J. Dyn. Differential Equations **5** (1993), 359–373.

[31] A.-M. Filip and S. Venakides, *Existence and modulation of traveling waves in particle chains*. Comm. Pure Appl. Math. **52**, 693-735 (1999).

[32] P.C. Fife, *Mathematical aspects of reacting and diffusing systems*, Lecture Notes in Biomathematics **28**. Springer-Verlag, Berlin, 1979.

[33] J. P. Keener, *Propagation and its failure in coupled systems of discrete excitable cells*, SIAM J. Appl. Math. **47** (1987), 556–572.

[34] J.R. King and S.J. Chapman, *Asymptotics beyond all orders and Stokes lines in nonlinear differential-difference equations*. Eur. J. Appl. Math. **12**, 433-463 (2001).

[35] G. Fáth, *Propagation failure of traveling waves in a discrete bistable medium*. Physica D **116**, 176-190 (1998).

[36] A. Carpio and L.L. Bonilla, *Wave front depinning transition in discrete one-dimensional reaction-diffusion systems*. Phys. Rev. Lett. **86**, 6034-6037 (2001).

[37] A. Carpio and L.L. Bonilla, *Depinning transitions in discrete reaction-diffusion equations*. SIAM J. Appl. Math. **63**, 1056-1082 (2003).

[38] A. Carpio and L.L. Bonilla, *Pulse propagation in discrete systems of coupled excitable cells*. SIAM J. Appl. Math. **63**, 619-635 (2003).

[39] A. Carpio, *Asymptotic construction of pulses in the Hodgkin Huxley model for myelinated nerves*. Phys. Rev. E **72**, 011905 (2005).

[40] R. Hobart, *Peierls-barrier minima*, J. Appl. Phys., 36 (1965), pp. 1948–1952.

[41] A. Amann, A. Wacker, L. L. Bonilla, and E. Schöll, *Dynamic scenarios of multistable switching in semiconductor superlattices*, Phys. Rev. E (3), 63 (2001), pp. 1–8.

[42] J. Kastrup, R. Hey, K. Ploog, H. T. Grahn, L. L. Bonilla, M. Kindelan, M. Moscoso, A. Wacker, and J. Galán, *Electrically tunable GHz oscillations in doped GaAs-AlAs superlattices*, Phys. Rev. B (3), 55 (1997), pp. 2476–2488.

[43] L.L. Bonilla, J. Phys.: Cond. Matter **14**, R341 (2002).

[44] G. Bastard *Wave mechanics applied to semiconductor heterostructures* Les Éditions de Physique.Halsted Press (1988)

[45] Gloria Platero and Ramón Aguado *Photon-assisted transport in semiconductor nanostructures* (2004)

[46] Álvaro Perales Eceiza *Tesis Universidad Carlos III de Madrid: Dinámica electrónica en superredes semiconductoras* (2003)

[47] L.L. Bonilla, J.Galán, J.A. Cuesta, F.C. Martínez, and J.M. Molera *Dynamics of electric field domains and oscilations of the photocurrent in a simple superlattice model.* Phys Rw B Vol 50, No 12 /8644 (1994)

[48] Steven H. Strogatz *Nonlinear dinamics and chaos* Perseus Books (1998)

[49] G.Benettin, L.Galgani, A. Giorgilli and J.M.Strelcyn, Mecanica 15, 21 (1980)

[50] O.M.Bulashenco, M.J. García y L.L. Bonilla *Chaotic dynamics of elecric-field domains in periodically driven superlattices* Physical RWB Vol 53 N^{a}15 10008 (1996)

[51] Alan WOLF, Jack B. SWIFT, Harry L. SWINNEY and John A. VASTANO "*Determining Lyapunov Exponents from a Time Series*," Physica D, Vol. 16, pp. 285-317, 1985

[52] L. L. Bonilla and S. W. Teitsworth, *Nonlinear wave methods for charge transport.* Wiley, New York, 2010.

[53] J. I. Arana, L. L. Bonilla and H. T. Grahn, Phys. Rev. B **81**, 035322 (2010).

[54] R. Courant and D. Hilbert, Methods of Mathematical Physics, vol. 2. Interscience, New York 1962.

[55] L. L. Bonilla, M. Kindelan, M. Moscoso and S. Venakides, SIAM J. Appl. Math. **57**, 1588 (1997).

[56] M.Hosoda, H.Mimura, N.Ohtami, K. Tominaga, K. Fujita, T Watanabe, M.Nakayama and H. Inomata *Observation of the* $\Gamma - X$ *resonances in type-I GaAs/AlAs semiconductor superlattices: Anomaly in photoluminescence* Phys Rw B Vol 55, 113689 (1997)

[57] Jörg Kastrup *Tesis Paul Drude Intitut: The superlattice oscilator: From stable to unstable electric field domains*, Berlin (1995)

[58] A.Carpio *Wave trains, Self-oscilations and synchronization in discrete media* Physica D 207 (2005) 117-136

[59] A.Carpio and L.L.Bonilla *Depinning transitions in discrete reaction-difusion equations* Siam J. APPL. Math Vol 63, No 3, (2003) pp 1056-1082

[60] Andreas Wacker and Antti-Pekka Jauho *Quantum Transport: The Link between Standard Approaches in Superlattices* Phys. Rev. Lett. 80, 369–372 (1998)

[61] H.T. Grahn, K. von Klitzing, and K.Ploog *Electrical transport in narrow-miniband semiconductor superlattices* Phys Rw B Vol 43,No 14 /12094 (1991)

[62] S.Rott, N.Linder and H.Döler *Field dependence of the hopping drift velocity in semiconductor superlattices* Phys Rw B Vol 65, 195301 (2002)

[63] Sadao Adachi *$GaAs, AlAs, Al_xGa_{1-x}As$, Material parameters for use in research and device aplications* J. Applied Physics Vol 58, Issue 3, pp. R1-R29 (1985)

[64] Stephan Rott *Tesis Friedrich-Alexander-Universität Erlangen-Nürnberg: Theory of electronic transport in semiconductor superlattices* (1999)

[65] K.Kalna, S.Roy, A.Asenov, K.Elgaid, I. Thayne *Scaling of pseudomorphic high electron mobility transistors to decanano dimensions* Solid-State Electronics 46 631-638 (2002)

[66] Craig Pryor *Geometry and material parameter dependence of InAs/GaAs Quantum dot electronic structure* Phys Rw B Vol 60 2869 (1999)

[67] B R Nag *Interface roughness scattering limited mobility in $AlAs/GaAs$, $Al_{0.3}Ga_{0.7}As/GaAs$ and $Ga_{0.5}InP/GaAs$ quantum wells.*Semicond. Sci. Technol. 19 (2004) 162-166

[68] Esaki L and Tsu R *Superlattice and negative differential conductivity in semiconductors* IBM J. Res. Dev. 14 61 (1970)

[69] BonillaLL *Dynamics of electric field domains in superlattices Nonlinear Dynamics and Pattern Formation in Semiconductors and Devices* ed F-J Niedernostheide (Berlin: Springer) pp 1–20 (1995)

[70] Bonilla L L, Platero G and S´anchez D 2000 *Microscopic derivation of transport coefficients and boundary conditions in discrete drift–diffusion models of weakly coupled superlattices* Phys. Rev. B 62 2786 (2000)

[71] M Alvaro and L L Bonilla *Nonequilibrium free energy, H theorem and self-sustained oscillations for Boltzmann-BGK descriptions of semiconductor superlattices* (2010)

[72] Federico Capasso et al *Resonant Tunneling Through Double Barriers, Perpendicular Quantum Transport Phenomena in Superlattices, and Their Device Applications.* IEEE journal of quantum electronics vol. QE-22 no 9 september (1986)

[73] H.Hilmer et all *Optical investigation on the mobility of two-dimensional excitons in $GaAs/Ga_{1-x}Al_xAs$ quantum wells.* Physical Review B volume 39 number 15 1may (1989)

[74] Ignacio Plans Beriso *PhD Thesis Discrete models of dislocations in crystal lattices: Formulation, analysis and applications* (2007)

[75] R. Martini,G. Klose, H. G. Roskos, H. Kurz, H. T. Grahn and R. Hey *Superradiant emission from Bloch oscillations in semiconductor superlattices* Physical Review B volume 54 number 20 Nov (1996)

[76] M. Wienold, L. Schrottke, M. Giehler, R. Hey, and H. T. Grahn *Nonlinear transport in quantum-cascade lasers: The role of electric-field domain formation for the laser characteristics* Journal of applied physics 109, 073112 (2011)